Advancements in remote sensing of the thermodynamic cloud phase using Meteosat satellites

Johanna Mayer

München 2024

Advancements in remote sensing of the thermodynamic cloud phase using Meteosat satellites

Johanna Mayer

Dissertation
der Fakultät für Physik
der Ludwig-Maximilians-Universität
München

vorgelegt von
Johanna Mayer
aus München

München, den 20. August 2024

Contents

Zusammenfassung

Wolken können aus flüssigen Tröpfchen, Eiskristallen oder einer Mischung aus beidem, genannt Mischphase, bestehen. Kenntnisse über die thermodynamische Phase von Wolken sind essentiell für das Verständnis des Strahlungshaushalts der Erde, der Prozesse in Wolken und Atmosphäre und des Wasserkreislaufs. Die mikrophysikalischen Prozesse, die Wolkenphasen und Phasenübergänge steuern, sind jedoch nur unzureichend verstanden, was zu großen Unsicherheiten bei Klimaprognosen führt. Insbesondere Mischphasenwolken stellen nach wie vor eine Herausforderung dar. Die zuverlässigsten Methoden zur Bestimmung der Wolkenphase mit Hilfe von Satelliten sind derzeit synergetische Lidar-Radar Methoden wie das Produkt DARDAR (liDAR-raDAR). Die aktive Fernerkundung wird jedoch durch ihr schmales Sichtfeld und ihre geringe zeitliche Auflösung eingeschränkt. Diese fehlenden Informationen können von geostationären passiven Sensoren geliefert werden. Die passive Fernerkundung von Wolkenphasen ist jedoch schwierig, und insbesondere die komplexe Mischphase wird nur selten untersucht. Diese Studie befasst sich mit diesen Herausforderungen und liefert eine umfassende Analyse des Potenzials des SEVIRI-Instruments an Bord des geostationären Satelliten Meteosat Second Generation zur Phasenerkennung. Zunächst zeigt die Analyse der geographischen und zeitlichen Verteilung der Wolkenphasen auf der SEVIRI-Scheibe unter Verwendung der zuverlässigen DARDAR-Daten als "Ground Truth", dass alle Wolkenphasen für SEVIRI relevant sind, einschließlich der Mischphase. Zweitens wird der Informationsgehalt der Brightness Temperature Differences (BTDs) von SEVIRI-Kanälen im atmosphärischen Fenster untersucht. Die Sensitivität der BTDs gegenüber allen strahlungsrelevanten Wolkenparametern wird mittels Strahlungstransferrechnungen untersucht und zeigt eine komplexe Phasenabhängigkeit der BTDs, wobei die dominante Verbindung zwischen BTDs und Phase über die Wolkentemperatur besteht. Diese Analyse trägt zum Verständnis des Potenzials und der Limitierungen von BTDs für die Phasenbestimmung bei. Basierend auf diesen Ergebnissen wird eine neue Methode, PRObabilistic cloud top Phase retrieval for SEVIRI (ProPS), entwickelt. Es verwendet einen probabilistischen Bayes'schen Ansatz zur Erkennung von Wolken und deren Phase, der auf kollokierten DARDAR-SEVIRI Daten basiert. ProPS unterscheidet zwischen wolkenfreiem Himmel, optisch dünnen Eis-, optisch dicken Eis-, Mischphasen-, unterkühlten Wasser- und warmen Wasserwolken. Die Methode hat eine hohe Detektionswahrscheinlichkeit (>80%) für Wasser- und Eiswolken und klassifiziert mehr als die Hälfte der schwierigen Mischphasen- und unterkühlten Wasserwolken korrekt. Die neue Methode ermöglicht die Untersuchung der zeitlichen Entwicklung von Wolkenphasen, insbesondere auch von Mischphasenwolken und unterkühlten Wasserwolken, die bisher nur selten mit geostationären Satelliten untersucht wurden. Diese Studie leistet damit einen Beitrag zu den weltweiten Bemühungen, die Wolkenphase zu beobachten und zu verstehen, um ihre Darstellung in numerischen Modellen zu verbessern und die Unsicherheiten von Klimaprognosen zu reduzieren.

Abstract

Clouds can consist entirely of liquid droplets, ice crystals or a mixture of both, called mixed-phase. Knowledge of the thermodynamic cloud phase is crucial for understanding the Earth's radiation budget, cloud and atmospheric processes, and the water cycle. However, the microphysical processes governing cloud phase and phase transitions are not well understood, leading to large uncertainties in climate predictions. Especially mixed-phase clouds still pose a challenge. To date, the most reliable methods for cloud phase determination from satellites are synergistic lidar-radar techniques, such as the DARDAR (liDAR-raDAR) product. But active remote sensing is limited by its narrow field of view and low temporal resolution. These missing pieces can be provided by geostationary passive sensors. However, passive remote sensing of cloud phase is challenging and remote sensing of the more complex mixed-phase in particular is rarely done. This study addresses these challenges and provides a comprehensive analysis of the phase detection capabilities of the SEVIRI instrument aboard the geostationary Meteosat Second Generation satellite. First, an analysis of the geographic and temporal distribution of cloud phases on the SEVIRI disc using the reliable DARDAR data as "ground truth" shows that all cloud phases are relevant for SEVIRI, including the mixed-phase. Second, the information content of infrared-window brightness temperature differences (BTDs) of SEVIRI is investigated. Sensitivities of the BTDs to all radiatively relevant cloud parameters are assessed using radiative transfer calculations and reveal a complex phase dependence of the BTDs, where the dominant link between BTDs and phase is through the cloud top temperature. This analysis helps to understand the potential and limitations of BTDs in phase retrievals. Using these findings, the new PRObabilistic cloud top Phase retrieval for SEVIRI (ProPS) is developed. It employs a probabilistic Bayesian approach for cloud and phase detection based on collocated DARDAR-SEVIRI data. ProPS distinguishes between clear sky, optically thin ice, optically thick ice, mixed-phase, supercooled, and warm liquid clouds. The retrieval has a high ($>80\%$) probability of detection for liquid and ice pixels and classifies more than half of the challenging mixed-phase and supercooled clouds correctly. The new method enables the study of the temporal evolution of cloud phases, in particular also mixed-phase and supercooled clouds, which have so far been rarely studied from geostationary satellites. This thesis contributes to the global effort to observe and understand cloud phases in order to improve their representation in numerical models and to constrain the large uncertainties in climate projections.

Publications

This thesis builds on the three first-author publications listed below (abbreviated P1-3). The author contributions of each publication are given in detail in Chapters 6, 7 and 8. In addition, the work on this thesis led to three co-authored publications (P4-6) and further co-authored publications which are currently in review (P7-8).

First-author publications:

- **P1:** Mayer J., Ewald F., Bugliaro L., Voigt C. (2023). "Cloud Top Thermodynamic Phase from Synergistic Lidar-Radar Cloud Products from Polar Orbiting Satellites: Implications for Observations from Geostationary Satellites". *Remote Sensing.* doi:10.3390/rs15071742

- **P2:** Mayer J., Mayer B., Bugliaro L., Meerkötter R., Voigt C. (2024). "How well can brightness temperature differences of spaceborne imagers help to detect cloud phase? A sensitivity analysis regarding cloud phase and related cloud properties". *Atmospheric Measurement Techniques* [accepted]. Preprint available at doi:10.5194/egusphere-2024-540

- **P3:** Mayer J., Bugliaro L., Mayer B., Piontek D., Voigt C. (2024). "Bayesian cloud-top phase determination for Meteosat Second Generation". *Atmospheric Measurement Techniques.* doi:10.5194/amt-17-4015-2024

Co-authored publications:

- **P4:** Jurkat-Witschas T. et al. (2023). "Overview of Cloud Microphysical Measurements during the SENS4ICE Airborne Test Campaigns: Contrasting Icing Frequencies from Climatological Data to First Results from Airborne Observations". *Conference Paper at SAE International.* doi:10.4271/2023-01-1491

- **P5:** Walbröl A. et al. (2024). "Environmental conditions in the North Atlantic sector of the Arctic during the HALO–(AC)^3 campaign". *Atmospheric Chemistry and Physics.* doi:10.5194/acp-24-8007-2024

- **P6:** Wendisch, M. et al. (2024). "Overview: Quasi-Lagrangian observations of Arctic air mass transformations – Introduction and initial results of the HALO–(AC)^3 aircraft campaign". *Atmospheric Chemistry and Physics* [accepted]. Preprint available at doi:10.5194/egusphere-2024-783

- **P7:** [**submitted**] Jurkat-Witschas T. et al. (2024). "CIRRUS-HL – Picturing the high- and mid-latitude summer cirrus with airborne measurements from the High Altitude- and LOng-range research aircraft HALO". *Bulletin of the American Meteorological Society (BAMS).*

- **P8: [submitted]** Ehrlich, A. et al. (2024). "A comprehensive in situ and remote sensing data set collected during the HALO–(AC)^3 airborne campaign". *Earth System Science Data (ESSD)*. Preprint available at doi:10.5194/essd-2024-281

Disclaimer:
Parts of this thesis are heavily based on the three first-author publications (P1-3) and the correspondence with the reviewers and editors of the publications. Some sentences or parts of sentences have been taken verbatim or have only been slightly modified.

Chapter 1

Introduction

1.1 Why are geostationary observations of the cloud phase important?

Clouds cover a large part of the Earth, with a mean global coverage of 60% to 70% (Mao et al., 2019; Sullivan and Hoose, 2023). Their interaction with radiation has a major influence on the Earth's radiative balance by reflecting incoming solar radiation and absorbing and re-emitting thermal radiation. However, clouds and cloud related physical processes are difficult to characterise and model. Furthermore, it is unclear how cloud properties will change in a changing climate. In fact, cloud feedbacks constitute the highest contribution to the overall uncertainty in future climate projections (Intergovernmental Panel on Climate Change (IPCC), 2021).

One important cloud property is the cloud thermodynamic phase (Matus and L'Ecuyer, 2017; Sullivan and Hoose, 2023). The cloud phase has a direct impact on the radiative effect of clouds. For a given water content, a liquid cloud typically contains more and smaller particles than an ice cloud. As a result, the liquid cloud has a greater optical depth and therefore reflects more shortwave radiation back to space than the ice cloud (Cesana and Storelvmo, 2017; Matus and L'Ecuyer, 2017; Sullivan and Hoose, 2023). A phase change from ice to liquid or vice versa near the cloud top can therefore have a large effect on the cloud albedo (Matus and L'Ecuyer, 2017). A liquid cloud is also more opaque to infrared (IR) radiation than its glaciated counterpart with the same water content (Cesana and Storelvmo, 2017; Matus and L'Ecuyer, 2017). In addition to this direct interaction with radiation, the cloud phase also affects the evolution and lifetime of cloud particles. Phase transitions can lead to changes in cloud fraction, humidity, temperature profiles, cloud and atmospheric dynamics and precipitation formation (Cheng et al., 2012; Cesana et al., 2015; Mioche et al., 2015; Jäkel et al., 2016; McCoy et al., 2016). These changes in turn affect the radiative effects of the clouds. Hence, cloud thermodynamic phase is a critical parameter in understanding the earth radiation budget, the hydrological cycle, and atmospheric processes.

However, the processes governing cloud phase and phase transitions are not well under-

stood. Phase transition processes are influenced by multiple factors, including temperature, humidity, aerosol abundance and type, vertical velocity and turbulence, and are therefore complex to understand and represent in models - from large eddy simulations to global climate models (Morrison et al., 2011; Mioche et al., 2015; Zhang et al., 2015; Korolev et al., 2017; Coopman et al., 2021; Ricaud et al., 2024).

As a transition between pure ice and liquid clouds, mixed-phase (MP) clouds contain both ice crystals and supercooled liquid droplets. The coexistence of liquid and ice phases is metastable as it is not in thermodynamic equilibrium and leads to complex microphysical interactions, including the Wegener-Bergeron-Findeisen (WBF) process, particle nucleation and secondary ice formation. Additionally, in-cloud dynamics are crucial for the formation and maintenance of MP conditions, making MP clouds complex and highly dynamic systems. MP clouds occur in various regions of the Earth but represent a challenge for both observations and models: Remote sensing techniques struggle to accurately observe these clouds because the signals from the liquid and ice phases overlap, creating ambiguity in the retrievals of cloud properties. For airborne in-situ observations the distinction between phases is difficult for particles smaller than about $100\,\mu m$ in diameter (Baumgardner et al., 2014). An additional difficulty is that the concentrations of liquid and ice particles can differ by several orders of magnitude (Korolev et al., 2017; Kirschler et al., 2023; Moser et al., 2023). MP clouds are also challenging to represent in models, as the different dynamic and microphysical cloud processes happen on sub-grid scales and are difficult to parameterize (Korolev et al., 2017). Our knowledge and understanding of MP cloud microphysical processes remain incomplete, despite many decades of observational and theoretical work (Korolev et al., 2017; Matus and L'Ecuyer, 2017).

Numerous studies have shown that the cloud phase has a significant impact on climate sensitivity in global climate models (Gregory and Morris, 1996; Doutriaux-Boucher and Quaas, 2004; Cesana et al., 2012; Tan et al., 2016; Bock et al., 2020). An important cloud feedback mechanism involves phase changes in high latitude MP clouds, especially over the Southern Ocean (SO). The occurrence of ice is expected to decrease relative to liquid as temperatures increase, leading to a stronger reflection of radiation (negative cloud feedback) (Komurcu et al., 2014; Ceppi et al., 2017). However the magnitude of these processes is highly uncertain. Long-standing model biases have included too few supercooled cloud droplets in the present-day climate model simulations, leading to strong phase changes in future scenarios and a correspondingly strong negative cloud-phase feedback (Tan et al., 2016). In the latest Coupled Model Intercomparison Project Phase 6 (CMIP6), the fraction of supercooled cloud droplets in the current climate is larger than in previous models, leading to a reduced negative cloud-phase feedback (Bock et al., 2020). As a consequence, the overall positive cloud feedbacks are stronger. This could explain the increased mean temperature ($3.8\,K$) and equilibrium climate sensitivity (1.8 to $5.6\,K$) after a CO_2 doubling observed in CMIP6 compared to previous model intercomparisons (Bock et al., 2020). Some of these CMIP6 models with very high ($> 5\,K$) or very low ($< 2\,K$) equilibrium climate sensitivity also simulate a warming that is above or below the IPCC very likely range of temperature change respectively (Intergovernmental Panel on Climate Change (IPCC), 2021). This discussion shows that the representation of the cloud phase has a large effect

on the predicted warming and contributes to large discrepancies between different global climate models.

In order to improve our physical understanding of processes involving the cloud phase and the representation of cloud phases in climate models, accurate observations of cloud occurrence and their thermodynamic phase are essential (Atkinson et al., 2013; Cesana et al., 2015; Tan et al., 2016; Matus and L'Ecuyer, 2017; Bock et al., 2020; Cesana et al., 2022; Hahn et al., 2023; Kirschler et al., 2023; Moser et al., 2023). Satellite remote sensing is an important method to determine global cloud properties (Stubenrauch et al., 2013; Miller et al., 2014; Stubenrauch et al., 2017; Li et al., 2022; Zhou et al., 2022). In recent years, significant progress has been made using active remote sensing techniques for cloud phase identification, and in particular synergistic lidar-radar techniques are considered to be the most reliable techniques for satellite observations of the cloud phase (Zhang et al., 2010; Korolev et al., 2017). However, active spaceborne instruments cannot provide a large-scale view or observations of cloud evolution over time. This is problematic because the temporal evolution of cloud phases and phase transitions are of particular interest for understanding the dynamical processes and microphysical interactions that govern cloud properties. For such observations, geostationary passive instruments such as the Spinning Enhanced Visible and Infrared Imager (SEVIRI) aboard the Meteosat Second Generation (MSG) satellite are crucial. Their main advantages are that, first, they provide information over a wide field of regard, which allows, in addition to microphysical quantities, the retrieval of macrophysical quantities such as the spatial extent of clouds. Second, they allow measurements at any time of day, so that the temporal evolution of clouds can be studied with high temporal resolution (15 min for SEVIRI). While passive sensors can only observe the upper layers of a cloud according to the penetration depth of their channels, these upper layers are important because they are critical for evaluating the radiative effect of a cloud (Zaremba et al., 2020). In addition, MP and supercooled liquid (SC) cloud layers, which are crucial for understanding cloud feedbacks as described above, are often found at cloud top (Rauber and Tokay, 1991; Khain et al., 2022). However, accurately distinguishing cloud phases, especially MP and SC, using passive imagers is challenging, and passive cloud phase retrievals are typically less reliable than phase retrievals from active instruments. As a result, the occurrence of cloud phases, in particular MP and SC, is rarely studied using geostationary imagers. These much-needed observations for understanding the distribution and temporal evolution of cloud phases are therefore still lacking.

For passive instruments, there is an additional motivation for accurately detecting the cloud phase as it often is a necessary first step in remote sensing retrievals of other cloud properties, such as optical thickness, effective particle radius, and water path. Incorrect phase assignment can lead to significant errors in this downstream retrieval of cloud properties, as ice and liquid cloud particles differ in their absorption and scattering properties (Marchant et al., 2016).

To summarize, reliable observations of geostationary imagers of cloud phase are important to 1) improve our physical understanding of cloud processes, 2) improve climate models and 3) ensure accurate retrievals of other microphysical cloud properties. Especially the MP is of particular interest as our understanding of MP cloud processes remains

incomplete and they play an important but highly uncertain role in future climate scenarios.

1.2   Aim of this work

As motivated in the last section, reliable cloud phase observations of geostationary imagers, especially MP and SC, are of crucial interest, but challenging (Korolev et al., 2017). One of the main difficulties is identifying MP clouds, as passive observations often only distinguish between ice and liquid clouds (or ice/liquid/unknown) (e.g., Key and Intrieri, 2000; Knap et al., 2002; Bugliaro et al., 2011; Baum et al., 2012; Bessho et al., 2016; Marchant et al., 2016; Benas et al., 2017; Platnick et al., 2017). However, there is a growing awareness that a further distinction is needed to also identify MP and SC clouds (Wang et al., 2019; Pavolonis and Calvert, 2020; Li et al., 2022). These clouds occur most frequently at high latitudes, which are difficult to observe with geostationary satellites. Consequently, it is not a priori clear if MP and SC clouds make up a relevant fraction of the SEVIRI cloud occurrence on its field of regard, and to the best of our knowledge there is no information available on the occurrence of the MP and SC phases at the SEVIRI pixel level yet.

The most reliable retrievals for cloud phase from satellites are synergistic lidar-radar methods, as mentioned above (Delanoë and Hogan, 2008; Zhang et al., 2010; Wang, 2012; Korolev et al., 2017; Ewald et al., 2021; Aubry et al., 2024). The combination of lidar and radar on polar orbiting satellites is particularly well suited for cloud phase determination, as both instruments complement each other due to their different penetration depths and sensitivities to particle sizes (Donovan and Van Lammeren, 2000; Delanoë and Hogan, 2008; Wang, 2012; Korolev et al., 2017; Ewald et al., 2021). In recent years, spaceborne synergistic active remote sensing has therefore been used in several studies to obtain vertical profiles of the thermodynamic cloud phase and to study their geographical and temporal distribution (Hu et al., 2009; Luke et al., 2010; Zhang et al., 2010; Mioche et al., 2015; Cesana and Storelvmo, 2017; Matus and L'Ecuyer, 2017; Listowski et al., 2019). One powerful synergistic lidar-radar cloud product is the liDAR/raDAR (DARDAR) product (Delanoë and Hogan, 2010; Ceccaldi et al., 2013), which has been used for various cloud studies (Huang et al., 2012; Delanoë et al., 2013; Huang et al., 2015; Mioche et al., 2015; Listowski et al., 2019). It is based on the synergy of radar and lidar measurements from the A-Train satellites CloudSat and CALIPSO.

However, the cloud phase distribution results from these studies are expected to differ from the cloud phase distributions that a passive geostationary imager would observe. Typically, studies using active remote sensing include the entire vertical profile of cloud phase at a given time and location. In contrast, a passive geostationary instrument can mainly observe the upper layer of a cloud according to the penetration depth of its channels. Passive geostationary instruments also tend to have a coarser spatial resolution in the order of 2–5 km, while cloud phase is expected to vary on smaller scales. Given these considerations, this thesis addresses the scientific question:

SQ-1: *Do the perspective and the spatial characteristics of a geostationary imager such as SEVIRI allow the study of mixed-phase and supercooled clouds?*

The knowledge gained from the cloud phase spatial and temporal distribution at the sensor's pixel level helps to design and validate cloud phase retrievals for SEVIRI. However, in order to design optimal cloud phase retrievals, it is also necessary to understand the capabilities and limitations of the instrument's channels.

One popular technique for cloud phase retrievals from passive instruments is to use the brightness temperature difference (BTD) of IR window channels (Ackerman et al., 1990; Strabala et al., 1994; Key and Intrieri, 2000; Baum et al., 2000, 2012; Finkensieper et al., 2016; Hünerbein et al., 2022; Benas et al., 2023; Mayer et al., 2024). The use of BTDs is a widespread method in passive remote sensing: Besides cloud phase retrievals, they are often used to detect clouds or to retrieve cloud properties such as optical thickness (τ) or effective radius (R_{eff}), especially for ice clouds (e.g., Inoue, 1985; Krebs et al., 2007; Heidinger et al., 2010; Garnier et al., 2012; Kox et al., 2014; Vázquez-Navarro et al., 2015; Strandgren et al., 2017).

The physical reason why BTDs are helpful for retrieving cloud properties is that the optical properties of clouds, i.e. how much radiation is absorbed, scattered and emitted, depend on the wavelength of radiation observed by the imager channels according to their spectral response. Since cloud optical properties also depend on the properties of the cloud particles (e.g. phase, R_{eff}, habit), spectral variations in transmitted and emitted radiation can, in principle, be attributed to certain microphysical parameters. Note, however, that this is generally an under-determined problem, since 1) the spectral variation is not necessarily unique for each combination of cloud microphysical properties, and 2) many other factors influence the IR radiation on its path through the atmosphere: The vertical distribution of cloud water content and cloud temperature are important for cloud transmission and emission. In addition, the atmosphere absorbs IR radiation and different surface types can have different emissivities. Hence, radiative transfer (RT) through clouds and the atmosphere is complex, with many parameters that can affect the BTDs.

To understand this complexity, one can use RT calculations to simulate atmospheric and cloud properties and test their effects on the BTDs. This has been done in previous studies to analyse the sensitivities of BTDs to cloud properties and to improve corresponding retrieval methods (e.g. Parol et al., 1991; Strabala et al., 1994; Baum et al., 2000; Dubuisson et al., 2008; Nasiri and Kahn, 2008). Cloud parameters considered include thermodynamic phase, τ, R_{eff}, ice crystal habit, and cloud top height (CTH). However, these studies have each focused on only a small number of these cloud parameters, and an investigation of the relative importance of all cloud parameters is still lacking. In particular, the influence of CTH or the closely related cloud top temperature (CTT) on BTDs has not been studied in detail in conjunction with the other relevant properties.

In addition, previous studies have focused on applications, such as how to use BTDs to infer given cloud properties. Physical explanations for the observed phenomena are often missing or incomplete. For cloud phase retrievals, variations in the refractive indices of ice and water across the IR window are sometimes used to explain the sensitivity of BTDs to

the cloud phase (Key and Intrieri, 2000; Baum et al., 2000, 2012; Finkensieper et al., 2016). However, this explanation is incomplete, as the phase is also correlated with other cloud parameters such as CTT and R_{eff}, which in turn have large effects on the BTDs. Which of these cloud parameters are dominant in influencing BTDs in different scenarios is still open. In addition, traditional explanations of RT through clouds often neglect scattering effects, which can be significant. Thus, the physical reasons for the observed phase dependence of BTDs are not well understood. However, to design optimal cloud (phase) retrievals and to be aware of their limitations, a full understanding of the satellite channel dependencies is critical. To address these gaps in the knowledge of the relationship between IR window BTDs and cloud properties, this study investigates the following scientific question:

SQ-2: *What is the information content of brightness temperature differences (BTDs) from spaceborne imagers with respect to the cloud phase? What are the implications for phase retrievals?*

Insights from SQ-1 and SQ-2 help to understand the capabilities of SEVIRI to retrieve the cloud phase. To meet the needs expressed in Sect. 1.1 for reliable identification of MP and SC clouds from geostationary platforms, new cloud phase retrieval approaches are required. For SEVIRI such a phase distinction is not yet available, but as will be shown in P1 (see Sect. 3.1 and Chapter 6), MP and SC cloud tops are common in the SEVIRI disc and deserve dedicated retrieval algorithms. In recent years, retrieval algorithms have been developed for imagers on geostationary satellites, such as the Advanced Baseline Imager (ABI) aboard the U.S. GOES-R series and the Advanced Himawari Imager (AHI) aboard the Japanese Himawari-8, that classify clouds into ice, liquid, and MP, and, for ABI, further into SC cloud tops (Wang et al., 2019; Pavolonis and Calvert, 2020; Li et al., 2022).

The mentioned retrieval algorithm for ABI is physically based and employs several threshold tests for quantities derived from IR channels, mainly so-called β ratios and effective emissivities (Pavolonis and Calvert, 2020), which are closely linked to microphysical properties and represent an alternative to BTDs to deal with IR channels (Pavolonis, 2010). These quantities rely on numerical weather predictions to perform RT for the (coarsened) ABI disc in four spectral IR channels centered at 7.4, 8.5, 11.0, 12.0 μm. The theoretical framework of the method has the advantage of being highly interpretable. At the same time, it is based on some assumptions and, as a threshold algorithm, it requires manual tuning, for which it is difficult to encompass all atmospheric scenarios and maintain optimal performance for diverse atmospheric conditions. As the data used to validate the ABI algorithm did not contain information on the cloud phase in the critical temperature range between 238 K and 268 K, the detection of MP and SC has not yet been validated (Pavolonis and Calvert, 2020). However, example results shown in the Algorithm Theoretical Basis Document (ATBD) for the ABI product (Pavolonis and Calvert, 2020) show very few MP cloud tops compared to DARDAR observations (as shown in P1 in Sect. 3.1 and Chapter 6). The phase retrieval algorithm for AHI (Li et al., 2022), on the other hand, uses a deep neural network (DNN) trained on one year of the lidar-radar 2B-CLDCLASS-LIDAR

product (Wang, 2012), and an additional year of data for validation. Neural networks are efficient at detecting spatial and spectral features, but lack interpretability and transparency. One year of data is a relatively small data set for training, and the authors additionally discarded all pixels in horizontally inhomogeneous cloud regions (Li et al., 2022), removing many of the more complicated cloud scenarios. In addition, the method does not distinguish between SC layers at cloud top with underlying ice and pure MP clouds (both cloud types are classified as MP), which limits its specificity. This algorithm for AHI was developed in parallel and independently from the phase retrieval described in P3 of this thesis. In general, only few initial approaches to extended cloud phase detection, i.e. including MP detection, for geostationary satellites have been tested.

Exploring other possibilities for phase retrievals could offer further advances. The synergistic lidar-radar DARDAR product has not yet been used as basis for cloud phase algorithms for passive imagers. Since DARDAR provides state-of-the-art phase detection and has been used in an increasing number of studies in recent years, we exploit these capabilities for phase detection for the SEVIRI passive instrument. In contrast to theoretically based retrievals, learning from measured lidar-radar data such as DARDAR has the advantage of encompassing most real-world atmospheric scenarios. In addition, an underlying reliable data set such as DARDAR can be used for rigorous validation. The third scientific question explores this idea:

SQ-3: *Can the phase retrieval capabilities of synergistic lidar-radar methods be transferred to passive imagers and how accurately can this be done?*

Investigating this question builds on the findings of SQ-1 and SQ-2, using results from the distribution of cloud phases and knowledge of the phase information content of SEVIRI channels. The three scientific questions are explored in the three publications of this thesis (Chapters 6, 7 and 8). Summaries of the main points that answer the scientific questions are given in Chapter 3.

Chapter 2

Fundamentals

2.1 Thermodynamic phases of clouds

2.1.1 Formation of liquid, ice and mixed-phase clouds

Clouds can be composed of liquid droplets, ice crystals or a mixture of both, called mixed-phase (MP). Liquid and frozen water in clouds originates from ambient water vapor. For nucleation of water vapor to occur, either the partial water vapor pressure e can be increased or the temperature can be lowered. For a flat surface, the *Clausius-Clapeyron equation* describes the partial vapor pressure as a function of temperature required for the phase transition between water vapor and liquid water or water vapor and solid ice (called the *saturation vapor pressure* with respect to water, $e_{\mathrm{sat,w}}$, or ice, $e_{\mathrm{sat,i}}$) (Pruppacher and Klett, 2010). The saturation vapor pressures with respect to water and ice are different, with lower values for ice than water for all temperatures below 0°C ($e_{\mathrm{sat,i}} < e_{\mathrm{sat,w}}$). To describe the partial water vapor pressure in relation to the saturation vapor pressure one often uses the *relative humidity* with respect to water/ice, defined as $\mathrm{RH_{w/i}} = \frac{e}{e_{\mathrm{sat,w/i}}} 100\%$. In the atmosphere, saturation with respect to water/ice ($e = e_{\mathrm{sat,w/i}}$, meaning $\mathrm{RH_{w/i}} = 100\%$) is typically obtained as air rises and cools down due to adiabatic expansion.

However, the saturation of air with respect to water (i.e. $\mathrm{RH_w} = 100\%$) is not sufficient for the formation of liquid droplets in the atmosphere. Effects of the highly curved surface of droplets (*Kelvin effect*) make the formation of droplets from pure water vapor highly improbable. Instead, liquid cloud droplets form on a subset of atmospheric aerosol called *cloud condensation nuclei (CCN)* (Pruppacher and Klett, 2010). Concentrations of CCN in the atmosphere are typically high enough that liquid droplets form once an air parcel is saturated with respect to water. Liquid droplets can form not only above 0°C, but also exist at temperatures well below 0°C, in which case they are called *supercooled liquid* droplets. Supercooled liquid droplets can persist until a temperature of about −40°C (the exact threshold depends on the size of the droplets), for lower temperatures only the ice phase is possible (see below) (Wallace and Hobbs, 2006). Such supercooled liquid droplets are not in thermodynamic equilibrium because the solid ice phase is energetically favorable below

0°C (Wallace and Hobbs, 2006). However, a transition to the ice phase requires overcoming an energy barrier of a critical ice nucleus size; otherwise supercooled liquid droplets remain in their metastable liquid state.

This energy barrier can be overcome with the help of so-called *ice nucleating particles (INP)*, which aid the formation of an ice structure (Kärcher and Lohmann, 2003; Wallace and Hobbs, 2006). This ice formation process is called *heterogeneous* nucleation. Heterogeneous ice formation depends on the type of INPs available, their size, and the relative humidity and ambient temperature (Koop et al., 2000; Hoose and Möhler, 2012; Kanji et al., 2017). Several different processes of heterogeneous nucleation are possible, the most important of which involve INPs already contained in supercooled liquid droplets or INPs in the air coming into contact with supercooled liquid droplets and initiating freezing (Hoose and Möhler, 2012). However, INPs are much more scarce in the atmosphere than CCN. Some types of INPs become effective only at water vapor pressures much higher than the saturation vapor pressure over ice. INPs are necessary for the formation of ice crystals at temperatures between 0°C and about $-40°C$, meaning that in this temperature regime, in the absence of effective INPs, supercooled liquid droplets remain in their metastable liquid state. At lower temperatures (below about $-40°C$), ice crystals can form without the aid of INPs, which is called *homogeneous* nucleation. The water vapor pressure needed for homogeneous ice nucleation is smaller than the saturation vapor pressure with respect to liquid $e_{\mathrm{sat,w}}$ at these low temperatures, which means that no supercooled liquid droplets persist in this temperature regime (Hoose and Möhler, 2012). Whether heterogeneous or homogeneous nucleation dominates at these low temperatures depends on the relative humidity and the concentration and nucleation ability of the available INPs (Kärcher and Lohmann, 2003).

From the above it follows that between 0 and $-40°C$ both supercooled liquid droplets and ice crystals can exist simultaneously, i.e. a MP cloud. The coexistence of liquid and ice phases leads to complex microphysical interactions. Since ice has a lower saturation vapor pressure than water ($e_{\mathrm{sat,i}} < e_{\mathrm{sat,w}}$), existing ice crystals will grow at the expense of water molecules from liquid droplets. This process is called the Wegener-Bergeron-Findeisen (WBF) process (Bergeron, 1935; Findeisen, 1938) and is a fundamental process in MP clouds. If no new supercooled liquid droplets are formed, the MP cloud glaciates in a short amount of time through the WBF process, in the order of minutes (Korolev et al., 2003).

MP clouds are found globally, from the tropics to the poles, and in numerous meteorological conditions (Shupe et al., 2008; Tan et al., 2014; Coopman et al., 2021). They are associated with different cloud types, for instance lee-wave clouds, frontal clouds or convective clouds (Korolev et al., 2017). One of the most important types of MP clouds are stratiform MP clouds, which are often found in the atmospheric boundary layer at high latitudes. Typically, these clouds consist of thin MP layers (a few hundred meters deep) at cloud top with ice or ice virga below (Shupe et al., 2008; McFarquhar et al., 2011; Forbes and Ahlgrimm, 2014; Khain et al., 2022; Moser et al., 2023). Despite the WBF process, these MP clouds are observed to be very frequent and persistent, lasting for hours or even days (Shupe et al., 2006; Morrison et al., 2011; McFarquhar et al., 2011; Korolev et al., 2017; Coopman et al., 2021; Moser et al., 2023). The processes leading to such
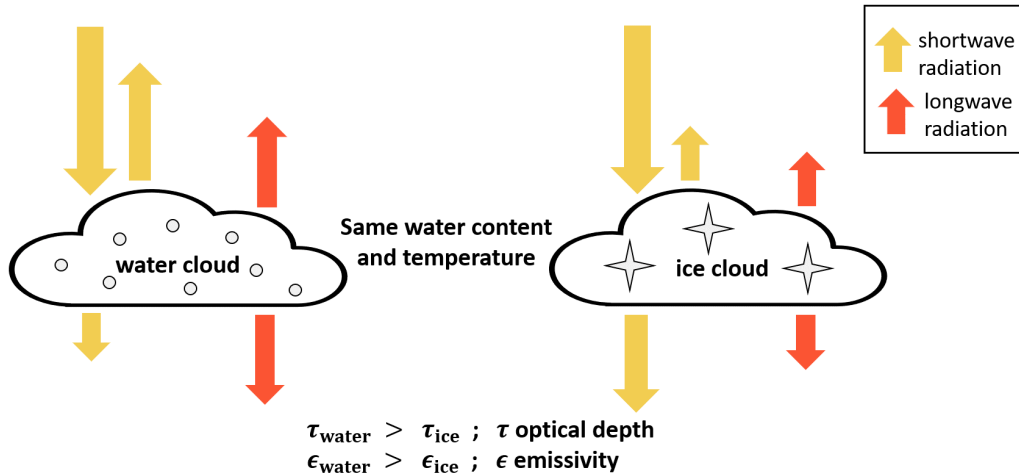
Figure 2.1: Schematic of the radiative effect of cloud phase for shortwave (yellow arrows) and longwave (red arrows) radiation for a given water content and temperature. Credit: Adapted from Cesana and Storelvmo (2017).

quasi-stable MP states are not fully understood. However, several studies have suggested the importance of cloud dynamics (Korolev and Field, 2008; Morrison et al., 2011): Super-cooled liquid droplets at the cloud top lead to strong radiative cooling, which in turn leads to turbulence and the permanent generation of new liquid droplets in updrafts (Morrison et al., 2011; Khain et al., 2022). At the same time, ice crystals grow through the WBF process at the expense of liquid water until they are large enough to precipitate. This balance between the formation of supercooled liquid droplets by upward motion in the cloud and their depletion by the WBF process has been shown to be capable of maintaining MP states (Morrison et al., 2011). However, the description of these highly dynamic, non-equilibrium processes governing the maintenance of MP clouds and phase transitions still presents complicated challenges (Korolev et al., 2017).

Hence, whether liquid or ice particles form and persist in the temperature range between 0 and $-40°C$ is complex. It depends on the local water vapor pressure and the in-cloud dynamics such as updraft velocities and ice formation and multiplication processes (Morrison et al., 2011; Korolev et al., 2017). For phase transitions from liquid to ice, the size of the cloud droplets is also important (Coopman et al., 2020b). In addition, atmospheric aerosol composition is thought to play an important role for the cloud phase, as several studies have found that aerosol can strongly influence the fraction of liquid and ice particles in a cloud (Tan et al., 2014; Bruno et al., 2021).

2.1.2 Effects of the cloud phase

As mentioned in the Introduction, the cloud phase affects the interactions of clouds with radiation, which is schematically shown in Fig. 2.1. A liquid cloud typically consists of more and smaller cloud particles than an ice cloud with the same water content. This means

that the liquid cloud has a greater optical depth and reflects more solar radiation back to space than the ice cloud, i.e. the liquid cloud has a greater albedo (Hogan et al., 2003; Matus and L'Ecuyer, 2017; Sullivan and Hoose, 2023). Particularly in the top layers of clouds, phase transitions therefore have a large effect on the albedo and hence the radiative effect of clouds (Matus and L'Ecuyer, 2017).

The cloud phase also affects the amount of absorbed shortwave and longwave radiation (Matus and L'Ecuyer, 2017). For the same water content, liquid clouds, consisting of more and smaller cloud particles, are typically more opaque to radiation than ice clouds at the same temperature (Cesana and Storelvmo, 2017). The amount of absorbed radiation influences the local heating rates in the cloud, i.e. the temperature and humidity profile of the atmosphere. This can in turn influence cloud fraction, cloud optical depth and the cloud top temperature (Harrop and Hartmann, 2016) as well as atmospheric dynamics (Matus and L'Ecuyer, 2017).

In addition to the influence of the cloud phase on cloud-radiation interactions, the cloud phase also influences the development of precipitation and the lifetime of clouds (Mülmenstädt et al., 2015). The smaller liquid droplets tend to stay suspended in the air longer than the typically larger ice crystals which may sediment. As ice crystals grow to larger sizes, clouds containing ice crystals are more effective at precipitation, which in turn affects cloud lifetime (Tao et al., 2014).

2.2 Radiative transfer theory

In atmospheric physics, radiative transfer (RT) describes the path of electromagnetic radiation through the Earth's atmosphere. The theory is crucial for interpreting and accurately modeling observations from satellite remote sensing instruments. In this section, the fundamentals of atmospheric RT for this thesis are summarized, based mainly on Liou (2002), Wallace and Hobbs (2006), Stull (2015) and Mayer and Kylling (2005).

2.2.1 Radiation in the atmosphere

The two main sources of electromagnetic radiation in the atmosphere are 1) the Sun and 2) the Earth and its atmosphere, which emit thermal radiation. The wavelengths of the main part of this radiation range from ultraviolet (UV) through visible wavelengths to IR wavelengths (in the order of about 0.1 to 100 µm, as shown in Fig. 2.2). In remote sensing, radiation of solar origin is also called *shortwave radiation* and dominates at wavelengths shorter than about 4 µm (see Fig. 2.2), while radiation of terrestrial origin (i.e. from the Earth-atmosphere system) is called *longwave radiation.*

To describe the path of radiation through the atmosphere one often uses the *radiance*, $L_\lambda(\mathbf{r}, \Omega, t)$, defined as energy per time per area per solid angle for a given wavelength λ (in units of $\text{W m}^{-2} \text{ sr}^{-1} \text{ µm}^{-1}$); $\mathbf{r}$ is the positional vector, Ω is the solid angle and t is the time. Integration over the solid angle gives the so-called spectral *irradiance* $E_\lambda(\mathbf{r}, t)$ in units of $\text{W m}^{-2} \text{ µm}^{-1}$.
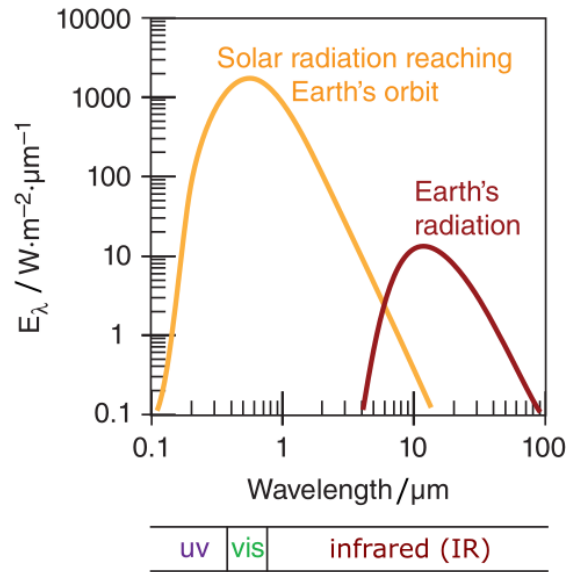
Figure 2.2: Yellow line: Spectral irradiance E_λ^* from the Sun reaching top of Earth's atmosphere, approximating the Sun as a black body. Red line: Spectral irradiance E_λ^* from a black body with a typical temperature of the Earth-atmosphere system (255 K). Credit: Adapted from Stull (2015) p. 39, Fig. 2.10 (CC BY-NC-SA 4.0 `https://creativecommons.org/lice nses/by-nc-sa/4.0/`)

2.2.2   Interactions of radiation with the atmosphere

On its way through the atmosphere, radiation interacts with atmospheric constituents such as gases, aerosols and clouds. When radiation encounters matter, one of three things can happen: The radiation can be transmitted, absorbed or scattered. In addition, radiation can be emitted by matter as a source term. The most important interactions of radiation with atmospheric constituents are briefly explained below, focusing on visible and infrared wavelengths, as these are the wavelengths typically used by passive imagers.

Absorption

Absorption occurs when the energy of a photon matches the difference between two energy levels of a molecule, raising its energy level. This process depends on the molecular structure and the energy (i.e. wavelength) of the incident radiation. The energy of the absorbed photon is then usually converted into thermal energy by the collision of molecules, i.e. the temperature of the absorbing matter is raised. The amount of absorption varies greatly from molecule to molecule and from wavelength to wavelength (see Fig. 2.3). Liquid water and ice (i.e. clouds) absorb very little in the visible wavelengths, but very much in the infrared wavelengths (Liou, 2002).

When radiance L_λ passes through a layer of matter with path length ds and is (partly) absorbed, the change of radiance can be expressed as
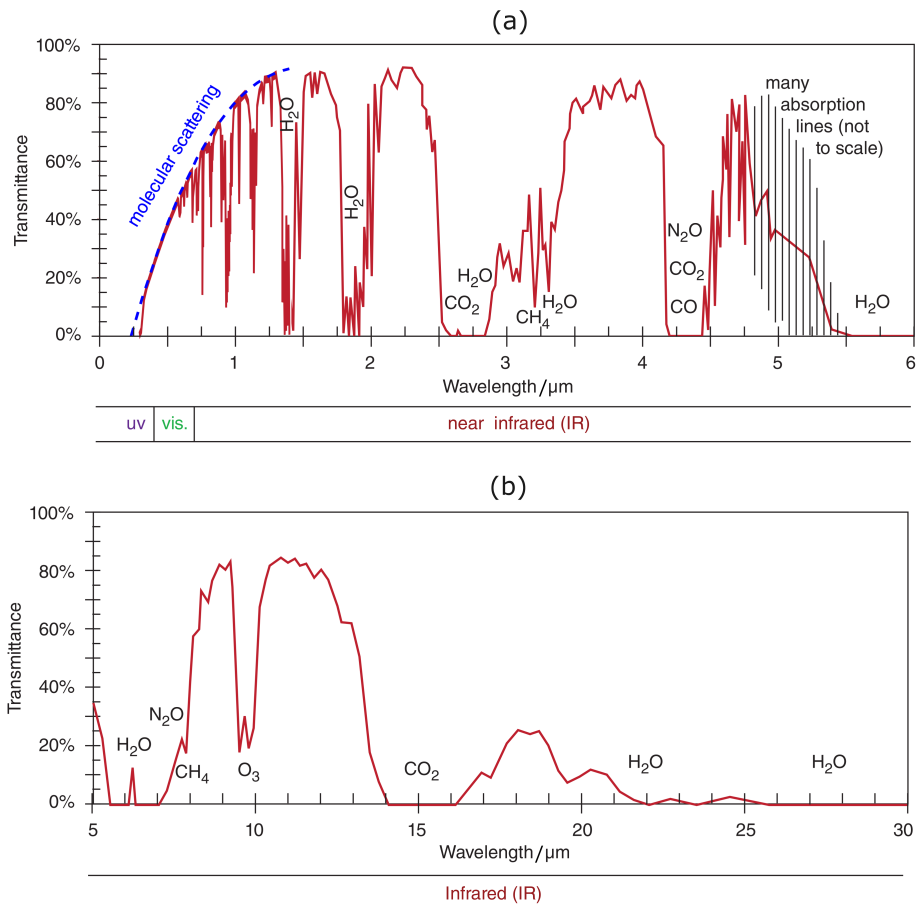
Figure 2.3: Atmospheric transmittance of radiation for the wavelengths (a) 0 to 6 µm and (b) 5 to 30 µm. For regions of strong absorption (i.e. low transmittance) the dominant absorbing chemical is given. For short wavelengths (< 0.4 µm) the effects of molecular scattering are indicated by the blue dashed line. Credit: Adapted from Stull (2015) p. 222-223, Fig. 8.4 (CC BY-NC-SA 4.0 `https://creativecommons.org/licenses/by-nc-sa/4.0/`). Panel (a) is a combination of Fig. 8.4a and b, and panel (b) is adapted from Fig. 8.4c

$$\frac{\mathrm{d}L_{\lambda,\mathrm{abs}}}{\mathrm{d}s} = -\beta_{\mathrm{abs}}(\lambda)\, L_{\lambda} \tag{2.1}$$

where β_{abs} is the absorption coefficient with units of m^{-1}, that depends on the properties of the absorbing matter.

Emission

Emission can be regarded as an "inverse" process to absorption, where energy is released in the form of photons. The emission strongly depends on the temperature of the matter.

For an idealized *black body*, thermal emission of radiation follows *Planck's radiation law*

$$B_\lambda(T) = \frac{2hc^2}{\lambda^5} \frac{1}{\left(e^{\frac{hc}{\lambda k_B T}} - 1\right)} \, , \tag{2.2}$$

where B_λ is the emitted spectral radiance, T is the temperature of the black body, h is the Planck constant, c is the speed of light in vacuum and k_B is the Boltzmann constant.

The emission spectra of the Sun and the Earth roughly follow Planck spectra (see Fig. 2.2). Since the Sun and the Earth have very different temperatures, the corresponding Planck spectra peak at different wavelengths (at about $0.5\,\mu m$ and at about $11\,\mu m$ respectively). Even though Planck curves as described in Eq. 2.2 do not overlap, there is an overlap region in Fig. 2.2. The reason is that the solar radiation in the figure is not as emitted by the Sun, but the radiation that reaches the top of the Earth's atmosphere. Since the emitted radiation spreads out radially, the amount of energy per unit area scales with the inverse of the square of the distance, and only a fraction of the radiation emitted by the Sun reaches the Earth. As a result, terrestrial radiation dominates at longer wavelengths. This simplifies remote sensing applications, because the radiation source (solar or terrestrial) is unambiguous for most wavelengths (see also Sect. 2.3.1).

To describe the emitted radiation of real objects (which are in general not black bodies) one uses the so-called *emissivity* ϵ_λ, defined as

$$\epsilon_\lambda = \frac{L_{\lambda,\mathrm{emi}}}{B_\lambda(T)} \, , \tag{2.3}$$

where $L_{\lambda,\mathrm{emi}}$ is the by the object emitted radiance. For a real object (called *gray body*), $\epsilon_\lambda < 1$.

In thermal equilibrium, *Kirchhoff's law* states that the emissivity is equal to the absorptivity of a body (Kirchhoff, 1978). Although the Earth's atmosphere as a whole is evidently not in thermodynamic equilibrium, in localised volumes below about 60–70 km the atmosphere can be considered to be in local thermodynamic equilibrium to a good approximation (Liou, 2002). This means that the change of radiance due to a layer of emitting matter can be written as

$$\frac{\mathrm{d}L_{\lambda,\mathrm{emi}}}{\mathrm{d}s} = \beta_{\mathrm{abs}}(\lambda)\, B_\lambda(T) \, , \tag{2.4}$$

applying Kirchhoff's law.

Scattering

Scattering is the deflection of radiance by particles or molecules in the atmosphere. Photons can be scattered away from the direction of interest, reducing the radiance, or in the direction of interest, acting as a source term for the radiance. The mathematical description of the scattering process is complex and depends on the wavelength and the size and shape of the scattering object. In different size regimes, relative to the wavelength of the radiation, scattering can be treated differently:

- **Rayleigh scattering:** Is an approximation for particles much smaller than the wavelength. The amount of scattering in this regime is approximately proportional to λ^{-4}, meaning that shorter wavelengths are scattered more efficiently than longer wavelengths. The scattering is divided evenly between the forward and backward direction, as indicated in Fig. 2.4(a).

- **Geometric optics:** Is an approximation for particles much larger than the wavelength. For visible radiation, this applies to raindrops, for example. Here, radiance is treated as straight rays that are refracted according to *Snell's law* and reflected according to *Fresnel's equations.*

- **Lorenz–Mie scattering:** Can, for spherical particles, be derived directly from *Maxwell's equations* and is an exact solution. It is used for particles comparable in size to the wavelength, such as cloud particles in the case of visible and IR radiation. The amount of scattering as a function of wavelength exhibits a damped oscillatory behaviour (Wallace and Hobbs, 2006). This means that a whole range of wavelengths are scattered, resulting for example in the white appearance of clouds. Lorenz–Mie scattering is strongly anisotropic, depending on the size of the scattering particle, with a preference in the forward direction (see Fig. 2.4(c)).

For atmospheric molecules, scattering is relevant at visible wavelengths where the Rayleigh approximation applies (shown in the top panel of Fig. 2.3). Molecular scattering can be neglected at IR wavelengths. For cloud particles on the other hand, scattering (Lorenz–Mie scattering in this case) is relevant for both visible and IR radiation. For IR radiation, however, absorption is the dominant process.

To describe the amount of scattering, the so-called *scattering coefficient* β_{sca} is used, analogous to the absorption coefficient, with units of m^{-1}. The scattering phase function $p(\Omega, \Omega')$ gives the probability of scattering the incident radiation with angular direction Ω' to the new direction Ω. The change of radiance by a layer of scattering matter can then be written as

$$\frac{\mathrm{d}L_{\lambda,\text{sca}}}{\mathrm{d}s} = -\beta_{\text{sca}}(\lambda)L_\lambda + \frac{\beta_{\text{sca}}(\lambda)}{4\pi}\int_{4\pi} p(\Omega, \Omega')L_\lambda(\Omega')d\Omega'. \tag{2.5}$$

The first term on the right hand side describes the radiance which is scattered out of the direction of interest. The second term is a source term, describing the radiance which is scattered from all other directions Ω' into the direction of interest Ω.

2.2.3 Radiative transfer equation

Taking all processes of RT together (absorption, emission and scattering), one gets the *radiative transfer equation*

$$\begin{aligned}
\frac{\mathrm{d}L_\lambda}{\mathrm{d}s} &= \frac{\mathrm{d}L_{\lambda,\text{abs}}}{\mathrm{d}s} + \frac{\mathrm{d}L_{\lambda,\text{sca}}}{\mathrm{d}s} + \frac{\mathrm{d}L_{\lambda,\text{emi}}}{\mathrm{d}s} \\
&= -(\beta_{\text{abs}} + \beta_{\text{sca}})L_\lambda + \frac{\beta_{\text{sca}}}{4\pi}\int_{4\pi} p(\Omega, \Omega')L_\lambda(\Omega')\mathrm{d}\Omega' + \beta_{\text{abs}}B_\lambda(T),
\end{aligned}$$
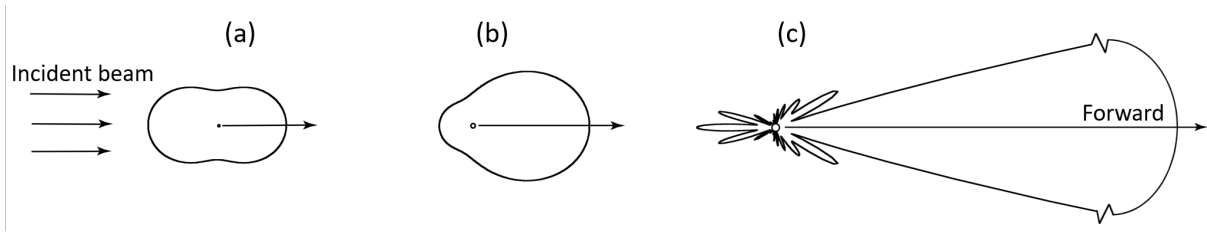
Figure 2.4: Schematic of the angular patterns of the intensity of visible radiation (with a wavelength of 0.5 µm) scattered by spherical particles with radii of (a) 10^{-4} µm, (b) 0.1 µm, and (c) 1 µm. The forward scattering for the 1 µm particle is extremely large and is scaled for presentation purposes. Credit: Adapted from Liou (2002), p.7.

which describes the propagation of radiation through a medium (in this case the atmosphere) with various sinks (first term on the right hand side) and sources (second and third term on the right hand side), that depend on the atmospheric constituents. Note that the dependencies on position, angle and wavelength have been largely omitted to keep the equation more easily readable. The radiative transfer equation is an integro-differential equation where the radiance in one direction depends on the radiance from all other directions. It can usually not be solved analytically (or only for very simplified special cases). However, there are sophisticated numerical solvers that can compute solutions, like the RT package libRadtran (Mayer and Kylling, 2005; Emde et al., 2016), which is used in the second publication (P2) of this thesis.

2.2.4 Optical properties of clouds

Section 2.2.2 introduced the optical properties β_{abs}, β_{sca} and $p(\Omega, \Omega')$. For RT through a cloud, the interplay of these optical properties determines how much radiation is transmitted through a cloud and, in combination with the cloud temperature, how much radiation is emitted from it.

The combined loss of radiance due to scattering and absorption is called *extinction*, with the extinction coefficient β_{ext}, defined as

$$\beta_{\text{ext}} = \beta_{\text{abs}} + \beta_{\text{sca}}. \tag{2.6}$$

Integrating β_{ext} over a cloud with geometric thickness Δs gives the so-called *optical thickness* of the cloud, which is an important quantity in remote sensing to describe cloud properties,

$$\tau_\lambda := \int_{\Delta s} \beta_{\text{ext}}(s) \, \mathrm{d}s.$$

Another important parameter to describe cloud properties in remote sensing is the effective radius (R_{eff}) (Hansen and Travis, 1974), defined for spherical particles as

$$R_{\text{eff}} = \frac{\int \pi \, r^3 n(r) \mathrm{d}r}{\int \pi \, r^2 n(r) \mathrm{d}r}, \tag{2.7}$$

where r is the particle radius and $n(r)$ is the number of particles with a radius in the size range $r + \mathrm{d}r$. The $\mathrm{R_{eff}}$ is an effective mean radius of an ensemble of particles that takes into account that spherical particles scatter radiation proportionally to their cross section (Liou, 2002). It has been shown that the RT through a cloud depends primarily on this quantity, independently of the details of the particle size distribution (Liou, 2002).

For cloud particles β_{abs}, β_{sca} and $p(\Omega, \Omega')$ depend not only on the wavelength of the radiation but also on the cloud phase, $\mathrm{R_{eff}}$, and on the shape of the cloud particles (especially relevant for ice crystals). Hence, different cloud (microphysical) properties lead to different amounts of transmitted and emitted radiance. Since the optical properties also depend on wavelength, measurements of radiances at different wavelengths can be used to infer cloud properties - the basic principle of the passive remote sensing of clouds.

2.3   Satellite remote sensing of clouds

Satellite remote sensing plays a crucial role in global observations of clouds and their properties. There are different remote sensing methods, which can be divided into passive and active remote sensing methods. This thesis focuses mainly on passive remote sensing, but some cloud products from active remote sensing are also used. A brief overview of the different methods and instruments is given below.

2.3.1   Passive satellite remote sensing of clouds

Passive satellite sensors measure reflected solar radiation and emitted terrestrial radiation at top of atmosphere (TOA). Examples for important passive satellite sensors are SE-VIRI (Schmetz et al., 2002), ABI (Schmit et al., 2017), AHI (Bessho et al., 2016) and the Moderate Resolution Imaging Spectroradiometer (MODIS) (King et al., 1992). The instruments measure radiation at several different wavelength ranges, called *channels* or *spectral bands*, according to the instrument-specific spectral response functions. Depending on the wavelength, the radiation reaching TOA is affected by different atmospheric constituents.

In the visible wavelengths, radiation at TOA is reflected solar radiation. Satellite channels at visible wavelengths are therefore only available during the day. Atmospheric gases are nearly transparent in the visible, and for cloud-free conditions the visible channels are therefore closely related to the Earth's albedo. Liquid droplets and ice crystals scatter effectively at visible wavelengths, resulting in a high amount of reflected solar radiation (that depends on the cloud properties) (see Sect. 2.2.2). This makes the visible channels suitable for cloud remote sensing. The measured radiance of a visible channel is often converted into a *reflectance R*, i.e. the amount of reflected radiance, L_λ, compared to the incoming solar irradiance, $E_{\odot,\lambda}$, both integrated over the spectral response function of the satellite channel, φ_λ,

$$R = \frac{\pi \int \varphi_\lambda \, L_\lambda \, \mathrm{d}\lambda}{\cos\theta_\odot \int \varphi_\lambda \, E_{\odot,\lambda} \, \mathrm{d}\lambda}. \tag{2.8}$$

Scaling by the cosine of the solar zenith angle $\theta_\odot$ accounts for the fact that the amount of incident solar radiation reaching the Earth per unit area depends on the solar zenith angle.

Radiation at TOA in the IR wavelength range comes from emission by the Earth and the atmospheric constituents. In large parts of the IR spectrum water vapor is highly absorbing (see Fig. 2.3). At these wavelengths, radiation emitted by the Earth's surface or low clouds is largely absorbed by overlying layers of the atmosphere containing water vapor, which in turn emit radiation according to their temperature. Satellite channels at these wavelengths are therefore sensitive to the amount and distribution of water vapor in the atmosphere, which obscures signals from clouds in the lower troposphere. There is however a so-called *atmospheric window* in the IR spectrum from about 8.3–12.5 µm, where radiation can travel through the atmosphere with only little absorption, except for an ozone absorption band (see Fig. 2.3) (Liou, 2002). In contrast, liquid water and ice absorb and emit strongly in the atmospheric window, making this wavelength range suitable for cloud remote sensing. Since the emitted radiation depends on the temperature of the emitting objects, channels in the atmospheric window are very sensitive to the temperature of clouds or, in cloudless conditions, the surface. To reflect this fact and to make IR channels more comparable, the radiance measured in an IR channel is often converted to the (equivalent black body) brightness temperature (BT) using Planck's radiation law (see Eq. 2.2). The BT is the temperature of a fictitious black body that emits the same amount of radiance at a given wavelength as the measured amount of radiance of the observed grey body.

Advantages of passive remote sensing are their wide field of regard and, in the case of geostationary satellites, high temporal resolution. They can provide large scale observations of clouds and their temporal development. However, as the extinction (scattering and absorption) of clouds is very high, passive instrument observations are confined to cloud-tops.

The geostationary imager MSG/SEVIRI

The main instrument used in this work is SEVIRI aboard the MSG satellites operated by the European Organisation for the Exploitation of Meteorological Satellites (EUMETSAT). The MSG satellites are positioned in a geostationary orbit at an altitude of approximately 36,000 km above the equator. The primary operational position for MSG satellites is at 0°E, directly over the Greenwich Meridian. SEVIRI's field of view covers nearly one third of the globe, including Africa, Europe and parts of the Middle East, South America and the Atlantic. The temporal resolution for covering the full disc is 15 minutes.

SEVIRI operates on 11 spectral channels with a spatial resolution of 3 km at the sub-satellite point. These channels include three channels in the visible and near-infrared and eight channels in the IR. An additional 12th channel, called high resolution visible (HRV) channel, covers half of the SEVIRI disc in a higher resolution (1 km) in a broad range of visible wavelengths. An example scene for all SEVIRI channels is shown in Fig. 2.5. Some SEVIRI channels cover specific atmospheric components, for instance water vapor with two channels centered at 6.2 µm and 7.3 µm, ozone with a channel centered at 9.7 µm or carbon dioxide with a channel centered at 13.4 µm. For cloud remote sensing, mainly the
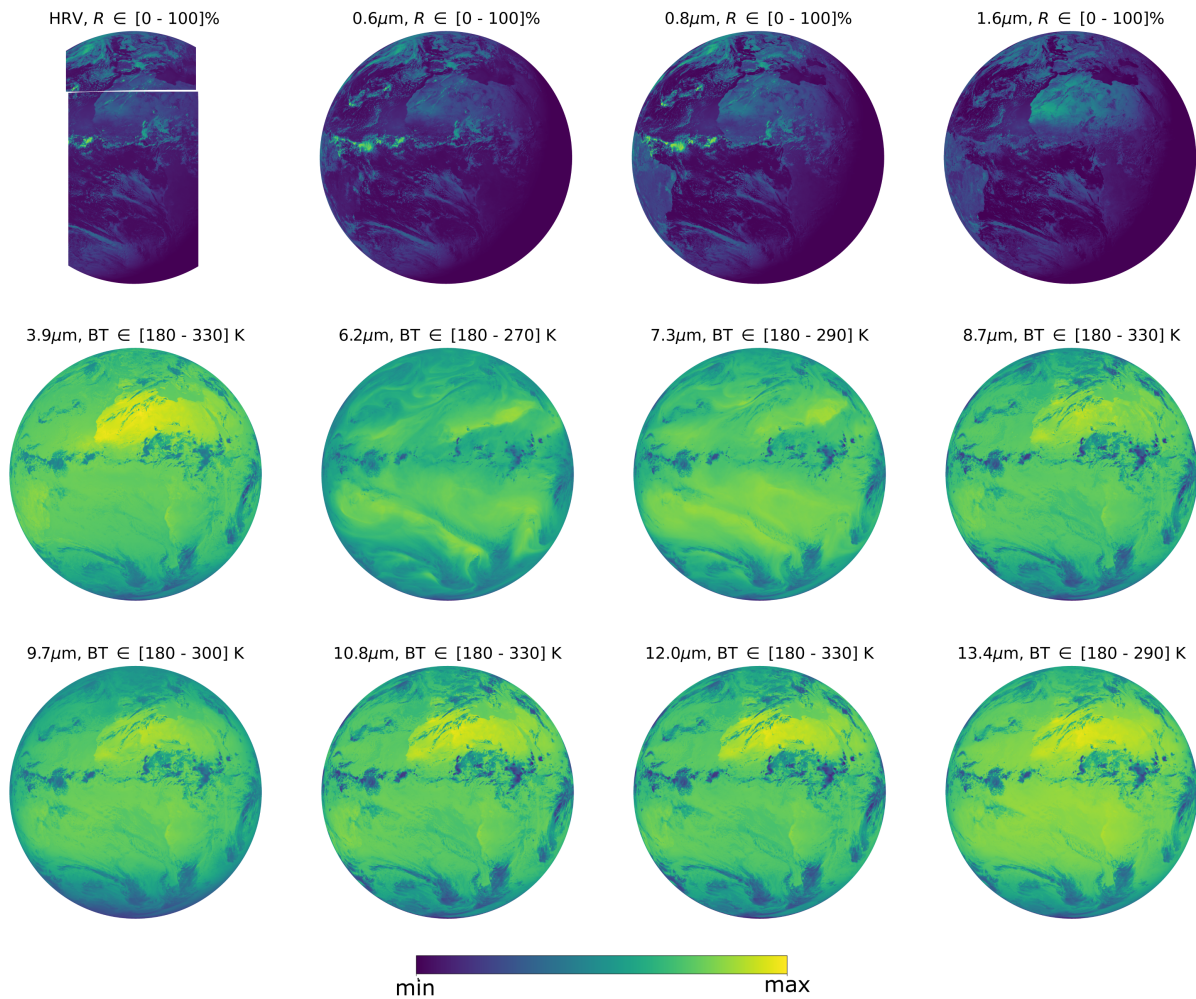
Figure 2.5: Reflectances (R) and brightness temperatures (BT) for the 12 MSG/SEVIRI channels for a scene at 11 June 2024, 15:00 UTC. The minimum and maximum values of the colorbar are given in brackets for each plot. Inspiration for figure from Piontek (2022).

two visible channels (centered at 0.6 and 0.8 µm), the near-infrared channel (at 1.6 µm) and the three channels in the IR atmospheric window (at 8.7, 10.8 and 12.0 µm) are suitable.

2.3.2 Active satellite remote sensing of clouds: Lidar and radar

The active satellite instruments lidar, such as the Cloud-Aerosol Lidar with Orthogonal Polarization (CALIOP) (Winker et al., 2003), and radar, such as the Cloud Profiling Radar (CPR) (Stephens et al., 2002), emit radiation and measure the radiation backscattered by clouds and aerosols. Satellites with active instruments therefore fly in orbits much closer to the Earth (a few hundred kilometers above the surface) compared to geostationary satellites. Lidar instruments use radiation at visible wavelengths; radar instruments use
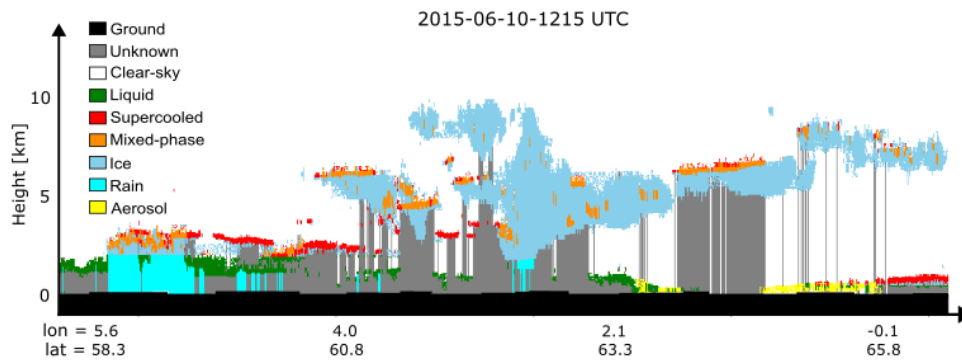
Figure 2.6: Example of the DARMASK-Simplified-Categorization variable of the synergistic lidar-radar DARDAR product on 10 June 2015 at 12:15 UTC. The scene shows a cross-section through a stationary occlusion front located just west of Norway. Adapted from P1.

microwave wavelengths. Both types of instruments emit short pulses of radiation and measure the time it takes for the backscattered radiation to return to the sensor. This time delay, combined with the speed of light, allows the distance to the scattering object to be determined, providing a vertical profile of the atmosphere.

Lidar instruments are highly sensitive to clouds and aerosols. However, lidar signals attenuate rapidly and are only able to penetrate optically thin clouds or the top layers of thick clouds. Radar, which uses longer wavelengths, is sensitive to larger particle sizes, such as ice crystals and precipitation. Their penetration depth is much larger compared to lidar and can scan optically thicker clouds. Synergies of lidar and radar, such as the DAR-DAR product, exploit the different sensitivities and penetration depths to derive vertical profiles of clouds and other atmospheric constituents. These methods are considered to be very reliable and sensitive even to optically very thin clouds. Figure 2.6 illustrates the capabilities of cloud and phase detection of the DARDAR product in an example curtain. However, in contrast to passive instruments, active instruments have a small footprint (CPR, for instance, has a resolution of 1.4 km across and 1.1 km along the satellite track). Due to this small footprint, active satellite instruments have a poor temporal resolution; in the case of CALIOP and CPR a return time of about 16 days.

Chapter 3

Summaries

The publications in this thesis (see Chapters 6, 7 and 8) explore the topic of thermodynamic cloud phase from the perspective of the passive instrument SEVIRI aboard the geostationary satellite MSG. They range from an analysis of the occurrence of cloud phases in the SEVIRI disc (P1), to a theoretical analysis of the phase information content of SEVIRI channels (P2), to the development of a novel retrieval method (P3). In the following sections, I briefly summarise the main findings of each publication, answering the three scientific questions posed in Sect. 1.2.

Parts of the following sections are based on the three publications (P1-3) and the correspondence with the reviewers and editors of the publications; some sentences or parts of sentences have been adopted verbatim or only slightly changed.

3.1 Summary of P1: Thermodynamic phase in the SEVIRI disc

The following results of P1 answer the first scientific question, namely *SQ-1: Do the perspective and the spatial characteristics of a geostationary imager such as SEVIRI allow the study of mixed-phase and supercooled clouds?*

P1 investigates the cloud phase spatial and temporal distribution from the perspective of the SEVIRI imager. To this end, I use the synergistic lidar-radar product DARDAR (Delanoë and Hogan, 2010; Ceccaldi et al., 2013), which contains information on the vertical profile of cloud phase, as a basis. Focusing only on the cloud-top layers to model a simple penetration depth of the passive SEVIRI instrument, I collocate and aggregate 5 years of the finer DARDAR data to SEVIRI's coarser spatial resolution. Thereby I distinguish between ice (IC), mixed-phase (MP), supercooled liquid (SC), and warm liquid (LQ) cloud tops. This modeled SEVIRI-like data set of cloud top phase (CTP) is used to study the geographic and seasonal distribution of CTP from a geostationary passive satellite perspective and to investigate the influence of spatial resolution on phase occurrence.

SEVIRI's field of view covers nearly one-third of the globe, including Africa, Europe, and parts of the Middle East, as well as the Atlantic Ocean, parts of South America and,
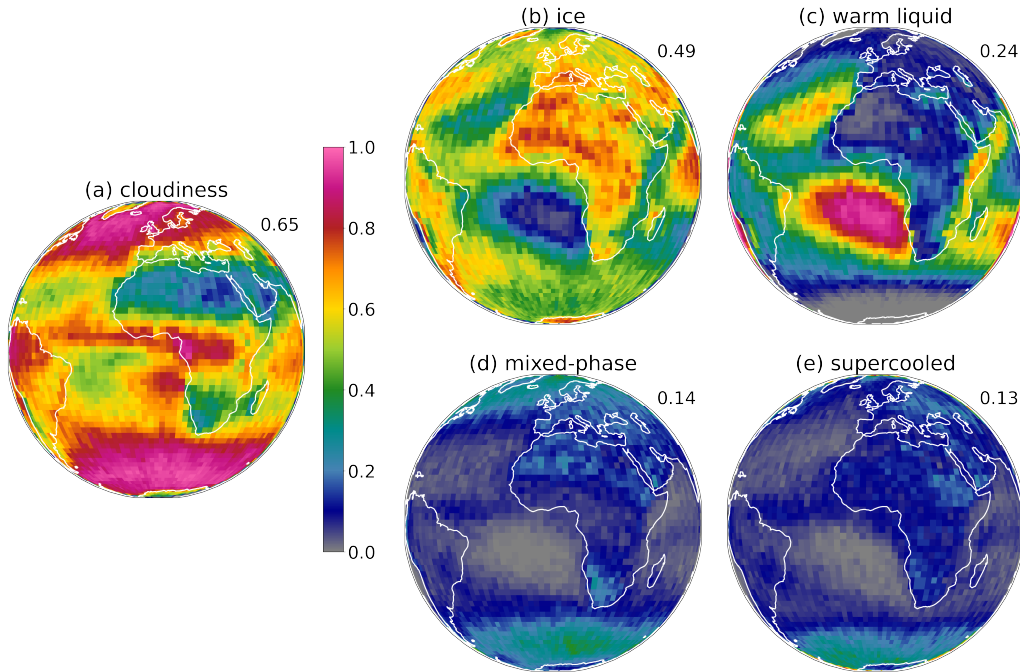
Figure 3.1: Relative frequency of occurrence of (a) clouds and (b-e) cloud-top phases given a cloud over 5 years of the SEVIRI-like data set in boxes of 2.5 °latitude by 2.5 °longitude. The number at the top right corner of each plot is the respective mean over all latitude-longitude boxes over the SEVIRI disc. Adapted from P1.

at high latitudes, parts of Greenland and Antarctica (see Sect. 2.3.1). The analysis of the 5-year SEVIRI-like data set reveals that 65% of SEVIRI pixels are cloudy, with 49% IC, 14% MP, 13% SC, and 24% LQ cloud tops; the distribution on the SEVIRI disc is shown in Fig. 3.1. SC clouds are most common at high southern latitudes, MP clouds at high northern and southern latitudes, LQ clouds in subsidence zones over oceans, and IC clouds elsewhere. Hence, all cloud phases occur in significant amounts at cloud top in the SEVIRI disc. Spatial resolution significantly affects CTP occurrence, especially for MP clouds, which are significantly more frequent at SEVIRI's lower resolution (14%) compared to DARDAR's higher resolution (9%). The physical reason is that extended MP clouds are typically not homogeneously mixed, but also contain SC and IC "pockets" at cloud top. With a smaller pixel size (e.g. DARDAR) these phases can be resolved better; with a larger pixel size (e.g. SEVIRI) signals from these phases are more likely to mix in a (larger) pixel, which is then considered MP. These results help to assess how representative geostationary measurements of CTP are compared to measurements from polar orbiting satellites and to interpret them in the correct way.

Since the cloud phase is related to temperature (see Sect. 2.1), the occurrence of CTP as a function of CTT is examined at SEVIRI resolution (shown in Fig. 3.2). The results show how the probability of ice particles increases with decreasing CTT: The occurrence
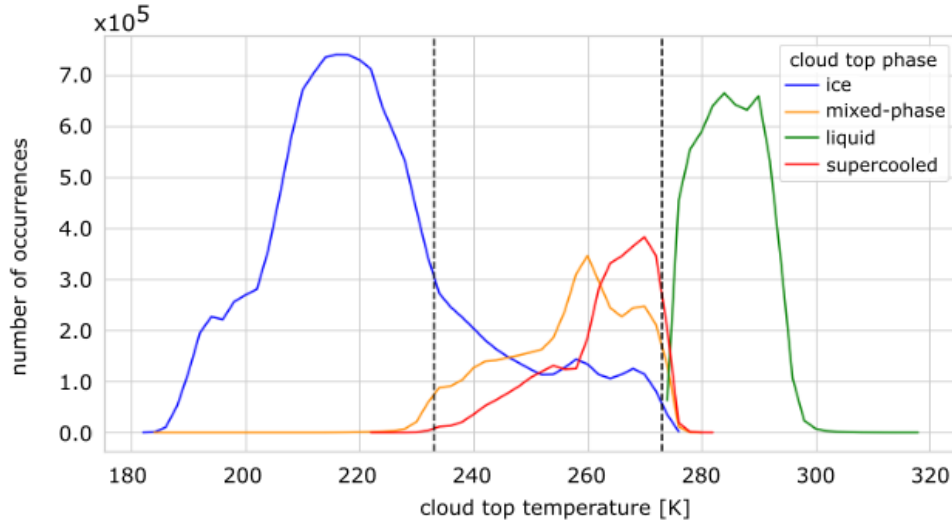
Figure 3.2: Number of occurrences of SEVIRI-like cloud-top phases (CTP) as a function of cloud top temperature from the 5-year SEVIRI-like data set. The distribution has bins of 1.0 K. Black dashed lines indicate the temperatures 233 K and 273 K. Adapted from P1.

of SC clouds peaks at -3°C and of MP clouds at -13°C. SC and MP clouds are more frequent between 0 and -27°C, while IC clouds dominate below -27°C. Closely related to the CTT is the CTH. The study examines how the CTH varies by geographical region: Over oceans, the CTH for all phases is lower than over land, with distinct peaks for MP, SC and IC clouds outside the tropics. In the tropics, the CTHs for MP, SC and LQ overlap significantly.

Another interesting aspect of cloud phase distribution is its seasonal cycle. IC and LQ clouds show seasonal cycles influenced by the Intertropical Convergence Zone (ITCZ). MP and SC clouds show less seasonal variability, except at high latitudes, especially in Antarctica, with notable seasonal differences.

The results of P1 show that across the SEVIRI disc, significant amounts of all thermodynamic phases, including MP and SC, are present at cloud tops in the SEVIRI disc. This demonstrates the potential of geostationary remote sensing instruments to study the thermodynamic phase of clouds, especially the less studied MP and SC clouds. It underlines the importance and potential of developing dedicated cloud phase retrievals for all cloud phases (IC, LQ, MP, SC) for geostationary satellites to better understand phase partitioning and to enable the study of the micro- and macrophysics of clouds with different phases, their temporal evolution and phase transitions.

The collocated data set of DARDAR and SEVIRI data developed for this study can serve as a reference for testing SEVIRI phase retrievals. As a first application the study evaluates the performance of the Cirrus Properties for SEVIRI (CiPS) algorithm, an artificial intelligence (AI) based ice cloud detection tool. The results indicate that CiPS effectively detects fully glaciated (IC) clouds but is not sensitive to ice crystals in MP clouds. This highlights the need for improved algorithms to distinguish all cloud phases.

Besides testing existing retrievals, this study can serve as a reference to develop new retrievals. The collocated data set provides valuable insights into the geographical and seasonal distribution of all cloud phases, which can be used as a basis for developing cloud phase retrieval algorithms - this is done in the follow-up study P3.

The analysis of the effects of spatial resolution highlights the fact that the occurrence and distribution of cloud-top phases can be different for different instruments. It shows that resolution effects can be particularly large for MP clouds due to the spatial variability of liquid and ice regions within an extended cloud deck. This is an important consideration when, for example, the results of retrievals from different instruments are compared with each other or with model results.

DARDAR was used as the ground truth for this study. While DARDAR is very reliable in terms of cloud and phase detection, there are still some possible sources of error that should be noted. These include possible grid misalignments of the input data from the CloudSat and CALIPSO satellites; temperature data errors from European Centre for Medium-Range Weather Forecasts (ECMWF) which is used for phase classification; and false positives for the detection of very low clouds ($< 1.5\,\mathrm{km}$) due to ground clutter where radar signals might be reflected from the ground or other non-cloud targets (Huang et al., 2012; McErlich et al., 2021). Unfortunately, the DARDAR product does not currently provide uncertainty values for phase classification, so the DARDAR results used in this and the follow-up study P3 are all considered "true".

3.2 Summary of P2: Information content of brightness temperature differences

The investigations of P2 answer the second scientific question: *SQ-2: What is the information content of BTDs from spaceborne imagers with respect to the cloud phase? What are the implications for phase retrievals?*

In P2, I approach the topic of remote sensing of the thermodynamic cloud phase from a theoretical perspective. This study supports the efforts to develop a new phase retrieval algorithm (see P3), specifically aiming to optimize the information content provided by SEVIRI IR channels and to physically understand their relation to the cloud phase. In P2, RT calculations are used to investigate the relation of cloud phase and other cloud parameters to BTDs of the SEVIRI imager. I focus on BTDs commonly used in (phase) retrievals, namely the BTD between channels centered at 8.7 and 10.8 µm, BTD(8.7-10.8), and between channels centered at 10.8 and 12.0 µm, BTD(10.8-12.0).

The aim is to gain a comprehensive and deep understanding of the behaviour of the two BTDs in order to improve (phase) retrievals. The first step is to investigate the effects of the computation of BTDs: Radiances are transformed to BTs using Planck's radiation law (see Sect. 2.3.1) and then to BTDs. This transformation is highly nonlinear. I find that this nonlinearity induces positive BTD values and a dependence on the CTT where naively one would not expect it. This effect contributes to the characteristic arc shape of

the BTDs as a function of τ (Inoue, 1985) and their dependence on CTT (see below).

Next, the sophisticated RT package libRadtran (Mayer and Kylling, 2005; Emde et al., 2016) is used to perform simulations for the three SEVIRI channels centred at 8.7, 10.8 and 12.0 µm to assess sensitivities of the BTDs on various parameters. These simulations are performed for a variety of ice and water clouds with different τ, R_{eff}, ice crystal habit, and CTT/CTH, such that all radiatively relevant cloud properties are included. The results of the simulated BTDs as a function of the cloud properties are analyzed in detail. Furthermore, the study focuses on the physical understanding of the RT effects on BTDs by switching on and off different RT processes, namely cloud particle scattering and molecular absorption. For small τ, spectral differences in absorption are responsible for the behaviour of both BTDs for varying phase (larger BTDs for ice compared to water clouds) and varying R_{eff} (larger BTDs for smaller R_{eff}). However, spectral differences in scattering, which are rarely studied for IR channels, lead to a weakening of the effects of phase and R_{eff} on BTD(8.7-10.8) and to an increase of the effects for BTD(10.8-12.0). In fact, the direct phase dependence of BTD(10.8-12.0) is mainly due to scattering effects. There are large effects of the CTT on both BTDs. This dependence on CTT is due to the nonlinearity effect (see above), molecular absorption (mainly above cloud) and the fact that larger surface-cloud temperature contrasts lead to enhanced sensitivity of the BTDs to spectral differences of the optical properties in the two channels of the given BTD.

Having understood the effects of the cloud properties individually, the study combines all effects in a sensitivity analysis. This sensitivity analysis provides an overview of the relative importance of the different cloud properties and their contributions to the observed phase dependence of BTDs.

The results of P2 show that the phase dependence of BTDs is more complex than sometimes assumed: Although both BTDs are directly sensitive to phase (holding all other cloud properties constant), this sensitivity is mostly small compared to other cloud properties such as τ, CTT and R_{eff}. Instead, apart from τ, the BTDs show the strongest sensitivity to CTT/CTH. Since CTT is associated with phase, this is the main factor leading to the observed phase dependence of BTDs. The study analyses for which cloud scenarios one can distinguish between liquid and ice clouds with high confidence, and when the BTDs for the two phases overlap, in order to derive implications for phase retrievals. The results show that "typical" high ice clouds and low liquid clouds can be distinguished by the BTDs. However, it is challenging to distinguish a mid-level ice cloud from a mid-level liquid cloud - especially if the R_{eff} is also similar.

P2 significantly advances the understanding of BTDs and their relationship with cloud phase and other radiatively important cloud parameters. The analysis of the BTD nonlinearity effects is an additional aspect needed to understand the BTDs. This knowledge can be used to refine phase retrieval algorithms using BTDs, as demonstrated in P3. Moreover, it can be used to improve BTD retrievals of other cloud properties, as the study examines the effects of all radiatively relevant cloud parameters (i.e. also τ, R_{eff}, CTT and ice crystal habit) in detail. The physical understanding of the effects of different cloud properties on the RT through the cloud can further be applied to the use of IR window satellite channels in general (e.g. β ratios (Parol et al., 1991; Pavolonis, 2010; Heidinger et al., 2015)).

Overall, P2 serves as a reference for the in-depth interpretation of spaceborne BTDs and as a resource for future research to develop or refine satellite retrievals.

A critical aspect of any retrieval algorithm is to understand its uncertainties and limitations. While BTDs have long been used in the satellite community, their dependencies are complex and unforeseen cloud or atmospheric conditions can lead to unexpected behaviour and retrieval errors. P2 shows for which cloud properties the phase can typically be detected and when ice and liquid cloud scenarios overlap from the passive IR point of view. This detailed sensitivity analysis helps to clarify the uncertainties and limitations of BTD retrievals. Note that it is important to understand the theoretical capabilities and limitations of BTDs, not only for physics-based retrievals, but also when considering AI methods that use BTDs. In cases where the information content of BTDs is ambiguous, AI methods may only learn the statistical frequency of an answer, rather than the actual physical relationships, potentially leading to false trends if the underlying statistics change, for example if climate change causes the frequency of a cloud phase to change. It is therefore crucial to consider the physical capabilities and limitations of satellite channels when using them.

3.3 Summary of P3: Method for the retrieval of thermodynamic phase

The phase retrieval method presented below provides an answer to the third scientific question: *SQ-3: Can the phase retrieval capabilities of synergistic lidar-radar methods be transferred to passive imagers and how accurately can this be done?*

The results of P1 demonstrate the need for dedicated phase retrieval algorithms for SEVIRI which can distinguish all cloud phases. As preparatory work for the development of such a retrieval, P2 investigates the information content of SEVIRI channel combinations (specifically BTDs) with respect to phase. As a next step P3 develops such a retrieval, called PRObabilistic cloud top Phase retrieval for SEVIRI (ProPS) (PRObabilistic cloud top Phase retrieval for SEVIRI), a new method for cloud detection and phase determination for SEVIRI. ProPS distinguishes between clear sky, optically thin ice (TI), optically thick ice (IC), mixed phase (MP), supercooled liquid (SC) and warm liquid (LQ) clouds, hereafter referred to as different *cloud states* with the abbreviation q.

The method used in the ProPS retrieval is a Bayesian approach and works as follows: As preparation in P1, 5 years of the lidar-radar cloud product DARDAR are collocated with SEVIRI. This collocated data set thus contains cloud state information (from DARDAR) and SEVIRI channel measurements and is used as a basis for the ProPS retrieval. From this collocated data set the probability of each cloud state q occurring on the SEVIRI disc per season, i.e. $P(q \,|\, \text{lat}, \text{lon}, \text{season})$, is calculated (similar to what is done in P1, see Fig. 3.1). This serves as a prior probability for each cloud state. Further, probabilities for SEVIRI channel (or channel combination) measurements M, conditioning on the cloud state q and additional parameters C, i.e. $P(M \,|\, q,\, C)$, are computed. These probabilities are computed

for carefully selected SEVIRI channels (or channel combinations) that contain information on the phase, namely channels at wavelengths 0.6, 1.6, 8.7, 10.8 and 12 μm, along with a texture parameter derived from the 10.8 μm channel. As shown in P2, the IR window channels (8.7, 10.8, and 12 μm) contain phase information, but can lead to ambiguities in distinguishing cloud phases in certain scenarios, so solar channels (at 0.6 and 1.6 μm) are used in addition. The conditions C in the probabilities of the SEVIRI measurements are used to remove confounding parameters (i.e. parameters that lead to spurious correlations between M and q) and to optimise the information content of the probabilities. These conditions are chosen for each probability using the mathematical framework of mutual information. Possible conditions can be other SEVIRI channels (or channel combinations) or auxiliary parameters (solar and satellite zenith angle, surface type, surface temperature, latitude, longitude and season). The computation of the prior probability for the cloud states and the probabilities for each SEVIRI channel (or channel combination) only needs to be done once as a preparation for the algorithm.

The cloud state retrieval ProPS works as follows: The prior knowledge of the cloud state is combined with the calculated probabilities for each measurement using Bayes' formula. Bayes' formula is the mathematical expression for how to update a belief when new information is available. In this framework, the method starts with the prior probability for the cloud state and successively updates this probability for each SEVIRI measurement using the precalculated probabilities and Bayes' formula. The output is a probability for the cloud state given all used SEVIRI measurements and auxiliary data for each SEVIRI pixel, i.e. $P(q \,|\, \{M\}, \{A\})$ with $\{M\}$ the set of all used SEVIRI measurements (i.e. channels and channel combinations) and $\{A\}$ the set of all auxiliary parameters used. As a final step of the retrieval, the cloud state with the highest probability in each pixel is selected as the final result. Figure 3.3 shows an example application of ProPS and the corresponding false color RGB for comparison. The retrieval has a daytime and a nighttime version. In the nighttime version, the solar channel updates are omitted and the cloud state probability is computed using the IR channels only. Since the algorithm outputs probabilities for each cloud state, it is straightforward to develop a measure of certainty (a quality measure) associated with the result: The certainty is maximal when the highest probability is 1 and all other probabilities are 0. The closer the highest probability is to the probabilities of other cloud states, the lower the certainty becomes.

The validation of ProPS using six months of independent DARDAR data as ground truth demonstrates promising results: The daytime algorithm successfully detects 93% of clouds and 86% of clear sky pixels. For phase determination, ProPS accurately classifies 91% of IC, 78% of TI, 52% of MP, 58% of SC and 86% of LQ pixels. The main challenges for cloud detection are very thin cirrus clouds and the detection of LQ clouds with similar cloud temperatures as the surface at night, which leads to an overestimation of clouds at night (false alarm rate of 24%). The most challenging distinction is between MP and SC, as ProPS frequently classifies MP as SC and vice versa. This challenge is expected because SC and MP cloud tops often occur under very similar conditions (e.g. similar latitudes and CTTs) and because the radiative properties of both cloud states can be similar when a MP cloud top consists mainly of liquid droplets. Unfortunately, data on such microphysical
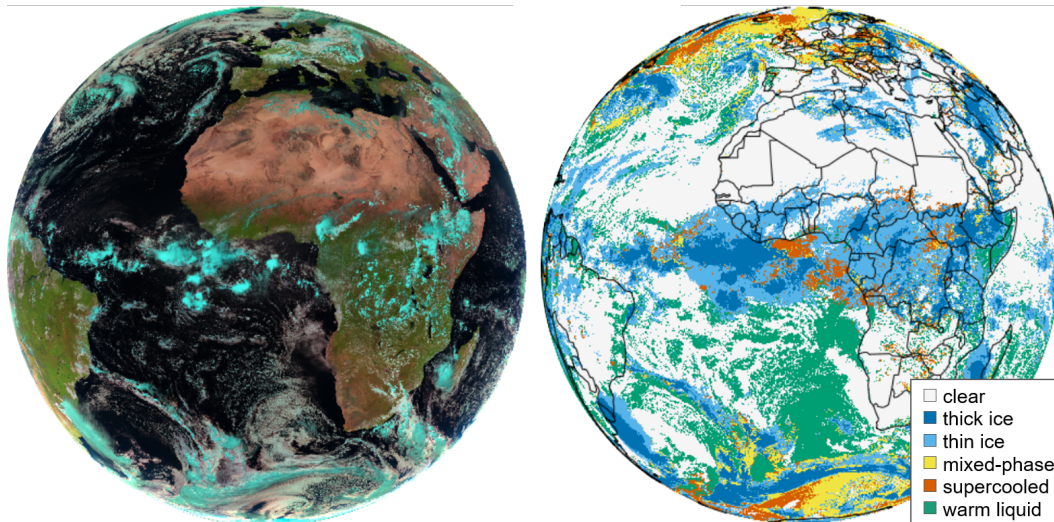
Figure 3.3: False colour RGB composite (left) and example application of ProPS (right) for a SEVIRI scene on the 2022-04-25 at 12:00 UTC. Adapted from P3.

properties of liquid containing clouds are not available for the current version of DARDAR, so it is not possible to identify the cloud properties for which the distinction between MP and SC works or fails. The certainty parameter is shown to be a useful measure of the reliability of the results, as the phase detection probabilities consistently increase with higher certainty and the false alarm rates decrease.

To summarize the response to SQ-3: The ProPS algorithm applies a Bayesian approach to extend the phase retrieval capabilities of synergistic lidar-radar methods to passive imagers, using probabilities extracted from the lidar-radar product DARDAR. The Bayesian approach offers several advantages, including its transparency and a quantification of the certainty of the retrieval results. ProPS represents a significant advancement in discriminating cloud-top phases compared to traditional retrieval methods.

The new ProPS method allows the detection of clouds with different phases, enabling the study and comparison of their microphysical and macrophysical properties. This is particularly interesting for MP and SC clouds, which have been little studied from geostationary satellites. The geostationary perspective allows the analysis of the temporal evolution of clouds with different phases as well as phase transitions.

While ProPS is an advancement compared to traditional retrieval methods, which mostly only distinguish liquid and ice, it is important to be aware of its limitations. Most passive imager phase retrievals do not attempt to distinguish between SC and MP. ProPS implements a new approach that relies on the DARDAR phase product to make this distinction (along with cloud detection and distinguishing the other phases). While the distinction between SC and MP is the most challenging, ProPS is still able to correctly detect more than 50% of both cloud phases. This is a step in the right direction for passive imagers.

ProPS takes a different approach from the other two recently or in parallel developed

phase retrieval methods that include MP detection, described in Sect. 1.2. While the ABI algorithm is based on theoretical principles and the AHI algorithm uses a DNN, ProPS takes an approach that integrates the strengths of both methods: Like theoretically based methods, it maintains transparency and interpretability, through its statistical approach. At the same time, it utilizes measured data as a reference, like DNNs. ProPS is the first passive phase retrieval method to use the reliable DARDAR phase product as its basis. Using measured data such as DARDAR as a basis has the advantage over threshold methods of not requiring manual tuning and covering most real atmospheric scenarios. For ProPS, an extensive data set of 4,5 years of DARDAR data was used as a basis for computing the needed probabilities, which is an advantage over the AHI algorithm, which had only 1 year of data available for training. In addition, having an underlying reliable data set as ground truth allows for rigorous validation, which is a significant advantage over the ABI method (see section. 1.2).

Furthermore, the use of probabilities in the retrieval method offers some important advantages. The transition from pure liquid to MP to ice in clouds is in reality continuous. Probabilities can represent this continuous spectrum more accurately than thresholds or a neural network classification. Moreover, the calculated probabilities can help to identify which channels contribute to phase distinction in specific scenarios. Another advantage of using probabilities is that it is straightforward to define a certainty value, as described above.

Chapter 4

Conclusions

Numerous studies emphasize the importance of cloud phase on climate sensitivity in global climate models (Gregory and Morris, 1996; Doutriaux-Boucher and Quaas, 2004; Cesana et al., 2012; Tan et al., 2016; Bock et al., 2020). Accurate satellite retrievals of cloud phase are crucial for understanding the cloud radiative effect and to improve cloud representations in numerical models (Atkinson et al., 2013; Komurcu et al., 2014; Cesana et al., 2015; Matus and L'Ecuyer, 2017; Forster et al., 2021; Cesana et al., 2022). Combinations of state-of-the-art geostationary satellites can provide almost global observations of cloud-top phases and their temporal development - a unique advantage of geostationary satellites. Such observations of the temporal evolution of cloud-top phases and phase transitions are of particular interest for understanding the dynamic and microphysical processes governing cloud properties. This thesis is a comprehensive and innovative study of the remote sensing of thermodynamic cloud phases with a geostationary satellite. It discusses the capabilities of passive imagers, in particular SEVIRI aboard the geostationary MSG, to observe cloud phases and presents a new retrieval method.

This thesis shows that all cloud phases are abundant at cloud tops in the SEVIRI disc - also MP and SC clouds which are rarely studied with passive imagers. This highlights the potential of geostationary imagers such as SEVIRI to contribute to their study.

For phase retrievals with passive imagers, specific channel combinations, namely BTDs of IR window channels, are often used. This thesis closes the gaps in the understanding of the information content of these BTDs with respect to the cloud phase. To this end, RT calculations are used to investigate the relationship between all radiatively relevant cloud parameters and BTDs. This improves the understanding of BTDs, which benefits the development of phase retrievals.

With these findings in mind, the ProPS cloud and phase retrieval method is developed. Key characteristics of ProPS are: 1) it uses the most accurate observations of cloud phase available so far, i.e. synergistic lidar-radar methods, as ground truth, 2) it implements a physical approach with emphasis on transparency and traceability of the results and 3) it uses probabilities (Bayesian approach) to make explicit where SEVIRI channels are confident or ambiguous about the cloud phase. ProPS shows promising results, correctly identifying clouds and their phases in the majority of cases.

Developing various retrieval methods such as ProPS is crucial for identifying effective approaches and challenges. This study provides important insights into the capabilities and limitations of SEVIRI in distinguishing cloud phases, contributing to global efforts to improve satellite products and to achieve a common understanding of cloud phases.

Chapter 5

Outlook

5.1 Applications of the phase retrieval method

The new ProPS method enables the study of microphysical, macrophysical and radiative properties of clouds with different phases, in particular also MP and SC clouds, which have so far been little studied from geostationary satellites. Knowledge of these cloud properties is crucial for understanding the life cycle of clouds, precipitation formation and radiative effects. SEVIRI's geostationary perspective allows analysing the temporal evolution of cloud properties as well as phase transitions. The nighttime version of ProPS performs almost as well as the daytime version in detecting cloud phases given a detected cloud. This indicates that ProPS is well suited for the study of the complete daily cycle of cloud phases. SEVIRI has been operational for two decades (2004-2024). The application of ProPS to this extensive dataset allows thus a broad range of cloud phase studies.

Statistics on the occurrence of different phases could be compared with climate models. Such comparisons have so far been made mainly for active instruments (e.g. Jiang et al., 2012; Cesana and Chepfer, 2013; Komurcu et al., 2014; Cesana et al., 2022), which have the advantage of providing vertical profiles. ProPS results for passive geostationary sensors, on the other hand, provide a different aspect of model evaluation as they are available at all times of the day.

One of the most pressing topics regarding cloud phases and their representation in climate models is high latitude clouds, especially over the Southern Ocean (SO): The SO is one of the cloudiest regions on Earth. It has a high frequency of stratiform SC and MP cloud-top layers (Korolev et al., 2017; Coopman et al., 2021). Misrepresentations of these clouds have been shown to be responsible for large biases in their cloud radiative effect (Bodas-Salcedo et al., 2014; Bock et al., 2020). Phase transitions are a key process for the cloud radiative feedback over the SO but are still highly uncertain, as explained in Sect. 1.1 (Gettelman and Sherwood, 2016; Zelinka et al., 2020). Figure 5.1(a) shows the CMIP6 net cloud feedback parameter (i.e. the change in radiative flux at the top of atmosphere due to altered cloud properties with warming, normalised by the global mean surface temperature increase). The cloud feedback involving phase changes of MP clouds is responsible for the
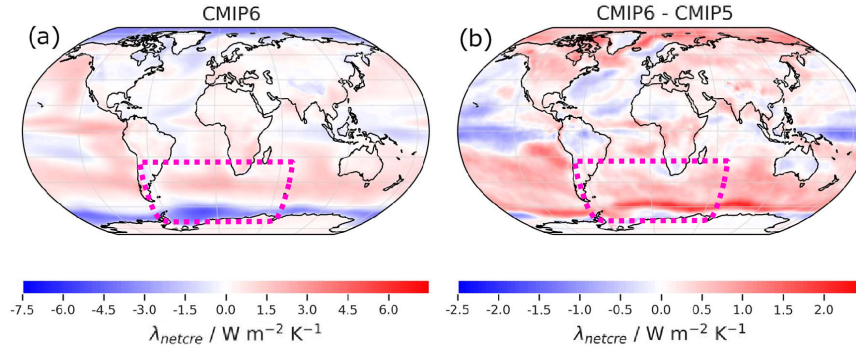
Figure 5.1: (a) Cloud net feedback parameter for CMIP6 (multimodel mean) and (b) the differences to the CMIP5 multimodel mean cloud feedback parameter. The pink dotted line indicates approximately the region shown in Fig. 5.2 in the SEVIRI projection. Credit: Adapted from Bock et al. (2020) (CC BY 4.0 `https://creativecommons.org/licenses/by/4.0/`).

negative sign of the feedback parameter in high latitudes. The comparison with the earlier CMIP5 models in Fig. 5.1(b) shows that there are large discrepancies between earlier and the most previous models in these regions thus pointing at uncertainties in the simulation of such clouds. To gain an improved understanding and to compare with model simulations, satellite observations of the cloud phases of these SO clouds and their phase transitions are crucial. ProPS allows the study of the temporal evolution of SO clouds (see the pink dotted region in Fig. 5.1(a)), including the for this region most important SC and MP cloud tops. A crucial aspect that can be studied with ProPS is the diurnal cycle of SO cloud phases; an example of a diurnal cycle is shown in Fig. 5.2. Note that the region with high occurrences of MP and SC clouds corresponds to the region of negative cloud feedback and large discrepancies between models in Fig. 5.1. Also of interest is the stability of the MP and SC layers at the cloud top, studying how long these layers exist and under what conditions they glaciate. These aspects, where the observation of the temporal evolution is crucial, can only be addressed with a geostationary satellite. A second advantage of geostationary satellites is their wide field of regard. Thus, ProPS can provide large scale observations of the cloud cover and the spatial distribution of cloud phases at any time during the 20 years of available data. Furthermore, this wide field of regard enables the study of the horizontal distribution of liquid and ice particles within SO clouds. Whether the liquid and ice particles are homogeneously mixed or in spatially separated liquid and ice 'pockets' affects how they interact with each other. This can have a large impact on the stability of a SC or MP cloud layer and therefore on the radiative properties of the clouds (Tan and Storelvmo, 2016; Korolev et al., 2017).

Knowledge of the thermodynamic phase is a crucial aspect of aerosol-cloud interactions (ACI), which have a potentially large but uncertain effect on the Earth's radiative balance. In fact, the uncertainty in ACI dominates the total uncertainty in future climate projections (Hansen et al., 2011; Sullivan and Hoose, 2023). The amount and type of aerosol have an impact on cloud phase, as the presence of INPs is crucial for the glaciation of cloud droplets. For instance, it has been suggested that the hemispheric difference in aerosol loading, with
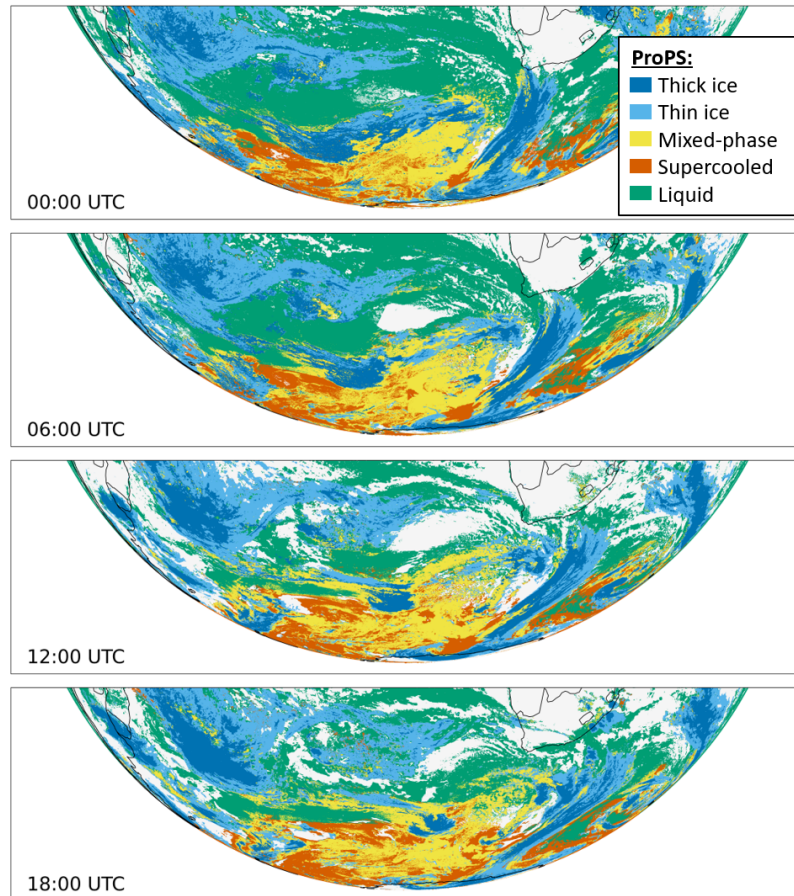
Figure 5.2: Example of ProPS for the diurnal cycle of Southern Ocean clouds on 2022-01-01.

more aerosol in the northern hemisphere, leads to a higher occurrence of ice clouds in the northern hemisphere compared to the southern hemisphere (Tan et al., 2014; Zhang et al., 2018; Li et al., 2017; Villanueva et al., 2021). With ProPS, differences in the occurrence of cloud phases between polluted and unpolluted regions in the SEVIRI disc can be assessed. In this context, aerosol events such as a Saharan dust event provide a suitable scenario to compare regions affected and unaffected by an aerosol event, and study the temporal evolution of phases following the disturbance.

Another cloud type for which ProPS enables novel studies is convective clouds. Here, the height and time of phase transition from liquid to MP to fully glaciated during the development of convective cells strongly affects the microphysical, macrophysical and radiative properties of convective clouds including their lifetime. Convection remains a challenge for numerical simulations and the processes governing the phase transition are still poorly understood (Korolev et al., 2017; Coopman et al., 2020a). ProPS can be used to follow convective cells from convective initiation to full glaciation and beyond. Interesting questions include the analysis of glaciation temperature and speed, and their dependence on microphysical and macrophysical cloud and aerosol parameters. Establishing the relationship

between these phase transition properties and the properties of the fully grown convective cells allows to estimate the impact of phase transition characteristics on anvil properties, which are responsible for warming radiative effects in the course of the convective cloud life cycle. Figure 5.3 shows an example of a tracked mesoscale convective system and its phase transition using ProPS.
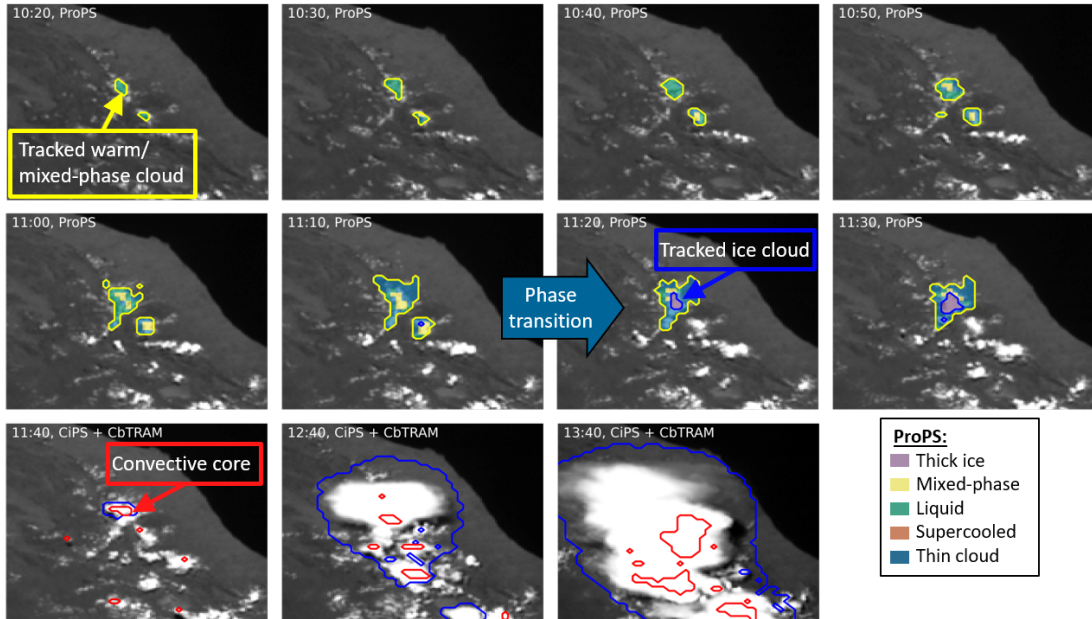
Figure 5.3: Time evolution of a convective system close to Rome on 2015-07-07. Each figure shows the SEVIRI High Resolution Visible (HRV) channel in black and white and an overlay with the tracked convective cell in color. The convective initiation (until 11:30 UTC; first two rows) is tracked with ProPS and the color code shows the cloud phase. Glaciation, i.e. a phase transition, of the main cell occurs between 11:10 and 11:20 UTC. The tracked convective initiation was added to an existing data set of tracked convective systems using the ice cloud detection CiPS and the convective core detection Cumulonimbus Tracking and Monitoring (Cb-TRAM) (Zinner et al., 2008), which track the convective cell in its later stages (third row). Details about this data set and the tracking algorithm can be found in Strandgren (2018). The tracking algorithm has been extended to include different cloud top phases.

.

Correctly identifying the presence of supercooled liquid droplets (both in pure SC and in MP clouds) is further important for aviation safety. When an aircraft flies through clouds containing supercooled droplets, ice can form on the aircraft surface, disturbing the wing profile and inducing control problems (International Air Transport Association (IATA), 2022). ProPS can be used for near real-time detection of areas to avoid. As droplet size and water content affect the severity of such freezing events, other satellite measurements of these properties can ideally be added to the cloud phase information from ProPS.

5.2   Next steps and future retrieval developments

One way to further validate ProPS is to compare its results with in-situ data. A suitable aircraft campaign is the 2023 campaign of the EU project Sensors for Certifiable Hybrid Architectures for Safer Aviation in Icing Environment (SENS4ICE). Here, in particular, clouds containing supercooled droplets were measured, which is rarely done for safety reasons. Figure 5.4 shows an example scene during the SENS4ICE campaign, where many SC and MP clouds were present. These in-situ measurements can be used to compare and validate, in particular, the more difficult SC and MP detection of ProPS. Such a comparison has been started in a Master thesis project for a first flight and can be extended to the whole campaign period (Menekay, 2023). A second option for validation is to compare ProPS to other remote sensing methods, as for instance retrievals of cloud phase from the spectrometer of the Munich Aerosol Cloud Scanner (specMACS) (Ewald et al., 2016; Weber et al., 2024). SpecMACS is an airborne high-spatial-resolution hyperspectral and polarized imaging system capable of retrieving cloud properties at cloud tops with high reliability. Its retrieval methods using its hyperspectral and polarized imaging capabilities are distinct from those of a moderate-spectral resolution radiometer such as SEVIRI and are therefore suitable for independent validation. Such comparisons help to improve the understanding of the situations in which a ProPS retrieval works well or fails, and to identify the reasons why.

There are several options how to further develop and improve ProPS. Similar channels to those used for ProPS are available in most current operational polar and geostationary passive imagers. The algorithm can therefore be extended to other satellites with little modification, for example by using spectral band adjustment factors as proposed by Piontek et al. (2023). One of these geostationary satellites is the follow-on mission to MSG (Meteosat Third Generation (MTG), launched on 13 December 2022 (Durand et al., 2015)) with the passive Flexible Combined Imager (FCI) instrument. FCI offers a higher spatial and temporal resolution, which allows to study cloud processes even closer. Since the resolution can have an effect on the observed cloud phases, as shown in P1, to use ProPS for FCI one must first collect a data set of collocated active observations to compute the necessary prior cloud phase distribution. In the future, this could be done with the Earth Clouds, Aerosols and Radiation Explorer (EarthCARE) satellite (Wehr et al., 2023) (launched May 2024). Since FCI has additional near-infrared channels that contain cloud phase information and could in principle improve phase detection, this information could be added to ProPS by computing probabilities for these additional channels using such collocated EarthCARE data.

Future versions of the DARDAR product will provide vertical information on cloud microphysical parameters (for instance droplet sizes and water content) for all cloud types. Adding this information to the collocated dataset (see P1) would allow a detailed analysis of the microphysical conditions under which SEVIRI channels are sensitive to the distinct cloud phases and in particular SC and MP. Furthermore, microphysical parameters from DARDAR could allow to implement retrievals for these parameters from SEVIRI, in the same way as ProPS now for cloud phase. Of particular interest is the detection of the
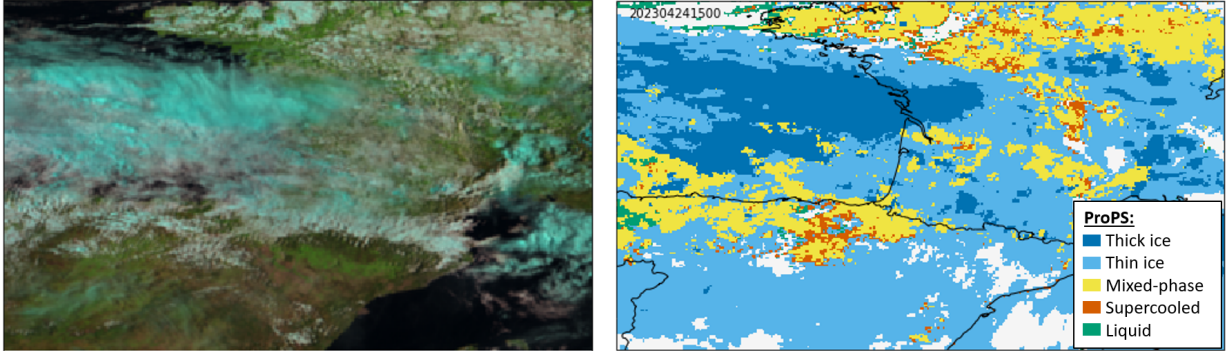
Figure 5.4: Example scene on 2023-04-24 at 15 UTC during a measurement flight of the SENS4ICE campaign over France and Spain: False-color RGB composite (left) and corresponding ProPS results (right). According to ProPS, a thin ice cloud overlays a lower cloud, which is mostly mixed phase. The aircraft flew through the lower cloud deck.

liquid fraction in MP cloud tops, since it has a large influence on the radiative effect of the cloud. In this context, one could also further investigate the information content of the probabilities output by ProPS, which so far are "only" used to derive the certainty parameter. It would be interesting to see if the probabilities could be exploited to derive additional parameters such as the liquid fraction.

Finally, the collocated DARDAR and SEVIRI data set developed in P1 can be used for future studies and the development of new retrieval methods – as was done in P3. The data set includes all SEVIRI channels and many cloud and atmospheric parameters from DARDAR (e.g. CTT, CTH, ice microphysical parameters, ice optical thickness, aerosol, temperature profiles, . . .). In fact, it is already being used for a Master thesis project funded by the German Weather Service to develop ice crystal icing detection methods from satellite.

With regard to the future of passive satellite remote sensing, additional satellite channels may be useful to further improve cloud phase retrievals. For example, Peterson et al. (2022) show that far-IR channels (in the wavelength range between 16.7 and 25 µm) can be a useful addition for cloud phase detection. Moreover, at near-IR wavelengths between 1 and 3 µm, differential absorption features between liquid and ice can be used to infer phase, as suggested by Noh and Miller (2018). SEVIRI has only one channel in this spectral region (at 1.6 µm), while, as mentioned above, FCI aboard the follow-up MTG satellites has additional channels in this spectral region, namely at 1.3 and 2.2 µm, which is an advance for future phase retrieval efforts. Due to their different penetration depths, a combination of several such near-IR channels could also be used to probe the cloud phase below the cloud top (Noh and Miller, 2018). This would be particularly interesting for clouds with SC or MP cloud tops with ice underneath, as often found at high latitudes.

Chapter 6

P1: Thermodynamic phase of clouds in the SEVIRI disc

CLOUD TOP THERMODYNAMIC PHASE FROM SYNERGISTIC
LIDAR-RADAR CLOUD PRODUCTS FROM POLAR ORBITING
SATELLITES: IMPLICATIONS FOR OBSERVATIONS FROM
GEOSTATIONARY SATELLITES

Johanna Mayer, Florian Ewald, Luca Bugliaro, Christiane Voigt
Remote Sensing, 2023

Overview   The distribution of CTP from the perspective of the geostationary imager SEVIRI is not well known, especially whether SEVIRI can observe SC and MP clouds. In this study, we use 5 years of the cloud mask and cloud phase from the synergistic lidar-radar DARDAR product as ground truth to model a CTP from the perspective of SEVIRI. This modeled SEVIRI-like CTP allows to investigate the influence of spatial resolution on the occurrence of CTP and to analyze the geographic and seasonal CTP distribution on the SEVIRI disc. We find that all phases are found in significant amounts at the cloud top in the SEVIRI disc - notably also MP and SC clouds, which highlights the need for dedicated retrieval algorithms for these cloud phases from geostationary imagers. Finally, we use the SEVIRI-like CTP to evaluate an existing ice cloud detection algorithm for SEVIRI called CiPS.

Author contribution   I collected the DARDAR data for the collocated data set. I conceptualised and wrote the code for the collocation with SEVIRI with some help from LB. I performed the analysis of the data set and the comparison with CiPS. I prepared the figures and wrote the original draft of the manuscript, except for Section 2.1 on the DARDAR data set, which FE wrote. LB and CV revised the manuscript. All authors contributed to the research through discussion. LB and CV supervised the research and were responsible for the funding.

Article

Cloud Top Thermodynamic Phase from Synergistic Lidar-Radar Cloud Products from Polar Orbiting Satellites: Implications for Observations from Geostationary Satellites

Johanna Mayer [1,*] , Florian Ewald [1] , Luca Bugliaro [1] and Christiane Voigt [1,2]

1   Deutsches Zentrum für Luft- und Raumfahrt, Institut für Physik der Atmosphäre, 82234 Weßling, Germany
2   Institut für Physik der Atmosphäre, Johannes Gutenberg-Universität Mainz, 55099 Mainz, Germany
*   Correspondence: johanna.mayer@dlr.de

Abstract: The cloud thermodynamic phase is a crucial parameter to understand the Earth's radiation budget, the hydrological cycle, and atmospheric thermodynamic processes. Spaceborne active remote sensing such as the synergistic radar-lidar DARDAR product is considered the most reliable method to determine cloud phase; however, it lacks large-scale observations and high repetition rates. These can be provided by passive instruments such as SEVIRI aboard the geostationary Meteosat Second Generation (MSG) satellite, but passive remote sensing of the thermodynamic phase is challenging and confined to cloud top. Thus, it is necessary to understand to what extent passive sensors with the characteristics of SEVIRI are expected to provide a relevant contribution to cloud phase investigation. To reach this goal, we collect five years of DARDAR data to model the cloud top phase (CTP) for MSG/SEVIRI and create a SEVIRI-like CTP through an elaborate aggregation procedure. Thereby, we distinguish between ice (IC), mixed-phase (MP), supercooled (SC), and warm liquid (LQ). Overall, 65% of the resulting SEVIRI pixels are cloudy, consisting of 49% IC, 14% MP, 13% SC, and 24% LQ cloud tops. The spatial resolution has a significant effect on the occurrence of CTP, especially for MP cloud tops, which occur significantly more often at the lower SEVIRI resolution than at the higher DARDAR resolution (9%). We find that SC occurs most frequently at high southern latitudes, while MP is found mainly in both high southern and high northern latitudes. LQ dominates in the subsidence zones over the ocean, while IC occurrence dominates everywhere else. MP and SC show little seasonal variability apart from high latitudes, especially in the south. IC and LQ are affected by the shift of the Intertropical Convergence Zone. The peak of occurrence of SC is at $-3\,^{\circ}$C, followed by that for MP at $-13\,^{\circ}$C. Between 0 and $-27\,^{\circ}$C, the occurrence of SC and MP dominates IC, while below $-27\,^{\circ}$C, IC is the most frequent CTP. Finally, the occurrence of cloud top height (CTH) peaks lower over the ocean than over land, with MP, SC, and IC being undistinguishable in the tropics but with separated CTH peaks in the rest of the MSG disk. Finally, we test the ability of a state-of-the-art AI-based ice cloud detection algorithm for SEVIRI named CiPS (Cirrus Properties for SEVIRI) to detect cloud ice. We confirm previous evaluations with an ice detection probability of 77.1% and find a false alarm rate of 11.6%, of which 68% are due to misclassified cloud phases. CiPS is not sensitive to ice crystals in MP clouds and therefore not suitable for the detection of MP clouds but only for fully glaciated (i.e., IC) clouds. Our study demonstrates the need for the development of dedicated cloud phase distinction algorithms for all cloud phases (IC, LQ, MP, SC) from geostationary satellites.

Keywords: cloud phase; active remote sensing; passive remote sensing; DARDAR; Meteosat Second Generation; SEVIRI

1. Introduction

1.1. Background

Water in clouds in the Earth's atmosphere is present as both liquid droplets and ice crystals. While the liquid phase exists at temperatures above 0 °C and the ice phase at

temperatures below the homogeneous nucleation threshold of about $-40\ ^\circ$C, both ice crystals and supercooled droplets can exist in the range between these two temperature thresholds as well as mixtures of them—known as mixed-phase. Knowledge about the occurrence of cloud phases—liquid (warm or supercooled), mixed-phase, or ice—is crucial for several reasons: Liquid clouds are made up of many small droplets, while ice clouds have significantly fewer, larger crystals. This results in liquid clouds being optically thicker and tending to have a stronger cooling effect on the atmosphere [1,2]. Furthermore, the phase of clouds impacts the absorption and scattering of incoming solar and emitted infrared radiation, particle evolution, and lifetime [3–6], and hence the cloud's radiative effect [7–11]. Changes in cloud phase can lead to feedback impacting cloud fraction, humidity, and temperature profiles [9,12] as well as the formation of precipitation [13]. Moreover, aerosols impact thermodynamic phase change [14,15]. In order to better understand aerosol–cloud interactions a robust knowledge of the occurrence of different cloud phases is needed.

The thermodynamic phase transition of clouds is still not well understood, often leading to inaccurate representations of the distribution of ice and liquid in numerical models [10,13,16,17]. Mixed-phase clouds in particular are often poorly represented in global models as they tend to oversimplify the intricate microphysical processes that govern the transition between liquid and ice phases [4,10,18]. Constraining the phase transition mechanisms is particularly challenging since the physics and dynamics of mixed-phase clouds are nonlinear [10,19]. Numerous studies have also demonstrated the influence of cloud phase in climate sensitivity in general circulation models [16,20–22]. The phase partitioning of clouds and their parameterization are therefore of particular interest.

Satellite remote sensing is an important method to determine global cloud properties [23–26]. In recent years, spaceborne active remote sensing has been widely used to retrieve vertical profiles of thermodynamic cloud phases [10,27–32]. In particular, combinations of lidar and radar measurements provide a reliable way to determine the cloud phase, as both instruments complement each other due to their different penetration depths and different sensitivities to particle sizes [33–36]. For instance, the combined state-of-the-art CloudSat/CPR (Cloud Profiling Radar) and CALIPSO/CALIOP (Cloud-Aerosol Lidar and Infrared Pathfinder Satellite Observation/Cloud-Aerosol Lidar with Orthogonal Polarization) products have been used for statistical characterization of phase partitioning as well as statistics of the geographic and temporal occurrence of cloud phases [9,10,34,37,38].

Besides active instruments, passive sensors aboard geostationary satellites play an important role in observing the evolution and phase of clouds. Their main advantages are that, first, they provide information over a wide field of regard, which allows the retrieval of macrophysical quantities such as the sizes of clouds. Second, they allow measurements at any time of day, so that the temporal evolution of clouds can be studied with high temporal resolution. However, in contrast to active instruments, a passive sensor can only observe the upper layer of a cloud according to the penetration depth of its channels. For the evaluation of the radiative effect of a cloud, this cloud top layer is very important since it is where most solar radiation is reflected, and most infrared radiation is radiated to space [39]. Furthermore, since supercooled liquid and mixed-phase layers are usually located near the top of the cloud [40,41], they are expected to be observable with a passive instrument. In the past, phase retrievals of passive sensors often only distinguished between ice and liquid clouds (or ice/liquid/unknown) [42–46], but in recent years, retrieval algorithms for the imagers aboard the geostationary satellites GOES-R and Himawari have been developed to further distinguish between mixed-phase, liquid, and, for GOES-R, supercooled liquid cloud tops [25,47,48]. However, this distinction remains difficult, especially for mixed-phase and supercooled cloud tops [33]. For instance, the CiPS algorithm (Cirrus Properties from SEVIRI [49])—a neural network retrieval for the detection of ice clouds from SEVIRI aboard Meteosat Second Generation (MSG)—has been shown to (mis)classify supercooled clouds as ice clouds, especially when the temperature is close to the homogeneous nucleation threshold [50].

One of the difficulties in distinguishing between thermodynamic phases is that it cannot be performed on the basis of the cloud temperature alone, since ice, mixed-phase, and supercooled liquid clouds can all exist in the temperature range between 0 °C and −40 °C, as mentioned above. Distinguishing the cloud phase with passive sensors, therefore, requires additional consideration of radiative properties due to differences in absorption and scattering between liquid droplets and ice crystals [33,51]. However, cloud particles show large variations in habit and size and atmospheric conditions such as humidity or aerosol concentration and type can vary considerably in time and space. Moreover, the observed brightness temperatures and reflectivities are affected by other cloud and atmospheric properties as well as viewing geometry and, for reflectivities, by solar zenith angle. All these aspects make retrieval of the cloud thermodynamic phase a complex task. A further difficulty for passive instruments is that vertically thick clouds often consist of different thermodynamic phases in different layers. A passive sensor might receive signals from several of these layers, making classification difficult.

There are several studies on the geographic and temporal distribution of cloud phase from active spaceborne instruments [9,10,37,52]. However, results from these studies cannot be adopted one-to-one for passive geostationary satellites. Typically, studies using active remote sensing consider the total vertical profile of a cloud at a given time and location to define a phase for the cloud, while for passive, geostationary instruments, only the top layers of a cloud are relevant. Furthermore, passive, geostationary instruments usually have coarser resolutions, which has an influence on the cloud phases that fill the single pixels.

1.2. Scope of Present Work

Since, as outlined above, active spaceborne measurements constitute the most reliable way to determine the cloud phase from satellite observations, we use these measurements to determine a "ground truth" for cloud phase distributions from the perspective of a passive geostationary instrument. To this end, we use vertical profiles of the cloud phase from active remote sensing to model observations of the cloud top phase of a geostationary sensor. In particular, we use the spaceborne CALIPSO-CloudSat product DARDAR (liDAR/raDAR [53]) obtained with an along-track resolution of 1.1 km to deduce a cloud phase at cloud top as a ground truth for the MSG/SEVIRI geostationary passive instrument. Thereby we (1) restrict our analysis to the field of regard of SEVIRI (i.e., the Meteosat disk); (2) use the spatial resolution of SEVIRI (3×3 km^2 at nadir, degrading towards the edge of the disk); (3) consider only the part of the cloud relevant for a passive sensor (mainly the upper layer); (4) aggregate DARDAR cloud phase results in every SEVIRI pixel to obtain a meaningful phase representation at SEVIRI resolution. This procedure results in an aggregated cloud top phase (CTP) in SEVIRI resolution—called "SEVIRI-like" CTP in the following. We test the influence of the resolution of SEVIRI on measurements of CTP by comparing the aggregated CTP in SEVIRI resolution with the corresponding CTP in DARDAR resolution, assessing how representative geostationary measurements of CTP are compared to measurements of polar-orbiting satellites. We confirm that the aggregation of the DARDAR cloud phase to the lower SEVIRI resolution preserves the relevant physical relationship between the SEVIRI-like CTP and temperature. To the best of our knowledge, the distribution of CTP derived from lidar/radar measurements as a "ground truth" has never been studied from the SEVIRI perspective—that is, at SEVIRI resolution and restricted to the top of the cloud. We fill this gap and study the geographic and seasonal distribution of the SEVIRI-like CTP. We also examine the differences between the various CTPs in terms of cloud top height (CTH), or more specifically, in which CTH regimes the CTPs occur. The results of these analyses can be used as a basis for testing and improving CTP determination algorithms for SEVIRI. Our approach allows us to assess the relative importance of liquid, ice, supercooled liquid, and mixed-phase cloud tops in SEVIRI observations at the spatial scale of the native SEVIRI grid. We focus in particular on the occurrence of mixed-phase and supercooled clouds. Since existing phase retrievals of

passive sensors often are not able to detect these two cloud types as mentioned above, it is not a priori clear how many mixed-phase and supercooled clouds can be observed from a geostationary satellite. Furthermore, the SEVIRI-like CTP on the SEVIRI grid with variable pixel sizes can be interpreted in view of polar-orbiting active observations with constant along-track resolution. As a first application of the SEVIRI-like CTP data set, we evaluate the existing ice cloud retrieval algorithm for SEVIRI, CiPS (Cirrus Properties from SEVIRI).

Section 2 starts with an overview of the lidar-radar product DARDAR, the SEVIRI instrument, and CiPS. This is followed by the collocation and aggregation procedure of DARDAR and SEVIRI, yielding a data set containing CTP information in SEVIRI resolution. In Section 3, we study the influence of resolution on CTP observations and assess whether aggregating the DARDAR cloud phase to the lower SEVIRI resolution preserves physical relationships. We study the SEVIRI-like CTP as a function of different parameters such as geographical distribution, season, or land-ocean distribution. Finally, in Section 4, we compare the SEVIRI-like CTP with the ice cloud retrieval algorithm CiPS. We compute and assess the detection and false alarm rates of CiPS in order to better understand its strengths and weaknesses with respect to the detection of ice in the atmosphere as a preparation for a novel cloud retrieval development in the future.

2. Materials and Methods

2.1. DARDAR Data Set

As a ground truth for the occurrence of cloud phases, this study uses the DARDAR-MASK product which is part of the active remote sensing product DARDAR (liDAR/raDAR [53]). The DARDAR-MASK product is part of the Varcloud algorithm which was introduced by Delanoë and Hogan [35] and its cloud phase classification was further improved by Ceccaldi et al. [54]. It is based on the combination of active radar and lidar measurements from the A-Train satellites CloudSat and CALIPSO and provides a consolidated classification of the measured cloud scenes. DARDAR-MASK combines the sensitivity of lidar to optically thin cirrus with the capability of radar to penetrate optically thicker clouds. Due to this unique approach, these products have been widely used for cloud studies [9,37,55–57].

The DARDAR-MASK data set provides vertical profiles of cloud thermodynamic phase collocated with CloudSat footprints with a spatial resolution of 1.1 km along and 1.7 km across the satellite track and a 60 m vertical resolution. Single measurements of 1.1 km × 60 m boxes are called gates in the following to avoid confusion with SEVIRI pixels. The product consolidates the CALIPSO Level 1B profiles of attenuated backscatter coefficient, β, at 532 nm and the CloudSat 2B-GEOPROF radar reflectivity at 94 GHz, Z, with the CALIPSO Lidar L2 Vertical Feature Mask (VFM) using a decision tree to obtain phase discrimination for optically thin and thick clouds. In the improved DARDAR-MASK version (v2.23), histogram-adapted thresholding is directly applied to the original lidar data of β at 60 m vertical resolution to identify atmospheric targets such as clouds or aerosols. After the feature detection, the VFM mask is used to filter out aerosols. Subsequently, remaining atmospheric targets are labeled as warm liquid clouds where the wet bulb temperature is >0 °C which is calculated from temperature, pressure, and humidity from the ECMWF-AUX data set [58]. In addition, cloud layers containing supercooled water are singled out using their strong lidar backscatter and subsequent attenuation in temperature regions between 0 °C and −40 °C. A further distinction into pure supercooled water without ice crystals is made using the absence of a radar return since the diameter of cloud droplets is mostly below the CloudSat sensitivity [59]. Below −40 °C, these layers with strong backscatter are attributed to highly concentrated ice. If the layer is thicker than 300 m in the 0 °C to −40 °C temperature range, it is assumed to be fully glaciated which is in line with observations [30] and modeling studies [60]. The same applies to atmospheric targets which are not labeled as aerosols in temperature regions below −40 °C. Further sub-divisions are made for spherical ice or 2D plates using their low depolarization and for regions above convective cores. Details regarding this phase discrimination technique can be found in [54]. The DARDAR product also contains temperature profiles taken from the

ECMWF-AUX data set, which are interpolated to DARDAR resolution [53]. We use these temperature profiles to determine a cloud top temperature (CTT) for each cloudy DARDAR profile. For this, we select the temperature in the top cloudy gate as CTT. Similarly, we define a cloud top height (CTH) as the height of every topmost cloudy gate in each cloudy DARDAR profile.

In the following, we use the *DARMASK_Simplified_Categorization* data set contained in the DARDAR-MASK (v2.23) product which comprises: four ice categories (ice, spherical or 2D ice, highly concentrated ice, top of convective towers) that we consider as "ice"; one category for mixtures of supercooled liquid and ice (supercooled+ice) that we consider as "mixed-phase"; two "pure" supercooled categories (supercooled, multiple scattering due to supercooled water) that we consider as "supercooled"; four liquid categories (liquid, warm rain + liquid clouds, cold rain + liquid clouds, rain maybe mixed with liquid) that we consider as "liquid" in the following. Thus, we distinguish between ice (IC), mixed-phase (MP), supercooled (SC), and warm liquid (LQ) cloud classes. We refer to these four classes in the following as *phases* for simplicity, although SC and LQ have the same thermodynamic phase (liquid) and MP contains water in two thermodynamic phases (solid and liquid). Note that we ignore other classifications included in DARDAR-MASK such as aerosols or stratospheric features for the cloud phase classification and treat them as clear sky.

Figure 1a gives an example of the Simplified Categorization variable of the DARDAR-MASK product for an A-Train curtain on 10 June 2015 at 12:15 UTC. The scene shows a cross-section through a stationary occlusion front located just west of Norway. With an overcast ice cloud layer in the lifted warm sector, mixed-phase clouds with embedded supercooled layers run ahead of the front, while a low and supercooled layer is trailing the front in the cold sector.
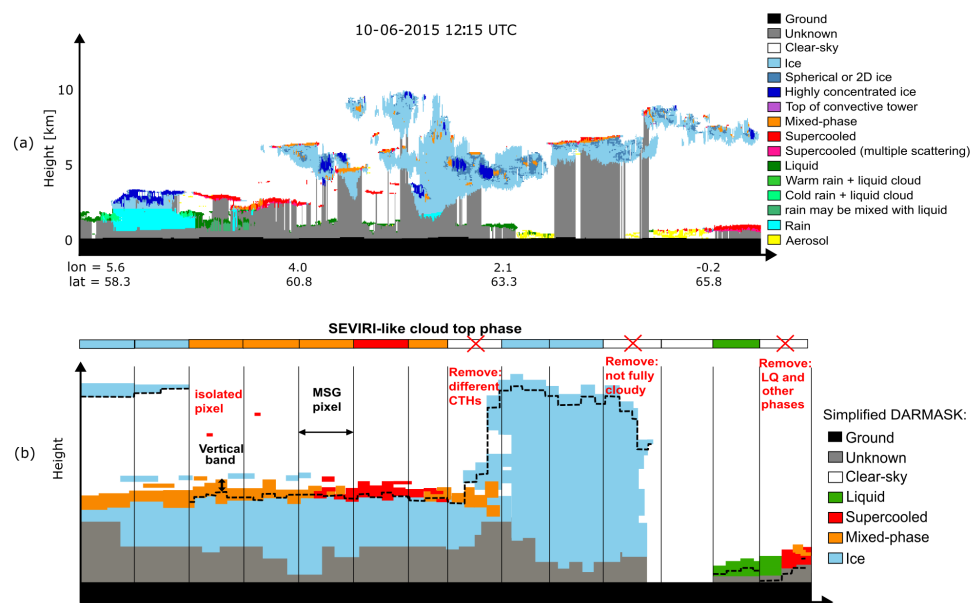
Figure 1. (**a**) Example of the DARDAR-MASK Simplified Categorization variable of the DARDAR-MASK product for an A-Train curtain on 10 June 2015 at 12:15 UTC. The scene shows a cross-section through a stationary occlusion front located just west of Norway. (**b**) Scheme of the SEVIRI-like cloud top phase (CTP) definition. Background: Synthetic two-dimensional DARDAR-MASK scene with phase categories simplified to ice, mixed-phase, supercooled, and liquid. Black vertical lines indicate collocated SEVIRI pixels. All DARDAR values in the vertical band (black dashed line) are considered for the averaging step in coarsening to a CTP in SEVIRI resolution. Isolated cloud gates in DARDAR-MASK are removed before the coarsening. SEVIRI pixels that do not have similar cloud top heights (CTHs) in all DARDAR gates are removed. The resulting SEVIRI-like CTP is shown in color code in the top bar of the figure.

2.2. MSG and CiPS

The MSG satellites have been operational since 2004 and are positioned at 0°E above the equator. SEVIRI has a spatial coverage from approximately 80°W to 80°E and 80°S to 80°N, covering the African and European continent as well as large parts of the Atlantic ocean. Apart from one high spatial resolution visible (HRV) channel, the imager has 11 channels between 0.6 and 14 μm with a spatial resolution of 3×3 km^2 at nadir and a temporal resolution of 15 min.

In Section 4, we use the aggregated SEVIRI-like CTP data set to evaluate the CiPS (Cirrus Properties from SEVIRI) algorithm. CiPS detects ice clouds, even in multilayered situations with lower "warm" clouds, and retrieves the corresponding CTH, ice optical thickness, and ice water path using the SEVIRI imager. The algorithm utilizes a set of artificial neural networks trained with MSG2/SEVIRI thermal observations, CALIOP L2 cloud and aerosol layer data version 3 (V3) with a spatial resolution of 5 km (CAL_LID_L2_05kmC | ALay-Prov-V3-0X [61]; abbreviated with CAL_LID_L2 in the following), surface temperature from ECMWF (ERA-Interim reanalysis) and auxiliary data over a time period of almost six years from April 2007 to January 2013 [49]. CiPS has been extensively validated [50]: it detects approx. 70% of the ice clouds with an optical thickness of 0.1, and this value increases rapidly with increasing optical thickness. According to [50], CiPS shows an overall probability of detection (POD) of 70% over the entire disk and a false alarm rate (FAR) of 4%, with the highest values of the FAR in the tropics and smallest values in mid-latitudes. Furthermore, CiPS has been shown to partly identify supercooled tops wrongly as ice, with FAR increasing with decreasing temperature: while only 6% of liquid tops are classified by CiPS as ice between −10 and −15 °C, this fraction increases to 35% for temperatures between −30 and −35 °C. Like the training of CiPS, the evaluation has been performed against CAL_LID_L2, which distinguishes "only" between the phases ice, liquid water, and undetermined.

2.3. Definition of the Cloud Top Phase

In the following sections, we explain the procedure to derive the SEVIRI-like CTP from the DARDAR-MASK product. Roughly summarized, the vertical profiles of the DARDAR product—which have a higher resolution along the track than the size of one SEVIRI pixel—are mapped to a one-dimensional CTP variable in the spatial resolution of SEVIRI (from now on called SEVIRI resolution). Note that the DARDAR data are always collected at the time of the overpass of the satellites CALIPSO and CloudSat. The frequency of occurrence of the deduced CTP can therefore only be representative of the respective overflight times for each location.

Figure 1b shows a (fictitious) DARDAR-MASK scene with clouds with different thermodynamic phases. The vertical black lines indicate the geostationary grid of SEVIRI. The horizontal bar above the DARDAR-MASK scene shows the resulting CTP in SEVIRI resolution after the vertical and horizontal averaging steps. These steps are explained in detail below.

2.3.1. Removal of Isolated Gates

The DARDAR algorithm sometimes identifies isolated gates as cloudy, typically classified as supercooled. It can be assumed that these isolated cloud gates are in most cases not physically meaningful but noisy artifacts of the lidar cloud mask algorithm and, due to their size, can never fill a SEVIRI pixel. Before regridding the DARDAR data to the coarser MSG resolution, these isolated cloud gates are filtered out from the two-dimensional DARDAR-MASK. Isolated cloud gates here refer to cloudy gates that have only non-cloudy gates as direct neighbors in a square of 3×3 gates (see Figure 1b).

2.3.2. Identification of the Cloud Top Layer

Radiation measured by passive instruments does not only stem from the very top of a cloud but some vertical extent of the cloud top layer (e.g., [62]). To account for this fact,

we do not consider only the topmost cloudy gate in the DARDAR product but a vertical band of four cloudy DARDAR gates (i.e., 240 m) starting from cloud top is used in the CTP definition (black dashed line in Figure 1b). Taking several vertical layers into account better represents clouds that have a mix of very thin layers (1–3 gates) of different phases at the cloud top from the point of view of passive imagers: A typical case is clouds with an MP or SC very thin vertical layer at the cloud top with IC underneath. Examples can be seen in Figure 1a at longitudes between about 0.5 and 1.0°E, where very thin SC layers are at cloud top with MP and IC layers underneath. For LQ and IC clouds (thin/thick cirrus, but not convective), that have the same phase over a large vertical extent, the consideration of these four gates below the cloud top has the same effect as considering the topmost gate alone. Finally, we consider cloudy gates to belong to different cloud layers when there is a vertical cloud gap of at least 2 km between them. For these multilayered clouds, e.g., a high IC cloud layer on top of lower clouds, we only consider the gates within the uppermost cloud layer (even if its geometrical thickness is thinner than 240 m). Although radiation from the lower cloud layer can be transmitted through the higher cloud and affect the satellite observation, this procedure ensures that we focus on the cloud that is closest to the satellite. Furthermore, this is consistent with the conventions of the CiPS algorithm [49] which will be evaluated in Section 4.

A more physical approach to identify the vertical layer that is most relevant to the passive spaceborne observations would be to calculate a vertical penetration depth as a function of the extinction coefficient of the clouds. However, in the absence of information about the extinction coefficient—which, by the way, is also wavelength dependent—for all cloud phases, a reasonable solution is to use a fixed vertical band. The value of 240 m for the vertical extension of the cloud top layer is a compromise to choose the vertical band thick enough to consider the presence of several thin vertical layers of different phases at the cloud top, which should be counted as MP, and thin enough to not give too much weight to lower layers that are too far away from cloud top. This is most important for clouds with SC layers at the top that are usually smaller than 300 m (see Section 2.1). This is shown schematically in Figure 1b, where the vertical band indicated by the black dashed line is thinner than the typical thickness of MP and SC layers at the cloud top, but includes most of the gates associated with these phases. Note that the scope of the work is not to study the effective phase for SEVIRI from which the radiation in the cloud originates, but to perform statistical studies for the dominant phase at the geometrical cloud top. We further discuss the influence of the choice of 240 m as the thickness of the vertical band in Appendix A.

2.3.3. Collocation and Aggregation

The SEVIRI-like CTP is defined as the aggregation of all DARDAR values mapped to a SEVIRI pixel which are included in the vertical band defined in the previous section, i.e., all DARDAR values contained in the two-dimensional stripe below the cloud top. The procedure works in the following manner.

1. The DARDAR profiles are collocated with SEVIRI pixels based on latitude, longitude, acquisition time, and CTH information of the topmost gate (see Figure 1b). Consideration of the CTH is needed since a DARDAR gate containing a high cloud can be assigned to a different SEVIRI pixel than suggested by the longitude and latitude due to the viewing angle of the geostationary satellite (parallax effect).
2. If no cloudy gates are present, the SEVIRI pixel is classified as clear-sky.
3. A cloudy pixel in SEVIRI resolution is required to contain only DARDAR gates that have a similar CTH. Otherwise the averaging might take place over two different clouds. Therefore, all SEVIRI pixels for which the CTHs of any of the contained DARDAR gates vary by more than 1 km are not considered further.
4. If a SEVIRI pixel is not fully covered by cloudy DARDAR gates, it is not considered further in order to avoid cloud edges.

5.   If a SEVIRI pixel is fully covered by cloudy DARDAR layers, the CTP is assigned by considering all DARDAR gates included in the vertical band mentioned above:

- If all DARDAR gates are of the same phase, the SEVIRI-like CTP adopts this phase classification.
- SEVIRI pixels which contain different DARDAR cloud phases, but only the phases IC, MP, or SC are classified as MP cloud tops.
- SEVIRI pixels that contain LQ and at least one more phase (IC, MP, or SC) are not considered further; this applies to edges between LQ clouds and clouds with other phases.

This way, a data set of SEVIRI-like CTP can be created with homogeneous pixel properties that give information about the presence of ice alone, warm liquid droplets, or supercooled liquid particles alone or mixed with ice crystals. Notice that the last case encompasses the mixed-phase cloud situation where ice and liquid are mixed at the microphysical level [63], but also the case where ice (or MP) and liquid are next to each other inside one MSG pixel.

For the analysis of the influence of the resolution on CTP (see Section 3.1), we also define a CTP in DARDAR resolution (DARDAR-CTP). The DARDAR-CTP is obtained by the same steps as described above (i.e., defining a vertical band at the cloud top and aggregating the phase values of this band to a CTP value), except for the horizontal aggregation to SEVIRI resolution. Hence, the only difference between the SEVIRI-like CTP and DARDAR-CTP is their different horizontal resolutions.

2.4. Data Set of Collocated DARDAR and MSG Cloud Top Phase

Following the steps defined above, the SEVIRI-like CTP and DARDAR-CTP are computed for the five years 2013–2017. We selected this time period because it has the longest overlap with a consistent operational MSG satellite (MSG3) and DARDAR data that was available to us at the time we conducted this study. Furthermore, concentrating on MSG3 prevents us from using observations with high aerosol load due to the volcanic eruptions in 2010 and 2011 (Eyjafjallajökull, Grimsvötn, Puyehue) that affect passive observations.

The SEVIRI-like data set is complemented with two other variables from the DARDAR data set: CTT and CTH. CTT at SEVIRI resolution is determined as an average over all CTTs at DARDAR resolution (Section 2.1) inside a given SEVIRI pixel. Similarly, CTH, which is computed for every topmost cloudy gate in DARDAR (see Section 2.1), is averaged over all cloud tops inside a SEVIRI pixel. Overall, the five years of data in SEVIRI resolution amount to roughly 77×10^6 data points. Since CloudSat was working in daylight-only mode, no data is collected during overflights of the Antarctic in southern winter, which results in fewer data points over the Antarctic compared to other regions.

As an additional parameter, the land-sea-mask from ERA5 [64] is used. The ERA5 land-sea-mask has an original resolution of $0.25° \times 0.25°$ in longitude and latitude which is coarser than the SEVIRI resolution. Regridding to the SEVIRI resolution is performed using the nearest neighbor algorithm.

3. Occurrence of Cloud Top Phase

In this section, we analyze the statistics of the five years of CTP (Section 2.3). First, we analyze the influence of the resolution of the instruments by comparing the CTP in DARDAR resolution with the lower resolution SEVIRI-like CTP (Section 3.1). Next, we assess whether aggregating the DARDAR CTP to the lower SEVIRI resolution preserves relevant physical relationships by studying the distribution of SEVIRI-like CTP as a function of CTT (Section 3.2). Finally, we study the geographic distribution, seasonal variability, and altitude of the SEVIRI-like CTP (Sections 3.3 and 3.4).

3.1. Resolution Effects and Geographic Distribution

We analyze the influence of the resolution on CTP by comparing the SEVIRI-like CTP to the DARDAR-CTP. In order to study the differences between the CTPs in different resolutions, $R \in$ {SEVIRI, DARDAR}, and their geographical distribution, we define a set of variables on a common grid. As in other publications dealing with the sparse active observations by CALIPSO-CloudSat (e.g., [10]), we select boxes of 2.5° latitude by 2.5° longitude over the MSG disk. The size of the latitude-longitude boxes is chosen to obtain good statistics and still show all the important features of the cloud phases on the Meteosat field of regard. Notice that differences are given in this investigation only by the filtering-averaging-aggregation procedure implemented in Section 2.3 and not to orbital parameters since all values are determined along the satellite track of CALIPSO-CloudSat. Notice that the procedure applied in Section 2.3 both modifies the occurrence of the single phases as well as the number of cloudy "observations" because of downscaling (averaging) but also because of the removal of inhomogeneous pixels. This removal of inhomogeneous pixels, i.e., pixels that are either not fully covered with cloudy gates or that contain clouds with large CTH differences (see Section 2.3), is depicted in Figure 2a. It shows the percentage of SEVIRI pixels per latitude-longitude grid box which are omitted. This percentage of omitted pixels is small in general ($\lesssim$20%), but it is higher on the one hand in regions where many small clouds (with a spatial extent smaller than a SEVIRI pixel) are present, such as cumulus clouds over subtropical oceanic regions, leading to partly covered pixels. On the other hand, the percentage is higher where many multi-layered clouds with large CTH differences are present, such as at the borders of the Intertropical Convergence Zone (ITCZ) with high anvil cirrus clouds over low clouds. Figure 2b shows the number of data points of the SEVIRI-like CTP data set per latitude-longitude grid box. The derived data set contains on average about 10^4 SEVIRI-like pixels per grid box and thus enough data for robust statistics. The inhomogeneous spatial distribution of the number of data points on the Meteosat disk is the result of several factors, such as the increasing size of SEVIRI pixels with distance from nadir, the fact that the flight path of CALIPSO/CloudSat passes over some SEVIRI pixels more frequently than others, and the seasonally changing coverage of CALIPSO/CloudSat in daytime mode.
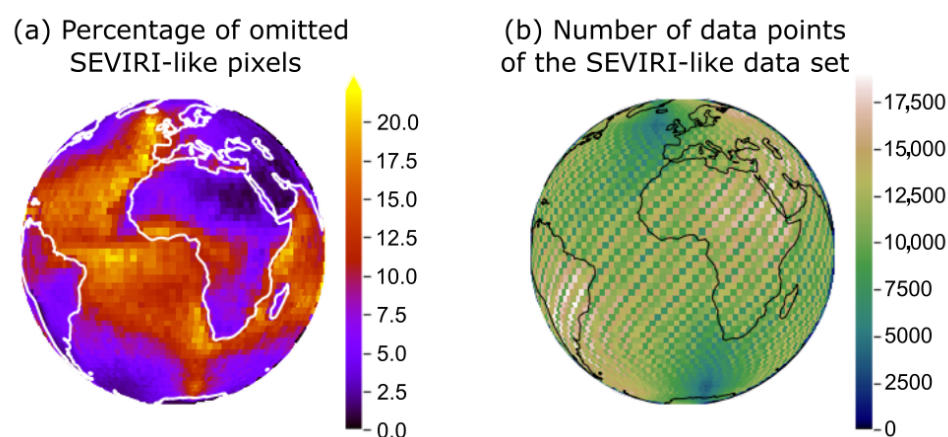
Figure 2. (**a**) Percentage of SEVIRI-like pixels that are omitted due to non-fully covered pixels in SEVIRI resolution or large CTH differences in a SEVIRI pixel; (**b**) Number of data points of the SEVIRI-like CTP data set. Boxes of 2.5° latitude by 2.5° longitude are used.

To study the differences between CTPs at different resolutions and their geographic distribution, we define the *cloudiness*—i.e., the probability that a geographic box is cloudy—$P_R(\text{cloud} \mid \text{lat}, \text{lon})$, and the *phase occurrence*—i.e., the probability that a given phase occurs

in a geographic box—$P_R(q \,|\, \text{lat, lon})$ with $q \,\epsilon\, \{\text{IC, MP, SC, LQ}\}$ in each latitude-longitude grid box according to

$$P_R(q \,|\, \text{lat, lon}) = \frac{N_R(q, \text{lat, lon})}{N_R(\text{cloud, lat, lon})}, \qquad (1)$$

$$P_R(\text{cloud} \,|\, \text{lat, lon}) = \frac{N_R(\text{cloud, lat, lon})}{N_R(\text{lat, lon})},$$

where (lat, lon) label the latitude-longitude box, $N_R(q, \text{lat, lon})$ is the number of data points in the box with CTP q, $N_R(\text{cloud, lat, lon})$ is the number of cloudy data points in the box, i.e., $N_R(\text{cloud, lat, lon}) = \sum_q N_R(q, \text{lat, lon})$ and $N_R(\text{lat, lon})$ is the total number of data points in the box. From the definition of $P_R(q \,|\, \text{lat, lon})$, it follows that the sum over all CTPs q gives 1.0 at every latitude and longitude grid box.

Figure 3 shows the cloudiness and phase occurrence for SEVIRI and DARDAR resolution, respectively, in the left and middle columns. The right column shows the difference between SEVIRI and DARDAR resolution for cloudiness and phase occurrence. The number at the top right corner of each plot is the respective mean value over all latitude-longitude boxes. Comparing the plots at SEVIRI and DARDAR resolution, one first sees that the main characteristics of the geographic distribution of cloudiness and phase occurrence of each CTP are preserved in the aggregation procedure from DARDAR to the coarser resolution of SEVIRI.

The highest cloudiness values are found over the Southern Ocean and high northern latitudes over the ocean in both resolutions with cloudiness values up to 97%. In fact, the Southern Ocean and the Antarctic seas have the largest cloud fractions as already demonstrated in previous studies using other synergistic A-Train products [37,65–70]. In the tropics near the equator, cloudiness values are also enhanced compared to the average value on the Meteosat disk because of frequent convection. The lowest cloud probabilities occur close to the Tropic of Cancer and Tropic of Capricorn over land, in the subsidence regions.

All CTPs shown in Figure 3b–e have a strong geographic dependence. IC cloud tops are the most common cloud phase with a mean phase occurrence of 49% (50%) in SEVIRI (DARDAR) resolution. They occur over the whole Meteosat disk, but are most probable at high latitudes in the temperate zones as well as in the ITCZ and the African continent. LQ cloud tops are mainly found in the subtropics and over the ocean rather than on land. The process leading to the high occurrence of LQ cloud tops in these regions is shallow convection, which is typical for regions with high solar irradiation and abundant moisture from the ocean. The highest probabilities for LQ cloud tops (over 90% in both resolutions) are found over the ocean west of the African continent related to low stratocumulus clouds, which are very common in this region. Their probability of occurrence becomes smaller towards high latitudes N or S. In particular, LQ cloud tops are almost never observed at latitudes south of 60°S. MP and SC cloud tops on the other hand are most frequently observed at high latitudes north of 60°N or south of 60°S. SC cloud tops are especially prevalent over the Southern Ocean with mean values of about 30% in SEVIRI resolution and 35% in DARDAR resolution for latitudes south of 60°S.

Even if the general patterns of CTP are similar in both resolutions, significant differences in phase occurrence between SEVIRI and DARDAR resolutions are also found. For MP cloud tops in SEVIRI resolution, relatively high values of over 10% extend into the temperate zones, the Southern Ocean, Europe, and the northern Atlantic and are therefore well visible within the Meteosat disk. In contrast, MP cloud tops in DARDAR resolution are less common. As can be seen from the difference between SEVIRI and DARDAR resolution results for MP cloud tops in Figure 3c, MP phase occurrence is higher in SEVIRI resolution everywhere on the Meteosat disk. While in SEVIRI resolution the mean value of MP phase occurrence is 14%, only 9% of clouds are MP in DARDAR resolution. The MP values in SEVIRI resolution are, in some regions (e.g., over Scandinavia, South Africa, or the

central parts of the Southern Ocean), almost twice as high as in DARDAR resolution. These differences in the two resolutions are explained by the aggregation of different cloud phases in DARDAR resolution within a SEVIRI pixel: when DARDAR gates of more than one "cold" phase (IC/MP/SC) are present in a SEVIRI pixel, they are aggregated and contribute to the MP CTP in SEVIRI resolution (see Section 2.3). Physically, this corresponds to the mixing of clouds of different phases within a SEVIRI pixel such that, e.g., an SC cloud top contiguous to an IC cloud top in one SEVIRI pixel cannot be distinguished from an MP cloud top that extends over the whole SEVIRI pixel. Accordingly, IC and SC phase occurrences are lower in SEVIRI resolution compared to DARDAR resolution, in the same regions where MP phase occurrence is higher in SEVIRI resolution (see Figure 3b,e).
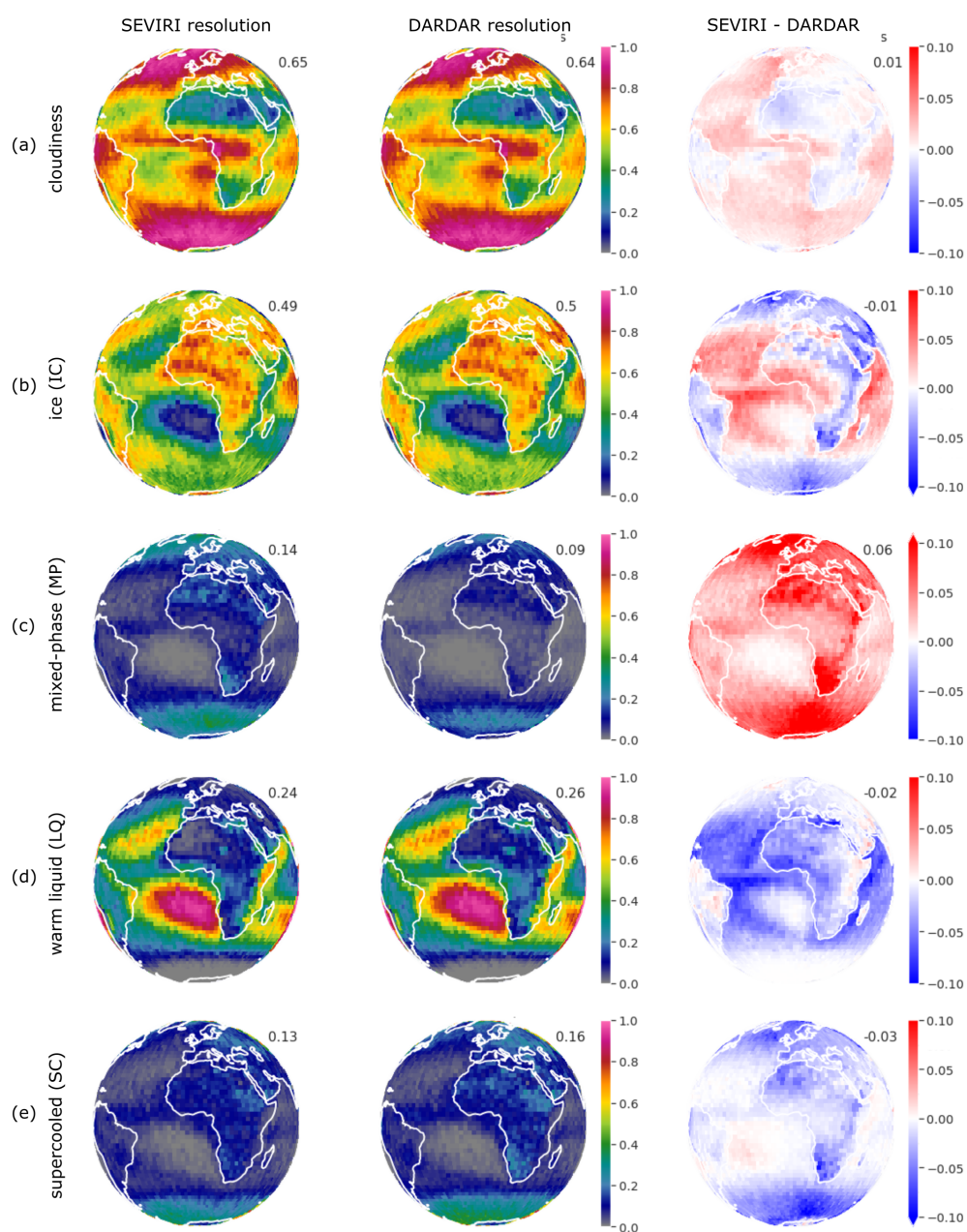
Figure 3. (**a**) Cloudiness and (**b–e**) phase occurrence for the CTPs IC (ice), MP (mixed-phase), LQ (liquid), and SC (supercooled) for SEVIRI resolution (left column), DARDAR resolution (middle column) and the difference SEVIRI minus DARDAR (right column). Boxes of 2.5° latitude by 2.5° longitude are used for all figures.

A second mechanism—besides aggregation—that causes differences between the phase occurrences in the two resolutions is that DARDAR results are not used and the corresponding SEVIRI pixels are omitted if they are either not fully covered with cloudy gates or if there are too large CTH differences (see Section 2.3 and Figure 2a).

In the phase occurrence probabilities, we see these differences due to non-fully covered pixels and cloud edges mainly in the IC and LQ CTPs in Figure 3b,d. The LQ phase occurrence is smaller for the SEVIRI resolution than for the DARDAR resolution. The reason is that when small-scale LQ clouds, which do not fully cover SEVIRI pixels, are omitted in SEVIRI resolution, the number of LQ data points decreases. As a consequence, the phase occurrence for LQ cloud tops decreases (see Equation (1)). This can be seen in Figure 3, as the difference between the SEVIRI and DARDAR resolutions for the LQ phase occurrence shows a similar pattern on the Meteosat disk as the percentage of SEVIRI pixels omitted.

Omitting DARDAR LQ values, which do not fully cover SEVIRI pixels, in going to SEVIRI resolution also has consequences for the IC phase occurrence. Comparing the differences between SEVIRI and DARDAR resolution for IC and LQ CTPs, we find higher values of IC phase occurrence in SEVIRI resolution compared to DARDAR resolution in the same spatial pattern as lower LQ phase occurrence values (see Figure 3b,d). This is explained by the following argument: Assuming a fixed number of IC data points, omitting LQ data points in going from DARDAR to SEVIRI resolution results in a decrease in the total number of cloudy data points and therefore an increase in the IC phase occurrence (see Equation (1)). Hence, a lower SEVIRI LQ phase occurrence compared to DARDAR is compensated by an increase in SEVIRI IC phase occurrence. This also holds for SC and MP cloud tops. However, from the phase occurrence plots in Figure 3b–e, one can see that SC and MP phase occurrence are low compared to the other two phases in the regions where we find differences between the two resolutions for LQ phase occurrence.

MP and SC cloud tops typically occur in mid and high latitudes as large and persistent boundary layer stratiform clouds [33]. Usually, there are no other clouds above these stratiform clouds and they can be well observed from a geostationary satellite. Therefore, pixels containing MP and SC cloud tops in SEVIRI resolution are rarely omitted, as can be seen in the distribution of the percentage of omitted SEVIRI pixels in Figure 2a.

Summarizing, all four CTPs occur in significant amounts in the SEVIRI-like CTP data set: The mean over all grid boxes is larger than 10% for all phases in SEVIRI resolution. The resolution influences the phase occurrences significantly: MP cloud tops are significantly more frequent (mean values of 14% vs. 9%), while SC and IC cloud tops are less frequent in the lower SEVIRI resolution compared to the higher DARDAR resolution. The effects of non-fully covered pixels and edges between clouds mainly influence the occurrence of LQ and IC cloud tops in the SEVIRI-like data set. As a consequence, LQ cloud tops appear less often in SEVIRI than in DARDAR resolution, while the probability for IC cloud tops rises in the same regions.

3.2. Phase as a Function of Cloud Top Temperature

Figure 4 shows the number of occurrences of data points for each SEVIRI-like CTP as a function of CTT in bins of 1.0 K. As expected, IC cloud tops dominate in cold temperatures while the LQ phase is found for high CTTs. The data are (mostly) consistent with the fact that for temperatures below 233 K only IC clouds and for temperatures higher than 273 K only LQ clouds are observed (dashed black lines in Figure 4). In the temperature regime between these two thresholds, IC, MP, and SC cloud tops are observed, with the fraction of cloud tops containing ice increasing towards colder temperatures (from purely liquid SC to MP, which is partly glaciated, to fully glaciated IC cloud tops). In fact, for CTT > 262 K SC prevail with their peak at 270 K, between 262 K and 246 K MP are dominant with their peak at 260 K, and below CTTs of 246 K IC are the most frequent CTP.

A small fraction of MP cloud tops have CTTs below 233 K even if we expect only IC to appear below this threshold. This is due in part to the fact that a SEVIRI pixel containing

both IC and MP DARDAR values is classified as MP in the coarser SEVIRI resolution, while temperatures are averaged. For a SEVIRI pixel containing IC DARDAR gates with CTT < 233 K and MP DARDAR gates with CTT $\geq$ 233 K , an average over the CTTs of all gates can result in a value <233 K in SEVIRI resolution. Furthermore, a small fraction of MP, SC, and IC cloud tops are found at temperatures above 273 K where only LQ is expected. This is not an effect of the coarsening to SEVIRI resolution, but may be due to the fact that Delanoë and Hogan [53] use wet bulb temperature rather than ambient temperature to distinguish between "warm" (LQ) and "cold" (SC, MP, IC) cloud gates (see Section 2.1). The wet bulb temperature is the temperature at which ice particles falling through subsaturated air will melt [53,71]. For SC, MP, or IC clouds falling through warmer, subsaturated air layers, the ambient CTT may be >273 K, while the wet-bulb temperature is <273 K. There are also some very rare cases of very cold (CTT $\leq$ 225 K) MP tops. These cases result from very specific situations that are allowed by the phase definition (see Section 2.3). If the gates in the vertical band of a DARDAR profile are very dispersed in height, with large cloud-free gaps (<2 km, so the rule for multilayered clouds does not apply) between few upper IC gates (leading to the cold CTTs) and lower MP gates (where the temperature is already >233 K), this can lead to the categorization as MP with too cold CTTs in the aggregation. However, these very cold MP data points with CTT $\leq$ 225 K make up only 0.07% of all cloudy data points and are therefore not relevant in the statistics.
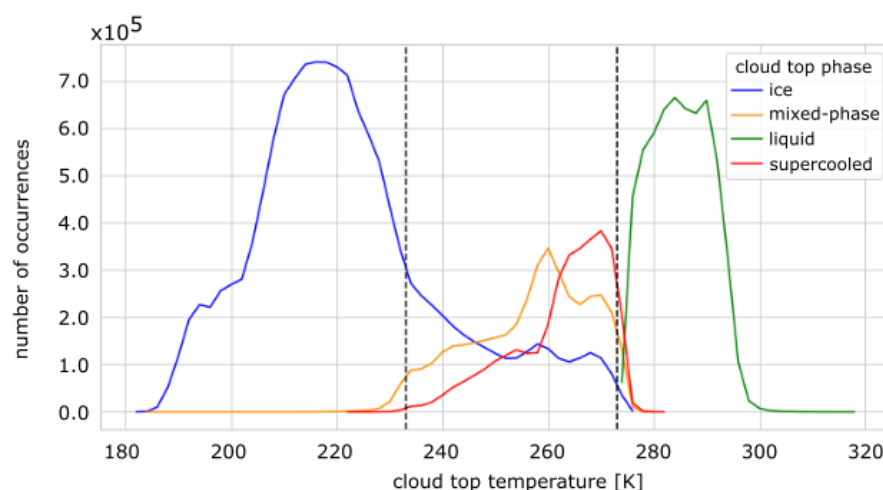
Figure 4. Number of occurrences of SEVIRI-like CTP as a function of cloud top temperature (CTT). The distribution has bins of 1.0 K. Black dashed lines indicate the temperatures 233 K and 273 K.

Overall, these results show that our definition of the SEVIRI-like CTP applied to the DARDAR data set yields physically meaningful results that are consistent with previous findings [33]. Hence, we conclude that aggregating the DARDAR cloud phase to the lower SEVIRI resolution preserves relevant physical relationships between temperature and cloud phase.

3.3. Phase Occurrence at Varying Cloud Top Heights

Next, we examine the height distribution of the SEVIRI-like CTP. The height of the cloud tops, i.e., CTH, is an important parameter for passive instruments because it is directly related to the CTT, which is important for infrared channels, and because it affects the path length of the radiation emitted by a cloud through the atmosphere. Figure 5 shows the height distribution of the number of occurrences of CTPs for the two surface types-land and ocean-, and three different latitude bands-the tropics (defined as latitude band 10°S to 10°N), mid-latitudes (latitude band 40° to 50°N or S), and polar latitudes (latitudes > 70°N or S). Bins of 500 m CTH are used for the analysis. The small vertical lines at the bottom of

each plot in Figure 5 mark the mean values of CTH for each CTP. The mean CTHs clearly decrease from the tropics towards the poles.

The distribution of CTHs is very different in the three latitude regimes. In the tropics, CTHs show a wide range from 0 km to over 17 km. The distribution is bimodal with mostly either very low or very high CTHs while the values in between are less frequent. The distribution of CTHs in the tropics is similar over land and ocean. The most significant differences between the surface types are observed for LQ clouds, which on average have larger CTHs over land than over ocean. Interestingly, MP and SC cloud tops have very similar height distributions and their average CTHs are very close (over the ocean 6.8 km for MP and 6.3 km for SC; over land 6.5 km for MP and 6.2 km for SC). The CTHs of the SEVIRI-like CTP are mostly within three CTH ranges: LQ roughly below 4.5 km, MP/SC in the altitude range of 4.5–8 km, and IC above 8 km. However, even though most IC cloud tops are found at altitudes above 8 km, the distribution of IC CTHs also has a large overlap with MP and SC CTHs.
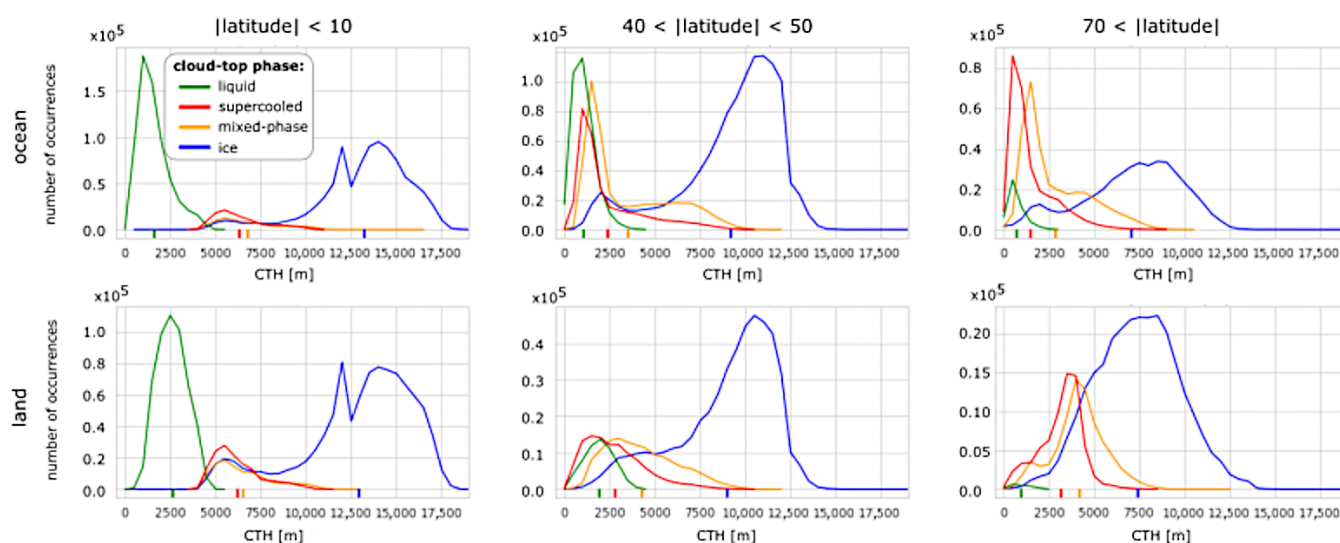
Figure 5. Number of occurrences of SEVIRI-like CTP as a function of CTH at different latitude regimes and land versus ocean, for CTH bins of 500 m. The small vertical lines at the bottom of each plot show the average CTH for each CTP.

In polar latitudes the range of CTH is smaller, ranging up to about 12.5 km. The distributions of CTH of the different CTPs have a large overlap. IC clouds reach similar average CTHs of 7.1 km over the ocean and 7.4 km over land. In contrast to the tropics, MP clouds in polar latitudes have on average significantly larger CTHs than SC clouds (2.8 km for MP and 1.5 km for SC over the ocean; 4.2 km for MP and 3.2 km for SC over land). Both CTPs have lower CTHs over the ocean than over land. LQ clouds occur at low heights below 2.5 km and only very rarely over land (less than 1% of clouds in polar latitudes over land are LQ).

The mid-latitudes constitute the transition between the tropics and polar latitudes in terms of the CTH distribution. The average CTH over the ocean (land) for IC clouds is about 9.2 km (9.0 km), for MP clouds 3.5 km (4.3 km), for SC clouds 2.4 km (2.8 km), and for LQ clouds 1.1 km (1.9 km). LQ, SC, and MP clouds have higher CTHs over land than over the ocean. MP clouds have higher CTHs than SC, which in turn have larger CTHs than LQ clouds. The overlap between the different phases in mid-latitudes is quite large. In general, the influence of the surface type decreases with altitude; while IC clouds show hardly any differences between land and ocean, the differences increase with decreasing CTH.

3.4. Variability with Season and Surface Type

Finally, we analyze the SEVIRI-like CTP data set in terms of seasonal variability and land-ocean differences. Figure 3 suggests that the geographical distribution of CTP is mainly controlled by latitude and surface type (ocean or land) and to a lesser degree by longitude. Therefore, in the following, the probability of phase occurrence is calculated only as a function of latitude (zonal mean), surface type, and season to obtain more robust statistics. Analog to Equation (1), incorporating season s and surface type ls leads to the probability of occurrence for phase q and the cloudiness

$$P(q\,|\,\text{lat, s, ls}) = \frac{1}{n_{lon}}\sum_{lon} P(q\,|\,\text{lon, lat, s, ls}) = \frac{1}{n_{lon}}\sum_{lon}\frac{N(q,\text{lon, lat, s, ls})}{N(\text{cloud, lon, lat, s, ls})},$$

$$P(\text{cloud}\,|\,\text{lat, s, ls}) = \frac{1}{n_{lon}}\sum_{lon} P(\text{cloud}\,|\,\text{lon, lat, s, ls}) = \frac{1}{n_{lon}}\sum_{lon}\frac{N(\text{cloud, lon, lat, s, ls})}{N(\text{lon, lat, s, ls})},$$

where n_{lon} is the number of longitude bins for the given (lat, s, ls) configuration. As before, grid cells of 2.5° are used for the longitude and latitude. Figure 6 shows the cloudiness and probability of CTP q as a function of latitude for the four seasons (DJF, MAM, JJA, SON) and two surface types (ocean, land). Because of the daylight-only mode of CloudSat, there are no data points south of 70°S for the months JJA. Due to few land masses in the southern latitudes between 40° and 70°S, the statistics over land in these latitudes are not as robust, and the curves are therefore not as smooth as for other latitudes. The gap in the probability curves over land corresponds to latitudes where less than a minimum of 200 data points (SEVIRI-like CTPs for a given phase) are available.

In general, cloudy conditions are more frequent over the ocean than over land: mean cloudiness is about 68% over the ocean and 55% over land. This is true for most latitudes, as shown in Figure 6a,b. The only exception to this is the ITCZ because of stronger convective activity over land than over the ocean. The partitioning into CTPs, $P(q\,|\,\text{lat, s, ls})$, shows ocean–land differences as well. Particularly large differences can be observed for LQ cloud tops, which in some regions in low latitudes are twice as likely to occur over the ocean than over land (26% of cloudy data points over the ocean and 16% over land). In contrast, IC cloud tops are more common over land (56%) than ocean (46%). Compared to LQ and IC cloud tops, SC and MP cloud tops show only small ocean–land differences: SC cloud tops are only slightly more common over the ocean (14%) than land (13%); MP cloud tops are equally frequent over ocean and land (14%).

Note that IC cloud tops are more frequent in the Northern than in the Southern Hemisphere: 53% of cloud tops are IC in the Northern Hemisphere, while 45% of cloud tops are IC in the Southern Hemisphere. This hemispheric difference in the occurrence of IC clouds has been reported in several studies and is attributed to the hemispheric difference in aerosol loading [72–75]. More specifically, it is attributed to the higher concentration of ice nucleating particle (INP) active mineral dust aerosol in the Northern Hemisphere, which is due to the larger land mass (especially deserts) [75]. This can also be an explanation for the hemispheric differences in SC cloud tops: for cloudy conditions, we find that 12% of the cloud tops in the Northern Hemisphere and 14% of cloud tops in the Southern Hemisphere are SC. At high latitudes, SC cloud tops are nearly twice as likely to be observed in the Southern Hemisphere, where few INPs are available for glaciation, as in the Northern Hemisphere. Huang et al. [56] also found that clouds over the Southern Ocean are more likely to be supercooled than at similar temperatures in the Northern Hemisphere, which might be connected to the availability of INPs [76].
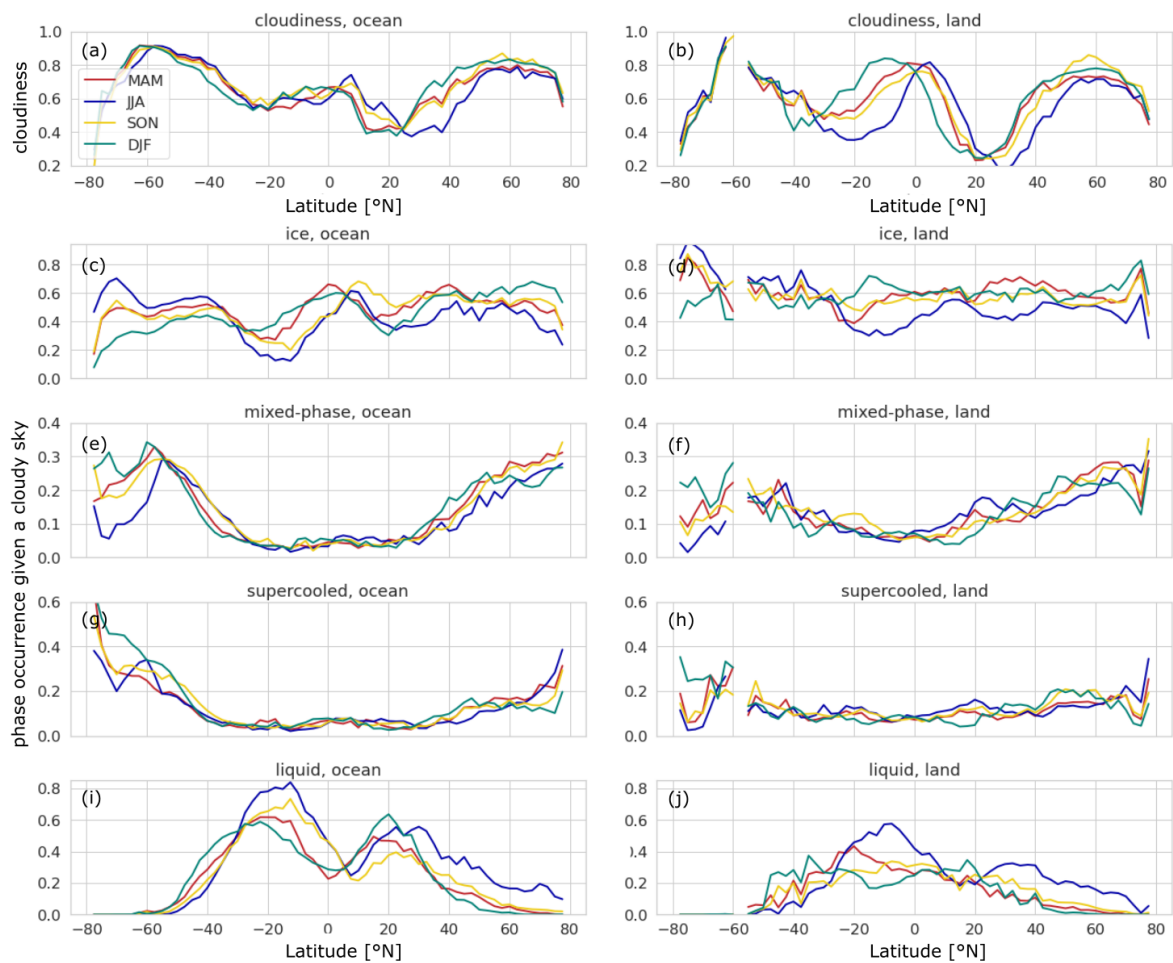
Figure 6. (**a**,**b**) Probability of cloudy conditions (cloudiness) and (**c–j**) probability of occurrence of CTPs as functions of latitude, season, and surface type (land or ocean). Bins of 2.5° are used for the latitude.

We also observe a distinct seasonal variability in cloudiness and the CTPs, especially for IC and LQ. Over the course of a year, the maxima in the zonal mean cloudiness and the IC phase occurrence shift northwards in JJA, and then back southwards in DJF, marking high convective clouds, and therefore, the ITCZ. This shift is more pronounced over land than over the ocean, due to the higher seasonal variability of the surface temperature on land compared to the ocean. The curves for MAM and SON are mostly in between the curves for JJA and DJF. In the Southern Hemisphere, the zonal mean of cloudiness stays approximately constant during the year. However, the partitioning between the different CTPs shows a large seasonal variability. In the subtropics, LQ and IC phase occurrences have maximal differences between seasons of up to 35%, with LQ (IC) being more frequent in JJA (DJF). In the southern high latitudes (south of 60°S), the largest seasonal variabilities are observed for IC and MP phase occurrences.

In contrast to the Southern Hemisphere, cloudiness shows large seasonal variability in the northern mid and high latitudes: Cloudiness is highest in DJF and lowest in JJA. A second difference to the Southern Hemisphere is that in the Northern Hemisphere LQ cloud tops are observed also at high latitudes, occurring mainly in JJA. The higher occurrences of LQ cloud tops during JJA are partially compensated through lower probabilities of occurrence for IC and MP cloud tops. In contrast to IC, MP, and LQ cloud tops, SC cloud tops exhibit little seasonal variability in the northern high latitudes.

4. Evaluation of CiPS

In this section, the performance of the ice cloud detection algorithm CiPS is evaluated using the SEVIRI-like CTP derived from DARDAR as a reference (see Section 2.2). The output of the CiPS ice detection is either "ice" or "non-ice" for every pixel. Hence, in order to compare the SEVIRI-like CTP to CiPS, we summarize the categories clear-sky, LQ, SC, and MP of the SEVIRI-like data set to the category "non-ice", while the IC CTP category of the SEVIRI-like data set is comparable to the CiPS "ice" category. For the evaluation of CiPS, we use one year (2013) of the SEVIRI-like data set and compare its "ice" and "non-ice" values pixel by pixel with the results of CiPS at the same latitude, longitude, and time. The number of data points in which both data sets agree (i.e., either "ice" or "non-ice" in both data sets) or disagree (i.e., "ice" in one data set and "non-ice" in the other data set) are counted. The results of this comparison are displayed in Table 1. It shows the percentage of pixels classified by CiPS as either ice or non-ice pixels with respect to a fixed category of the SEVIRI-like data set. For the SEVIRI-like data set, all ice cloud pixels observed during the year 2013 amount to about 1.9×10^6 data points, while non-ice pixels amount to about 4.2×10^6 data points. Of these pixels classified as ice in the SEVIRI-like data set, CiPS detects 77.1% as ice as well, i.e., its probability of detection (POD) amounts to this value. The ice clouds that remain undetected by CiPS are mainly optically thin clouds with optical thickness < 1, which are known to be difficult to detect with passive methods [50]. As mentioned in Section 2.2, CiPS was trained to detect ice crystals with CAL_LID_L2, which distinguishes "only" between ice clouds, liquid water clouds, and "undetermined". Consequently, in the previous characterization of Strandgren et al. [50], it was not possible to test how CiPS performs for MP clouds, particularly whether CiPS is sensitive to ice crystals present in MP clouds. Using the collocated data set of SEVIRI-like CTP and CiPS, this can now be examined. We find that CiPS categorizes only 22% of MP clouds as ice. The rest of the MP clouds, i.e., 78%, are categorized as non-ice. Thus, the detection of cloud ice by CiPS is mostly limited to pure ice clouds.

Table 1. Percentages of pixels classified as ice or non-ice by CiPS with respect to the SEVIRI-like classification.

	DARDAR: Ice	**DARDAR: Non-Ice**
CiPS: ice	77.1%	11.6%
CiPS: non-ice	22.9%	88.4%

The false alarm rate, FAR, (i.e., the fraction of SEVIRI-like non-ice pixels which are classified as ice by CiPS) is 11.6%. Of these pixels falsely classified as ice by CiPS, 32% are clear-sky according to the SEVIRI-like data set, and the rest are cloudy with 28% LQ, 27% MP, and 13% SC cloud tops. Since the fraction of misclassified MP clouds is overproportionally large compared to the occurrence of this phase, we can conclude that phase discrimination between IC and MP clouds is a particular challenge for CiPS. In order to understand the FAR of CiPS better, we examine its dependencies. We find that the FAR of CiPS for clear-sky (i.e., pixels classified as clear-sky in the SEVIRI-like data set and as ice by CiPS) depends mainly on the latitude, while the FAR of CiPS for non-ice cloudy pixels (i.e., pixels classified as LQ, SC or MP in the SEVIRI-like data set and as ice by CiPS) depends mainly on CTT. Figure 7a,b shows these dependencies of the FAR of CiPS for non-ice cloudy and clear-sky pixels. The panels below (Figure 7c,d) show the number of occurrences of the non-ice cloudy and clear-sky pixels to indicate the frequency at which the respective FARs occur. The FAR for non-ice cloudy pixels as a function of CTT (see Figure 7a) is nearly constant (and small, around 0.1) for clouds with CTT $\geq$ 250 K and increases strongly below this temperature for MP cloud tops. Interestingly, SC clouds are only responsible for a very small amount of false alarms, in contrast to the findings of Strandgren et al. [50] (see Section 2.2). The FAR for clear-sky conditions as a function of latitude (see Figure 7b) shows that most false alarms are found in the ITCZ with high

surface temperatures, which is a known weakness of CiPS [49] (see also Section 2.2). In the evaluation of CiPS Strandgren et al. [49,50] (as mentioned in Section 2.2), similar results were found for the POD (70%) as in this study, but lower values for the FAR (4%). Since CiPS was trained with CAL_LID_L2, a better agreement is to be expected. There are several factors that can account for these differences in FAR. One factor is differences in phase partitioning. According to the definition of the CTP, pixels at SEVIRI resolution composed of DARDAR gates that are partly ice and partly other phases (MP or SC) are classified as MP. Some such pixels composed mainly of ice with a small liquid fraction could fall into the ice category of the coarser CAL_LID_L2 product. This would lead to an increase in the FAR of CiPS. In addition, the two products DARDAR and CAL_LID_L2 use different algorithms to determine the cloud thermodynamic phase which could lead to inherent differences in the phase partitioning of the two products, increasing the FAR of CiPS. Furthermore, both products use different cloud masks: DARDAR uses the CALIPSO Vertical Feature Mask only to filter out aerosols and otherwise CALIOP backscatter directly, while the product used to train CiPS is version V3-01 of CAL_LID_L2_05kmC [61]. A third difference between the evaluation of CiPS in this study and the previous evaluation of Strandgren et al. [50] is that the training and previous evaluation of CiPS was performed with MSG2 data, while we use MSG3 data in this study. The channels of the two different satellites are not completely identical, and CiPS is expected to perform better on MSG2. Since the two evaluations cover different time periods, there is also the possibility that differences in clouds in the two time periods led to the differences in FAR.
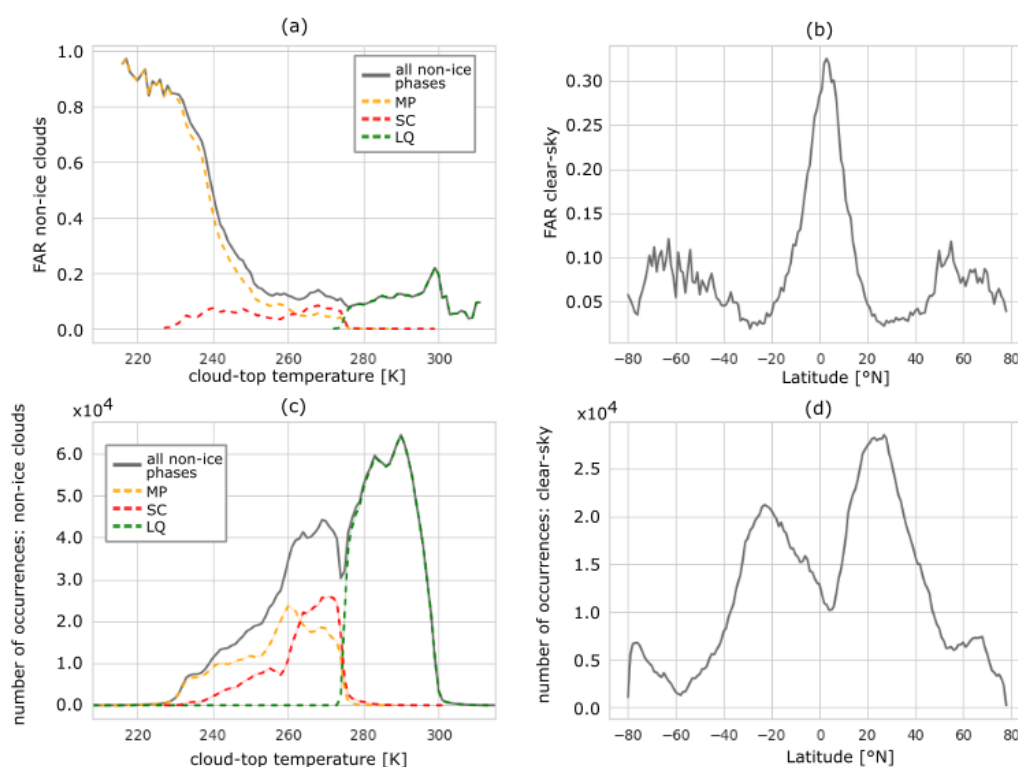
Figure 7. (**a**) FAR of CiPS with respect to non-ice clouds (grey line) as a function of CTT. The dashed lines show the contributions of the different CTPs to the overall FAR; (**b**) FAR of CiPS with respect to clear-sky as a function of latitude; (**c**) Number of occurrences of non-ice clouds in the SEVIRI-like data set (dashed lines show the contributions of the different CTPs); (**d**) Number of occurrences of clear-sky in the SEVIRI-like data set.

5. Discussion and Conclusions

Since phase partitioning is still an open question in climate modeling and has important implications for various cloud-related subjects (precipitation, cloud lifetime, cloud albedo, ...) the goal of this paper is to understand the importance of the four different phases (IC, MP, SC, and LQ) in terms of their frequency of occurrence from the geostationary perspective. Since MP and SC clouds are most prevalent at high latitudes which are difficult to see with a geostationary satellite, it is not a priori clear how many MP and SC cloud tops can be observed with SEVIRI. To our knowledge, no information about the occurrence of such phases is available at the SEVIRI pixel level.

To gain new insights about these questions, we use the lidar/radar remote sensing product DARDAR-MASK to deduce a cloud top phase (CTP) for the geostationary passive sensor SEVIRI aboard Meteosat Second Generation. This SEVIRI-like CTP is then used to test the influence of the resolution on CTP measurements and to study the geographic and seasonal distribution of CTPs from a geostationary passive satellite perspective as well as to evaluate the ice cloud detection algorithm for SEVIRI called CiPS.

To deduce the SEVIRI-like CTP from DARDAR measurements, we impose a (simplified) penetration depth of SEVIRI by only considering DARDAR values up to 240 m below cloud top and aggregating the DARDAR results to the spatial resolution of SEVIRI. This results in a CTP in SEVIRI resolution with four different thermodynamic "phases": ice (IC), mixed-phase (MP), supercooled (SC), and warm liquid (LQ). Testing this derived SEVIRI-like CTP against CTT shows that aggregating the DARDAR cloud phase to the lower SEVIRI resolution preserves physical relationships. Although the data set was derived for the viewing geometry and resolution of SEVIRI, it can be easily extended to other geostationary satellites, provided sufficient data are available for collocation. In this sense, it will not be possible to derive a similar data set for the Flexible Combined Imager (FCI) aboard the follow-on satellite of MSG (Meteosat Third Generation—MTG, launched on 13 December 2022 [77]), since the spaceborne active instruments from the A-Train will no longer be available in 2023. Future observations from the EarthCARE satellite [78] will be needed.

We use the aggregated SEVIRI-like CTP to test the effects of the resolution on the cloud phase measurements by comparing the CTP at SEVIRI resolution with a corresponding CTP at DARDAR resolution. Even though the general patterns of CTP are similar in both resolutions, we find that the resolution has a significant effect on the occurrence of the CTPs and their geographic distribution. The largest changes due to resolution are found for MP cloud tops, which occur significantly more often at the lower SEVIRI resolution (14% on average) than at the higher DARDAR resolution (9% on average). In contrast, the probability of measuring SC or IC cloud tops decreases for the lower SEVIRI resolution. We also find effects due to partly cloud-covered pixels and edges between clouds, which mainly influence the occurrence of LQ and IC cloud tops in the SEVIRI-like data set. These results help to assess how representative geostationary measurements of CTP are compared to measurements from polar orbit satellites and to interpret them in the correct way.

From the SEVIRI-like data set, we find that all four different CTPs are found in significant amounts on the Meteosat disk: In SEVIRI resolution, 65.0% of data points are cloudy, consisting of 49% IC, 14% MP, 13% SC, and 24% LQ cloud tops. For CTTs above 246 K, MP, or SC clouds are predominant, while IC clouds become dominant for lower temperatures. An analysis of the CTH distribution for different latitude regions reveals that the different CTPs have characteristic height regimes, however, with large overlaps, especially between MP and SC clouds. In the tropics, the CTH regimes of MP/SC and LQ are clearly separated, with LQ at lower heights, while the CTH regimes of LQ, SC, and MP strongly overlap in the mid- and high-latitudes. Even though the altitude regime of IC extends much higher than the other phases, it also has overlap with those of the other CTPs. Interestingly, MP and SC cloud tops have a very similar average CTH value and vertical distribution in the tropics with predominantly convective systems but show differences in CTH at mid and high latitudes where stratiform clouds dominate for MP and SC. For a

retrieval with SEVIRI, the observed differences in the characteristic height regimes of the CTPs can serve as a starting point for the distinction between phases. However, due to the large overlap of height regimes of the CTPs, a distinction can not be made on the basis of CTH (or the correlated CTT) alone.

The amount of cloudiness exhibits a distinct seasonal cycle, particularly over land where it follows the seasonal progression of the ITCZ. The probability of IC also varies in a similar manner to the ITCZ. LQ shows a clear seasonal cycle affected by the shift of the ITCZ as well, especially in the subtropics. On the contrary, MP and SC show less seasonal variability, with the largest seasonal fluctuations being observed in Antarctica. There, the probability of MP and SC clouds is at its minimum during JJA and at its peak during DJF, with a difference of up to 20% between seasons.

As an application of the SEVIRI-like CTP data set, we evaluate CiPS, a state-of-the-art AI-based ice cloud detection algorithm for SEVIRI. We find that CiPS performs well with a probability of detection of 77.1% and a false alarm rate of 11.6%. False alarms occur mainly for cold MP cloud tops and for clear-sky conditions in the ITCZ. Even though MP cloud tops have the highest FAR in cloudy conditions, CiPS classifies overall only 22% of MP clouds as ice. The rest of the MP cloud tops are classified as non-ice, which means that CiPS is not sensitive to the ice particles contained in MP clouds. This suggests that new methods are needed to detect MP cloud tops from SEVIRI data.

Finally, our results stress the need for phase determination algorithms for SEVIRI that are able to discriminate among all these phase conditions and can be used to develop or test phase retrievals. This study shows that all thermodynamic phases occur frequently over the Meteosat disk. Therefore, a retrieval for all thermodynamic phases for SEVIRI would provide an important contribution to better understand phase partitioning and enable us to investigate the micro- and macrophysics of MP, SC, and LQ clouds. This would be a valuable addition to the CiPS algorithm, which is "only" suited to detect fully glaciated clouds. In addition, the high temporal resolution of SEVIRI would also allow us to study the evolution of clouds and their top phase, thus extending the value of the DARDAR-MASK product to places and times where no data from CloudSat and CALIPSO are available because of their sun-synchronous polar orbits. In this context, the SEVIRI-like CTP could also serve as a "ground truth" to develop and test new phase retrievals for SEVIRI. There are nearly 20 years of data from the SEVIRI instrument (the Meteosat Second Generation satellites have been in operation since 2004) waiting to be evaluated with respect to CTP.

Appendix A

Since the assignment of the vertically aggregated phase depends on the thickness of the vertical band (see Section 2.3), we briefly discuss the influence of the choice of 240 m for its vertical extent.

One has first to notice that by design (see Section 2.1) DARDAR assigns the SC phase in layers of maximal 300 m geometrical thickness. Analyzing the distribution of SC layer thickness in the DARDAR product, one finds that the majority of SC layers have a vertical thickness of 240 m. Due to this definition of SC within DARDAR, when the cloud top layer would be defined to be larger than 4 gates (>240 m), SC will often be found with other phases (MP or IC) below as a consequence, thus usually leading to the disappearance of a pure SC in favor of MP. On the contrary, when defining a thin cloud top layer (60–120 m) the phase classification might not be representative for cloud top due, e.g., to DARDAR retrieval outliers. We thus want to have a certain thickness of the layer to be confident in the result of the categorization. Thus, we restrict ourselves to 240 m—the typical thickness of SC layers in DARDAR.

For phases other than SC as the topmost cloudy gate (i.e., IC, MP, and LQ) the choice of the size of the vertical layer to be investigated is less important. In fact, below LQ there will only be other LQ gates, below MP there could be IC gates (but the final CTP is still MP) and below IC at cloud top there are typically only IC gates.

In order to better understand which implication the aggregation procedure has for the resulting cloud top phase, we have analyzed which phase combinations have been obtained in every vertical profile over the five years used in the study. This is plotted Figure A1. It shows the number of occurrences of the possible phase combinations in the vertical band of 240 m in DARDAR resolution. Possible combinations are "pure IC", "pure MP", "pure LQ", "pure SC", "MP and SC", "MP and IC", "IC and SC" and "IC, MP and SC". The last four categories all fall under the MP category when vertically aggregated. The category "MP and IC" is, however, not really sensitive to the thickness of the vertical band since the majority of these cases come from stratiform clouds where MP resides on the cloud top. Thus, reducing or increasing the thickness of the vertical band does not affect the classification. The two MP subcategories not sensitive to a change in the thickness of the vertical band, "pure MP" together with "MP and IC", make up the majority (63%) of the aggregated MP category. Sensitive to the thickness of the vertical band are the three categories containing SC ("MP and SC", "IC and SC" and "IC, MP and SC") as explained above. Figure A1 shows that these three subcategories make up about 37% of the aggregated MP category. If the thickness of the vertical band is decreased, a fraction of these subcategories will move from MP to a different phase categorization (SC or IC). An increase in the thickness of the vertical band would not change the categorization as MP.

These are the reasons why we selected a geometric thickness of 240 m for the vertical band at the cloud top. It represents a suitable value for a robust phase categorization that allows us to consider four DARDAR gates—thus adding to the representativeness with respect to cloud top—but at the same time preserving SC cloud top layers during the aggregation process.
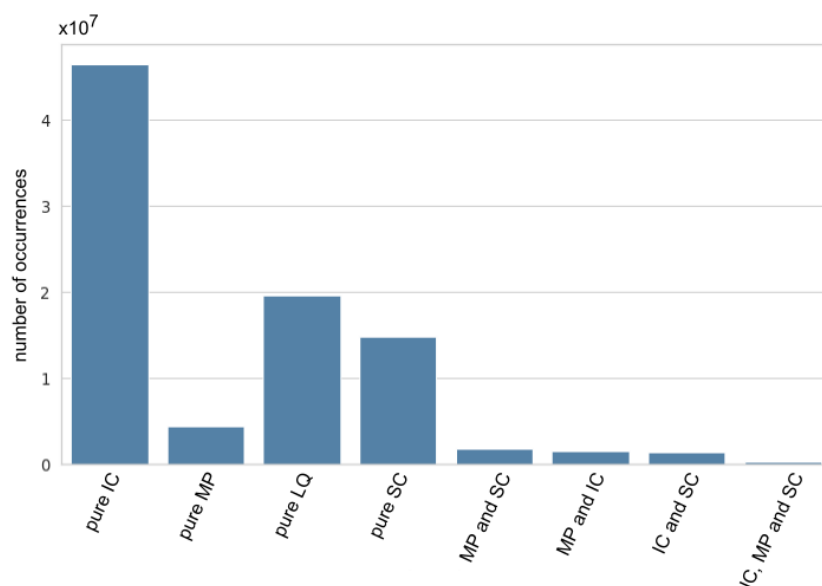
Figure A1. Number of occurrences of the different possible phase combinations in the vertical band of 240 m in DARDAR resolution. The four leftmost bars ("pure IC", "pure MP", "pure LQ" and "pure SC") mean that the vertical band contains only gates of the respective phase. The four rightmost bars ("MP and SC", "MP and IC", "IC and SC" and "IC, MP and SC") mean that gates of the respective two or three phases are contained in the vertical band. Hence, the four rightmost bars all fall under the MP category in the vertical aggregation step, as described in Section 2.3.

References

1. Boucher, O.; Randall, D.; Artaxo, P.; Bretherton, C.; Feingold, G.; Forster, P.; Kerminen, V.M.; Kondo, Y.; Liao, H.; Lohmann, U.; et al. Clouds and Aerosols. In *Climate Change 2013: The Physical Science Basis. Contribution of Working Group I to the Fifth Assessment Report of the Intergovernmental Panel on Climate Change*; Stocker, T.F., Qin, D., Plattner, G.-K., Tignor, M., Allen, S.K., Boschung, J., Nauels, A., Xia, Y., Bex, V., Midgley, P.M., Eds.; Cambridge University Press: Cambridge, UK; New York, NY, USA, 2013; pp. 571–658. [CrossRef]
2. Forster, P.; Storelvmo, T.; Armour, K.; Collins, W.; Dufresne, J.L.; Frame, D.; Lunt, D.; Mauritsen, T.; Palmer, M.; Watanabe, M.; et al. The Earth's Energy Budget, Climate Feedbacks, and Climate Sensitivity. In *Climate Change 2021: The Physical Science Basis. Contribution of Working Group I to the Sixth Assessment Report of the Intergovernmental Panel on Climate Change*; Masson-Delmotte, V., Zhai, P., Pirani, A., Connors, S.L., Péan, C., Berger, S., Caud, N., Chen, Y., Goldfarb, L., Gomis, M.I., et al., Eds.; Cambridge University Press: Cambridge, UK; New York, NY, USA, 2021; pp. 923–1054. [CrossRef]
3. Ehrlich, A.; Bierwirth, E.; Wendisch, M.; Gayet, J.F.; Mioche, G.; Lampert, A.; Heintzenberg, J. Cloud phase identification of Arctic boundary-layer clouds from airborne spectral reflection measurements: Test of three approaches. *Atmos. Chem. Phys.* **2008**, *8*, 7493–7505. [CrossRef]
4. Tan, I.; Storelvmo, T.; Zelinka, M.D. Observational constraints on mixed-phase clouds imply higher climate sensitivity. *Science* **2016**, *352*, 224–227. [CrossRef] [PubMed]
5. Thompson, D.R.; Kahn, B.H.; Green, R.O.; Chien, S.A.; Middleton, E.M.; Tran, D.Q. Global spectroscopic survey of cloud thermodynamic phase at high spatial resolution, 2005–2015. *Atmos. Meas. Tech.* **2018**, *11*, 1019–1030. [CrossRef]
6. McCoy, D.T.; Hartmann, D.L.; Zelinka, M.D.; Ceppi, P.; Grosvenor, D.P. Mixed-phase cloud physics and Southern Ocean cloud feedback in climate models. *J. Geophys. Res. Atmos.* **2015**, *120*, 9539–9554. [CrossRef]
7. Choi, Y.S.; Ho, C.H.; Park, C.E.; Storelvmo, T.; Tan, I. Influence of cloud phase composition on climate feedbacks. *J. Geophys. Res. Atmos.* **2014**, *119*, 3687–3700. [CrossRef]
8. Komurcu, M.; Storelvmo, T.; Tan, I.; Lohmann, U.; Yun, Y.; Penner, J.E.; Wang, Y.; Liu, X.; Takemura, T. Intercomparison of the cloud water phase among global climate models. *J. Geophys. Res. Atmos.* **2014**, *119*, 3372–3400. [CrossRef]
9. Mioche, G.; Jourdan, O.; Ceccaldi, M.; Delanoë, J. Variability of mixed-phase clouds in the Arctic with a focus on the Svalbard region: A study based on spaceborne active remote sensing. *Atmos. Chem. Phys.* **2015**, *15*, 2445–2461. [CrossRef]
10. Matus, A.V.; L'Ecuyer, T.S. The role of cloud phase in Earths radiation budget. *J. Geophys. Res. Atmos.* **2017**, *122*, 2559–2578. [CrossRef]
11. Ricaud, P.; Guasta, M.D.; Lupi, A.; Roehrig, R.; Bazile, E.; Durand, P.; Attié, J.L.; Nicosia, A.; Grigioni, P. Supercooled liquid water clouds observed over Dome C, Antarctica: Temperature sensitivity and surface radiation impact. *Atmos. Chem. Phys. Discuss.* **2022**. [CrossRef]

12. Cheng, A.; Xu, K.M.; Hu, Y.; Kato, S. Impact of a cloud thermodynamic phase parameterization based on CALIPSO observations on climate simulation. *J. Geophys. Res. Atmos.* **2012**, *117*, D09103. [CrossRef]

13. Cesana, G.; Waliser, D.E.; Jiang, X.; Li, J.L.F. Multimodel evaluation of cloud phase transition using satellite and reanalysis data. *J. Geophys. Res. Atmos.* **2015**, *120*, 7871–7892. [CrossRef]

14. Zhang, D.; Liu, D.; Luo, T.; Wang, Z.; Yin, Y. Aerosol impacts on cloud thermodynamic phase change over East Asia observed with CALIPSO and CloudSat measurements. *J. Geophys. Res. Atmos.* **2015**, *120*, 1490–1501. [CrossRef]

15. Braga, R.C.; Rosenfeld, D.; Weigel, R.; Jurkat, T.; Andreae, M.O.; Wendisch, M.; Pöschl, U.; Voigt, C.; Mahnke, C.; Borrmann, S.; et al. Further evidence for CCN aerosol concentrations determining the height of warm rain and ice initiation in convective clouds over the Amazon basin. *Atmos. Chem. Phys.* **2017**, *17*, 14433–14456. [CrossRef]

16. Coopman, Q.; Hoose, C.; Stengel, M. Analyzing the Thermodynamic Phase Partitioning of Mixed Phase Clouds Over the Southern Ocean Using Passive Satellite Observations. *Geophys. Res. Lett.* **2021**, *48*, e2021GL093225. [CrossRef]

17. Atkinson, J.D.; Murray, B.J.; Woodhouse, M.T.; Whale, T.F.; Baustian, K.J.; Carslaw, K.S.; Dobbie, S.; O'Sullivan, D.; Malkin, T.L. The importance of feldspar for ice nucleation by mineral dust in mixed-phase clouds. *Nature* **2013**, *498*, 355–358. [CrossRef] [PubMed]

18. Prenni, A.J.; Harrington, J.Y.; Tjernström, M.; DeMott, P.J.; Avramov, A.; Long, C.N.; Kreidenweis, S.M.; Olsson, P.Q.; Verlinde, J. Can Ice-Nucleating Aerosols Affect Arctic Seasonal Climate? *Bull. Am. Meteorol. Soc.* **2007**, *88*, 541–550. [CrossRef]

19. Morrison, H.; Zuidema, P.; Ackerman, A.S.; Avramov, A.; de Boer, G.; Fan, J.; Fridlind, A.M.; Hashino, T.; Harrington, J.Y.; Luo, Y.; et al. Intercomparison of cloud model simulations of Arctic mixed-phase boundary layer clouds observed during SHEBA/FIRE-ACE. *J. Adv. Model. Earth Syst.* **2011**, *3*, 66. [CrossRef]

20. Gregory, D.; Morris, D. The sensitivity of climate simulations to the specification of mixed phase clouds. *Clim. Dyn.* **1996**, *12*, 641–651. [CrossRef]

21. Doutriaux-Boucher, M.; Quaas, J. Evaluation of cloud thermodynamic phase parametrizations in the LMDZ GCM by using POLDER satellite data. *Geophys. Res. Lett.* **2004**, *31*, L06126. [CrossRef]

22. Cesana, G.; Kay, J.E.; Chepfer, H.; English, J.M.; Boer, G. Ubiquitous low-level liquid-containing Arctic clouds: New observations and climate model constraints from CALIPSO-GOCCP. *Geophys. Res. Lett.* **2012**, *39*, 53385. [CrossRef]

23. Stubenrauch, C.J.; Rossow, W.B.; Kinne, S.; Ackerman, S.; Cesana, G.; Chepfer, H.; Girolamo, L.D.; Getzewich, B.; Guignard, A.; Heidinger, A.; et al. Assessment of Global Cloud Datasets from Satellites: Project and Database Initiated by the GEWEX Radiation Panel. *Bull. Am. Meteorol. Soc.* **2013**, *94*, 1031–1049. [CrossRef]

24. Stubenrauch, C.J.; Feofilov, A.G.; Protopapadaki, S.E.; Armante, R. Cloud climatologies from the infrared sounders AIRS and IASI: Strengths and applications. *Atmos. Chem. Phys.* **2017**, *17*, 13625–13644. [CrossRef]

25. Li, W.; Zhang, F.; Lin, H.; Chen, X.; Li, J.; Han, W. Cloud Detection and Classification Algorithms for Himawari-8 Imager Measurements Based on Deep Learning. *IEEE Trans. Geosci. Remote Sens.* **2022**, *60*, 1–17. [CrossRef]

26. Zhou, G.; Wang, J.; Yin, Y.; Hu, X.; Letu, H.; Sohn, B.J.; Yung, Y.L.; Liu, C. Detecting Supercooled Water Clouds Using Passive Radiometer Measurements. *Geophys. Res. Lett.* **2022**, *49*, e2021GL096111. [CrossRef]

27. Hu, Y.; Winker, D.; Vaughan, M.; Lin, B.; Omar, A.; Trepte, C.; Flittner, D.; Yang, P.; Nasiri, S.L.; Baum, B.; et al. CALIPSO/CALIOP Cloud Phase Discrimination Algorithm. *J. Atmos. Ocean. Technol.* **2009**, *26*, 2293–2309. [CrossRef]

28. Hu, Y.; Rodier, S.; man Xu, K.; Sun, W.; Huang, J.; Lin, B.; Zhai, P.; Josset, D. Occurrence, liquid water content, and fraction of supercooled water clouds from combined CALIOP/IIR/MODIS measurements. *J. Geophys. Res.* **2010**, *115*, 2384. [CrossRef]

29. Luke, E.P.; Kollias, P.; Shupe, M.D. Detection of supercooled liquid in mixed-phase clouds using radar Doppler spectra. *J. Geophys. Res.* **2010**, *115*, 2884. [CrossRef]

30. Zhang, D.; Wang, Z.; Liu, D. A global view of midlevel liquid-layer topped stratiform cloud distribution and phase partition from CALIPSO and CloudSat measurements. *J. Geophys. Res.* **2010**, *115*, 2143. [CrossRef]

31. Cesana, G.; Storelvmo, T. Improving climate projections by understanding how cloud phase affects radiation. *J. Geophys. Res. Atmos.* **2017**, *122*, 4594–4599. [CrossRef]

32. Bruno, O.; Hoose, C.; Storelvmo, T.; Coopman, Q.; Stengel, M. Exploring the Cloud Top Phase Partitioning in Different Cloud Types Using Active and Passive Satellite Sensors. *Geophys. Res. Lett.* **2021**, *48*, 89863. [CrossRef]

33. Korolev, A.; McFarquhar, G.; Field, P.R.; Franklin, C.; Lawson, P.; Wang, Z.; Williams, E.; Abel, S.J.; Axisa, D.; Borrmann, S.; et al. Mixed-Phase Clouds: Progress and Challenges. *Meteorol. Monogr.* **2017**, *58*, 51–550. [CrossRef]

34. Wang, Z. *Level 2 Combined Radar and Lidar Cloud Scenario Classification Product Process Description and Interface Control Document*; Report 22; Jet Propulsion Laboratory: Pasadena, CA, USA, 2012.

35. Delanoë, J.; Hogan, R.J. A variational scheme for retrieving ice cloud properties from combined radar, lidar, and infrared radiometer. *J. Geophys. Res.* **2008**, *113*, D07204. [CrossRef]

36. Ewald, F.; Groß, S.; Wirth, M.; Delanoë, J.; Fox, S.; Mayer, B. Why we need radar, lidar, and solar radiance observations to constrain ice cloud microphysics. *Atmos. Meas. Tech.* **2021**, *14*, 5029–5047. [CrossRef]

37. Listowski, C.; Delanoë, J.; Kirchgaessner, A.; Lachlan-Cope, T.; King, J. Antarctic clouds, supercooled liquid water and mixed phase, investigated with DARDAR: Geographical and seasonal variations. *Atmos. Chem. Phys.* **2019**, *19*, 6771–6808. [CrossRef]

38. Okamoto, H.; Sato, K.; Hagihara, Y. Global analysis of ice microphysics from CloudSat and CALIPSO: Incorporation of specular reflection in lidar signals. *J. Geophys. Res.* **2010**, *115*, 13383. [CrossRef]

39. Zaremba, T.J.; Rauber, R.M.; McFarquhar, G.M.; Hayman, M.; Finlon, J.A.; Stechman, D.M. Phase Characterization of Cold Sector Southern Ocean Cloud Tops: Results From SOCRATES. *J. Geophys. Res. Atmos.* **2020**, *125*, 33673. [CrossRef]

40. Rauber, R.M.; Tokay, A. An Explanation for the Existence of Supercooled Water at the Top of Cold Clouds. *J. Atmos. Sci.* **1991**, *48*, 1005–1023. [CrossRef]

41. Khain, A.; Pinsky, M.; Korolev, A. Combined Effect of the Wegener–Bergeron–Findeisen Mechanism and Large Eddies on Microphysics of Mixed-Phase Stratiform Clouds. *J. Atmos. Sci.* **2022**, *79*, 383–407. [CrossRef]

42. Baum, B.A.; Menzel, W.P.; Frey, R.A.; Tobin, D.C.; Holz, R.E.; Ackerman, S.A.; Heidinger, A.K.; Yang, P. MODIS Cloud-Top Property Refinements for Collection 6. *J. Appl. Meteorol. Climatol.* **2012**, *51*, 1145–1163. [CrossRef]

43. Key, J.R.; Intrieri, J.M. Cloud Particle Phase Determination with the AVHRR. *J. Appl. Meteorol.* **2000**, *39*, 1797–1804. [CrossRef]

44. Platnick, S.; Meyer, K.G.; King, M.D.; Wind, G.; Amarasinghe, N.; Marchant, B.; Arnold, G.T.; Zhang, Z.; Hubanks, P.A.; Holz, R.E.; et al. The MODIS Cloud Optical and Microphysical Products: Collection 6 Updates and Examples From Terra and Aqua. *IEEE Trans. Geosci. Remote Sens.* **2017**, *55*, 502–525. [CrossRef]

45. Bessho, K.; Date, K.; Hayashi, M.; Ikeda, A.; Imai, T.; Inoue, H.; Kumagai, Y.; Miyakawa, T.; Murata, H.; Ohno, T.; et al. An Introduction to Himawari-8/9-Japan's New-Generation Geostationary Meteorological Satellites. *J. Meteorol. Soc. Japan. Ser. II* **2016**, *94*, 151–183. [CrossRef]

46. Benas, N.; Finkensieper, S.; Stengel, M.; van Zadelhoff, G.J.; Hanschmann, T.; Hollmann, R.; Meirink, J.F. The MSG-SEVIRI-based cloud property data record CLAAS-2. *Earth Syst. Sci. Data* **2017**, *9*, 415–434. [CrossRef]

47. Pavolonis, M. GOES-R Advanced Baseline Imager (ABI) Algorithm Theoretical Basis Document For Cloud Type and Cloud Phase. 2010. Available online: https://www.star.nesdis.noaa.gov/smcd/spb/aq/AerosolWatch/docs/GOES-R_ABI_AOD_ATBD_V4.2_20180214.pdf (accessed on 12 January 2023).

48. Wang, Z.; Letu, H.; Shang, H.; Zhao, C.; Li, J.; Ma, R. A Supercooled Water Cloud Detection Algorithm Using Himawari-8 Satellite Measurements. *J. Geophys. Res. Atmos.* **2019**, *124*, 2724–2738. [CrossRef]

49. Strandgren, J.; Bugliaro, L.; Sehnke, F.; Schröder, L. Cirrus cloud retrieval with MSG/SEVIRI using artificial neural networks. *Atmos. Meas. Tech.* **2017**, *10*, 3547–3573. [CrossRef]

50. Strandgren, J.; Fricker, J.; Bugliaro, L. Characterisation of the artificial neural network CiPS for cirrus cloud remote sensing with MSG/SEVIRI. *Atmos. Meas. Tech.* **2017**, *10*, 4317–4339. [CrossRef]

51. Baum, B.A.; Spinhirne, J.D. Remote sensing of cloud properties using MODIS airborne simulator imagery during SUCCESS: 3. Cloud Overlap. *J. Geophys. Res. Atmos.* **2000**, *105*, 11793–11804. [CrossRef]

52. Cesana, G.; Chepfer, H. Evaluation of the cloud thermodynamic phase in a climate model using CALIPSO-GOCCP. *J. Geophys. Res. Atmos.* **2013**, *118*, 7922–7937. [CrossRef]

53. Delanoë, J.; Hogan, R.J. Combined CloudSat-CALIPSO-MODIS retrievals of the properties of ice clouds. *J. Geophys. Res.* **2010**, *115*, 12346. [CrossRef]

54. Ceccaldi, M.; Delanoë, J.; Hogan, R.J.; Pounder, N.L.; Protat, A.; Pelon, J. From CloudSat-CALIPSO to EarthCare: Evolution of the DARDAR cloud classification and its comparison to airborne radar-lidar observations. *J. Geophys. Res. Atmos.* **2013**, *118*, 7962–7981. [CrossRef]

55. Delanoë, J.; Protat, A.; Jourdan, O.; Pelon, J.; Papazzoni, M.; Dupuy, R.; Gayet, J.F.; Jouan, C. Comparison of Airborne In Situ, Airborne Radar–Lidar, and Spaceborne Radar–Lidar Retrievals of Polar Ice Cloud Properties Sampled during the POLARCAT Campaign. *J. Atmos. Ocean. Technol.* **2013**, *30*, 57–73. [CrossRef]

56. Huang, Y.; Siems, S.T.; Manton, M.J.; Protat, A.; Delanoë, J. A study on the low-altitude clouds over the Southern Ocean using the DARDAR-MASK. *J. Geophys. Res. Atmos.* **2012**, *117*, 17800. [CrossRef]

57. Huang, Y.; Protat, A.; Siems, S.T.; Manton, M.J. A-Train Observations of Maritime Midlatitude Storm-Track Cloud Systems: Comparing the Southern Ocean against the North Atlantic. *J. Clim.* **2015**, *28*, 1920–1939. [CrossRef]

58. Benedetti, A. *CloudSat AN-ECMWF Ancillary Data Interface Control Document, Technical Document*; CloudSat Data Processing Center: Fort Collins, CO, USA, 2005.

59. Hogan, R.J.; Francis, P.N.; Flentje, H.; Illingworth, A.J.; Quante, M.; Pelon, J. Characteristics of mixed-phase clouds. I: Lidar, radar and aircraft observations from CLARE'98. *Q. J. R. Meteorol. Soc.* **2003**, *129*, 2089–2116. [CrossRef]

60. Westbrook, C.D.; Illingworth, A.J. The formation of ice in a long-lived supercooled layer cloud. *Q. J. R. Meteorol. Soc.* **2013**, *139*, 2209–2221. [CrossRef]

61. Winker, D. *CALIPSO LID_L2_05kmALay-Prov HDF File-Version 3.30*; Atmospheric Science Data Center: Washington, DC, USA, 2013. [CrossRef]

62. Platnick, S. Vertical photon transport in cloud remote sensing problems. *J. Geophys. Res. Atmos.* **2000**, *105*, 22919–22935. [CrossRef]

63. Korolev, A.; Milbrandt, J. How Are Mixed-Phase Clouds Mixed? *Geophys. Res. Lett.* **2022**, *49*, 99578. [CrossRef]

64. Hersbach, H.; Bell, B.; Berrisford, P.; Hirahara, S.; Horányi, A.; Muñoz-Sabater, J.; Nicolas, J.; Peubey, C.; Radu, R.; Schepers, D.; et al. The ERA5 global reanalysis. *Q. J. R. Meteorol. Soc.* **2020**, *146*, 1999–2049. [CrossRef]

65. Verlinden, K.L.; Thompson, D.W.J.; Stephens, G.L. The Three-Dimensional Distribution of Clouds over the Southern Hemisphere High Latitudes. *J. Clim.* **2011**, *24*, 5799–5811. [CrossRef]

66. Bromwich, D.H.; Nicolas, J.P.; Hines, K.M.; Kay, J.E.; Key, E.L.; Lazzara, M.A.; Lubin, D.; McFarquhar, G.M.; Gorodetskaya, I.V.; Grosvenor, D.P.; et al. Tropospheric clouds in Antarctica. *Rev. Geophys.* **2012**, *50*, 363. [CrossRef]

67. Adhikari, L.; Wang, Z.; Deng, M. Seasonal variations of Antarctic clouds observed by CloudSat and CALIPSO satellites. *J. Geophys. Res. Atmos.* **2012**, *117*, 16719. [CrossRef]

68. McFarquhar, G.M. Observations of Clouds, Aerosols, Precipitation, and Surface Radiation over the Southern Ocean: An Overview of CAPRICORN, MARCUS, MICRE, and SOCRATES. *Bull. Am. Meteorol. Soc.* **2021**, *102*, E894–E928. [CrossRef]

69. Schima, J.; McFarquhar, G.; Romatschke, U.; Vivekanandan, J.; D'Alessandro, J.; Haggerty, J.; Wolff, C.; Schaefer, E.; Järvinen, E.; Schnaiter, M. Characterization of Southern Ocean Boundary Layer Clouds Using Airborne Radar, Lidar, and In Situ Cloud Data: Results From SOCRATES. *J. Geophys. Res. Atmos.* **2022**, *127*, e2022JD037277. [CrossRef]

70. Truong, S.C.H.; Huang, Y.; Siems, S.T.; Manton, M.J.; Lang, F. Biases in the thermodynamic structure over the Southern Ocean in ERA5 and their radiative implications. *Int. J. Climatol.* **2022**, *42*, 7685–7702. [CrossRef]

71. Hogan, R.J.; O'Connor, E.J. Facilitating Cloud Radarand Lidar Algorithms: The Cloudnet InstrumentSynergy/Target Categorization Product. 2006. Available online: www.cloud-net.org/data/products/categorize.html (accessed on 20 March 2023).

72. Tan, I.; Storelvmo, T.; Choi, Y.S. Spaceborne lidar observations of the ice-nucleating potential of dust, polluted dust, and smoke aerosols in mixed-phase clouds. *J. Geophys. Res. Atmos.* **2014**, *119*, 6653–6665. [CrossRef]

73. Zhang, D.; Wang, Z.; Kollias, P.; Vogelmann, A.M.; Yang, K.; Luo, T. Ice particle production in mid-level stratiform mixed-phase clouds observed with collocated A-Train measurements. *Atmos. Chem. Phys.* **2018**, *18*, 4317–4327. [CrossRef]

74. Li, J.; Lv, Q.; Zhang, M.; Wang, T.; Kawamoto, K.; Chen, S.; Zhang, B. Effects of atmospheric dynamics and aerosols on the fraction of supercooled water clouds. *Atmos. Chem. Phys.* **2017**, *17*, 1847–1863. [CrossRef]

75. Villanueva, D.; Senf, F.; Tegen, I. Hemispheric and seasonal contrast in cloud thermodynamic phase from A-Train spaceborne instruments. *J. Geophys. Res. Atmos.* **2021**, *126*, e2020JD034322. [CrossRef]

76. Twohy, C.H.; DeMott, P.J.; Russell, L.M.; Toohey, D.W.; Rainwater, B.; Geiss, R.; Sanchez, K.J.; Lewis, S.; Roberts, G.C.; Humphries, R.S.; et al. Cloud-Nucleating Particles Over the Southern Ocean in a Changing Climate. *Earth's Future* **2021**, *9*, 1673. [CrossRef]

77. Durand, Y.; Hallibert, P.; Wilson, M.; Lekouara, M.; Grabarnik, S.; Aminou, D.; Blythe, P.; Napierala, B.; Canaud, J.L.; Pigouche, O.; et al. The Flexible Combined Imager Onboard MTG: From Design to Calibration. *Proc. SPIE* **2015**, *9639*, 963903. [CrossRef]

78. Illingworth, A.J.; Barker, H.W.; Beljaars, A.; Ceccaldi, M.; Chepfer, H.; Clerbaux, N.; Cole, J.; Delanoë, J.; Domenech, C.; Donovan, D.P.; et al. The EarthCARE Satellite: The Next Step Forward in Global Measurements of Clouds, Aerosols, Precipitation, and Radiation. *Bull. Am. Meteorol. Soc.* **2015**, *96*, 1311–1332. [CrossRef]

Chapter 7

P2: Information content of brightness temperature differences

How well can brightness temperature differences of spaceborne imagers help to detect cloud phase? A sensitivity analysis regarding cloud phase and related cloud properties

Johanna Mayer, Bernhard Mayer, Luca Bugliaro, Ralf Meerkötter, Christiane Voigt
Atmospheric Measurement Techniques, 2024

Overview   This study investigates the relationship between IR window BTDs of passive imagers and cloud properties, with particular emphasis on cloud phase. We focus on two BTD from the SEVIRI imager (the BTDs between channels centered at 8.7 and 10.8 μm, BTD(8.7-10.8), and between channels centered at 10.8 and 12.0 μm, BTD(10.8-12.0)), which are typically used for cloud (phase) retrievals. Using RT calculations, we analyse the sensitivity of the BTDs on all radiatively relevant cloud properties, namely cloud phase, τ, R_{eff}, ice crystal habit and CTT, and provide detailed physical explanations. These calculations show how the different cloud parameters contribute to the observed phase dependence of the BTDs. This knowledge helps to make the best use of BTDs in cloud phase retrievals and to understand their potential and limitations.

Author contribution   I reviewed the literature on RT calculations of BTDs. I performed the simulations using the libRadtran software package and analyzed the data with valuable feedback from LB, BM, and RM. I prepared the figures and took the lead in writing the manuscript. All authors provided feedback on the manuscript. All authors contributed to the project through discussions. LB and CV supervised the research and were responsible for the funding.

Note   At the present time, the manuscript has been accepted for publication by AMT, but the typesetting has not yet been completed. Therefore, the version printed here may contain some minor differences to the published version.

How well can brightness temperature differences of spaceborne imagers help to detect cloud phase? A sensitivity analysis regarding cloud phase and related cloud properties

Johanna Mayer[a], Bernhard Mayer[b,a], Luca Bugliaro[a], Ralf Meerkötter[a], and Christiane Voigt[a,c]

[a]Deutsches Zentrum für Luft- und Raumfahrt, Institut für Physik der Atmosphäre, Oberpfaffenhofen, Germany
[b]Ludwig Maximilians Universität, Institut für Meteorologie, Munich, Germany
[c]Johannes Gutenberg-Universität, Mainz, Germany

Correspondence: Johanna Mayer (johanna.mayer@dlr.de)

Abstract. This study investigates the sensitivity of two brightness temperature differences (BTDs) in the infrared (IR) window of the SEVIRI imager to various cloud parameters in order to understand their information content, with a focus on cloud thermodynamic phase. To this end, this study presents radiative transfer calculations, providing an overview of the relative importance of all radiatively relevant cloud parameters, including thermodynamic phase, cloud top temperature (CTT), optical thickness (τ), effective radius (R_{eff}) and ice crystal habit. By disentangling the roles of cloud absorption and scattering, we are able to explain the relationships of the BTDs to the cloud parameters on the one hand by spectral differences in the cloud optical properties. In addition, an effect due to the nonlinear transformation from radiances to brightness temperatures contributes to the specific characteristics of the BTDs and their dependence on τ and CTT. We find that the dependence of the BTDs on phase is more complex than sometimes assumed. Although both BTDs are directly sensitive to phase, this sensitivity is comparatively small in contrast to other cloud parameters. Instead, the primary link between phase and the BTDs lies in their sensitivity to CTT (or more generally the surface-cloud temperature contrast), which is associated with phase. One consequence is that distinguishing high ice clouds from low liquid clouds is straightforward, but distinguishing mid-level ice clouds from mid-level liquid clouds is challenging. These findings help to better understand and improve the working principles of phase retrieval algorithms.

1 Introduction

Passive spaceborne imagers, with their wide field of view and, in the case of geostationary satellites, high temporal resolution, allow global observations of clouds. These passive instruments typically use solar and/or infrared (IR) window channels to retrieve cloud properties. The advantage of pure IR-based retrievals is that they can be applied during both daytime and nighttime (Nasiri and Kahn, 2008; Cho et al., 2009). Such IR retrievals often use brightness temperature differences (BTDs) of IR window channels, to detect clouds or retrieve cloud properties like optical thickness (τ) or effective particle radius (R_{eff}) (e.g., Inoue, 1985; Krebs et al., 2007; Heidinger et al., 2010; Garnier et al., 2012; Kox et al., 2014; Vázquez-Navarro et al., 2015; Strandgren et al., 2017).

Another cloud parameter which is often retrieved using BTDs (either alone or in combination with other measures) is the cloud thermodynamic phase (ice, liquid, mixed) (Ackerman et al., 1990; Strabala et al., 1994; Finkensieper et al., 2016; Key and Intrieri, 2000; Baum et al., 2000, 2012; Hünerbein et al., 2022; Benas et al., 2023; Mayer et al., 2024). Accurate satellite retrievals of cloud phase are important for various reasons. Firstly, the cloud phase plays an important role in cloud-radiation interactions (Komurcu et al., 2014; Choi et al., 2014; Matus and L'Ecuyer, 2017; Ruiz-Donoso et al., 2020; Forster et al., 2021; Cesana et al., 2022). Several studies highlight its impact on climate sensitivity within general circulation models (Gregory and Morris, 1996; Doutriaux-Boucher and Quaas, 2004; Cesana et al., 2012; Tan et al., 2016; Bock et al., 2020). Accurate observations of the cloud phase are thus essential to improve cloud representation in climate models (Cesana et al., 2015; Atkin-

son et al., 2013; Matus and L'Ecuyer, 2017; Bock et al., 2020). Additionally, determining cloud phase is often a prerequisite in the remote sensing retrieval of cloud properties, including τ, R_{eff} and water path (Marchant et al., 2016).

However, determining cloud parameters such as the thermodynamic phase from BTDs is a challenging task. Radiative transfer through clouds and the atmosphere is complex, with many parameters that can in principle influence satellite observations. Although radiative transfer models are capable to correctly account for all of these quantities, the relative importance of these parameters is often not fully understood.

Ackerman et al. (1990) were the first to observe a correlation between BTDs in High-Resolution Interferometer Sounder (HIS) data and the different cloud phases as determined by concurrent lidar data. They proposed a trispectral technique to distinguish between ice, water, and clear sky using the BTDs between channels at about 8 μm and 11 μm (BTD(8.0-11.0)) and between channels at about 11 μm and 12 μm (BTD(11.0-12.0)). Strabala et al. (1994) expanded on their findings, using MODIS airborne simulator data. They considered clouds of varying τ and found that distinguishing between ice and water clouds using these BTDs is difficult for optically thin clouds. Parol et al. (1991) and Dubuisson et al. (2008) studied the sensitivity of BTDs to effective radius R_{eff} and particle shape for cirrus clouds. Parol et al. (1991) found that the BTD(11.0-12.0) for the Advanced Very High Resolution Radiometer AVHRR aboard the NOAA satellites is sensitive to whether cloud particles are spherical or non-spherical. Dubuisson et al. (2008) showed that the impact of different non-spherical ice crystal shapes on BTD(10.6-12.0) and BTD(8.7-10.6) of the Infrared Imaging Radiometer IIR aboard CALIPSO is small compared to their sensitivity to R_{eff}. The effect of R_{eff} on the BTDs was also considered by Baum et al. (2000), who further extended the trispectral method for MODIS phase retrievals by incorporating information about the horizontal variability of the BTDs. Similar to the study of Strabala et al. (1994), the radiative transfer simulations of Baum et al. (2000) primarily focused on low-level water clouds and high cirrus clouds, and did not consider midlevel clouds. To bridge this gap, Nasiri and Kahn (2008) conducted a sensitivity study that considered also midlevel clouds for the MODIS BTD(8.5-11.0). They showed that BTD(8.5-11.0) is sensitive to cloud top height (CTH) and that this leads to limitations in the phase discrimination in the cloud temperature regime where both liquid and ice can exist.

These studies show that many different parameters influence the BTDs: Cloud parameters considered in previous studies include thermodynamic phase, τ, R_{eff}, ice crystal habit, and CTH. As outlined above, most of the studies so far have however each focused on only a small number of these cloud parameters; an overview over the relative importance of all these cloud parameters is still missing. Especially the influence of CTH or cloud top temperature (CTT) on BTDs has not been studied in detail, with exception of Nasiri and Kahn (2008). Besides cloud parameters also the amount of water vapor in the atmosphere (mainly above the clouds) affects BTDs even in the (relatively) transparent spectral window region 8–12 μm. This has been pointed out by several authors (Strabala et al., 1994; Nasiri and Kahn, 2008; Dubuisson et al., 2008), but the relative importance of atmospheric absorption compared to cloud parameters on BTDs has not been studied systematically.

In addition, the origin of the dependence of BTDs on cloud thermodynamic phase, as observed in satellite measurements and radiative transfer results, is not fully understood. Although phase retrievals are usually based on accurate radiative transfer calculations that take into account all radiative effects, it is argued that variations in the refractive indices of ice and water across the infrared window cause the BTDs to be sensitive to cloud phase (Finkensieper et al., 2016; Key and Intrieri, 2000; Baum et al., 2000, 2012). However, besides these effects of the cloud phase, the phase also correlates with other cloud parameters like CTT and R_{eff}, which in turn have large effects on the BTDs as mentioned above. It is not fully understood which cloud parameters dominate the response of the BTDs in given cloud scenarios. Additionally, traditional explanations of the phase dependence of BTDs have often neglected scattering effects, which as we will show can be substantial. Thus, it is not well understood which physical processes are responsible for the observed phase dependence of the BTDs. A full understanding of the satellite channel dependencies is however critical to design optimal cloud (phase) retrievals and to understand their limitations.

To compute BTDs, satellite radiances are first transformed into brightness temperatures (BT). This transformation by means of Planck's radiation law is a nonlinear function. As nonlinear functions can lead to unexpected behaviour, we expect that there are some effects of the nonlinear relationship between satellite radiances and BTs on BTDs. To our knowledge, the effect of this nonlinear relationship has not been analysed before.

We use Radiative Transfer (RT) calculations to study two BTDs of the SEVIRI imager aboard Meteosat Second Generation (Schmetz et al., 2002): The BTDs between the IR window channels centered at 8.7 and 10.8 μm (BTD(8.7-10.8)) and between those centered at 10.8 and 12.0 μm (BTD(10.8-12.0)). These are the BTDs that are mainly used to identify cloud top phase and determine (ice) cloud properties. Figure 1 shows an example scene of SEVIRI as RGB composite and the two BTDs for the same scene. In this study we first investigate the effect of the nonlinear relationship between radiances and BTs on the BTDs. We then use the RT calculations to analyse dependencies and sensitivities of the BTDs with respect to all radiatively important cloud parameters, namely phase, CTT, R_{eff}, ice crystal habit and optical thickness (τ) at 550 nm, disentangling effects of cloud particle scattering and absorption. We also consider the effect of water vapor in the atmosphere on BTDs by comparing the
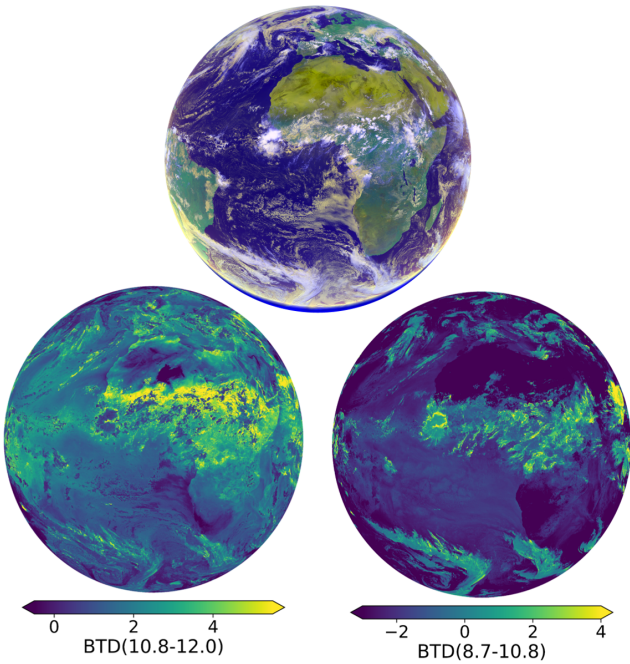
Figure 1. Example scene from SEVIRI on 11.06.2023, 12:00 UTC. Top row: RGB composite with yellow cloud colours indicating higher CTTs; white/blue indicating lower CTTs. Bottom row: the two BTDs for the same example scene.

Figure 2. Causal diagram of cloud parameters that are connected to the cloud phase. Arrows indicate causal links.

computed BTDs with scenarios without molecular absorption. The findings of these RT calculations are then used to analyse the information content of the BTDs with respect to cloud phase. Overall in this study we focus on the effect of cloud parameters; the effects of other parameters like viewing angle, surface emissivity or atmospheric temperature profiles are not studied.

The aim of this study is twofold: First, it provides an analysis of the effects of all cloud parameters on the two BTDs, disentangling the interactions among the different parameters. Second, this study improves the physical understanding of the role of the different radiative processes leading to different BTD values. This helps to understand the information content of the BTDs with respect to the thermodynamic phase in order to better understand and improve the working principles of phase retrieval algorithms that use BTDs and to understand their uncertainties and limitations. We focus on the phase, but our results are also useful to better understand the dependencies of BTDs for other remote sensing applications where they are typically used, such as the retrieval of τ and R_{eff}. Since BTDs also depend on atmospheric and surface parameters whose effects are not studied here, this study does not aim at explaining every phenomenon encountered with BTDs. However, understanding the effects of the cloud parameters helps to disentangle different physical cloud-related processes in all atmospheric or surface conditions.

Finally, we note that besides BTDs, there are other popular methods for retrieving cloud phase and other cloud properties, such as β ratios (Parol et al., 1991; Pavolonis, 2010; Heidinger et al., 2015). While this study is specifically aimed at BTDs, understanding the effects of different cloud properties on the radiative transfer through clouds is also useful to better understand the physics underlying β ratio retrievals.

2 Physical background

To visualize relationships and dependencies between radiation at top of atmosphere (TOA) and cloud properties, the representation in form of a causal diagram is very useful. Figure 2 shows cloud parameters that are related to the cloud phase, connected by arrows indicating causal relationships. Other factors influencing the radiation at TOA (in particular passive satellite observations), like satellite viewing angles, surface temperature or atmospheric properties, are summarized under "other" in the diagram.

In this paper we use the terms "direct" and "indirect" influence of the cloud phase on the TOA radiation. Direct influence means the effect of changing the cloud phase while all other cloud parameters (R_{eff}, CTT, τ, ...) remain the same (represented by the arrow from phase to TOA radiation in Fig. 2). The indirect influence of the cloud phase is represented by all other paths from phase to TOA radiation in Fig. 2. For example, the phase affects τ and R_{eff}, which in turn affect TOA radiation. Information on these two parameters can give an indication about the cloud phase – e.g. clouds with small R_{eff} are typically liquid clouds; clouds with very low τ are typically ice clouds. Ice crystal habit can influence the TOA radiation as well, but is of course only relevant for ice clouds. CTT and CTH are closely related variables that influence radiation through temperature-dependent cloud emissions and by affecting the atmospheric

column above the cloud that can absorb radiation, respectively. CTT is critical for phase determination since for temperatures above 0°C only liquid and below −40°C only ice is physically possible. Between these thresholds, the probability for ice (liquid) clouds increases (decreases) as CTTs get colder (Mayer et al., 2023).

In order to calculate the radiative transfer through a cloud with given cloud (microphysical) parameters, it is necessary to know how much radiation is absorbed, scattered and emitted, i.e. the optical properties of the cloud. The translation from cloud (microphysical) parameters to optical parameters is given by the so-called *single scattering properties*. The single scattering properties are the volume extinction coefficient β_{ext}, the single scattering albedo ω_0 and the scattering phase function p. As an alternative to β_{ext} and ω_0 one can equivalently describe radiative transfer by the absorption coefficient β_{abs} and scattering coefficient β_{sca}, which can be easier to interpret. Definitions and physical interpretations of the single scattering properties can be found in appendix A. The interplay of the single scattering properties, in combination with the cloud water path, determines how much radiation is transmitted through a cloud and, in combination with the cloud temperature, how much radiation is emitted from it. The single scattering properties depend on the wavelength of the radiation and on the cloud parameters R_{eff}, habit and phase. They are shown in Fig. 3 for varying R_{eff} and cloud phase. The variations of the single scattering properties due to habit are mostly small in comparison and therefore not shown. Instead of p we show the asymmetry parameter g, as a simpler measure to characterize the scattering process (see appendix A). The spectral variations of β_{abs}, β_{sca} and g translate into different BTD values for different cloud parameters. This will be investigated in detail in the next sections using radiative transfer calculations.

3   Radiative transfer calculations

Simulations for the three IR window channels of the SEVIRI instrument centered at 8.7, 10.8 and 12.0 μm were performed for a variety of water and ice clouds using the sophisticated radiative transfer package libRadtran (Mayer and Kylling, 2005; Emde et al., 2016; Gasteiger et al., 2014). LibRadtran represents water and ice clouds in detail and realistically. It has been validated against observations and in several model intercomparison campaigns and has been extensively used to develop or validate remote sensing retrievals (e.g. Mayer et al., 1997; Meerkötter and Bugliaro, 2009; Bugliaro et al., 2011; Stap et al., 2016; Piontek et al., 2021b; Bugliaro et al., 2022). The optical properties of water droplets are calculated using Mie theory. For ice crystals, we use the Baum et al. (2011) parameterization of optical properties for three different habits (general habit mixture, columns, rough aggregates). Simulations of TOA radiances for the SEVIRI IR window channels are made using the one-dimensional radiative

transfer solver DISORT (Discrete Ordinate Radiative Transfer) 2.0 by Stamnes et al. (2000) and Buras et al. (2011) with parameterized SEVIRI channel response functions as described by Gasteiger et al. (2014). The complete permutation of τ, R_{eff}, CTT/CTH, crystal habits and phase was simulated and is listed in table 1. The CTT is set to the atmospheric temperature at the altitude of the CTH and represents the temperature at cloud top. For simplicity we keep the cloud geometric thickness constant at 1 km; the impact of variable geometric thickness is discussed in Sect. 6.3. We only consider single-phase (ice or water) and single layered clouds. True mixed-phase clouds and multilayered clouds are not considered.

The simulation setup in terms of atmosphere, satellite/solar geometry and surface type is summarized as well in table 1. In this study, we focus on the influence of cloud parameters. Therefore, we choose a relatively simple setup for the atmospheric parameters, surface parameters and satellite geometry, which is kept constant for all simulations. We use the US standard atmosphere (Anderson et al., 1986) and a surface temperature of 290 K. We place the simulations over the ocean where the surface emissivity is nearly constant for the three IR window channels and set it to 1. The satellite zenith angle (SATZ) is kept constant at 0° (nadir view).

To disentangle cloud effects from effects of the atmosphere, we also compute simulations with molecular absorption switched off. LibRadtran further has the possibility to simulate the IR window channels for cloud layers for which scattering is switched off, meaning that the scattering coefficient in the simulation is set to zero while the absorption coefficient remains constant. This allows to disentangle effects of scattering and absorption in a cloud.

4   Effects of Planck's law: the BTD Nonlinearity Shift

Before analysing the results of the RT calculations, we examine the effects of the nonlinear relationship between radiances and BTs on the BTDs. We call these effects *BTD Nonlinearity Shift*. The BTD Nonlinearity Shift is purely due to the nonlinearity in the computation of BTDs and not due to wavelength dependent optical properties of the cloud, which we will focus on in the next sections of this study. BTDs are calculated from measured radiances using Planck's radiation law, which describes the spectral radiance B_λ of a black body emitting radiation at temperature T

$$B_\lambda(T) = \frac{2hc^2}{\lambda^5}(e^{\frac{hc}{\lambda k_B T}} - 1)^{-1}, \tag{1}$$

where h is the Planck constant, c is the speed of light in vacuum and k_B is the Boltzmann constant. The inverse Planck function accordingly maps spectral radiance R_λ to the corresponding temperature

$$T_\lambda(R_\lambda) = \frac{hc}{k_B \lambda} \frac{1}{\ln(\frac{2hc^2}{\lambda^5 R_\lambda} + 1)} \tag{2}$$
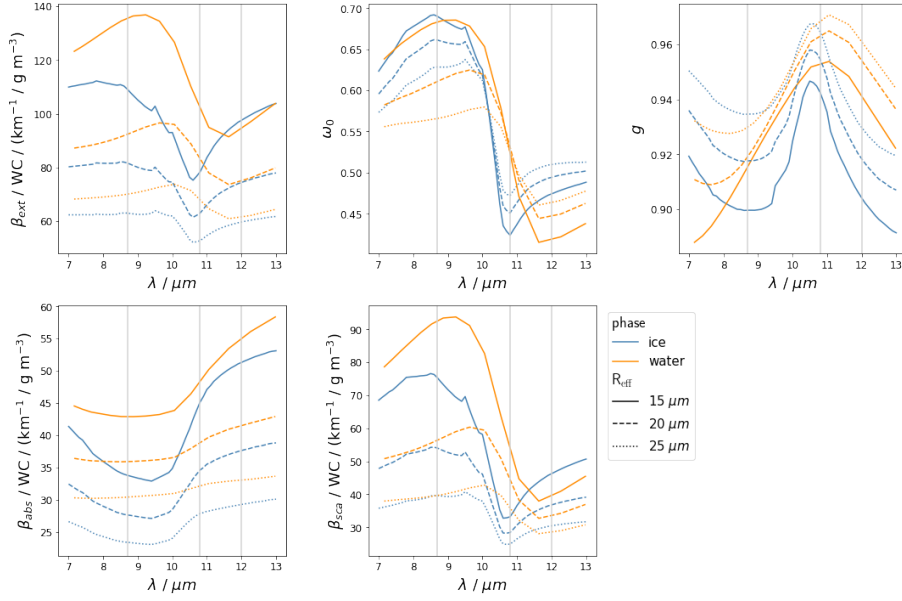
Figure 3. Single scattering properties extinction coefficient β_{ext}, single scattering albedo ω_0 and asymmetry parameter g, as well as absorption coefficient β_{abs} and scattering coefficient β_{sca} (computed from β_{ext} and ω_0) as functions of wavelength for varying cloud phase and effective radius R_{eff}. β_{ext}, β_{abs} and β_{sca} are scaled by the cloud water content WC. Parameterisations for ice according to Baum et al. (2011), for liquid droplets according to Mie theory. For ice clouds, the "general habit mix" was used as ice crystal habit. Vertical grey lines indicate the centre wavelengths of the three IR window channels.

and is used to compute BTs from measured radiances in remote sensing.

The simplest version of the BTD Nonlinearity Shift can be explained using the Schwarzschild equation for radiative transfer. The Schwarzschild equation is a simple version of radiative transfer assuming no cloud scattering and no atmosphere. Its solution for one cloud layer is

$$R_{\text{TOA},\lambda}^{\text{S}}(\tau_\lambda) = e^{-\tau_\lambda} B_\lambda(T_s) + (1 - e^{-\tau_\lambda}) B_\lambda(\text{CTT}), \quad (3)$$

where $R_{\text{TOA},\lambda}^{\text{S}}$ is the radiance at TOA at a given wavelength λ with the superscript S for Schwarzschild, and τ_λ is the optical thickness of the cloud for this wavelength. The first term in the equation is the transmitted radiance coming from the surface with the surface temperature T_s; the second term is the radiation emitted by the cloud, assuming that the cloud layer has an approximately constant temperature $T \approx \text{CTT}$. To demonstrate the BTD Nonlinearity Shift we set τ_λ equal for all wavelengths, $\tau_\lambda = \tau$. Figure 4(a) shows the Planck function of the surface temperature, $B_\lambda(T_s)$, and the cloud temperature, $B_\lambda(\text{CTT})$, in grey for exemplary values of $T_s = 290\,K$ and $\text{CTT} = 200\,K$. According to the Schwarzschild equation (Eq. 3), $R_{\text{TOA},\lambda}^{\text{S}}$ lies between these two curves, approaching $B_\lambda(T_s)$ for $\tau \to 0$ and $B_\lambda(\text{CTT})$ for $\tau \to \infty$. Figure 4(a) illustrates $R_{\text{TOA},\lambda}^{\text{S}}$ for $\tau = 0.5$ (black line). From $R_{\text{TOA},\lambda}^{\text{S}}$ we can now compute the TOA BTs at the three IR wavelengths of interest as $\text{BT}_\lambda^{\text{S}} = T_\lambda(R_{\text{TOA},\lambda}^{\text{S}}(\tau))$, where the superscript S again stands for Schwarzschild. The corresponding Planck curves, i.e.

$B_\lambda(\text{BT}_\lambda^{\text{S}})$ for $\lambda \in \{8.7, 10.8, 12.0\}$, are shown in Fig. 4(a) as dashed colored lines. Recall that in this example calculation we have set a constant $\tau = 0.5$, i.e. the same optical properties (transmittance and emissivity) for all wavelengths (see Eq. 3). Naively, one might expect a BTD = 0 (i.e. equal BTs) in this scenario. However, it is evident from the figure that the three BTs are different, with $\text{BT}_{8.7}^{\text{S}} > \text{BT}_{10.8}^{\text{S}} > \text{BT}_{12.0}^{\text{S}}$. Since these differences between the three BTs are not due to optical cloud properties, they must be caused by the nonlinear transformation from radiances to BTs. Hence, the BTD Nonlinearity Shift induces a BTD in situations where, naively, no BTD would be expected.

To get an overview of the BTD Nonlinearity Shift, we compute BTD^{S} for both wavelength combinations (BTD(8.7-10.8) and BTD(10.8-12.0)) from the results of the Schwarzschild equation (Eq. 3) for varying τ and CTT as

$$\text{BTD}^{\text{S}}(\lambda_0 - \lambda_1) = T_{\lambda_0}(R_{\text{TOA},\lambda_0}^{\text{S}}(\tau)) - T_{\lambda_1}(R_{\text{TOA},\lambda_1}^{\text{S}}(\tau)). \quad (4)$$

Fig. 4(b) shows the computed BTD^{S} as a function of τ for different CTTs and a fixed $T_s = 290\,K$. These BTD^{S} resemble an arc shape (similar to the well-known BTD arc from Inoue (1985)) and show higher values for lower CTTs, even though the amplitudes of their curves are smaller than for the full RT model, as we will see later. Thus, even if τ_λ is the same for all three wavelengths, $\tau_\lambda = \tau$, the nonlinearity of the inverse Planck function induces positive BTD^{S} values and a dependence on the CTT. More generally, this dependence is mainly
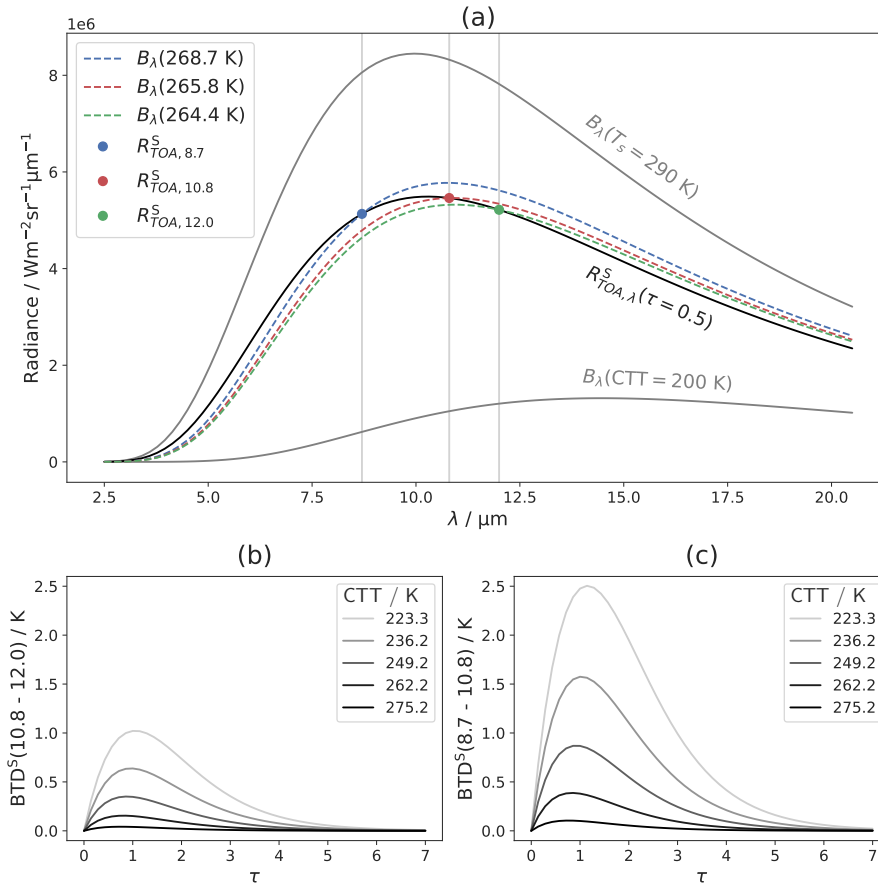
Figure 4. (a) Radiance at top of atmosphere ($R^{\mathrm{S}}_{\mathrm{TOA},\lambda}$) computed with the Schwarzschild equation (black line). Vertical grey lines indicate the centre wavelengths of the three IR window channels with blue, red and green dots at $R^{\mathrm{S}}_{\mathrm{TOA},8.7}$, $R^{\mathrm{S}}_{\mathrm{TOA},10.8}$ and $R^{\mathrm{S}}_{\mathrm{TOA},12.0}$ respectively. The blue, red and green dashed lines correspond to the Planck curves of these three TOA radiances, i.e. $B_\lambda(T_\lambda(R^{\mathrm{S}}_{\mathrm{TOA},\lambda}))$ for each wavelength, where B_λ is the Planck function and T_λ the inverse Planck function. The grey solid curves show the Planck curves of the surface temperature T_s and the CTT as reference. (b) Brightness temperature differences computed with the Schwarzschild equation, BTD$^{\mathrm{S}}$, as functions of τ for different CTTs and a fixed T_s=290 K.

a sensitivity to the thermal contrast $\Delta T := T_s -$ CTT; however, for a fixed T_s, as shown in the examples here, it reduces to a dependence on CTT. Notice that for these examples the BTD induced this way reaches up to 2.5 K and thus cannot be neglected.

In the next section we will discuss the effects of cloud properties on the BTDs due to the wavelength-dependent optical properties in the full RT model (described in Sect. 3). The BTD Nonlinearity Shift adds to these effects and is therefore co-responsible for the (positive) BTD values and the CTT dependence of the BTDs which we will discuss in more detail in Sect. 5.6. In appendix B we further analyse the BTD Nonlinearity Shift for the Schwarzschild model as well as the full RT model and disentangle this nonlinearity effect from the physical effects of wavelength-dependent optical properties on the BTDs in RT calculations.

Summarizing this section:

– There is an effect (BTD Nonlinearity Shift) coming from the nonlinearity of the inverse Planck function that induces positive BTD(8.7-10.8) and BTD(10.8-12.0) values and a dependence on the CTT (or more generally the surface-cloud-temperature contrast ΔT) in a simple RT model (Schwarzschild equation) even if cloud optical properties (transmittance and emissivity) are the same for all wavelengths.

5   Effects of cloud properties on BTDs

In this section we analyse the results of the RT calculations described in Sect. 3. We start with the effects of scattering on the BTs of the three window channels separately. We then combine the BTs to BTDs and analyse them as functions of τ, phase, R_{eff}, ice crystal habit and CTT, focusing on the physical relationships between these cloud prop-

Table 1. Setup and cloud Properties for libRadtran radiative transfer calculations (SATZ = satellite zenith angle, SKT = skin temperature)

cloud properties	
phase	liquid, ice
R_{eff} (liquid clouds)	5, 10, 15, 20 μm
R_{eff} (ice clouds)	20, 30, 40, 50 μm
τ	0, 0.1, 1, 2, 3, 5, 7, 10, 15, 30
ice habit	general habit mix (ghm), rough aggregates, solid columns
optical properties	for ice after Baum et al. (2011) for liquid droplets Mie
CTH (liquid clouds)	1, 2, 4, 6, 8 km
CTT* (liquid clouds)	281.7, 275.2, 262.2, 249.2, 236.2 K
CTH (ice clouds)	4, 6, 8, 10, 12 km
CTT* (ice clouds)	262.2, 249.2, 236.2, 223.3, 216.7 K
geometric thickness	1 km
cloud particle scattering	on / off

* corresponds to CTH

setup of atmosphere, geometry and surface	
atmosphere	US-standard (total column water vapor: 14.3 kg/m2)
molecular absorption	on / off
SATZ	0°
SKT	290 K
surface type	ocean

erties and the BTDs. In order to disentangle the effects of the different cloud parameters, we always vary only one or two parameters and keep the remaining cloud parameters at fixed "default" values, namely CTH=6 km (corresponding to CTT=249.2 K), R_{eff}=20 μm for both cloud phases and the general habit mix as ice crystal habit.

The following conventions are used throughout this section: blue colours indicate the ice phase; orange/red colours indicate the liquid phase. Solid lines represent a 'normal' atmosphere with molecular absorption; dashed lines mean that molecular absorption is switched off.

5.1 Effects of scattering on brightness temperatures

Scattering in the infrared window only needs to be considered for cloud particles; Rayleigh scattering by atmospheric molecules is negligible in the infrared window. The effects of cloud particle scattering on the BTs is shown in Fig. 5. It shows the difference between the BTs for a cloud with scattering and a cloud with scattering switched off for the three window channels, i.e. $BT_\lambda - BT_\lambda^{no\,sca}$ for each channel with centre wavelength λ. This is shown as a function of τ (at 550 nm) for an ice and a water cloud with all other

cloud parameters held constant. Switching off scattering in a cloud changes the optical thickness of that cloud, since only absorption now contributes to the extinction of radiation. However, to be able to compare scenarios with and without scattering for fixed cloud microphysics (same water content, R_{eff}, ...), the τ parameter used for this figure is still the "original" optical thickness (with absorption and scattering).

All curves in Fig. 5 are negative everywhere, meaning that scattering is a radiation sink for all three wavelengths: Part of the radiation coming from below the cloud is scattered back downwards. However, the amount of radiation lost to scattering is different for the different wavelengths. Scattering has a larger effect on the radiation at 8.7 μm than at 10.8 or 12.0 μm, as expected from β_{sca} which is higher at 8.7 μm than at the other two wavelengths (see Fig. 3). For 8.7 and 12.0 μm, scattering by ice clouds is more significant than by water clouds; for 10.8 μm, scattering leads to a similar radiation loss for both water and ice clouds. Interestingly, scattering effects are visible even when the cloud is opaque (black, τ=30). An explanation is that the observed radiance at TOA does not just come from the top of the cloud. Rather, it comes from the upper layers within the cloud (with decreasing intensity as one moves deeper into the cloud). Radiation emitted anywhere below the cloud top is still subject to scattering on its way to the cloud top.

Using different CTT or Reff values in the calculations (for both the liquid and the ice cloud) mainly changes the magnitude of the negative peaks, but does not change the qualitative results shown in Fig. 5. Similarly, changing the ice crystal habit does not change the qualitative results and has only a small effect on the values shown.

5.2 Effects of optical thickness on BTDs

We begin the study of BTDs by analysing the physical factors that drive the BTDs' behavior in relation to τ. Fig. 6 shows BTD(8.7-10.8) and BTD(10.8-12.0) as functions of τ for both an ice and a liquid cloud and with molecular absorption switched on and off.

As τ approaches zero in all panels of Fig. 6, i.e. no cloud is simulated, the BTD curves with atmospheric absorption switched on (solid lines) do not go to zero. They remain above zero for BTD(10.8-12.0) and below zero for BTD(8.7-10.8). This is the effect of atmospheric absorption, since radiation at 8.7μm and 12.0 μm is more strongly absorbed by water vapor than at 10.8μm: Compare the curves with (solid lines) and without (dashed lines) molecular absorption for τ approaching zero. As τ increases, the curved shape of the BTD functions is (largely) due to the interplay of transmission and emission from the cloud. As discussed in Sect. 4 the BTD Nonlinearity Shift adds to these effects. Where transmission is dominant (small τ), the spectral differences in extinction (see Fig. 3) lead to an increase in BTD values. Where emission is dominant (large τ), BTD values are small, giv-
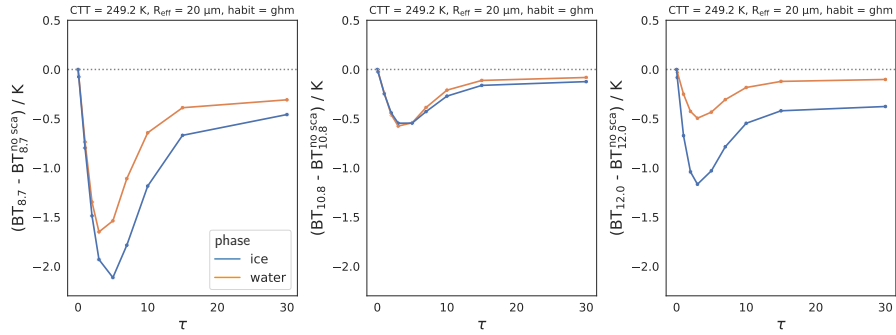
Figure 5. Scattering effects on brightness temperatures (BT): Difference between the BTs for a cloud with scattering and a cloud with scattering switched off for all three IR window channels, i.e. $BT_\lambda - BT_\lambda^{no\,sca}$ for each channel with centre wavelength $\lambda \in \{8.7\mu m, 10.8\mu m, 12.0\mu m\}$, for liquid and ice clouds as functions of optical thickness τ.
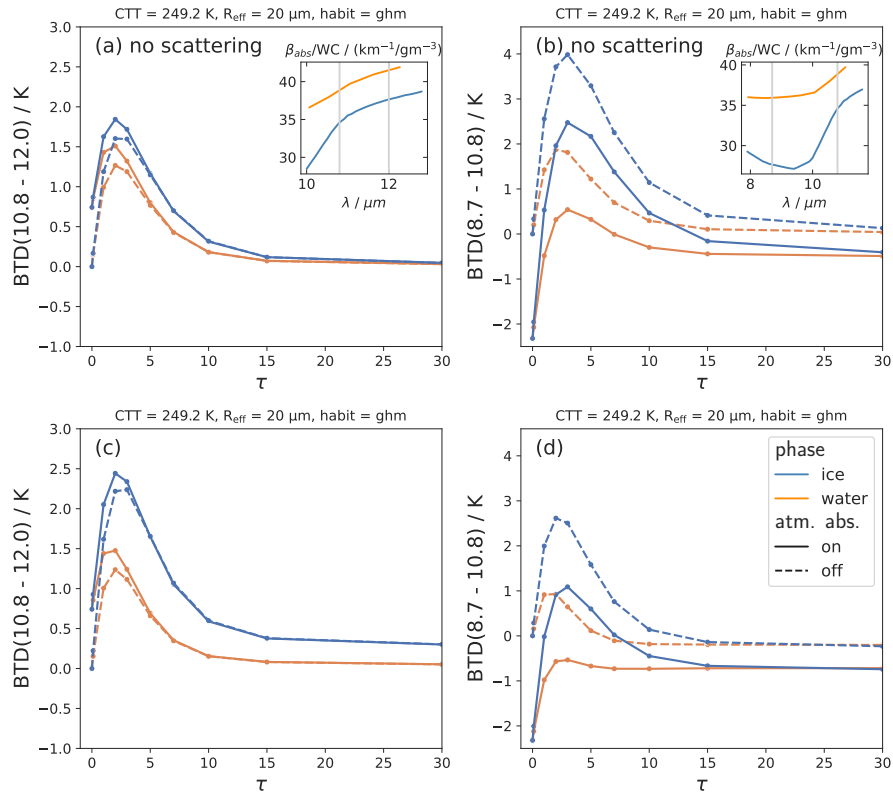
Figure 6. Brightness temperature differences BTD(10.8-12.0) and BTD(8.7-10.8) as functions of τ for cloud particle scattering (a,b) switched off and (c,d) switched on for liquid and ice clouds. Solid lines indicate a "normal" absorbing atmosphere, dashed lines indicate that molecular absorption is switched off.

ing rise to the curved shape of the BTD functions (the well-known BTD arc from Inoue (1985)). The BTD curves become constant at about $\tau \gtrsim 15$.

To disentangle the effects of cloud absorption and scatter-⁵ ing, Fig. 6(a,b) show the BTDs with cloud particle scattering switched off. As explained in the previous section, the τ parameter used for these figures is still the "original" optical thickness (with absorption and scattering). In Fig. 6(c,d) scattering is switched on. BTD(10.8-12.0) in Fig. 6(a) is pos-¹⁰ itive, meaning that radiation at a wavelength of $12.0\,\mu$m is more strongly absorbed than at $10.8\,\mu$m and more radiation is transmitted through the cloud at $10.8\,\mu$m. This matches the absorption coefficient, which is higher at 12.0 than $10.8\,\mu$m (shown as an inset for the given R_{eff} for convenience, as well ¹⁵ as in Fig. 3).

Analogously, Fig. 6(b) shows that radiation at $10.8\,\mu$m is more strongly absorbed by the cloud than at $8.7\,\mu$m, especially for ice clouds. The stronger absorption at 10.8 compared to $8.7\,\mu$m can again be seen in the absorption co-²⁰ efficient (shown in inset and in Fig. 3). The spectral differences in the absorption coefficient are stronger between 8.7 and 10.8 than between 10.8 and $12.0\,\mu$m, leading to higher values of BTD(8.7-10.8) than BTD(10.8-12.0) (compare Fig. 6(a) to Fig. 6(b)). For BTD(8.7-10.8), note that ²⁵ molecular absorption plays an important role even for optically thick clouds, decreasing BTD(8.7-10.8) everywhere by at least $0.5\,$K, since radiation at $8.7\,\mu$m is more strongly absorbed by atmospheric molecules (water vapor) than at $10.8\,\mu$m.

³⁰ Switching on particle scattering (Fig. 6(c)), the BTD(10.8-12.0) values increase for ice clouds and stay about the same for liquid clouds. This will be further discussed in the next section (Sect. 5.3). For opaque clouds (large τ), the spectral differences in scattering effects lead to non-vanishing ³⁵ BTD(10.8-12.0) values for ice clouds (BTD(10.8-12.0) $\approx$ $0.3\,$K).

For BTD(8.7-10.8), switching on scattering leads to a decrease, since scattering has a stronger effect at 8.7 compared to $10.8\,\mu$m (see Fig. 5). However, the increase in BTD(8.7-⁴⁰ 10.8) due to cloud absorption (Fig. 6(a)) outweighs this opposing scattering effect and the BTD(8.7-10.8) curve is still positive (when atmospheric absorption is not considered). Note the differences with BTD(10.8-12.0), where cloud absorption and scattering are concurrent effects, both leading to ⁴⁵ an increase in BTD(10.8-12.0).

The following list summarizes the most important results:

– Stronger absorption and scattering at 12.0 compared to $10.8\,\mu$m lead to positive values of BTD(10.8-12.0).

– Stronger absorption at 10.8 compared to $8.7\,\mu$m lead to ⁵⁰ positive values of BTD(8.7-10.8); scattering has a mediating effect, reducing BTD(8.7-10.8) values.

– These trends are consistent with expectations based on absorption and scattering coefficients.

5.3 Effects of cloud phase on BTDs

We now discuss the direct dependence of BTD(10.8-12.0) ⁵⁵ and BTD(8.7-10.8) on phase shown in Fig. 6. Direct dependence means that all other parameters such as R_{eff} or CTT are held constant. BTD(10.8-12.0) in Fig. 6(c) has higher values for the ice phase than the liquid phase for all τ. Comparing the curves with and without scattering (Fig. 6(a) and ⁶⁰ Fig. 6(c)), we see that this difference between liquid and ice is mainly due to the different scattering properties of cloud particles at the two wavelengths: For liquid clouds the scattering has a similar effect at 10.8 and $12.0\,\mu$m, while for ice clouds radiation at $12.0\,\mu$m is scattered more than at $10.8\,\mu$m ⁶⁵ (see Fig. 5), leading to higher BTD(10.8-12.0) values for ice clouds.

BTD(8.7-10.8) directly depends on phase only for small to moderate τ ($\tau \lesssim 15$), with higher values for ice than for liquid. This difference is due to absorption properties: The spec-⁷⁰ tral difference in absorption between the two wavelengths is larger for ice clouds (see β_{abs} in the inset of Fig. 6(b) or Fig. 3). Switching on cloud scattering reduces the differences between ice and liquid clouds in BTD(8.7-10.8) (compare Fig. 6(b) with Fig. 6(d)). The reason for this can be seen ⁷⁵ in Fig. 5: The effect of scattering at $8.7\,\mu$m is stronger for ice than for water, while it is similar for ice and for water at $10.8\,\mu$m. This leads to a stronger decrease in BTD(8.7-10.8) values for ice than for water clouds when scattering is switched on. However, overall the effect of absorption (lead-⁸⁰ ing to larger BTD(8.7-10.8) values for ice than for water) outweighs this contrasting scattering effect.

In summary, the most important findings are:

– There is a direct phase dependence of the BTDs due to the dependence of the single scattering properties on ⁸⁵ cloud phase.

– This effect is of the order of 0.5–1.5 K for BTD(10.8-12.0) and 0–2 K for BTD(8.7-10.8), depending on τ, in all modeled scenarios.

– For BTD(10.8-12.0), mainly scattering is responsible ⁹⁰ for the direct dependence on cloud phase.

– For BTD(8.7-10.8), absorption is responsible for the direct dependence on cloud phase, scattering reduces the differences between the phases.

5.4 Effects of effective radius on BTDs

⁹⁵

Fig. 7 shows BTD(10.8-12.0) and BTD(8.7-10.8) as a function of τ and R_{eff} for ice clouds (top row) and liquid clouds (bottom row) for the full RT model (i.e. scattering switched on). Note that the range of R_{eff} values for ice and liquid clouds are different in order to simulate realistic cloud con-¹⁰⁰ ditions. For low τ ($\tau \lesssim 10$), smaller R_{eff} lead to larger values for both BTDs. The effect becomes stronger in a nonlinear
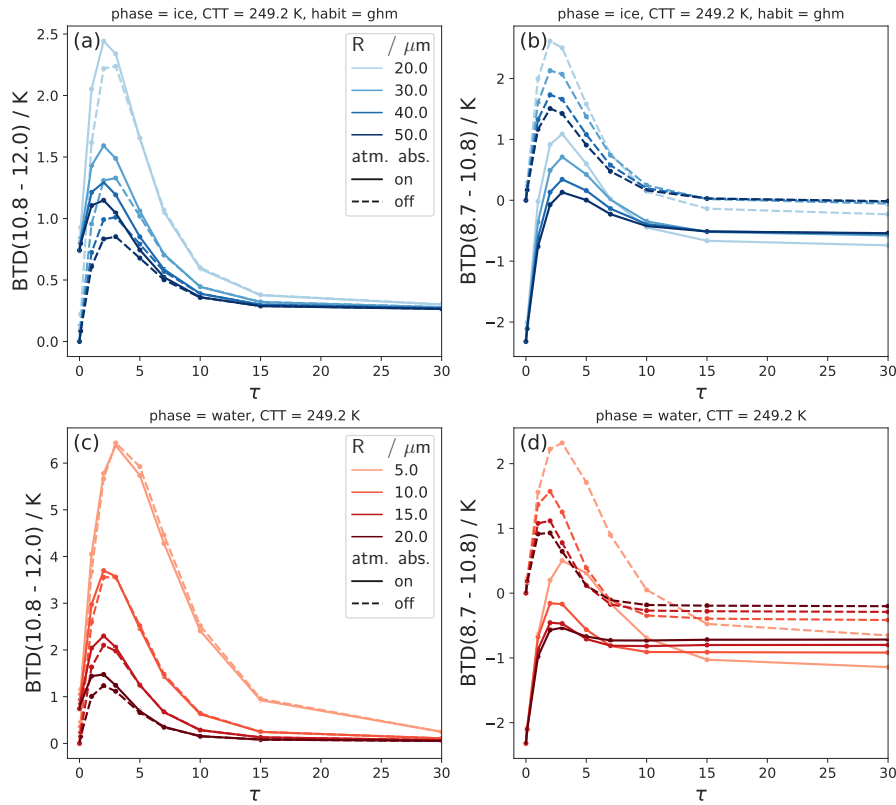
Figure 7. Effects of varying R_{eff} on BTD(10.8-12.0) and BTD(8.7-10.8) as functions of τ for ice clouds (top row) and liquid clouds (bottom row). Solid lines indicate a "normal" absorbing atmosphere, dashed lines indicate that molecular absorption is switched off.

way as the R_{eff} becomes smaller. This confirms previous results, for instance Dubuisson et al. (2008), who also found a strong and nonlinear dependence of BTDs on R_{eff}.

The effect of R_{eff} on BTD(10.8-12.0) results physically from the dependence of particle absorption on R_{eff}: The spectral differences of the absorption coefficient are larger for smaller R_{eff} (see Fig. 3), resulting in lower transmission at 12.0 than at 10.8 μm, and thus higher BTD(10.8-12.0) values for smaller R_{eff} values. The effect of scattering on BTD(10.8-12.0) is similar for varying R_{eff} and comparatively small (increases (decreases) the BTD by $\lesssim 0.5$ K for ice (water) clouds). For the interested reader, Fig. C1 in appendix C shows the sensitivity of both BTDs with R_{eff} broken down into effects of absorption and scattering.

For BTD(8.7-10.8), the R_{eff} dependence for small τ is, like the phase dependence, the result of two opposite effects: For smaller R_{eff}, absorption increases for 10.8 compared to 8.7 μm, leading to an increase in BTD(8.7-10.8). On the other hand scattering increases more for 8.7 than for 10.8 μm, leading to a decrease in BTD(8.7-10.8). However, the effect due to absorption is stronger and therefore the BTD(8.7-10.8) increases with decreasing R_{eff}. Unlike BTD(10.8-12.0), BTD(8.7-10.8) is still dependent on R_{eff} at large τ: here BTD(8.7-10.8) increases with increasing R_{eff},

contrary to the R_{eff} trend at small τ. The smaller the R_{eff}, the more important this effect becomes.

Summarizing the most important insights:

– The BTDs depend strongly and nonlinearly on R_{eff}.

– Physically this dependence is due to larger spectral differences in the absorption coefficient for smaller R_{eff}.

– For BTD(8.7-10.8), stronger scattering for smaller R_{eff} mediates the absorption effects.

5.5 Effects of ice crystal habit on BTDs

Figure 8 shows the sensitivity of the BTDs on ice crystal habits (in ice clouds). For both BTDs, rough aggregates lead to the smallest BTD values. For BTD(8.7-10.8), ice crystals with the general habit mix (ghm) lead to the largest BTD values, while for BTD(10.8-12.0), solid columns lead to slightly higher values. However, the sensitivity on ice crystal habits is relatively small ($\lesssim 0.5$ K) compared to other cloud properties. This confirms Dubuisson et al. (2008), who showed that the habit has a small effect on BTDs compared to the effect of R_{eff} also for other ice crystal shapes than the ones considered here. The relative importance of different cloud parameters will be further discussed in Sect. 6.
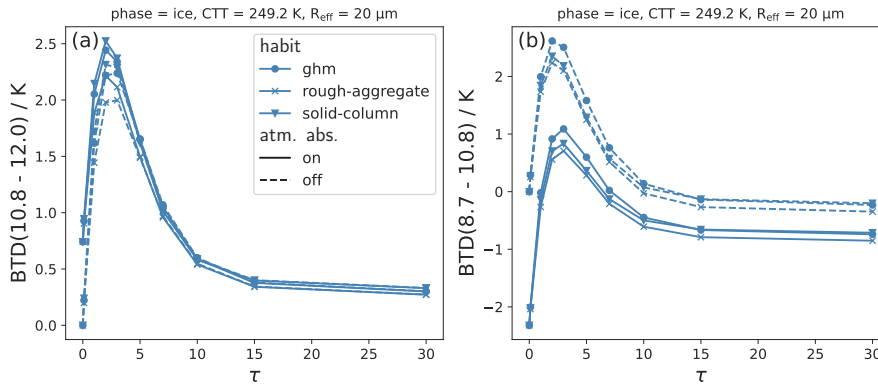
Figure 8. Effects of varying ice crystal habit on (a) BTD(10.8-12.0) and (b) BTD(8.7-10.8) as functions of τ for ice clouds. Solid lines indicate a "normal" absorbing atmosphere, dashed lines indicate that molecular absorption is switched off.

5.6 Effects of cloud top temperature on BTDs

Figure 9 shows the sensitivity of both BTDs to CTT – and thus to CTH – for ice (top row) and liquid (bottom row) clouds. The results with molecular absorption switched off (dashed lines) show how much of this sensitivity is due to the atmosphere. Note that the CTT ranges for ice and liquid clouds are different in order to simulate realistic cloud conditions.

For BTD(8.7-10.8), molecular absorption is relevant for all τ values: Clouds with high CTT, i.e. low CTH, have more absorbing atmosphere above cloud top, leading to more radiation absorbed at 8.7 compared to $10.8\,\mu$m. For BTD(10.8 - 12.0), this effect is less pronounced and molecular absorption is only relevant when there is a long path through the atmosphere (i.e. low CTH or small τ).

At low τ ($\lesssim$ 10), both BTD(8.7-10.8) and BTD(10.8-12.0) show a strong dependence on CTT that is not due to molecular absorption. Since the single scattering properties are not CTT dependent (see Sect. 2), this CTT effect on the BTDs is also not (directly) due to spectral differences in the single scattering properties - in contrast to the effects of the other cloud parameters discussed above. Instead, there are more subtle reasons for this effect: In Sect. 4 we found that the BTD Nonlinearity shift leads to a CTT dependence of the BTDs with higher BTD values for lower CTTs even when optical cloud properties are the same for all wavelengths. This explains part of the CTT dependence in Fig. 9. In appendix B we further discuss the BTD Nonlinearity Shift, allowing also wavelength dependent optical properties. It can be shown that for the Schwarzschild BTD$^{\mathrm{S}}$, spectral differences in the extinction coefficient are scaled by the difference between the surface and the cloud top radiance, $B_\lambda(T_s) - B_\lambda(\mathrm{CTT})$ (see appendix B for a detailed discussion). Hence, the effects of spectral differences in optical properties on BTD$^{\mathrm{S}}$ are amplified by larger ΔT, i.e. differences between T_s and the CTT. This is the main reason (be-

sides the BTD Nonlinearity Shift) for the CTT dependence of the BTDs. Colder CTTs (or rather larger ΔT) thus increase both the BTD Nonlinearity Shift and the effects of spectral differences in optical properties.

The following list summarizes the CTT / CTH effects on the BTDs:

– For BTD(8.7-10.8), CTH has a large effect, due to molecular absorption mainly above cloud top.

– Both BTDs show a strong dependence on CTT (or more generally on ΔT) with higher values for lower CTTs (larger ΔT).

– The BTD Nonlinearity Shift is co-responsible for the positive BTD values and the CTT (or ΔT) dependence of the BTDs, adding to the effects stemming from spectral differences in absorption and scattering properties.

6 Implications for phase retrievals

In the last section we analysed the effects of cloud properties on the BTDs individually, by varying only one cloud property at a time (besides τ). In this section we combine the phase related cloud parameters τ, R$_{\mathrm{eff}}$, ice habit, CTT and thermodynamic phase for a sensitivity analysis of the BTDs. From this analysis we determine typical BTD ranges for ice and liquid clouds and understand which cloud parameters are responsible for the phase information contained in the BTDs. We analyse for which cloud scenarios we can distinguish between liquid clouds and ice clouds, and when they overlap, allowing us to derive implications for phase retrievals. First, in Sect. 6.1, we perform sensitivity analyses for each BTD individually. Next, in Sect. 6.2, we study the sensitivities and phase information content of the two BTDs combined.
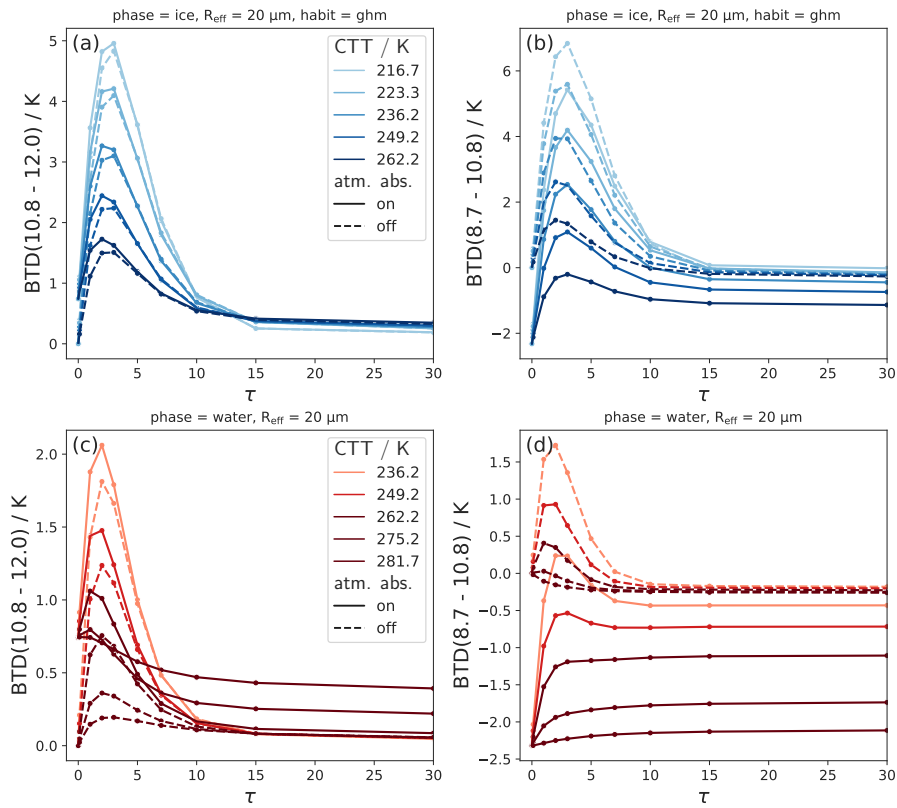
Figure 9. Effects of varying cloud top temperature (CTT) on BTD(10.8-12.0) and BTD(8.7-10.8) as a function of τ for ice clouds (top row) and liquid clouds (bottom row). Solid lines indicate a "normal" absorbing atmosphere, dashed lines indicate that molecular absorption is switched off.
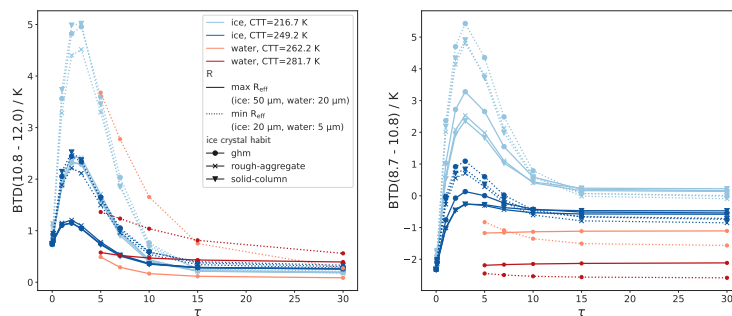
Figure 10. Sensitivity analysis for each BTD varying the phase related cloud parameters τ, R_{eff}, habit, CTT and thermodynamic phase: BTD(10.8-12.0) and BTD(8.7-10.8) for typical upper and lower boundaries of CTT and R_{eff} for ice (blue colors) and liquid (orange/ red colors) clouds. For ice clouds, different habits are shown as different markers. The figures show typical BTD ranges for ice and liquid clouds.

6.1 Sensitivity analysis for each BTD

To study when BTDs can typically distinguish between liquid and ice clouds, Fig. 10 gives an overview of the sensitivities of the BTDs for "typical" cloud scenarios, as defined in the following. The figure shows the BTDs for upper and lower boundaries of CTT ($217 - 249$ K for ice, $262 - 282$ K for liquid water) and R_{eff} ($20 - 50\,\mu$m for ice, $5 - 20\,\mu$m for liquid water). These ranges are representative for mid-latitude clouds (between 30 and $50°$N or S) and are chosen as follows: The CTT boundaries are derived from the active remote sensing product DARDAR (liDAR/raDAR, Delanoë and Hogan (2010)) - specifically, values close to the 15th and 85th percentiles of ice and liquid CTTs observed for mid-latitude clouds, covering about 70% of CTTs (see Mayer et al. (2023) for detailed information on the data set). The cloud scenarios with the two CTT boundary values per phase are shown in different colors in Fig. 10 (light blue and dark blue for ice clouds; orange and red for liquid clouds). For the R_{eff} boundaries we select the upper and lower limits of all computed R_{eff} scenarios (see table 1). Additionally, as liquid clouds rarely have $\tau < 5$, these values are omitted, since we focus for this sensitivity analysis on "typical" cloud scenarios. For ice clouds, different habits are shown as different markers. Hence, the cloud parameters in Fig. 10 are chosen such that the majority of mid-latitude cloud events for each phase lie between the very bottom and top blue curves for ice and the very bottom and top orange/red curves for liquid.

To verify that the computed ranges of BTD values are realistic, we compare the RT results with measured SEVIRI data using cloud phase information from DARDAR. More details on this comparison and its results can be found in Appendix D. We find good agreement between the RT results and the measured SEVIRI data and conclude that the results of the RT calculations are realistic.

In Fig. 10 BTD(10.8-12.0) shows the highest sensitivity to τ, CTT and R_{eff}. BTD(8.7-10.8) shows the highest sensitivity to τ, CTT and molecular absorption (closely linked to CTH). In comparison to τ and CTT/CTH the sensitivity to R_{eff} is lower for BTD(8.7-10.8) and mainly relevant for small CTT. For both BTDs, the direct sensitivity to cloud phase, i.e. holding all other cloud parameters constant, plays mostly only a minor role: For BTD(10.8-12.0) the direct phase dependence is of the order of 0.5–1.5 K; for BTD(8.7-10.8) the direct influence of phase is only significant for small τ values ($\lesssim 10$) and then of the order of 1–2 K (see Sect. 5.3).

For a phase retrieval we need to know for which cloud properties liquid and ice clouds overlap and where they separate for both BTDs. The largest BTD(10.8-12.0) values in the "typical" cloud scenarios (about 2.5 to 5 K in Fig. 10) are only observed for optically thin and cold ice clouds with small R_{eff}. Thus BTD(10.8-12.0) is useful to detect cirrus clouds, especially if they have small R_{eff} (like contrails), and classify them as ice in a phase retrieval. However, our calculations show that certain liquid cloud scenarios with exceptionally low R_{eff} and cold CTTs can also induce remarkably high BTD(10.8-12.0). This can lead to misclassification of these liquid clouds as ice. However, most liquid clouds have lower BTD(10.8-12.0), below about 2.5 K in Fig. 10. Since such low BTD(10.8-12.0) may also indicate ice clouds with "warm" CTTs and/or large R_{eff}, or ice clouds with τ close to zero, a phase classification based on BTD(10.8-12.0) alone is challenging. The lowest BTD(10.8-12.0) values (about 0 to 1 K in Fig. 10) indicate optically thick clouds, but do otherwise not contain much phase information.

As for BTD(10.8-12.0), large BTD(8.7-10.8) (around 1 to 5.5 K in Fig. 10) can indicate ice phase, since only ice clouds with low τ of about $1 < \tau < 7$ reach these values. Low BTD(8.7-10.8) (lower than about -0.5 in Fig. 10) can arise from very thin ice clouds (as BTD(8.7-10.8) decreases to about -2 K as τ goes to zero) or optically thick clouds. For optically thick clouds, BTD(8.7-10.8) decreases with higher CTT (due to lower CTHs and stronger molecular absorption) and smaller R_{eff} - both characteristics typical of liquid clouds. As a general guideline for optically thick clouds, lower BTD(8.7-10.8) indicate a higher probability of a liquid cloud. Overall, the phase information contained in BTD(8.7-10.8) originates mainly from its sensitivity to CTT for clouds with $\tau \lesssim 10$, while for optically thick clouds it stems mainly from its sensitivity to molecular absorption (closely linked to CTH) and (to a lesser extent) R_{eff}. Only in cases of optically thin clouds ($\tau \lesssim 10$) is the phase information of BTD(8.7-10.8) additionally due to the direct phase influence on the (different) absorption properties of liquid and ice particles.

To summarize the main findings:

- The sensitivities of the BTDs are complex.

- BTD(10.8-12.0) shows the highest sensitivity to τ, CTT and R_{eff}. BTD(8.7-10.8) shows the highest sensitivity to τ and CTT/CTH.

- Thin ice clouds can be detected by both BTD(10.8-12.0) and BTD(8.7-10.8) as long as $\tau \gtrsim 1$.

- BTD(8.7-10.8) also provides CTH and R_{eff} information for optically thick clouds, which can be useful for phase determination.

- For BTD(10.8-12.0), typical liquid and ice clouds overlap for most cloud scenarios, with the exception of cold, thin ice clouds. For BTD(8.7-10.8), liquid and ice clouds separate better, but the BTD values of the two phases are close when CTTs (CTHs) are similar. This phase separation is mainly due to the sensitivity of BTD(8.7-10.8) to CTT/ CTH.

6.2 Sensitivity analysis for the combination of both BTDs

We perform a similar sensitivity analysis as in the last section for the combination of both BTDs. As Fig. 10, Fig. 11
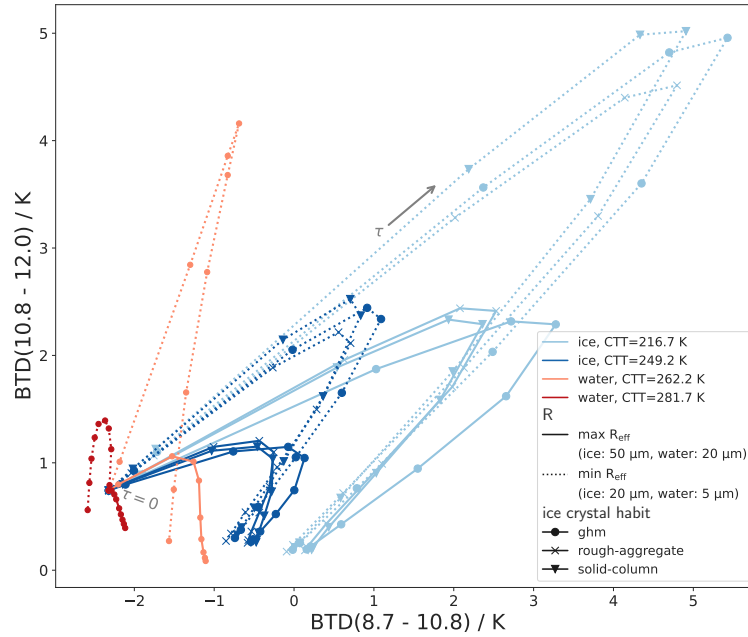
Figure 11. Sensitivity analysis combining both BTDs and varying the phase cloud parameters τ, R_{eff}, habit, CTT and thermodynamic phase:: Blue lines show ice clouds; orange/red lines show liquid clouds for typical upper and lower boundaries of CTT and R_{eff}. Along each line, τ increases from 0 to 30. For ice clouds, different habits are shown as different markers

shows the BTDs for the same upper and lower boundaries of CTT and R_{eff}, but in the space spanned by BTD(8.7-10.8) and BTD(10.8-12.0). Along each line, τ increases from 0 to 30. To make the shape of the curves easier to understand, here also liquid clouds with $\tau < 5$ are shown (in contrast to Fig. 10).

Figure 11 shows that the combined knowledge of both BTD(8.7-10.8) and BTD(10.8-12.0) leads to a better phase classification than considering BTD(8.7-10.8) and BTD(10.8-12.0) individually. For instance, liquid clouds at cold CTTs and small R_{eff} (orange dotted line) separate from ice clouds in Fig. 11 as long as τ is not too large ($\lesssim 10$). In contrast, the same cloud scenario overlaps with ice cloud scenarios when only BTD(8.7-10.8) or BTD(10.8-12.0) are considered individually (Fig. 10).

In order to better showcase the range of BTD values for both phases and identify overlap regions, we use an additional type of plot: Instead of showing only the boundary cases (as in Fig. 11), the left column of Fig. 12 shows (almost) all computed BTD values within the defined boundaries of CTT and R_{eff} in the space spanned by the two BTDs. Only optically thick clouds ($\tau \geq 10$) with very low ($< 233\,\mathrm{K}$) or very high ($> 273\,\mathrm{K}$) CTTs are removed, i.e. the clouds that are easily categorised as liquid or ice by a CTT proxy such as $BT_{10.8}$ and for which a categorisation by the BTDs

is therefore not necessary. Liquid clouds are shown as round markers, while ice clouds are shown as crosses. The three subfigures in the left column of Fig. 12 vary only by their color code which encodes τ, CTT and R_{eff} respectively. They show that there is little overlap between the "typical" liquid and ice clouds (i.e. the clouds within the defined CTT and R_{eff} boundaries). The only overlap is for very small τ ($\tau \lesssim 1$), since the BTDs approach the same values for all clouds, determined by atmospheric properties, as $\tau \to 0$ (best seen in Fig. 11). This means that a phase classification for "typical" liquid and ice cloud cases is possible in BTD(8.7-10.8) – BTD(10.8-12.0) – space for $\tau \gtrsim 1$ when atmospheric parameters are known.

However, Fig. 11 and the left column in Fig. 12 also show that liquid and ice BTD values are closest for clouds with similar CTTs. To further explore this issue and to test the limitations of a phase classification using the BTDs, the right column of Fig. 12 shows BTD values also for clouds outside the "typical" cloud boundaries. The three subfigures show the whole range of computed cloud scenarios (see table 1), including also exceptionally cold liquid clouds and exceptionally warm ice clouds. Only the "easy" to distinguish cases ($\tau \geq 10$ and either CTT$< 233\,\mathrm{K}$ or CTT $> 273\,\mathrm{K}$) are removed as before. The figures show that the overlap between liquid and ice clouds is significantly larger compared to the
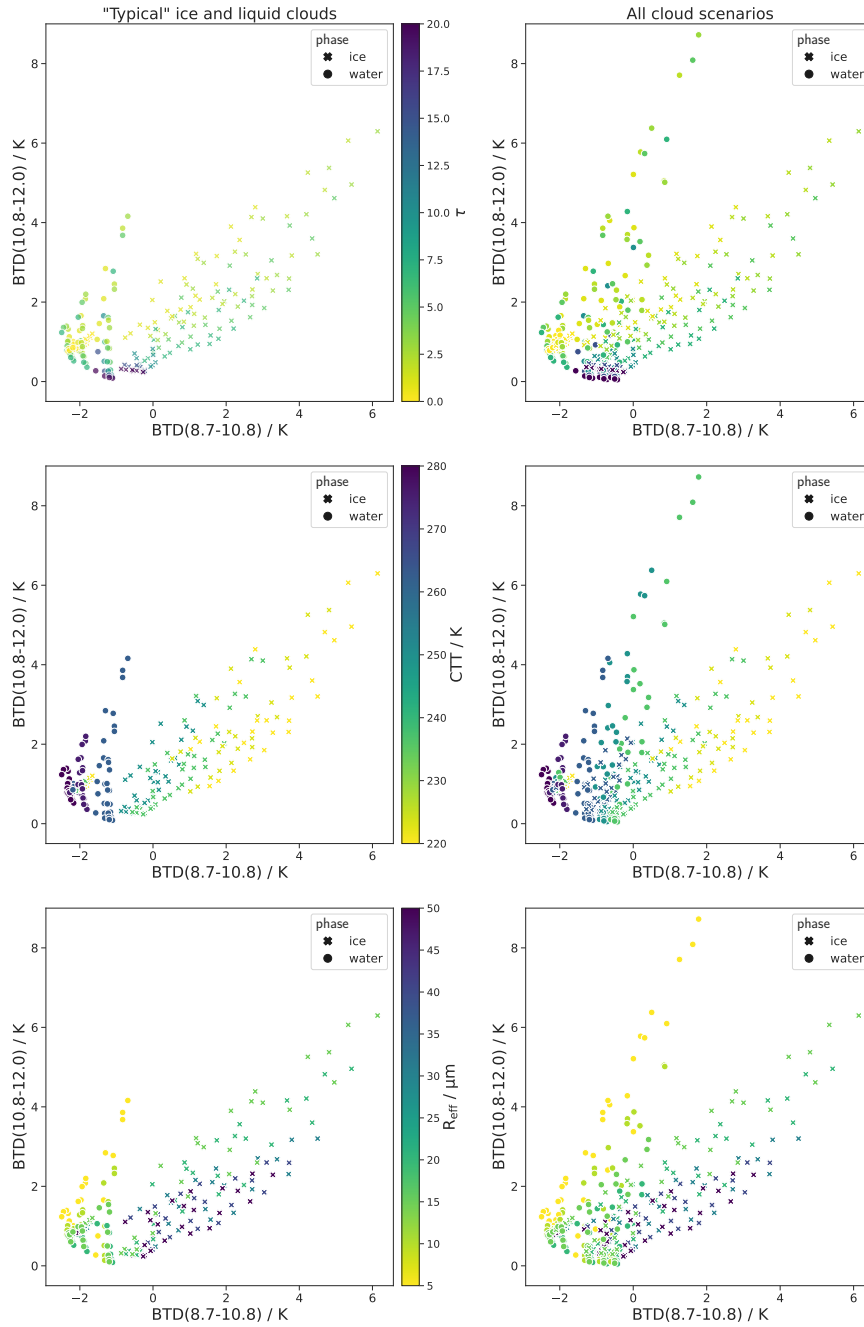
Figure 12. Left column: BTD(10.8-12.0) and BTD(8.7-10.8) values within the defined "typical" boundaries of CTT. Round markers indicate liquid clouds; crosses indicate ice clouds. Clouds which can be distinguished using a CTT proxy like $BT_{10.8}$, i.e. optically thick clouds ($\tau \geq 10$) with very low (< 233 K) or very high (> 273 K) CTTs, are not shown. The color code in the three rows encodes τ, CTT and R_{eff} respectively. Right column: Same as left column but for the whole range of computed cloud scenarios (see table 1), including also exceptionally cold liquid clouds and exceptionally warm ice clouds. The color codes of the three rows correspond to the color codes in the left column. Clouds which can be distinguished using a CTT proxy are again not shown.

"typical" cloud cases (left column of Fig. 12). The clouds in the overlap region are mainly liquid and ice clouds which have similar CTTs in the midlevel temperature range, i.e. rather cold liquid clouds (CTT $\lesssim$ 260 K) and rather warm ice clouds (CTT $\gtrsim$ 250 K). We discussed in the last section (Sect. 6.1) that the CTT/CTH is the most important contributor to the differences between liquid and ice clouds for both BTDs. It is therefore not surprising that phase discrimination for clouds with similar CTT/CTH is difficult even when knowledge of both BTDs is combined. Note also that additional information from $BT_{10.8}$, which is often used as a proxy for CTT, does not help much in distinguishing between phases in these cases of midlevel CTTs. For the phase classification of these midlevel clouds, the R_{eff} also plays a role: For R_{eff} values that are rather large for the respective phase, the overlap occurs for all τ values; for R_{eff} values that are rather small for the respective phase, the overlap occurs only for very small or very large τ values.

To summarize the most important results:

– The combined use of BTD(8.7-10.8) and BTD(10.8-12.0) is better suited for phase discrimination than the two BTDs individually.

– The combined use of BTD(8.7-10.8) and BTD(10.8-12.0) can discriminate cloud phase for liquid and ice clouds in their "typical" CTT regimes as long as τ is not too small ($\tau \gtrsim 1$) and when atmospheric parameters are known.

– Clouds in the midlevel CTT regime are challenging: If liquid clouds are particularly cold or ice clouds particularly warm, they can often not be distinguished by the two BTDs. This is especially true for clouds with large R_{eff} for the respective phase.

6.3 Sensitivity to additional cloud parameters: Effects of geometric thickness and vertical R_{eff} inhomogeneity

Cloud properties that have not been discussed so far are cloud geometric thickness and vertical inhomogeneities of microphysical parameters. Both can have an impact on BTDs (Piontek et al., 2021a; Zhang et al., 2010). To estimate how large these effects are, we performed a sensitivity analysis for varying cloud geometric thickness and for vertical inhomogeneities of R_{eff}. Results of this analysis are shown in Fig. E1 and Fig. E2 in the appendix. We find that the sensitivity to both geometric thickness and vertical Reff inhomogeneity is small compared to other cloud parameters ($\lesssim 0.5$ K in most cases). This sensitivity does not significantly affect the regions in the space spanned by the two BTDs which are associated with the different phases and therefore has a comparatively small effect on a potential phase retrieval.

7 Conclusions

The aim of this study is to characterize and physically understand the relation of two IR window BTDs that are typically used for satellite retrievals of the thermodynamic cloud phase. As an example, we select BTD(8.7-10.8) and BTD(10.8-12.0) of the SEVIRI imager, but the main findings can be generalised to other imagers with similar thermal channels. Although modern phase retrievals often rely not only on BTDs but also on other satellite measurements (Baum et al., 2012; Hünerbein et al., 2022; Benas et al., 2023; Mayer et al., 2024), it is important to understand the BTD characteristics and capabilities. This knowledge helps to design optimal cloud phase retrievals and to understand their potential and limitations.

We present RT calculations that analyse the sensitivities of the two BTDs to cloud phase and all radiatively important cloud parameters related to phase, namely τ, R_{eff}, ice crystal habit and CTT/ CTH. Previous studies of BTDs have tended to focus on only a small number of cloud parameters, and an overview of the relative importance of all cloud parameters and their interdependencies is still missing. We perform a sensitivity analysis of the BTDs, which to our knowledge has never been done for all cloud parameters combined. This provides an overview over the effects of all cloud parameters and shows which parameters are responsible for the observed phase dependence of the BTDs, which is often used for phase retrievals (Ackerman et al., 1990; Strabala et al., 1994; Finkensieper et al., 2016; Key and Intrieri, 2000; Baum et al., 2000, 2012; Hünerbein et al., 2022; Benas et al., 2023; Mayer et al., 2024). Even though the RT calculations were performed for a specific atmospheric and surface setup, the main insights of this study, including the physical understanding of the effects of cloud properties on BTDs and their relative importance, are valid for any atmospheric or surface condition.

To understand the behaviour of the BTDs, we examine the effects of the nonlinear relationship between radiances and BTs through Planck's radiation law on the BTDs. This nonlinearity induces positive BTD values and a dependence on the CTT (or more generally the surface-cloud-temperature contrast ΔT) in a simple RT model, even when cloud optical properties (transmittance and emissivity) are the same at all wavelengths. This effect is co-responsible for the arc shape of the BTDs as functions of τ and their CTT dependence, in addition to effects due to spectral differences in cloud optical properties. These spectral differences in cloud optical properties can explain the (remaining) dependence of the BTDs on the different cloud parameters.

We find that the dependence on phase is more complex than is sometimes assumed: Although both BTDs are directly sensitive to phase (holding every other cloud parameter constant), this sensitivity is mostly small compared to other cloud parameters, as τ, CTT and R_{eff}. Instead, apart from τ for which the sensitivity is well known, the BTDs

show the strongest sensitivity to CTT/ CTH. Since the CTT is associated with phase, this is the main factor leading to the observed phase dependence of the BTDs. Note that more generally, this CTT dependence of the BTDs is more accurately described as a dependence on the surface-cloud temperature contrast ΔT, which reduces to a CTT dependence in our case with a fixed surface temperature. The direct phase dependence merely adds to the CTT/CTH effect, increasing differences between ice and liquid (for BTD(8.7-10.8) only for small $\tau \lesssim 10$).

The sensitivity analysis shows that it is straightforward to distinguish "typical" high ice clouds from low liquid clouds using the BTDs. However, it is challenging to distinguish a mid-level ice cloud from a mid-level liquid cloud - especially if the R_{eff} is also similar. The combination of both BTDs increases phase information content and is therefore preferable in a retrieval.

This study was conducted for a simple fixed setup of the atmosphere, surface and satellite viewing geometry in order to focus on the effects of cloud properties. If this setup is changed, we expect the cloud effects on the BTDs discussed in this paper to be superimposed by additional effects: For example, changes in water vapor content or satellite zenith angle shift BTD(8.7-10.8) due to its sensitivity to water vapor absorption. This shift is larger the more water vapor is above the cloud top and therefore depends on the CTH and the vertical atmospheric profile. A different type of surface with spectral differences in surface emissivity (as for instance a desert surface) shifts the values of both BTDs for optically thin clouds. For potential phase retrievals, these effects should ideally be taken into account.

This study focuses on liquid and ice clouds. We expect the BTD values of mixed-phase clouds to lie between ice and liquid values, as they represent a transition between the two. Depending mainly on the CTT/ CTH and to a lesser extent the R_{eff} of mixed-phase clouds, their BTD values are expected to be closer or further away from the liquid or ice BTD values. In that sense, we expect that BTDs can make a useful contribution to the retrieval of mixed-phase clouds and their composition. However, as the CTT/ CTH and R_{eff} values overlap between liquid, mixed-phase and/or ice clouds, we expect the regions of the different phases in the space spanned by BTD(8.7-10.8) and BTD(10.8-12.0) to also overlap, introducing ambiguity. The use of additional satellite channels containing, for instance, particle size or phase information is necessary to increase the phase information content for a retrieval.

Appendix A: Single scattering properties

The single scattering properties are the volume extinction coefficient β_{ext}, the single scattering albedo ω_0 and the scattering phase function p. The volume extinction coefficient β_{ext} describes how much radiation is removed through scattering and absorption (=extinction) from a ray when passing through the cloud and can be expressed as

$$\beta_{ext} = \beta_{sca} + \beta_{abs} \tag{A1}$$

where β_{sca} and β_{abs} are the scattering and absorption coefficient, with units of m^{-1}, measuring how much radiation is absorbed and scattered by cloud particles. Note that in this study τ is β_{ext} at wavelength $\lambda = 550\,nm$ integrated over the path through the cloud; the optical thickness τ_λ at other wavelengths λ is in general different from τ, depending on the other microphysical cloud parameters. The single scattering albedo ω_0 is a measure of the relative importance of scattering and absorption, defined as

$$\omega_0 = \frac{\beta_{sca}}{\beta_{sca} + \beta_{abs}} = \frac{\beta_{sca}}{\beta_{ext}}. \tag{A2}$$

Hence, as an alternative to β_{ext} and ω_0 one can equivalently describe radiative transfer by β_{abs} and β_{sca}, which can be easier to interpret. The scattering phase function $p(\Omega)$ gives the probability of the scattering angle Ω, i.e. the angle between the incident radiation and the scattered radiation. To understand radiative transfer through a cloud, the most important property of p is the angular anisotropy of the scattering process. This anisotropy is indicated to first order by the asymmetry parameter g, which is calculated from p as the mean cosine of the scattering angle Ω.

$$g = \int_{-1}^{1} p(\cos\Omega') \cos\Omega' \, d\cos\Omega' \tag{A3}$$

If a particle scatters more in the forward direction ($\Omega = 0°$), g is positive; g is negative if the scattering is more in the backward direction ($\Omega = 180°$) (Bohren and Huffman, 2008).

Appendix B: Disentangling the BTD Nonlinearity Shift from effects of wavelength dependent optical properties

An instructive way to look at the BTD Nonlinearity Shift and to disentangle it from effects of wavelength dependent optical properties is the following: To make the radiances at different wavelengths more comparable, we use the Planck radiance corresponding to the surface temperature T_s as a reference. For typical atmospheric profiles (without temperature inversions), this Planck radiance $B_\lambda(T_s)$ is the maximal possible radiance in each wavelength, corresponding to $\tau \to 0$ (see Eq. 3). We express the TOA radiance as fractions f_λ of
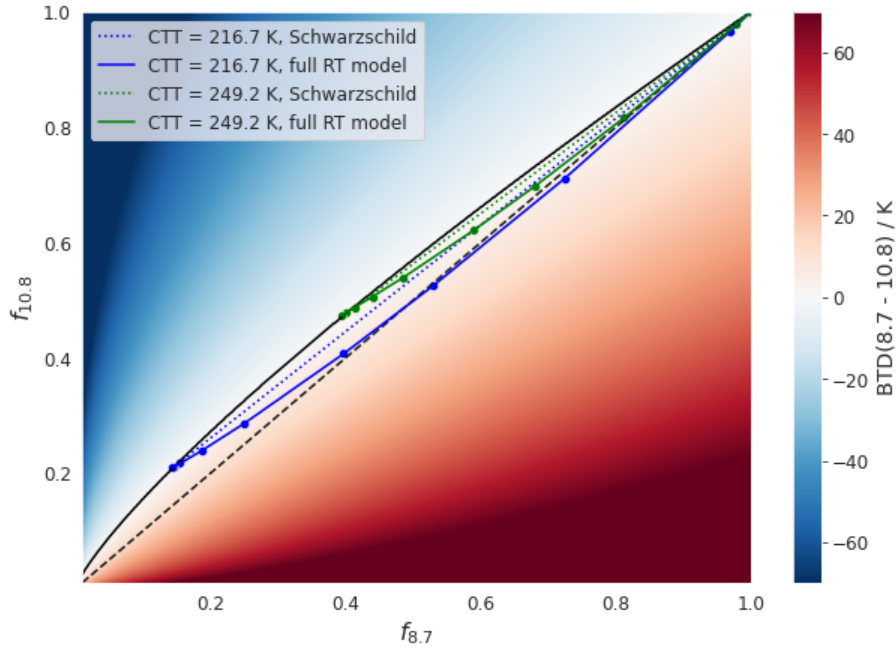
Figure B1. BTD(8.7-10.8) in the space spanned by the radiance fraction $f_{8.7}$ and $f_{10.8}$ (defined as the radiance at TOA scaled by the Planck radiance of the surface with temperature $T_s = 290$ K: $f_\lambda = R_{TOA,\lambda}/B_\lambda(T_s)$). The black solid line indicates BTD(8.7-10.8) = 0; the black dashed line indicates $f_{8.7} = f_{10.8}$. The blue and green lines show $f_{8.7}$ and $f_{10.8}$ values for varying τ at a given CTT: The dotted lines show $f_{8.7}$ and $f_{10.8}$ computed with the Schwarzschild equation (with $\tau_{8.7} = \tau_{10.8}$); solid lines show $f_{8.7}$ and $f_{10.8}$ values computed with the full RT model.

this maximal possible radiance, called *radiance fraction* in the following, i.e.

$$f_\lambda = \frac{R_{TOA,\lambda}}{B_\lambda(T_s)}, \quad \text{with } f_\lambda \in [0,1]. \tag{B1}$$

The BTDs can then be expressed as functions of the radiance fractions f_λ

$$\text{BTD}(\lambda_0 - \lambda_1) = T_{\lambda_0}(f_{\lambda_0}B_{\lambda_0}(T_s)) - T_{\lambda_1}(f_{\lambda_1}B_{\lambda_1}(T_s)). \tag{B2}$$

For the sake of brevity, in the following we only discuss BTD(8.7-10.8) as function of $f_{8.7}$ and $f_{10.8}$; BTD(10.8-12.0) has qualitatively the same properties and the same conclusions apply. Figure B1 shows BTD(8.7-10.8) in $f_{8.7}$-$f_{10.8}$-space for $T_s = 290$ K. If $f_{8.7}$ is (much) larger than $f_{10.8}$, the BTD is positive and if $f_{8.7}$ is (much) smaller than $f_{10.8}$, the BTD is negative, as expected. However, the BTD(8.7-10.8) = 0 line is not at $f_{8.7} = f_{10.8}$ (black dashed line in Fig. B1) as one might naively expect but has a convex shape in $f_{8.7}$-$f_{10.8}$-space (shown as black solid line), such that BTD(8.7-10.8) = 0 for $f_{8.7} < f_{10.8}$. Or to put it another way, if the radiance at TOA is the same fraction of its maximal possible radiance at both wavelengths, $f_{8.7} = f_{10.8}$, the BTD is positive. Note that this is a completely general statement, that does not depend on a RT model but simply shows what happens mathematically when the inverse Planck function, T_λ,

is applied on fractions of Planck radiance, $f_\lambda B_\lambda(T_s)$, at different wavelengths.

To understand the role of the BTD Nonlinearity Shift we add results of RT computations to Fig. B1 in the following steps: First, we study how radiances computed with the Schwarzschild equation look like in $f_{8.7}$-$f_{10.8}$-space. To see the pure BTD Nonlinearity Shift we again set the optical thickness constant at both wavelengths, $\tau_{8.7} = \tau_{10.8} = \tau$. Next, we explore the changes in the Schwarzschild radiance when τ differs at the two wavelengths, i.e. $\tau_{10.8} \neq \tau_{8.7}$. In this case, both the mathematical BTD Nonlinearity Shift and the physical effect of spectrally dependent optical properties are present. Third, we study how the radiance computed with the full RT model looks like in $f_{8.7}$-$f_{10.8}$-space.

We start with the Schwarzschild radiance in $f_{8.7}$-$f_{10.8}$-space with constant optical thickness at both wavelengths, $\tau_{8.7} = \tau_{10.8} = \tau$. We compute the radiances $R_{\text{TOA},8.7}^{\text{S}}$ and $R_{\text{TOA},10.8}^{\text{S}}$ from the Schwarzschild equation as functions of τ for different values of CTT, as before (see Fig. 4(b)). These radiance results, expressed as radiance fractions $f_{8.7}$ and $f_{10.8}$, are shown in Fig. B1 as dotted lines for two different CTTs. For $\tau = 0$, the TOA radiance is the radiance emitted by the surface and $f_{8.7} = f_{10.8} = 1$. As τ increases, $f_{8.7}$ and $f_{10.8}$ get smaller and BTD(8.7-10.8) > 0, since $f_{10.8}$ and $f_{8.7}$ show a linear relationship and the BTD(8.7-10.8) = 0 line is convex. For large τ ($\tau = 30$) the TOA radi-

ance approaches the radiance emitted by a black body with a temperature equal to the CTT. Hence, the radiance fractions for large τ depend on the CTT and lie on the BTD(8.7-10.8) = 0 line (see Fig. B1). Overall, for increasing τ from 0 to 30, the Schwarzschild radiance fractions form a line from $f_{8.7} = f_{10.8} = 1$ to the radiance fraction values corresponding to the CTT black body radiance. It follows from the convex shape of the BTD(8.7-10.8) = 0 line that lower CTTs lead to larger BTD(8.7-10.8) values (see Fig. B1). The fact that the Schwarzschild radiance fraction line deviates from the BTD(8.7-10.8) = 0 line such that BTD(8.7-10.8) > 0, depending on the CTT, is a representation of the BTD Nonlinearity Shift equivalent to Fig. 4(b). The property that $f_{10.8}$ is a linear function of $f_{8.7}$ can be shown from the Schwarzschild equation. Solving Eq. 3 for $e^{-\tau}$ for a given wavelength λ_0 and inserting it into the Schwarzschild equation for a second wavelength λ_1 gives

$$R_{\mathrm{TOA},\lambda_1}^{\mathrm{S}} = k + m\, R_{\mathrm{TOA},\lambda_0}^{\mathrm{S}}, \qquad (B3)$$

with

$$m = \frac{B_{\lambda_1}(T_s) - B_{\lambda_1}(\mathrm{CTT})}{B_{\lambda_0}(T_s) - B_{\lambda_0}(\mathrm{CTT})}, \qquad (B4)$$

$$k = B_{\lambda_1}(T_s) - B_{\lambda_0}(T_s)\, m, \qquad (B5)$$

i.e. a linear relationship between R_{TOA,λ_1} and R_{TOA,λ_0} and therefore also between f_{λ_1} and f_{λ_0}.

So far we have set τ constant for all wavelengths in the Schwarzschild equation. To see what happens in the Schwarzschild model for different τ at different wavelengths, i.e. $\tau_{\lambda_0} \neq \tau_{\lambda_1}$, we add a small perturbation to τ_{λ_1},

$$\tau_{\lambda_1} = \tau_{\lambda_0} + \delta\tau. \qquad (B6)$$

Since the Schwarzschild equation neglects scattering, τ_λ is determined by the absorption coefficient $\beta_{\mathrm{abs},\lambda}$ and the cloud water path. For $\lambda_1 = 10.8\,\mu\mathrm{m}$ and $\lambda_0 = 8.7\,\mu\mathrm{m}$, the absorption coefficients $\beta_{\mathrm{abs},8.7} < \beta_{\mathrm{abs},10.8}$, meaning that if scattering is neglected $\tau_{8.7} < \tau_{10.8}$ and $\delta\tau > 0$ for this case. Solving Eq. 3 for a given λ_0 analogue to above for $e^{-\tau_{\lambda_0}}$ and inserting into Eq. 3 for λ_1 gives

$$R_{\mathrm{TOA},\lambda_1}^{\mathrm{S}} = k + m\, R_{\mathrm{TOA},\lambda_0}^{\mathrm{S}} - \delta\tau\, e^{-\tau_{\lambda_0}}\left(B_{\lambda_1}(T_s) - B_{\lambda_1}(\mathrm{CTT})\right), \qquad (B7)$$

where we used $e^{-\delta\tau} \approx 1 - \delta\tau$. Hence, since $\delta\tau > 0$ for $\lambda_1 = 10.8\,\mu\mathrm{m}$ and $\lambda_0 = 8.7\,\mu\mathrm{m}$, $R_{\mathrm{TOA},10.8}^{\mathrm{S}}$ decreases when we add a perturbation $\tau_{10.8} = \tau_{8.7} + \delta\tau$. This makes physical sense, since a larger $\tau_{10.8}$ compared to $\tau_{8.7}$ means that less radiance is transmitted through the cloud at 10.8 compared to 8.7 μm. The amount by which $R_{\mathrm{TOA},10.8}^{\mathrm{S}}$ decreases is determined by the difference between surface and cloud top radiance, $B_{\lambda_1}(T_s) - B_{\lambda_1}(\mathrm{CTT})$, and the factor $\delta\tau\, e^{-\tau_{\lambda_0}}$. For $\tau_{\lambda_0} \to 0$, meaning that the cloud water path approaches zero, $\delta\tau \to 0$.

For large τ_{λ_0}, $e^{-\tau_{\lambda_0}} \to 0$. Hence, the last term in Eq. B7 vanishes for very small or large τ_{λ_0}. For the τ_{λ_0} values in between, the perturbation $\delta\tau$ leads to a decrease of $R_{\mathrm{TOA},10.8}^{\mathrm{S}}$ and therefore of $f_{10.8}$. As a result, the Schwarzschild radiance fraction line in $f_{8.7}$-$f_{10.8}$-space deviates from a linear to a concave line. This deviation is stronger for larger $\delta\tau$ (i.e. larger differences between $\tau_{10.8}$ and $\tau_{8.7}$), as well as for larger differences between the surface and the cloud top radiance, $B_{\lambda_1}(T_s) - B_{\lambda_1}(\mathrm{CTT})$.

As a last step of this analysis, we study the full RT model in $f_{8.7}$-$f_{10.8}$-space. Recall that in the full RT model, in general, $\tau_{8.7} \neq \tau_{10.8} \neq \tau$, where τ as usually refers to the optical thickness at 550 nm. Figure B1 shows the radiance fractions $f_{8.7}$ and $f_{10.8}$ computed with the full RT model for an ice cloud for varying τ and two different CTTs in blue and green solid lines. Molecular absorption is switched off for these examples. Note that this is an equivalent representation of BTD(8.7-10.8) as the corresponding CTT curves in Fig. 9. For increasing τ from 0 to 30, the radiance fractions of the full RT model form curves from $f_{8.7} = f_{10.8} = 1$ to the radiance fraction values corresponding to the black body radiance of their CTT. These curves are concave, as expected from our theoretical considerations above (see Eq. B7). This concave shape, as explained above, can be attributed to differences in the absorption coefficients of the two wavelengths, $\beta_{\mathrm{abs},8.7} < \beta_{\mathrm{abs},10.8}$. The concave shape results in higher BTD values compared to the Schwarzschild $\mathrm{BTD}^{\mathrm{S}}$ values, where $\tau_{8.7} = \tau_{10.8} = \tau$ (compare BTD(8.7-10.8) along the solid and dotted lines in Fig. B1). The figure also shows that the deviation from the linear Schwarzschild radiance fraction lines is larger for lower CTTs - in accordance with our theoretical considerations (see Eq. B7).

This leads to the following interpretation of Fig. B1: The Schwarzschild radiance fraction lines in Fig. B1 (dotted lines) represent the pure BTD Nonlinearity Shift, which induces positive BTD values even though τ is the same in all wavelengths. Adding spectral differences between the cloud optical properties "pushes" the radiance fraction lines into a concave shape and further increases BTD. Hence, the difference between the BTD(8.7-10.8) = 0 line and the Schwarzschild radiance fraction lines in Fig. B1 is due to the Nonlinearity of the transformation from radiances to BTs; the difference between the Schwarzschild radiance fraction lines and the full RT model (solid lines) in Fig. B1 is due to the spectral differences in cloud optical properties. Lower CTTs increase both the BTD Nonlinearity Shift and the effects of spectral differences between the cloud optical properties.

Appendix C: Effects of R$_{\mathrm{eff}}$ on BTDs - disentangling absorption and scattering effects

Figure C1 shows the sensitivity of both BTDs with R$_{\mathrm{eff}}$ broken down into effects of absorption and scattering. The two rows show the same cloud scenarios, once with scattering
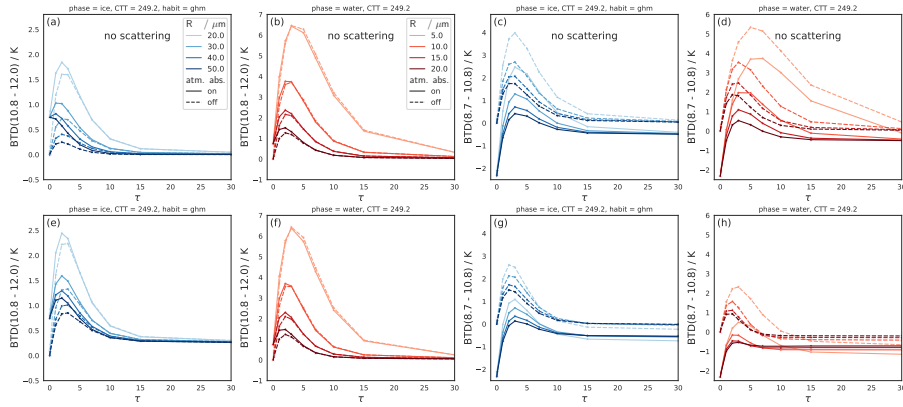
Figure C1. Effects of varying R_{eff} on BTD(10.8-12.0) and BTD(8.7-10.8) as functions of τ for ice clouds (blue) and liquid clouds (orange/red) and scattering switched off (top row) and switched on (bottom row). Solid lines indicate a "normal" absorbing atmosphere, dashed lines indicate that molecular absorption is switched off.

switched off (top row) and once with scattering switched on (bottom row). The figure shows that the effects of absorption lead to increasing values for smaller R_{eff} for both BTDs (top row of Fig. C1).

For BTD(10.8-12.0), the effect of scattering is similar for varying R_{eff} and comparatively small (increases (decreases) BTD(10.8-12.0) by $\lessgtr 0.5$ K for ice (water) clouds; compare Fig. C1(a,b) with (e,f)). For BTD(8.7-10.8), scattering effects are stronger than for BTD(10.8-12.0) and depend on R_{eff}: Scattering leads to a stronger decrease of BTD(8.7-10.8) for smaller R_{eff} (compare Fig. C1(c,d) with (g,h)). Since, however, the absorption effects are stronger, BTD(8.7-10.8) increases with decreasing R_{eff} (Fig. C1(g,h)).

Appendix D: Comparison to measured satellite data

Figure D1 shows a comparison of the RT results with measured SEVIRI data. The SEVIRI data was collocated with the active satellite product DARDAR (Delanoë and Hogan, 2010) containing information on the cloud phase (for more details see Mayer et al. (2023)). The plot on the left shows ice clouds; the plot on the right water clouds. As in Sect. 6.1 and Sect. 6, the RT results show boundary cases of "typical" cloud scenarios in blue and red, as indicated in the legend. In addition to SATZ=0°, we also show the RT results for SATZ=50°, in order to be able to compare the RT results to a large number of measurements with angles between these two cases. The measured SEVIRI data with the corresponding constraints (i.e. data of ice or water clouds within CTT and SATZ boundaries as for the RT calculations) are plotted on top of the RT results in grey. The figure shows that the RT results and measured SEVIRI data have a large overlap. Hence, the computed ranges of BTD values are realistic.

Appendix E: Effects of cloud geometric thickness and vertical R_{eff} inhomogeneity on BTDs

Figure E1 shows a sensitivity analysis for varying cloud geometric thickness between 1 km and 4 km. For constant τ, a larger cloud geometric thickness means that radiation originates from deeper within the cloud (in terms of geometric depth, implying a larger temperature difference). This depth can differ for different wavelengths, leading to a dependence of BTDs on geometric thickness (Piontek et al., 2021a). Figure E1 shows that the sensitivity to geometric thickness is comparably small and mostly $\lessgtr 0.5$ K. An exception are liquid clouds with very small R_{eff} for BTD(10.8-12.0), where the sensitivity to geometric thickness can exceed 1 K. For the case of liquid clouds with CTT $= 281.7$ K the CTH is at an altitude of 1 km in the US-standard atmospheric profile. Geometric thicknesses > 1 km are therefore not possible in this case.

Figure E2 shows the sensitivity of the BTDs to vertical inhomogeneity of R_{eff}. To model this inhomogeneity and capture its basic effects on BTDs we use a simple setup of clouds with a total geometric thickness of 2 km, consisting of two 1 km thick layers (layer 1 on top, layer 2 at the bottom, specified in the subscripts). Both layers have the same optical thickness, $\tau_1 = \tau_2 = \tau/2$. Cloud layer 1 has a $R_{\text{eff},1}$ which is either equal, smaller or larger to layer 2, $R_{\text{eff},1} \lessgtr R_{\text{eff},2}$ (case A, B or C), such that the average $\overline{R_{\text{eff}}}$ is the same for all three cases (case A: $R_{\text{eff},1} = R_{\text{eff},2} = \overline{R_{\text{eff}}}$; case B: $R_{\text{eff},1} = 0.8\,\overline{R_{\text{eff}}} < R_{\text{eff},2} = 1.2\,\overline{R_{\text{eff}}}$; case C: $R_{\text{eff},1} = 1.2\,\overline{R_{\text{eff}}} > R_{\text{eff},2} = 0.8\,\overline{R_{\text{eff}}}$). Hence, in case A, the R_{eff} is homogeneous; in case B and C it is inhomogeneous. This model of vertical inhomogeneity is of course very simplified, but it is useful for calculating a rough estimate of the magnitude of inhomogeneity effects and for understanding the underlying physics.
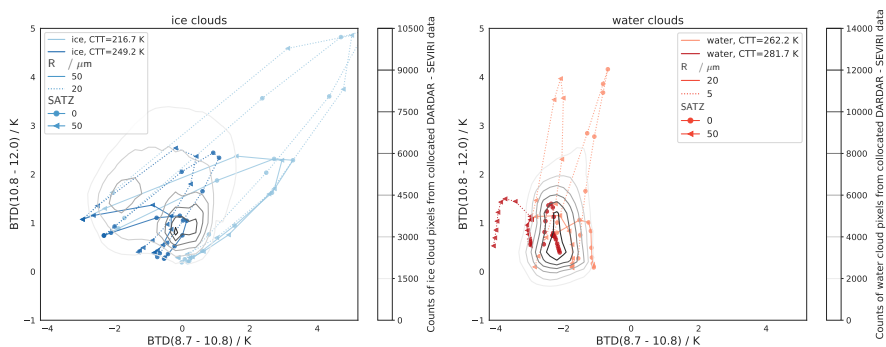
Figure D1. Comparison of RT results with measured SEVIRI data. The RT results are displayed as in Fig. 11, but for a fixed ice crystal habit (ghm) and two SATZ values (different markers). The corresponding counts of measured SEVIRI data is overlayed as contours in grey.
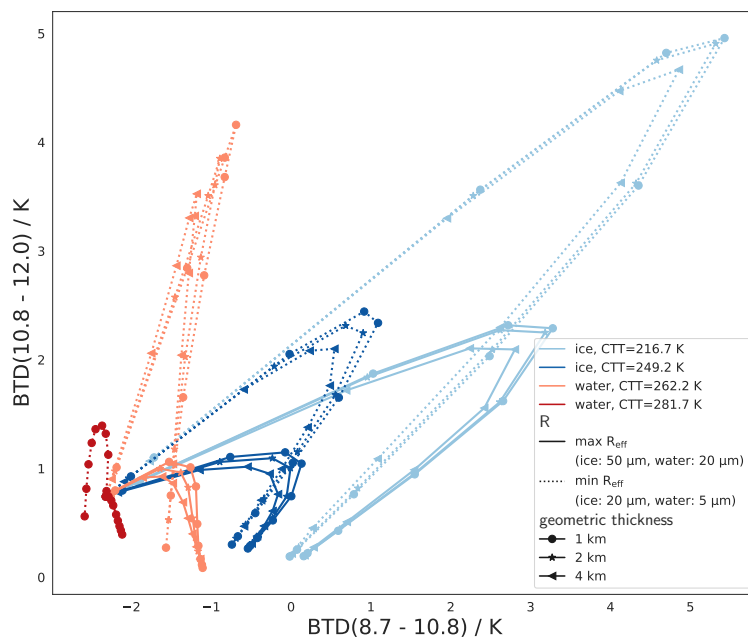
Figure E1. Same as Fig. 11, but for a fixed ice crystal habit (ghm) and varying geometric thickness of the cloud (in different markers)
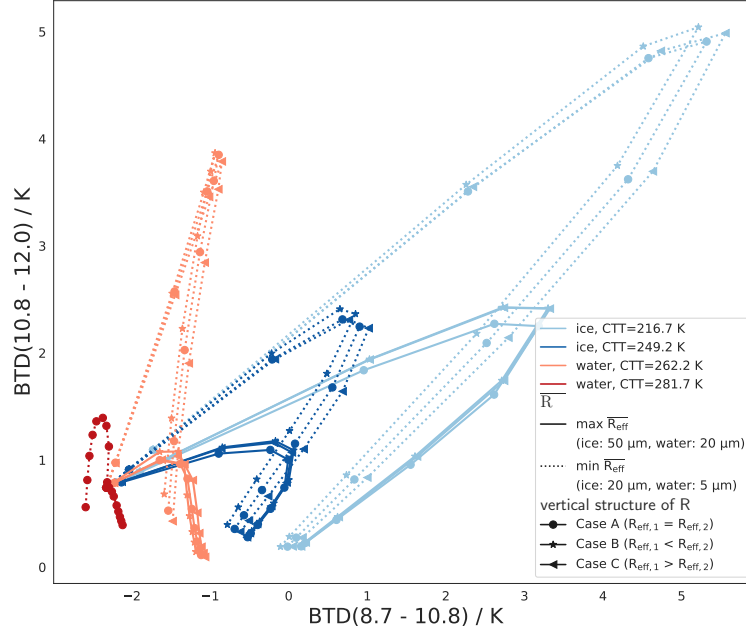
Figure E2. Same as Fig. 11, but for fixed ice crystal habit (ghm) and vertical inhomogeneity of R_{eff} (in different markers): the cloud consists of two layers (layer 1 on top, layer 2 at the bottom, specified in the subscripts), each with geometric thickness of 1 km and the same layer optical thickness, $\tau_1 = \tau_2 = \tau/2$. Cloud layer 1 has a $R_{eff,1}$ which is either equal, smaller or larger to layer 2, $R_{eff,1} \lesseqgtr R_{eff,2}$ (case A, B or C), such that the average $\overline{R_{eff}}$ is the same for all three cases (case A: $R_{eff,1} = R_{eff,2} = \overline{R_{eff}}$; case B: $R_{eff,1} = 0.8\,\overline{R_{eff}} < R_{eff,2} = 1.2\,\overline{R_{eff}}$; case C: $R_{eff,1} = 1.2\,\overline{R_{eff}} > R_{eff,2} = 0.8\,\overline{R_{eff}}$). No R_{eff} inhomogeneity is shown for the case of liquid clouds with CTT = 281.7 K, since their CTH is at an altitude of 1 km, leaving room for only one cloud layer.

Overall, the sensitivity to vertical R_{eff} inhomogeneity is comparatively small ($\lesssim 0.5$ K). The effects of the vertical R_{eff} inhomogeneity on the BTDs are due on the one hand to its effects on the transmittance of the surface radiance and on the other hand to its effects on the emittance of the cloud itself. Zhang et al. (2010) show (for ice clouds) that the nonlinear dependence of the optical properties on R_{eff} leads to an increased weighting of small particles in the signal of the transmitted radiance. This leads to larger BTDs for cases where the cloud is (partly) composed of particles smaller than the average (the inhomogeneous cases B and C), where transmittance is the dominant process (small τ). However, as can be seen in Fig. E2 for small τ ($\lesssim 2$), this effect is very small compared to other dependencies, since the cloud transmittance in the infrared window depends mainly on τ and less on the details of the vertical R_{eff} profile of the cloud (Zhang et al., 2010). On the other hand, when the cloud emittance dominates for increasing τ, the signal from the particles at the bottom of the cloud is (partially) absorbed by the top cloud layer. The BTD signal is then dominated by the R_{eff} of the top cloud layer ($R_{eff,1}$). This makes a difference mainly for small R_{eff} values (see min $\overline{R_{eff}}$ curves in Fig. E2), as the

BTDs depend non-linearly on R_{eff} (see Fig. 7). Figure E2 shows that these vertical R_{eff} inhomogeneity effects on cloud emittance (dominant for large τ) lead to larger overall effects on the BTDs compared to the effects on transmitted surface radiance (dominant for small τ).

References

Ackerman, S. A., Smith, W. L., Revercomb, H. E., and Spinhirne, J. D.: The 27-28 October 1986 FIRE IFO Cirrus Case Study: Spectral Properties of Cirrus Clouds in the 8-12 μm Window, Monthly Weather Review, 118, 2377–2388, https://doi.org/10.1175/1520-0493(1990)118<2377:TOFICC>2.0.CO;2, 1990.

Anderson, G., Clough, S., Kneizys, F., Chetwynd, J., and Shettle, E.: AFGL atmospheric constituent profiles (0–120 km), Tech.Rep. AFGL-TR-86-0110, Air Force Geophys. Lab., Hanscom Air Force Base, Bedford, Mass., 1986.

Atkinson, J. D., Murray, B. J., Woodhouse, M. T., Whale, T. F., Baustian, K. J., Carslaw, K. S., Dobbie, S., O'Sullivan, D., and Malkin, T. L.: The importance of feldspar for ice nucleation by mineral dust in mixed-phase clouds, Nature, 498, 355–358, https://doi.org/10.1038/nature12278, 2013.

Baum, B. A., Soulen, P. F., Strabala, K. I., King, M. D., Ackerman, S. A., Menzel, W. P., and Yang, P.: Remote sensing of cloud properties using MODIS airborne simulator imagery during SUCCESS: 2. Cloud thermodynamic phase, Journal of Geophysical Research: Atmospheres, 105, 11 781–11 792, https://doi.org/10.1029/1999jd901090, 2000.

Baum, B. A., Yang, P., Heymsfield, A. J., Schmitt, C. G., Xie, Y., Bansemer, A., Hu, Y.-X., and Zhang, Z.: Improvements in Shortwave Bulk Scattering and Absorption Models for the Remote Sensing of Ice Clouds, Journal of Applied Meteorology and Climatology, 50, 1037–1056, https://doi.org/10.1175/2010JAMC2608.1, 2011.

Baum, B. A., Menzel, W. P., Frey, R. A., Tobin, D. C., Holz, R. E., Ackerman, S. A., Heidinger, A. K., and Yang, P.: MODIS Cloud-Top Property Refinements for Collection 6, Journal of Applied Meteorology and Climatology, 51, 1145–1163, https://doi.org/10.1175/JAMC-D-11-0203.1, 2012.

Benas, N., Solodovnik, I., Stengel, M., Hüser, I., Karlsson, K.-G., Håkansson, N., Johansson, E., Eliasson, S., Schröder, M., Hollmann, R., and Meirink, J. F.: CLAAS-3: the third edition of the CM SAF cloud data record based on SEVIRI observations, Earth System Science Data, 15, 5153–5170, https://doi.org/10.5194/essd-15-5153-2023, 2023.

Bock, L., Lauer, A., Schlund, M., Barreiro, M., Bellouin, N., Jones, C., Meehl, G. A., Predoi, V., Roberts, M. J., and Eyring, V.: Quantifying Progress Across Different CMIP Phases With the ESMValTool, Journal of Geophysical Research: Atmospheres, 125, https://doi.org/10.1029/2019JD032321, 2020.

Bohren, C. F. and Huffman, D. R.: Absorption and scattering of light by small particles, John Wiley & Sons, 2008.

Bugliaro, L., Zinner, T., Keil, C., Mayer, B., Hollmann, R., Reuter, M., and Thomas, W.: Validation of cloud property retrievals with simulated satellite radiances: a case study for SEVIRI, Atmospheric Chemistry and Physics, 11, 5603–5624, https://doi.org/10.5194/acp-11-5603-2011, 2011.

Bugliaro, L., Piontek, D., Kox, S., Schmidl, M., Mayer, B., Müller, R., Vázquez-Navarro, M., Peters, D. M., Grainger, R. G., Gasteiger, J., and Kar, J.: VADUGS: a neural network for the remote sensing of volcanic ash with MSG/SEVIRI trained with synthetic thermal satellite observations simulated with a radiative transfer model, Natural Hazards and Earth System Sciences, 22, 1029–1054, https://doi.org/10.5194/nhess-22-1029-2022, 2022.

Buras, R., Dowling, T., and Emde, C.: New secondary-scattering correction in DISORT with increased efficiency for forward scattering, Journal of Quantitative Spectroscopy and Radiative Transfer, 112, 2028–2034, https://doi.org/10.1016/j.jqsrt.2011.03.019, 2011.

Cesana, G., Kay, J. E., Chepfer, H., English, J. M., and Boer, G.: Ubiquitous low-level liquid-containing Arctic clouds: New observations and climate model constraints from CALIPSO-GOCCP, Geophysical Research Letters, 39, https://doi.org/10.1029/2012GL053385, 2012.

Cesana, G., Waliser, D. E., Jiang, X., and Li, J.-L. F.: Multimodel evaluation of cloud phase transition using satellite and reanalysis data, Journal of Geophysical Research: Atmospheres, 120, 7871–7892, https://doi.org/10.1002/2014JD022932, 2015.

Cesana, G. V., Khadir, T., Chepfer, H., and Chiriaco, M.: Southern Ocean Solar Reflection Biases in CMIP6 Models Linked to Cloud Phase and Vertical Structure Representations, Geophysical Research Letters, 49, https://doi.org/10.1029/2022GL099777, 2022.

Cho, H.-M., Nasiri, S. L., and Yang, P.: Application of CALIOP Measurements to the Evaluation of Cloud Phase Derived from MODIS Infrared Channels, Journal of Applied Meteorology and Climatology, 48, 2169–2180, https://doi.org/10.1175/2009JAMC2238.1, 2009.

Choi, Y.-S., Ho, C.-H., Park, C.-E., Storelvmo, T., and Tan, I.: Influence of cloud phase composition on climate feedbacks, Journal of Geophysical Research: Atmospheres, 119, 3687–3700, https://doi.org/https://doi.org/10.1002/2013JD020582, 2014.

Delanoë, J. and Hogan, R. J.: Combined CloudSat-CALIPSO-MODIS retrievals of the properties of ice clouds, Journal of Geophysical Research, 115, https://doi.org/10.1029/2009JD012346, 2010.

Doutriaux-Boucher, M. and Quaas, J.: Evaluation of cloud thermodynamic phase parametrizations in the LMDZ GCM by using POLDER satellite data, Geophysical Research Letters, 31, n/a–n/a, https://doi.org/10.1029/2003GL019095, 2004.

Dubuisson, P., Giraud, V., Pelon, J., Cadet, B., and Yang, P.: Sensitivity of Thermal Infrared Radiation at the Top of the Atmosphere and the Surface to Ice Cloud Microphysics, Journal of Applied Meteorology and Climatology, 47, 2545–2560, https://doi.org/10.1175/2008JAMC1805.1, 2008.

Emde, C., Buras-Schnell, R., Kylling, A., Mayer, B., Gasteiger, J., Hamann, U., Kylling, J., Richter, B., Pause, C., Dowling, T., and Bugliaro, L.: The libRadtran software package for radiative transfer calculations (version 2.0.1), Geoscientific Model Development, 9, 1647–1672, https://doi.org/10.5194/gmd-9-1647-2016, 2016.

Finkensieper, S., Meirink, J. F., van Zadelhoff, G.-J., Hanschmann, T., Benas, N., Stengel, M., Fuchs, P., Hollmann, R., and Werscheck, M.: CLAAS-2: CM SAF CLoud property dAtaset using SEVIRI - Edition 2, https://doi.org/10.5676/EUM_SAF_CM/CLAAS/V002, 2016.

Forster, P., Storelvmo, T., Armour, K., Collins, W., Dufresne, J.-L., Frame, D., Lunt, D., Mauritsen, T., Palmer, M., Watanabe, M., Wild, M., and Zhang, H.: The Earth's Energy Budget, Climate Feedbacks, and Climate Sensitivity, Climate Change 2021: The Physical Science Basis. Contribution of Working Group I to the Sixth Assessment Report of the Intergovernmental Panel on

Climate Change, https://doi.org/10.1017/9781009157896.009., 2021.

Garnier, A., Pelon, J., Dubuisson, P., Faivre, M., Chomette, O., Pascal, N., and Kratz, D. P.: Retrieval of Cloud Properties Using CALIPSO Imaging Infrared Radiometer. Part I: Effective Emissivity and Optical Depth, Journal of Applied Meteorology and Climatology, 51, 1407–1425, https://doi.org/10.1175/JAMC-D-11-0220.1, 2012.

Gasteiger, J., Emde, C., Mayer, B., Buras, R., Buehler, S., and Lemke, O.: Representative wavelengths absorption parameterization applied to satellite channels and spectral bands, Journal of Quantitative Spectroscopy and Radiative Transfer, 148, 99–115, https://doi.org/10.1016/j.jqsrt.2014.06.024, 2014.

Gregory, D. and Morris, D.: The sensitivity of climate simulations to the specification of mixed phase clouds, Climate Dynamics, 12, 641–651, https://doi.org/10.1007/BF00216271, 1996.

Heidinger, A., Li, Y., Baum, B., Holz, R., Platnick, S., and Yang, P.: Retrieval of Cirrus Cloud Optical Depth under Day and Night Conditions from MODIS Collection 6 Cloud Property Data, Remote Sensing, 7, 7257–7271, https://doi.org/10.3390/rs70607257, 2015.

Heidinger, A. K., Pavolonis, M. J., Holz, R. E., Baum, B. A., and Berthier, S.: Using CALIPSO to explore the sensitivity to cirrus height in the infrared observations from NPOESS/VIIRS and GOES-R/ABI, Journal of Geophysical Research, 115, https://doi.org/10.1029/2009JD012152, 2010.

Hünerbein, A., Bley, S., Horn, S., Deneke, H., and Walther, A.: Cloud mask algorithm from the EarthCARE multi-spectral imager: the M-CM products, https://doi.org/10.5194/egusphere-2022-1240, 2022.

Inoue, T.: On the Temperature and Effective Emissivity Determination of Semi-Transparent Cirrus Clouds by Bi-Spectral Measurements in the $10\mu m$ Window Region, Journal of the Meteorological Society of Japan. Ser. II, 63, 88–99, https://doi.org/10.2151/jmsj1965.63.1_88, 1985.

Key, J. R. and Intrieri, J. M.: Cloud Particle Phase Determination with the AVHRR, Journal of Applied Meteorology, 39, 1797–1804, https://doi.org/10.1175/1520-0450-39.10.1797, 2000.

Komurcu, M., Storelvmo, T., Tan, I., Lohmann, U., Yun, Y., Penner, J. E., Wang, Y., Liu, X., and Takemura, T.: Intercomparison of the cloud water phase among global climate models, Journal of Geophysical Research: Atmospheres, 119, 3372–3400, https://doi.org/https://doi.org/10.1002/2013JD021119, 2014.

Kox, S., Bugliaro, L., and Ostler, A.: Retrieval of cirrus cloud optical thickness and top altitude from geostationary remote sensing, Atmospheric Measurement Techniques, 7, 3233–3246, https://doi.org/10.5194/amt-7-3233-2014, 2014.

Krebs, W., Mannstein, H., Bugliaro, L., and Mayer, B.: Technical note: A new day- and night-time Meteosat Second Generation Cirrus Detection Algorithm MeCiDA, Atmospheric Chemistry and Physics, 7, 6145–6159, https://doi.org/10.5194/acp-7-6145-2007, 2007.

Marchant, B., Platnick, S., Meyer, K., Arnold, G. T., and Riedi, J.: MODIS Collection 6 shortwave-derived cloud phase classification algorithm and comparisons with CALIOP, Atmospheric Measurement Techniques, 9, 1587–1599, https://doi.org/10.5194/amt-9-1587-2016, 2016.

Matus, A. V. and L'Ecuyer, T. S.: The role of cloud phase in Earths radiation budget, Journal of Geophysical Research: Atmospheres, 122, 2559–2578, https://doi.org/10.1002/2016JD025951, 2017.

Mayer, B. and Kylling, A.: Technical note: The libRadtran software package for radiative transfer calculations - description and examples of use, Atmospheric Chemistry and Physics, 5, 1855–1877, https://doi.org/10.5194/acp-5-1855-2005, 2005.

Mayer, B., Seckmeyer, G., and Kylling, A.: Systematic long-term comparison of spectral UV measurements and UVSPEC modeling results, Journal of Geophysical Research: Atmospheres, 102, 8755–8767, https://doi.org/10.1029/97JD00240, 1997.

Mayer, J., Ewald, F., Bugliaro, L., and Voigt, C.: Cloud Top Thermodynamic Phase from Synergistic Lidar-Radar Cloud Products from Polar Orbiting Satellites: Implications for Observations from Geostationary Satellites, Remote Sensing, 15, 1742, https://doi.org/10.3390/rs15071742, 2023.

Mayer, J., Bugliaro, L., Mayer, B., Piontek, D., and Voigt, C.: Bayesian Cloud Top Phase Determination for Meteosat Second Generation, EGUsphere, 2024, 1–32, https://doi.org/10.5194/egusphere-2023-2345, 2024.

Meerkötter, R. and Bugliaro, L.: Diurnal evolution of cloud base heights in convective cloud fields from MSG/SEVIRI data, Atmospheric Chemistry and Physics, 9, 1767–1778, https://doi.org/10.5194/acp-9-1767-2009, 2009.

Nasiri, S. L. and Kahn, B. H.: Limitations of Bispectral Infrared Cloud Phase Determination and Potential for Improvement, Journal of Applied Meteorology and Climatology, 47, 2895–2910, https://doi.org/10.1175/2008JAMC1879.1, 2008.

Parol, F., Buriez, J. C., Brogniez, G., and Fouquart, Y.: Information Content of AVHRR Channels 4 and 5 with Respect to the Effective Radius of Cirrus Cloud Particles, Journal of Applied Meteorology, 30, 973–984, https://doi.org/10.1175/1520-0450-30.7.973, 1991.

Pavolonis, M. J.: Advances in Extracting Cloud Composition Information from Spaceborne Infrared Radiances—A Robust Alternative to Brightness Temperatures. Part I: Theory, Journal of Applied Meteorology and Climatology, 49, 1992–2012, https://doi.org/10.1175/2010JAMC2433.1, 2010.

Piontek, D., Bugliaro, L., Kar, J., Schumann, U., Marenco, F., Plu, M., and Voigt, C.: The New Volcanic Ash Satellite Retrieval VACOS Using MSG/SEVIRI and Artificial Neural Networks: 2. Validation, Remote Sensing, 13, 3128, https://doi.org/10.3390/rs13163128, 2021a.

Piontek, D., Bugliaro, L., Schmidl, M., Zhou, D. K., and Voigt, C.: The New Volcanic Ash Satellite Retrieval VACOS Using MSG/SEVIRI and Artificial Neural Networks: 1. Development, Remote Sensing, 13, 3112, https://doi.org/10.3390/rs13163112, 2021b.

Ruiz-Donoso, E., Ehrlich, A., Schäfer, M., Jäkel, E., Schemann, V., Crewell, S., Mech, M., Kulla, B. S., Kliesch, L.-L., Neuber, R., and Wendisch, M.: Small-scale structure of thermodynamic phase in Arctic mixed-phase clouds observed by airborne remote sensing during a cold air outbreak and a warm air advection event, Atmospheric Chemistry and Physics, 20, 5487–5511, https://doi.org/10.5194/acp-20-5487-2020, 2020.

Schmetz, J., Pili, P., Tjemkes, S., Just, D., Kerkmann, J., Rota, S., and Ratier, A.: An Introduction to Meteosat Second Generation (MSG), Bulletin of the American Meteorological Society, 83, 992–992, https://doi.org/10.1175/1520-0477(2002)083<0977:AITMSG>2.3.CO;2, 2002.

Stamnes, K., Tsay, S.-C., Wiscombe, W., and Laszlo, I.: DISORT, a General-Purpose Fortran Program for Discrete-Ordinate-Method Radiative Transfer in Scattering and Emitting Layered Media: Documentation of Methodology, Tech. rep., Dept. of Physics and Engineering Physics, Stevens Institute of Technology, Hoboken, NJ 07030, 2000.

Stap, F., Hasekamp, O., Emde, C., and Röckmann, T.: Influence of 3D effects on 1D aerosol retrievals in synthetic, partially clouded scenes, Journal of Quantitative Spectroscopy and Radiative Transfer, 170, 54–68, https://doi.org/10.1016/j.jqsrt.2015.10.008, 2016.

Strabala, K. I., Ackerman, S. A., and Menzel, W. P.: Cloud Properties inferred from 8-12-μm Data, 33, 212–229, https://doi.org/10.1175/1520-0450(1994)033<0212:CPIFD>2.0.CO;2, 1994.

Strandgren, J., Bugliaro, L., Sehnke, F., and Schröder, L.: Cirrus cloud retrieval with MSG/SEVIRI using artificial neural networks, Atmospheric Measurement Techniques, 10, 3547–3573, https://doi.org/10.5194/amt-10-3547-2017, 2017.

Tan, I., Storelvmo, T., and Zelinka, M. D.: Observational constraints on mixed-phase clouds imply higher climate sensitivity, Science, 352, 224–227, https://doi.org/10.1126/science.aad5300, 2016.

Vázquez-Navarro, M., Mannstein, H., and Kox, S.: Contrail life cycle and properties from 1 year of MSG/SEVIRI rapid-scan images, Atmospheric Chemistry and Physics, 15, 8739–8749, https://doi.org/10.5194/acp-15-8739-2015, 2015.

Zhang, Z., Platnick, S., Yang, P., Heidinger, A. K., and Comstock, J. M.: Effects of ice particle size vertical inhomogeneity on the passive remote sensing of ice clouds, Journal of Geophysical Research: Atmospheres, 115, https://doi.org/10.1029/2010JD013835, 2010.

Chapter 8

P3: Method for the retrieval of thermodynamic phase

BAYESIAN CLOUD-TOP PHASE DETERMINATION FOR METEOSAT
SECOND GENERATION

Johanna Mayer, Luca Bugliaro, Bernhard Mayer, Dennis Piontek, Christiane Voigt
Atmospheric Measurement Techniques, 2024

Overview   We present the ProPS – a new method to detect clouds and their thermodynamic phase using SEVIRI. The new method distinguishes between clear sky, ice (optically thin/thick), MP, SC and warm liquid clouds. ProPS uses a Bayesian approach with the synergistic lidar-radar product DARDAR as reference data. Validation shows promising results with high detection rates and improved phase discrimination compared to traditional methods. The new method enables the study of clouds with different phases with high temporal resolution, in particular MP and SC clouds, which have been little studied from geostationary satellites so far.

Author contribution   I developed the methodology of the presented phase retrieval with valuable feedback from LB and BM. I wrote the code for the preparatory work, i.e. the computation of the mutual information and the probabilities of the SEVIRI channels. I wrote the algorithm for the retrieval, with help from DP in the final implementation of the algorithm. I performed the validation of the retrieval method against DARDAR and the comparison with CLoud property dAtAset using SEVIRI - Edition 3 (CLAAS-3). I prepared the figures and took the lead in writing the manuscript. All authors provided feedback on the manuscript. All authors contributed to the project through discussions. LB and CV supervised the research and were responsible for the funding.

Atmospheric
Measurement
Techniques

Bayesian cloud-top phase determination for Meteosat Second Generation

Johanna Mayer[1], **Luca Bugliaro**[1], **Bernhard Mayer**[1,2], **Dennis Piontek**[1], and **Christiane Voigt**[1,3]

[1]Deutsches Zentrum für Luft- und Raumfahrt, Institut für Physik der Atmosphäre, Oberpfaffenhofen, Germany
[2]Meteorologisches Institut, Ludwig-Maximilians-Universität München, Munich, Germany
[3]Institut für Physik der Atmosphäre, Johannes Gutenberg-Universität Mainz, Mainz, Germany

Correspondence: Johanna Mayer (johanna.mayer@dlr.de)

Abstract. A comprehensive understanding of the cloud thermodynamic phase is crucial for assessing the cloud radiative effect and is a prerequisite for remote sensing retrievals of microphysical cloud properties. While previous algorithms mainly detected ice and liquid phases, there is now a growing awareness for the need to further distinguish between warm liquid, supercooled and mixed-phase clouds. To address this need, we introduce a novel method named ProPS (PRObabilistic cloud top Phase retrieval for SEVIRI), which enables cloud detection and the determination of cloud-top phase using SEVIRI (Spinning Enhanced Visible and Infrared Imager), the geostationary passive imager aboard Meteosat Second Generation. ProPS discriminates between clear sky, optically thin ice (TI) cloud, optically thick ice (IC) cloud, mixed-phase (MP) cloud, supercooled liquid (SC) cloud and warm liquid (LQ) cloud. Our method uses a Bayesian approach based on the cloud mask and cloud phase from the lidar–radar cloud product DARDAR (liDAR/raDAR). The validation of ProPS using 6 months of independent DARDAR data shows promising results: the daytime algorithm successfully detects 93 % of clouds and 86 % of clear-sky pixels. In addition, for phase determination, ProPS accurately classifies 91 % of IC, 78 % of TI, 52 % of MP, 58 % of SC and 86 % of LQ clouds, providing a significant improvement in accurate cloud-top phase discrimination compared to traditional retrieval methods.

1 Introduction

Understanding and correctly identifying clouds and their thermodynamic phases in satellite remote sensing is crucial for several reasons. First, the phase critically affects cloud–radiation interactions (Choi et al., 2014; Komurcu et al., 2014; Matus and L'Ecuyer, 2017; IPCC, 2023; Cesana et al., 2022), and numerous studies have demonstrated the influence of the cloud phase on climate sensitivity in general circulation models (Gregory and Morris, 1996; Doutriaux-Boucher and Quaas, 2004; Cesana et al., 2012; Tan et al., 2016; Bock et al., 2020). Furthermore, phase transition processes depend on various factors like temperature, aerosol abundance and type, the Wegener–Bergeron–Findeisen process, vertical velocity and turbulence and are thus difficult to understand and model (Mioche et al., 2015; Korolev et al., 2017; Coopman et al., 2021; Ricaud et al., 2024). Accurate observations of cloud occurrence and thermodynamic phase are therefore essential to improve their representation in climate models (Atkinson et al., 2013; Cesana et al., 2015; Matus and L'Ecuyer, 2017; Moser et al., 2023; Hahn et al., 2023; Kirschler et al., 2023). Second, the reliable detection of clouds and the determination of the phase of each cloud is a critical first step in the remote sensing retrieval of cloud properties such as optical thickness, effective particle radius and water path. Ice and liquid cloud particles have different scattering and absorption properties, and an incorrect phase assignment can lead to significant errors in remotely retrieved cloud properties (Marchant et al., 2016).

Passive sensors aboard geostationary satellites play an important role in the observation of clouds and their thermodynamic phases. The advantages of these sensors are their

wide field of regard and their ability to observe the same area at any time of day, allowing the temporal evolution of clouds to be studied with high temporal resolution. However, determining the thermodynamic phases of clouds using passive sensors is a challenging task. In the past, passive-sensor phase retrievals often only distinguished between ice and liquid clouds (or between ice, liquid and unknown-phase clouds) (e.g. Key and Intrieri, 2000; Knap et al., 2002; Baum et al., 2012; Bessho et al., 2016; Marchant et al., 2016; Platnick et al., 2017; Benas et al., 2017). More recently, retrieval algorithms have been developed for imagers on geostationary satellites like the Advanced Baseline Imager (ABI) aboard GOES-R and the Advanced Himawari Imager (AHI) aboard Himawari-8, allowing for a further distinction between mixed-phase, liquid, and in the case of ABI supercooled liquid cloud tops (Pavolonis, 2010; Wang et al., 2019; Li et al., 2022). Nevertheless, accurately distinguishing between phases beyond just liquid and ice remains challenging (Korolev et al., 2017). Also, Mayer et al. (2023) show that mixed-phase and supercooled cloud tops are often present over the Meteosat disc, not only in regions like the Southern Ocean, and thus deserve dedicated retrieval algorithms.

We have developed a new cloud detection and cloud-top phase determination method for the Spinning Enhanced Visible and Infrared Imager (SEVIRI) on board the geostationary Meteosat Second Generation (MSG) satellite (Schmetz et al., 2002) that uses a Bayesian approach. Our focus is on the identification of mixed-phase and supercooled liquid clouds in addition to the "traditional" purely ice and warm liquid cloud tops. We use the lidar–radar cloud product DARDAR (liDAR/raDAR; Delanoë and Hogan, 2010) as the basis for this method. DARDAR is based on the combination of active radar and lidar measurements from the A-Train satellites CloudSat and CALIPSO and provides a consolidated classification of the measured clouds into different cloud phases. Synergistic lidar–radar techniques are considered the most reliable for cloud phase determination from satellites because the instruments used are complementary due to their different penetration depths and different particle size sensitivities (Wang, 2012; Delanoë and Hogan, 2008; Zhang et al., 2010; Korolev et al., 2017; Ewald et al., 2021). Over the years, they have been widely used to study the global horizontal and vertical distribution of cloud occurrence and cloud phases (Okamoto et al., 2010; Wang, 2012; Mioche et al., 2015; Matus and L'Ecuyer, 2017; Listowski et al., 2019). For our new phase retrieval method, we use the DARDAR product – which can distinguish between warm liquid, supercooled liquid, mixed-phase and ice clouds – as the ground truth for cloud and phase occurrence. We collocate 5 years of these data with SEVIRI measurements in selected channels and ancillary data to create a large collocated data set with information on the cloud-top phase from DARDAR. Our method then uses a probabilistic Bayesian approach as follows. We compute a prior representing the probability of cloud and phase occurrence as well as probabilities for SEVIRI chan-

nel measurements from the collocated data set. We update the prior with each successive SEVIRI measurement using Bayes' formula, resulting in probabilities for cloud occurrence and for the cloud-top phase based on the prior information and the selected SEVIRI measurements. The SEVIRI channels used in this calculation include three infrared channels (centred at 8.7, 10.8 and 12 µm), two visible channels (0.6 and 1.6 µm) and a local texture parameter derived from the 10.8 µm channel.

Bayesian approaches have proven successful in various classification problems using satellite data (Merchant et al., 2005; Mackie et al., 2010; Heidinger et al., 2012; Pavolonis et al., 2015; Meirink et al., 2022). One advantage of the Bayesian approach is its ability to handle complexity and consolidate diverse spectral information from different SEVIRI channels into a single metric (Pavolonis et al., 2015). Furthermore, it is straightforward to define a quality parameter for the result since the outcome of a Bayesian approach is a probability.

To test the performance of our method, we validate it using 6 months of DARDAR data which were not used for the computation of probabilities in order to keep the validation independent.

2 Data set

2.1 DARDAR-MASK

This study uses the product DARDAR-MASK, part of the synergistic active remote sensing product DARDAR, specifically the DARMASK_Simplified_Categorization data set (Delanoë and Hogan, 2010; Ceccaldi et al., 2013), as the ground truth for cloud occurrence and cloud thermodynamic phase. DARDAR-MASK is derived from the sun-synchronous, low-Earth-orbit satellites CloudSat (Stephens et al., 2002) and CALIPSO (Winker et al., 2003). To distinguish between cloud phases, DARDAR-MASK uses the wet-bulb temperature derived from the ECMWF-AUX data set (Benedetti, 2005) and the extent of cloud layers as well as the different sensitivities of lidar and radar to cloud particles of varying sizes: cloud layers containing water have a strong lidar backscatter and subsequent attenuation, while the CloudSat radar is mostly only sensitive to the larger ice crystals (Hogan et al., 2003). DARDAR-MASK provides the vertically resolved cloud thermodynamic phase along the tracks of the CALIPSO and CloudSat satellites with a spatial resolution of 1.1 km along track and 60 m in the vertical direction. For brevity, we use "DARDAR" instead of DARDAR-MASK to describe the cloud product in the following. An example curtain from DARDAR can be seen in the background of Fig. 6. We collocate 5 years (2013–2017) of DARDAR data with observations of the passive instrument SEVIRI aboard the geostationary satellite Meteosat-9 (part of the Meteosat Second Generation series) by merging over-

passes of the polar-orbiting satellites with the corresponding SEVIRI pixel for each time and latitude–longitude combination. The collocated DARDAR data are then aggregated to the spatial resolution of the SEVIRI sensor ($3 \times 3\,\mathrm{km}^2$ at the sub-satellite point). Details on how this collocation is done can be found in Mayer et al. (2023). From the DARDAR data, we extract two key pieces of information for each SEVIRI pixel: (1) whether a pixel is clear or cloudy and (2) the cloud-top phase. This cloud-top phase at SEVIRI's resolution is defined by horizontal and vertical averaging of DARDAR's gates using a simplified penetration depth (Mayer et al., 2023). We distinguish between warm liquid (LQ), supercooled liquid (SC), mixed-phase (MP) and ice clouds. MP cloud tops at SEVIRI's resolution are defined as containing either only gates classified as mixed phase by DARDAR or a mixture of liquid, ice and/or mixed-phase DARDAR gates in the cloud-top gates considered for the collocation (see Mayer et al., 2023, for details). To ensure that the averaging over DARDAR gates for a SEVIRI pixel is not done over two different clouds, the gates are all required to have a similar cloud-top height. For multilayered clouds, e.g. a high cirrus cloud on top of lower clouds, only the uppermost cloud layer is considered. For pure-ice clouds, we use information on the optical thickness contained in the DARDAR data to further distinguish between optically thin ice (TI) and thick ice (IC), where we use an optical thickness of 2 as the threshold. We employ this distinction since TI and IC have different radiative properties and are typically detected by different channel (combinations) of SEVIRI (see Sect. 4). The threshold for optical thickness is consistent with the cloud type categories of GOES-R (Pavolonis, 2010). To combine both aspects (cloudy/clear and the cloud-top phase), we introduce a "cloud state parameter", denoted as $q \in \{$clear, TI, IC, MP, SC, LQ$\}$. Note that in the following, when we use the terms "cloud state" or "cloud phase" in the context of our retrieval, we are referring to the phase of only the top of the cloud, as passive imagers such as SEVIRI cannot penetrate deep into a cloud.

2.2 Distribution of samples

Figure 1a shows the distribution of samples in the SEVIRI disc in latitude–longitude boxes of $2.5° \times 2.5°$. The figure demonstrates the good coverage of samples over the entire SEVIRI disc.

The DARDAR data are obtained from polar-orbiting satellites that follow a sun-synchronous orbit. Consequently, they can only provide information about clouds during the overflight times. This characteristic of the data has implications for our retrieval process, particularly for the use of solar channels and their dependence on solar and satellite viewing angles. Figure 1b shows the distribution of samples in the parameter space spanned by the solar zenith angle (sza) and the cosine of the satellite zenith angle (umu). Notably, there are two regions in this parameter space where no samples are
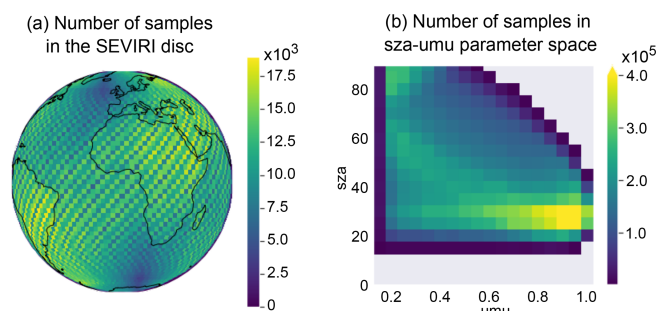
Figure 1. (a) Number of samples in latitude–longitude boxes of $2.5° \times 2.5°$ in the SEVIRI disc. (b) Number of samples in sza–umu (solar zenith angle–cosine of the satellite zenith angle) parameter space.

available: one is the region where sza values are below 20°; the other is the region with combinations of high umu and sza values. The use of solar channels in the retrieval is handled differently for these two regions. For sza values below 20°, the probabilities employed in the retrieval process are obtained from probabilities for sza values larger than 20°. For the regions of the parameter space that lack samples and have high sza and umu combinations, the solar channels are effectively not used. In a Bayesian update, this is done by imposing flat probability distributions for the solar channels in these regions of the parameter space; i.e. the cloud state probabilities are not changed by the solar channels. This is further explained in Sect. 6. In addition, since the DARDAR data do not contain data points at the sunglint, we also impose flat probability distributions for the solar channels close to the sunglint, defined as sunglint angles below 20°.

There are samples available for all other combinations of umu and sza. However, it is important to note that the data set does not include all of these possible combinations of angles for every latitude. For instance, at low latitudes, the overflight times always occur around noon, resulting in relatively low sza values (between 20 and 40° for latitudes between 0 and 10° N/S). The statistics for large sza values consequently originate from clouds in higher latitudes. This discrepancy could introduce a bias when using solar channels depending on angles, as meteorological and microphysical conditions in high latitudes may differ from those in lower latitudes.

In addition, as CloudSat operated in daylight-only mode, our data set only includes samples collected during the day. This could potentially introduce a bias into the nighttime retrieval for clouds whose properties differ between night and day.

2.3 Ancillary data

In addition, we include ancillary data such as surface temperature and surface type in the collocated data set. The surface temperature data are obtained from the ERA5 reanalysis (Hersbach et al., 2018) and interpolated to the SEVIRI grid.

For surface type classification, we have adopted the International Geosphere-Biosphere Programme (IGBP) scheme (Loveland and Belward, 1997) provided in the MODIS L3 product MCD12C1 (Friedl et al., 2010). Surface types are grouped into five categories (water, barren, permanent ice and snow, forest, and vegetation excluding forest) and projected onto the SEVIRI grid (for details, see Strandgren et al., 2017). In summary, our collocated data set includes the cloud state parameter q from DARDAR, SEVIRI observations, and ancillary data from ERA5 and IGBP for 5 years of data. These data spanning 5 years amount to over 40 million data points. The use of all these years should ensure that a reasonable amount of annual variability is accounted for.

3 Bayes' approach applied to satellite data

The output of our new cloud state retrieval method ProPS (PRObabilistic cloud top Phase retrieval for SEVIRI) is a probability for the cloud state, given all (useful) SEVIRI measurements (as defined in Sect. 4) and ancillary data. In the following, we explain how this probability is computed with the help of Bayes' formula. Figure 2 shows a schematic of the method.

3.1 Bayes' method

First, we use the collocated data set to compute probabilities $P(q \mid A)$ for the occurrence of each cloud state q, conditioning on a set of ancillary parameters A independent of the satellite observations. These probabilities serve as priors of the cloud state distribution and are updated for each SEVIRI measurement. The updated probability for the cloud state, $P(q \mid M_1, A)$, given a SEVIRI measurement M_1 (i.e. a brightness temperature (BT), a brightness temperature difference (BTD) or a solar observation; see below) and the set of ancillary parameters A already mentioned above, is calculated using Bayes' formula:

$$P(q \mid M_1, A) = \frac{P(M_1 \mid q, A) P(q \mid A)}{P(M_1 \mid A)}. \quad (1)$$

The first term in the numerator, $P(M_1 \mid q, A)$, is a conditional probability for the SEVIRI measurement M_1 and can be derived from the collocated SEVIRI–DARDAR data set (Sect. 2). The denominator $P(M_1 \mid A)$ acts as a normalization factor. It can be computed by breaking it down for each possible cloud state q, leading to the following decomposition: $P(M_1 \mid A) = \sum_q P(M_1 \mid q, A) P(q \mid A)$. Note that this is equal to the numerator of Eq. (1) summed over all cloud states q. Hence, all of the terms needed to compute the updated probability $P(q \mid M_1, A)$ can be derived from the collocated data set. We repeat the same step for subsequent SEVIRI measurements. Updating the probability with a second SEVIRI measurement M_2 leads to

$$P(q \mid M_2, M_1, A) = \frac{P(M_2 \mid q, M_1, A) P(M_1 \mid q, A) P(q \mid A)}{P(M_2 \mid M_1, A) P(M_1 \mid A)}, \quad (2)$$

with Bayes' formula applied twice. For a series of n measurements, the probability for cloud state q given all the measurements $M := (M_1, M_2, \ldots, M_n)$ and ancillary parameters A can be expressed as

$$P(q \mid M, A) = \frac{1}{N} P(M_n \mid q, M_{n-1}, \ldots, M_1, A) \ldots$$
$$P(M_2 \mid q, M_1, A) P(M_1 \mid q, A) P(q \mid A), \quad (3)$$

with the normalization factor

$$N = P(M_n \mid M_{n-1}, \ldots, M_1, A) \ldots P(M_2 \mid M_1, A) P(M_1 \mid A). \quad (4)$$

Thanks to Eq. (3), we can compute a probability for the cloud state q that takes into account (i) prior knowledge about q, (ii) all SEVIRI measurements M and (iii) all ancillary parameters A.

The data requirements for calculating each probability scale with the number of parameters used as conditions. Fortunately, the conditional probabilities on the right-hand side of Eq. (3) can be simplified by considering the dependencies of the different SEVIRI channels. For example, if the measurement of one channel, M_2, is (approximately) independent of the measurement of another channel, M_1, then its probability reduces to $P(M_2 \mid q, M_1, A) = P(M_2 \mid q, A)$. Similarly, if a measurement is independent of certain auxiliary parameters, these parameters can be removed from set A in the conditional probability (i.e. $A = \{a_1, a_2, a_3, \ldots\} \rightarrow A = \{a_1, a_3, \ldots\}$ if M_2 is independent of a_2). This simplification step is essential to ensure that the probabilities are meaningful and statistically valid. Given the size of our data set (about 40 million data points), we limit the number of conditions to a maximum of four per probability to ensure statistical validity. In cases where a SEVIRI measurement depends on more than four of the parameters in its conditional probability, we carefully select the most significant of these parameters and focus on those, removing the less significant parameters. The selection of channels and conditions for each probability is further explained in the following section (Sect. 4).

3.2 Retrieval result

The result of Eq. (3) is a probability for each cloud state q. As the final result of the retrieval method, we choose the most likely cloud state, q^*, i.e. the cloud state with the highest probability for each SEVIRI pixel:

$$q^* = \max_q (P(q \mid M, A)). \quad (5)$$

Thus, the final result is one cloud state per SEVIRI pixel.

3.3 Measure of certainty

There are several advantages of using (Bayesian) probabilities. First, they allow us to incorporate prior knowledge. This
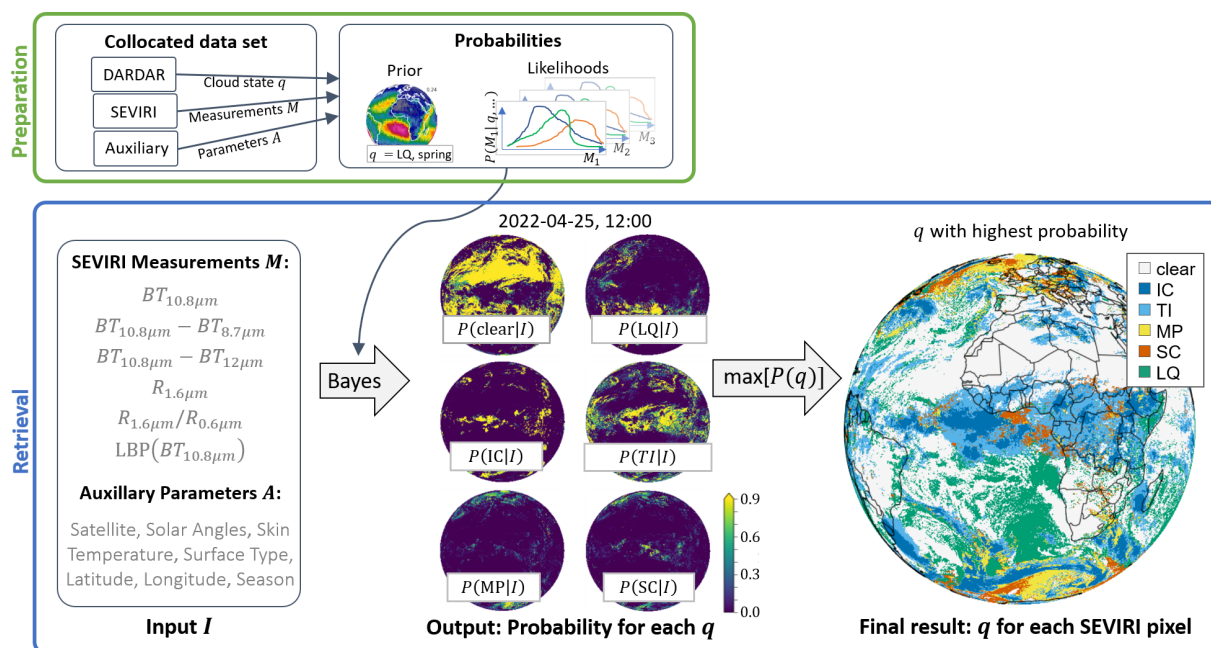
Figure 2. Scheme of the phase retrieval method ProPS. The green box shows the preparation for the retrieval, i.e. the calculation of the probabilities from the collocated data set. The blue box shows the phase retrieval steps of ProPS.

is in contrast to traditional decision-tree models, which typically do not take this valuable information into account. Second, Bayes' formula provides a standardized approach to integrating information from different channel measurements into a single objective metric. It eliminates the need for arbitrary rules when faced with conflicting cloud state indications from different measurements. Third, the approach maintains transparency; one can clearly understand the origin of the probability values assigned to each cloud state. Finally, since the outcome is a probability for each cloud state, it is straightforward to develop a measure of certainty (a quality measure) associated with the outcome. We define the certainty c as the difference between the probability for q^* and the average probability of the remaining cloud states q':

$$c = P(q^* \mid M, A) - \frac{1}{5} \sum_{q'} P(q' \mid M, A). \tag{6}$$

This certainty is a number between 0 and 1. It is close to 1 when the highest probability is much larger than the other probabilities. The certainty becomes small when the probabilities for other cloud states are close to the highest probability.

4 Selection of channels and dependencies

This section describes which SEVIRI channels and conditions are used for each probability. From the collocated data set, we have the following set of ancillary parameters:

$$A = \{\text{sza, umu, sfc, skt, lat, long, season}\}, \tag{7}$$

where "sza" is the solar zenith angle, "umu" is the cosine of the satellite zenith angle, "sfc" is the surface type, "skt" is the surface temperature, "lat" is the latitude, "long" is the longitude and "season" is one of the four seasons of the year (December–January–February, March–April–May, June–July–August or September–October–November).

To choose the SEVIRI channels and their most important dependencies for the retrieval, we combine theoretical principles of the physics involved with statistical tools. First, we select channels and channel combinations that are known to carry information about the cloud state. We also consider only a selection of conditions for the probability of each channel (or channel combination) that make sense from a physical perspective. From this selection of physically meaningful conditions, we decide on the optimal conditions for the probability of each channel (or channel combination) using the statistical tool of *mutual information* (Shannon and Weaver, 1949; Cover and Thomas, 2005). The mutual information $I(M_i; q)$ between a channel (or channel combination) M_i and q is a measure of the information content of M_i with respect to q: the higher the mutual information, the greater the information that can be gained from M_i in a retrieval of q. We calculate the mutual information $I(M_i; q \mid C)$ for different sets of conditions C to find the set of conditions C^* which maximizes the mutual information. These optimal sets of conditions are then used for the respective conditional probabilities, $P(M_i \mid q, C^*)$. A selection of computed mutual information values for different SEVIRI channels (or channel combinations) and sets of conditions are displayed in Table 1. To gain insights into the contributions of different

Table 1. The first part of the table shows the mutual information I between the latitude and the cloud state q (first row), cloudy/clear state (abbreviated to "c/c"; second row), and cloud phase (third row) for different sets of conditions C. This represents the information content of the different priors we considered, where latitude is a fixed condition, i.e. $P(q\,|\,\mathrm{lat}, C)$. The other parts of the table show the mutual information I between SEVIRI channels (or channel combinations) and cloud state q, c/c and cloud phase for different sets of conditions C. Columns with no condition C refer to the starting point of I before conditions are introduced. The different mutual information values for q, c/c and phase indicate whether a channel (or channel combination) contributes more to cloud or phase detection. The blue boxes indicate the sets of conditions selected for ProPS.

		long	sfc	skt	sza	long, season	sfc, season
$I(\mathrm{lat}; q)$	0.066	0.085	0.065	0.02	0.046	0.1	0.076
$I(\mathrm{lat}; c/c)$	0.031	0.042	0.025	0.013	0.026	0.05	0.031
$I(\mathrm{lat}; \mathrm{phase})$	0.067	0.085	0.074	0.017	0.042	0.098	0.085
				conditions C			

		skt	skt, lat	skt, umu	skt, lat, umu
$I(BT_{10.8}; q)$	0.21	0.21	0.21	0.25	0.25
$I(BT_{10.8}; c/c)$	0.12	0.13	0.14	0.17	0.17
$I(BT_{10.8}; \mathrm{phase})$	0.18	0.17	0.17	0.19	0.19
			conditions C		

	$BT_{10.8}$	$BT_{10.8}$, sfc	$BT_{10.8}$, lat	$BT_{10.8}$, umu, sfc	$BT_{10.8}-$skt, umu, sfc
$I(BTD_{10.8-8.7}; q)$	0.074	0.073	0.066	0.075	0.065
$I(BTD_{10.8-8.7}; c/c)$	0.026	0.027	0.02	0.016	0.017
$I(BTD_{10.8-8.7}; \mathrm{phase})$	0.085	0.082	0.08	0.099	0.083
			conditions C		

	$BT_{10.8}$	$BT_{10.8}$, sfc	$BT_{10.8}$, $BTD_{10.8-8.7}$	$BT_{10.8}$, lat
$I(BTD_{10.8-12}; q)$	0.09	0.11	0.11	0.059	0.1
$I(BTD_{10.8-12}; c/c)$	0.011	0.013	0.016	0.014	0.018
$I(BTD_{10.8-12}; \mathrm{phase})$	0.059	0.085	0.083	0.041	0.076
		conditions C			

	$BT_{10.8}$	sfc	sfc, sza	sfc, sza, umu
$I(R_{1.6}; q)$	0.066	0.058	0.11	0.11	0.12
$I(R_{1.6}; c/c)$	0.05	0.039	0.11	0.12	0.13
$I(R_{1.6}; \mathrm{phase})$	0.042	0.047	0.046	0.041	0.047
		conditions C			

	sfc	umu, sza	sfc, sza, umu	umu, sza, $R_{1.6}$	sfc, umu, sza, $R_{1.6}$
$I(RR_{1.6/0.6}; q)$	0.13	0.14	0.14	0.16	0.15	0.12
$I(RR_{1.6/0.6}; c/c)$	0.11	0.11	0.11	0.13	0.11	0.06
$I(RR_{1.6/0.6}; \mathrm{phase})$	0.075	0.094	0.093	0.11	0.12	0.12
			conditions C		

	sfc	sfc, lat	sfc, umu	sfc, $BT_{10.8}$
$I(\mathrm{LBP}(BT_{10.8}); q)$	0.063	0.076	0.086	0.096	0.059
$I(\mathrm{LBP}(BT_{10.8}); c/c)$	0.048	0.062	0.061	0.072	0.027
$I(\mathrm{LBP}(BT_{10.8}); \mathrm{phase})$	0.044	0.047	0.06	0.064	0.058
		conditions C			

channels (or channel combinations) to cloud and phase detection, we additionally calculate the mutual information between each channel M_i and the cloud classification cloudy/-clear as well as that between M_i and the phase classification under the specified conditions C. By comparing the mutual information values for $I(M_i; q\,|\,C)$, $I(M_i; \mathrm{cloudy/clear}\,|\,C)$ and $I(M_i; \mathrm{phase}\,|\,C)$, we can assess the extent to which each channel contributes to the detection of cloudy or clear conditions and to the determination of cloud phase.

In the following, we briefly describe which conditional probabilities are consequently used for the retrieval. We discuss the physical connection between each channel (or channel combination) and the cloud state q, and we explore the physical reasons why the chosen conditions for the probabilities might enhance their information content.

4.1 Prior

We use the probability

$$P(q \mid \text{lat, long, season}) \qquad (8)$$

as prior knowledge. This means that the prior is the probability for each cloud state per latitude, longitude and season, calculated from the 5 years of collocated data. Besides latitude, longitude and season, the set of ancillary parameters A introduced above in Sect. 4 also includes surface type, surface temperature and solar/satellite zenith angles. However, since latitude and longitude are already constrained, incorporating surface type or satellite viewing angle as additional constraints becomes unnecessary. Furthermore, our mutual information calculations show that conditioning on latitude, longitude and season yields the prior with the optimal information content compared to other possible sets of conditions (see Table 1). This means that location (latitude and longitude) and season are the main dependencies.

4.2 Brightness temperature at 10.8 μm

We use the BT centred at 10.8 μm wavelength, $\text{BT}_{10.8}$, located in the atmospheric window of the electromagnetic spectrum, as the first SEVIRI measurement. At this wavelength, the atmosphere is more transparent than at all the other SEVIRI infrared channels. Therefore, it is a good approximation for the temperature of the surface and (optically thick) cloud tops – one of the most important parameters for cloud detection and phase discrimination. This can also be seen in Table 1, as the mutual information between q and $\text{BT}_{10.8}$ has higher values compared to all other SEVIRI channel mutual information values. We use the conditional probability

$$P(\text{BT}_{10.8} \mid q, \text{umu, skt}). \qquad (9)$$

By conditioning on skt, we take into account the temperature difference (contrast) between $\text{BT}_{10.8}$ and the surface temperature. This is particularly important for cloud detection. The dependence on umu is particularly relevant for optically thin clouds, where a higher satellite zenith angle means an effective increase in optical thickness and therefore smaller $\text{BT}_{10.8}$ values.

4.3 Brightness temperature difference between the 10.8 and 8.7 μm channels

The BTD between the 10.8 and 8.7 μm window channels is commonly used in phase determination algorithms (Menzel et al., 2002; Platnick et al., 2003; Zhou et al., 2022). This BTD, denoted as $\text{BTD}_{10.8-8.7}$, provides valuable information about the cloud phase in several ways. Firstly, it is sensitive to the amount of water vapour present above the cloud top. This is because the 8.7 μm channel is more strongly affected by water vapour absorption in the atmosphere com-

pared to the 10.8 μm channel. Thus, the BTD is closely related to the cloud-top height and thus to the cloud-top temperature, which, in turn, is related to the cloud phase. Secondly, the BTD is influenced by the effective radius of cloud particles (Ackerman et al., 1990). This parameter provides a clue about the phase of the cloud, since ice crystals generally have larger effective radii than liquid droplets. Thirdly, $\text{BTD}_{10.8-8.7}$ is sensitive to cloud optical thickness (for small optical thicknesses; Ackerman et al., 1990). On the one hand, this is helpful for the detection of optically thin clouds; on the other hand, this can indirectly indicate the cloud phase, since only ice clouds, such as cirrus clouds, typically show very low optical thicknesses. Note, however, that dissipating clouds or fractional cloud cover can also result in low optical thickness in SEVIRI pixels, which could bias the interpretation of these clouds as ice clouds. Lastly, the BTD also has a direct dependence on cloud phase for optically thin clouds, i.e. when transmission through the cloud is significant, since the variation in scattering and absorption properties between the wavelengths 8.7 and 10.8 μm is different for ice crystals and liquid droplets. We use the conditional probability

$$P(\text{BTD}_{10.8-8.7} \mid q, \text{BT}_{10.8}, \text{umu, sfc}). \qquad (10)$$

Conditioning on umu takes into account that the satellite zenith angle affects the path length and therefore both the amount of water vapour above the cloud and the effective cloud optical thickness. We also condition on the surface type since the typical values of $\text{BTD}_{10.8-8.7}$ for clear sky differ between surface types – especially for deserts such as the Sahara or the Arabian Peninsula due to the low spectral emissivity of desert dust at 8.7 μm (Masiello et al., 2014). The relationship with $\text{BT}_{10.8}$ is obvious since it is contained in $\text{BTD}_{10.8-8.7}$.

4.4 Brightness temperature difference between the 10.8 μm and 12.0 μm channels

The BTD between the two window channels at wavelengths of 10.8 and 12.0 μm is often used in satellite retrievals for cloud detection and cloud properties (e.g. Key and Intrieri, 2000; Pavolonis et al., 2005; Krebs et al., 2007; Kox et al., 2014; Hünerbein et al., 2023). $\text{BTD}_{10.8-12.0}$ is mainly sensitive to optical thickness and effective radius. Both of these quantities contain information about the cloud phase, as mentioned above. Furthermore, $\text{BTD}_{10.8-12.0}$ also depends directly on the phase, especially for small optical thicknesses, since (just as for $\text{BTD}_{10.8-8.7}$) the scattering and absorption properties between the two wavelengths 12.0 and 10.8 μm vary differently for ice crystals and liquid droplets (Key and Intrieri, 2000). We use the conditional probability

$$P(\text{BTD}_{10.8-12.0} \mid q, \text{BT}_{10.8}, \text{sfc}). \qquad (11)$$

Since the main sensitivity is to optical thickness, $\text{BTD}_{10.8-12.0}$ is mainly useful for detecting thin ice clouds.

This is particularly useful when combined with $BT_{10.8}$, as $BTD_{10.8-12.0}$ can distinguish between warm cloud-top temperatures and optically thin clouds with warm surface temperatures, which may have the same value of $BT_{10.8}$.

4.5   Reflectivity of the 1.6 µm channel

The reflectivity of solar radiation is generally a good indicator of the presence of a cloud, as clouds are usually brighter (more reflective) than the surface for clear-sky conditions. Further, the near-infrared (NIR) reflectivity, like the 1.6 µm channel, is a well-established indicator of cloud phase, as the reflectivity at 1.6 µm, $R_{1.6}$, is sensitive to the effective radius of cloud particles. The typically small liquid droplets reflect more radiation at this wavelength than the typically large ice crystals. In addition to its sensitivity to the effective radius, $R_{1.6}$ is also sensitive to the phase itself, since ice absorbs more radiation than water at this wavelength. We use the conditional probability

$$P(R_{1.6} \mid q, \text{sza}, \text{umu}, \text{sfc}). \qquad (12)$$

Conditioning on the solar and satellite zenith angles, sza and umu, takes into account that reflectivities are angle dependent. The sensitivity of $R_{1.6}$ to azimuth angle is comparatively small; we therefore neglect it in order to keep the number of conditions small. The surface type, sfc, is a proxy for surface albedo, as different surface types have their own typical albedo values.

4.6   Reflectivity ratio of the 0.6 and 1.6 µm channels

For the next observation, we consider the reflectivity ratio $RR_{1.6/0.6} = \frac{R_{1.6}}{R_{0.6}}$. The combination of an NIR channel ($R_{1.6}$) and a visible channel ($R_{0.6}$) is often used to retrieve cloud microphysical parameters such as effective radius and optical thickness (Nakajima and King, 1990). These microphysical parameters contain phase information, so combining NIR and visible channels is useful for a phase retrieval (Knap et al., 2002; Marchant et al., 2016). We use the ratio between the two channels to reduce the dependence on the solar and satellite viewing angles as well as that on particle number concentration (Chylek et al., 2006). We use the probability

$$P(RR_{1.6/0.6} \mid q, R_{1.6}, \text{sza}, \text{umu}). \qquad (13)$$

Apart from the dependence on $R_{1.6}$, we again consider the solar and satellite zenith angles for the same reasons as for the conditional probability of $R_{1.6}$.

4.7   Local binary pattern at 10.8 µm

Finally, we use the local binary pattern (LBP) of the 10.8 µm infrared channel, $LBP(BT_{10.8})$. The LBP technique is used for texture analysis. This characterizes the spatial variations of pixel intensities by comparing the central pixel with its surrounding neighbours within a defined local region. Texture parameters have already been used in Bayesian retrieval methods for cloud detection (Merchant et al., 2005). The texture of clouds differs in most cases from the texture of the surface, so the LBP can help in the detection of clouds. Further, the texture of cloudy regions can differ for different cloud types; for example, small cumulus clouds show large local spatial variations, whereas large smooth cirrus clouds show small variations. Since different cloud types are associated with different cloud phases, the LBP is also a suitable parameter for phase detection.

To compute the LBP, the central pixel is compared with eight surrounding pixels in a defined neighbourhood: if the intensity value of a neighbour is greater than or equal to the intensity of the central pixel, a binary 1 is assigned; otherwise, a binary 0 is assigned for each neighbour. The sum of these binary values contains valuable texture information: a maximum sum value of 8 indicates a uniform image region, while lower values indicate non-uniform regions. For example, a sum of 4 indicates an even distribution of neighbours with both higher (or equal) and lower intensities compared to the central pixel. A Gaussian filter is then applied to smooth the results to obtain a continuous value.

The infrared channel $BT_{10.8}$ is well suited for calculating a texture, as the atmosphere is more transparent at this wavelength compared to all other SEVIRI infrared channels. The advantage of choosing an infrared channel is that it is also available during the night. The LBP of $BT_{10.8}$ is particularly useful for detecting low clouds during the night, which are otherwise difficult to distinguish from clear sky for infrared channels. We use the conditional probability

$$P(LBP(BT_{10.8}) \mid q, \text{sfc}, \text{umu}). \qquad (14)$$

The conditioning on surface type, sfc, takes into account that different surface types have different textures. The conditioning on umu takes into account that pixel sizes, and therefore the computed texture from LBP, vary with umu.

5   The PRObabilistic cloud top Phase retrieval for SEVIRI (ProPS)

This section gives an overview of the ProPS retrieval method using the equations and probabilities explained in the last two sections (Sects. 3 and 4). Figure 2 gives a schematic overview of the retrieval method.

5.1   Cloud-top phase

The output of the Bayesian method is the probability $P(q \mid M, A)$ for each cloud state $q \epsilon$ {clear, TI, IC, MP, SC, LQ}. We use the cloud state with the highest probability, q^*, as the final result.

5.2 Daytime

Using the probabilities for the selection of SEVIRI channels, as explained in the previous section, the cloud state retrieval equation for ProPS (see Eq. 3) becomes

$$P(q \mid M, A) = \frac{1}{N} P(\text{LBP}(\text{BT}_{10.8}) \mid q, \text{sfc}, \text{umu})$$

$$P(\text{RR}_{1.6/0.6} \mid q, R_{1.6}, \text{sza}, \text{umu})$$

$$P(R_{1.6} \mid q, \text{sza}, \text{umu}, \text{sfc})$$

$$P(\text{BTD}_{10.8–12.0} \mid q, \text{BT}_{10.8}, \text{sfc})$$

$$P(\text{BTD}_{10.8–8.7} \mid q, \text{BT}_{10.8}, \text{umu}, \text{sfc})$$

$$P(\text{BT}_{10.8} \mid q, \text{umu}, \text{skt}) \, P(q \mid \text{lat}, \text{long}, \text{season}), \tag{15}$$

with the normalization factor $N = N(M, A)$ defined such that $\sum_q P(q \mid M, A) = 1$. M is the set of SEVIRI channels (or channel combinations),

$$M = \{\text{LBP}(\text{BT}_{10.8}), \text{RR}_{1.6/0.6}, R_{1.6}, \text{BTD}_{10.8–12.0},$$

$$\text{BTD}_{10.8–8.7}, \text{BT}_{10.8}\}, \tag{16}$$

and A the set of ancillary parameters (see Eq. 7).

5.3 Nighttime

During the night, only thermal SEVIRI channels are available. For the night version of ProPS, we therefore only use probabilities of the thermal channels from Eq. (15):

$$P(q \mid M, A) = \frac{1}{N} P(\text{LBP}(\text{BT}_{10.8}) \mid q, \text{sfc}, \text{umu})$$

$$P(\text{BTD}_{10.8–12.0} \mid q, \text{BT}_{10.8}, \text{sfc})$$

$$P(\text{BTD}_{10.8–8.7} \mid q, \text{BT}_{10.8}, \text{umu}, \text{sfc})$$

$$P(\text{BT}_{10.8} \mid q, \text{umu}, \text{skt}) \, P(q \mid \text{lat}, \text{long}, \text{season}). \tag{17}$$

6 Computation of probabilities

We use the method of kernel density estimation (KDE) to compute the probabilities needed for ProPS from the collocated data set. KDE is a technique for estimating a probability density function (pdf) which better represents the details of the pdf compared to traditional histograms (Węglarczyk, 2018). The KDE technique provides a smooth estimate of the pdf without imposing assumptions about its shape. Further advantages are that, unlike histograms, it includes all sample point locations and can more convincingly suggest the presence of multiple modes (Węglarczyk, 2018). Consider a variable of interest x with an unknown probability distribution $P(x)$ and a sample of n observations, $x_1, x_2, \ldots x_n$, of that variable. To compute the kernel estimate $\hat{P}(x)$ for the true probability distribution $P(x)$, we assign a kernel function $K(x_i, x)$ to each sample data point x_i as follows (Silverman, 1986; Węglarczyk, 2018):

$$\hat{P}(x) = \frac{1}{n} \sum_{i=1}^{n} K(x_i, x). \tag{18}$$
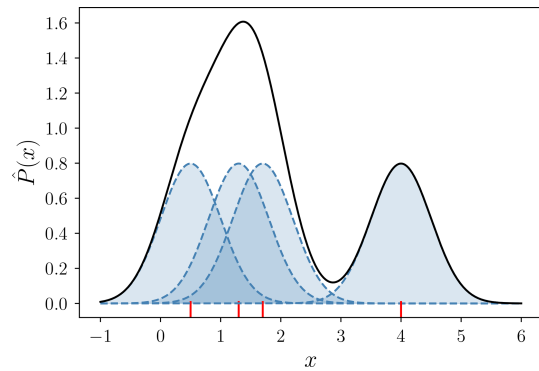
Figure 3. Construction of a kernel density estimate (continuous line) with a Gaussian kernel (dashed lines) for four samples of the true probability distribution (vertical red line segments). Figure adapted from Węglarczyk (2018) (CC BY 4.0, https://creativecommons.org/licenses/by/4.0/, last access: 1 February 2024).

The kernel function $K(x_i, x)$ is centred at x_i and normalized to unity, i.e. $\int_{-\infty}^{+\infty} K(x_i, x) \mathrm{d}x = 1$. We employ a Gaussian kernel function, which is commonly used. The kernel transforms the discrete point location represented by x_i into a smooth distribution centred around x_i. Figure 3 illustrates this technique for the one-dimensional case. For $d > 1$ dimensions, both x and x_i become d-dimensional vectors instead of scalars. For example, in our case, to compute the probability $P(\text{BT}_{10.8}, q, \text{umu}, \text{skt})$, the variable x is a four-dimensional vector $\boldsymbol{x} = (\text{BT}_{10.8}, q, \text{umu}, \text{skt})$.

The width of the kernel function determines the amount of smoothing and is represented by a parameter called the bandwidth h. Too small values of h may result in a probability estimate that shows insignificant details, while too large values of h may smooth out important features (Węglarczyk, 2018). A certain compromise is needed. We choose to use an (effectively) dynamic bandwidth h since there are regions of parameter space with many samples that allow small values of h and other regions with few samples that require large h values. Before computing the kernel estimate $\hat{P}(x)$, the variable x is transformed: $x^t = f(x) := \arctan\left(\frac{1}{\beta}(x - \alpha)\right)/\gamma$. As a non-linear transformation, $f(x)$ can reshape the distribution of the data by stretching or compressing certain regions by fine-tuning the α, β and γ parameters. The parameters of the transformation are chosen for each variable x in such a way that the samples of the variable x_i are more evenly distributed in the transformed space. The arctan function in the transformation is particularly useful for this purpose, as it has the ability to condense the edges of parameter space, where there are typically fewer samples, while expanding the central region. The parameters α and β can be understood as the global mean and variance of the variable x. Additionally, these transformation parameters are chosen to ensure that all transformed variables fall within a similar range, typically

Table 2. Parameters for transforming and computing the kernel density estimate (KDE) for SEVIRI measurements and ancillary parameters.

Variable	Transformation parameters	Bandwidth
$BT_{10.8}$	$\alpha = 270, \beta = 30, \gamma = 1$	0.04
$BTD_{10.8-8.7}$	$\alpha = 2.3, \beta = 2, \gamma = 1.5$	0.04
$BTD_{10.8-12}$	$\alpha = 1, \beta = 3, \gamma = 1.1$	0.04
$R_{1.6}$	$\alpha = 30, \beta = 40, \gamma = 1$	0.04
$RR_{1.6/0.6}$	$\alpha = 0.7, \beta = 1.1, \gamma = 1$	0.04
$LBP(BT_{10.8})$	$\alpha = 6, \beta = 2, \gamma = 1$	0.04
sza	$\alpha = 45, \beta = 120, \gamma = 1$	0.04
umu	$\alpha = 0.58, \beta = 1.2, \gamma = 1$	0.04
skt	$\alpha = 290, \beta = 20, \gamma = 1$	0.04
lat	No transformation	2
long	No transformation	2

Figure 4. Examples of the probability distribution $P(BT_{10.8} \,|\, q, \text{umu}, \text{skt})$ computed using KDE with fixed values for umu and skt.

around -1 to 1, to maintain similar smoothness in the directions of all variables. This requires (in some cases) linear scaling with the γ parameter in the transformation function. After the transformation, the kernel estimate $\hat{P}^t(x^t)$ is computed in the transformed space using a constant bandwidth. The variable is finally transformed back to the original variable space: $\hat{P}^t(x^t) = \hat{P}^t(f(x)) =: \hat{P}(x)$. This approach results in a narrower kernel in regions with many x_i samples and a wider kernel in regions with fewer x_i samples. Consequently, our procedure allows for detailed features in the kernel estimate $\hat{P}(x)$ where numerous samples are available while maintaining reasonable smoothness and flatness in regions with limited samples. The transformation parameters as well as the bandwidth for each variable are shown in Table 2.

In the case of discrete variables such as q, season or surface type, the KDE method cannot be used directly. Instead, we divide the variable space into subcategories based on all possible combinations of the discrete variables of the probability in question. For each subset, we utilize the KDE method to calculate the probability for the continuous variables within that specific subcategory. Subsequently, we normalize the probabilities to obtain a normalized probability distribution that incorporates both discrete and continuous variables.

Using the computed kernel estimate $P(x)$, where x is the d-dimensional vector $\boldsymbol{x} = (X^1, X^2, \dots X^d)$, a conditional probability can be computed using the relationship

$$P\left(X^1 \,|\, X^2, \dots, X^d\right) = \frac{P\left(X^1, X^2, \dots, X^d\right)}{P\left(X^2, \dots, X^d\right)}$$
$$= \frac{P\left(X^1, X^2, \dots, X^d\right)}{\sum_{X^1} P\left(X^1, X^2, \dots, X^d\right)}. \quad (19)$$

The probabilities are only computed for the locations in parameter space where a sufficient number of samples, x_i, are available. If too few samples are available, the pdf is set
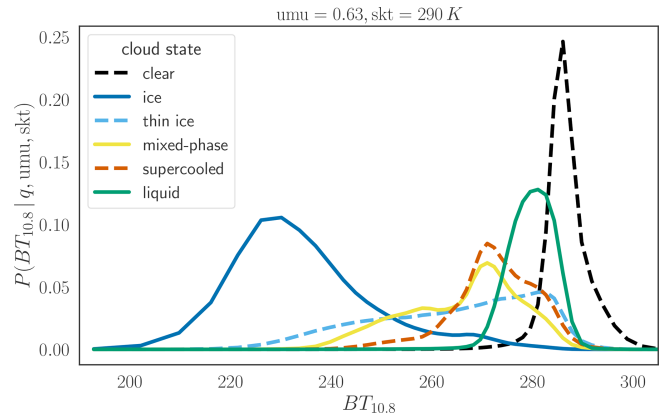
to a flat distribution; i.e. it contains no information and does not change the probability for cloud state q when multiplied as in the retrieval equation (15). Since the collocated data set is quite large, this is only necessary for a few special cases. Most notably, this is necessary for the solar channel $R_{0.6}$ and channel combination $RR_{1.6/0.6}$ for the regions of sza–umu parameter space where no samples are available (see Sect. 2.2 and Fig. 1). There is, however, one important special case for the probabilities of the solar channel $R_{0.6}$ and channel combination $RR_{1.6/0.6}$ in which we proceed differently. DARDAR data are not available for sza values below 20° (see Sect. 2.2), as the sun-synchronous orbits of the polar-orbiting satellites CALIPSO and CloudSAT never reach low sza values. For these relatively low sza values, the dependence of the reflectivity on sza is small compared to other dependencies. As a simple solution for this special case, we therefore use the probabilities calculated for the lowest available sza for the smaller values of sza too.

Using this KDE method, we compute all probability distributions needed for the ProPS algorithm (see Eq. 15). Figure 4 shows examples of the probability $P(BT_{10.8} \,|\, q, \text{umu}, \text{skt})$, i.e. the probability of measuring particular $BT_{10.8}$ values, given the cloud states q (in different colours) and with fixed values for the surface temperature (skt) and satellite zenith angle (umu). As expected, for clear sky, the probability peaks at $BT_{10.8}$ values close to the surface temperature. The probability distribution shifts to lower $BT_{10.8}$ values upon shifting from LQ to SC to MP to IC clouds. There are, however, large overlap regions, which show that the cloud state cannot be determined from $BT_{10.8}$ measurements alone. TI clouds have a relatively flat probability distribution over a wide range of $BT_{10.8}$ values since the radiation from the surface is transmitted to a varying degree. More examples of probability distributions can be found in the Appendix (see Fig. A1).

7 Example application of ProPS

Figure 5 (right) shows the output of the ProPS retrieval for an example of a SEVIRI scene obtained on 25 April 2022 at 12:00 UTC. For comparison, the natural colour RGB of the scene is also shown on the left of the figure. The result of the ProPS retrieval looks sensible. The retrieval detects (most of) the clouds which can be seen in the RGB. The distribution of phases on the SEVIRI disc makes physical sense, with, for example, mainly IC in the Intertropical Convergence Zone (ITCZ), LQ over the subtropical ocean and SC/MP mainly over the Southern Ocean and at northern high latitudes.

8 Performance evaluation using DARDAR

In this section, we evaluate how well ProPS is able to reproduce the DARDAR cloud detection and phase classification. To this end, we randomly select 6 months from the 5-year collocated data set as a validation data set (under the constraint that every season must be represented), which amounts to about 3.7 million data points. These data points of the validation data set are not used for the computation of the probabilities (see Sect. 6), allowing us to perform an independent validation.

8.1 Comparison to DARDAR example tracks

We start the performance evaluation with two example curtains from DARDAR to highlight the strengths of the ProPS retrieval and the challenges posed by, for example, complex cloud scenes or the different viewing geometries of polar-orbiting and geostationary satellites (see Fig. 6). These two examples demonstrate how the retrieval works at different latitudes and under different meteorological conditions. Both examples show a DARDAR curtain coarsened to SEVIRI resolution and the corresponding results of the ProPS algorithm in the plots above, i.e. the probabilities for cloud state q and the certainty measure along the track. Overlaid on the DARDAR curtain, the figures also show the most likely cloud state from ProPS, q^*, and the cloud state retrieved from DARDAR, q_{dardar}, which is an aggregate of all DARDAR values per SEVIRI pixel over a vertical depth of 240 m from the cloud top (see Sect. 2.1 and Mayer et al., 2023, for details).

The ProPS and DARDAR cloud states, q^* and q_{dardar}, match well in most cases. For the high-latitude example in Fig. 6a, ProPS is able to detect MP and SC clouds, even for very low (< 1 km) cloud-top heights. Figure 6b shows that MP and SC clouds are also present in low latitudes close to the Equator, where convection is the main cloud formation mechanism, and that ProPS is mostly able to detect them. This might be very useful for future studies of the life cycle and phase transitions of convective clouds (Coopman et al., 2020). The two figures also show some examples of small cirrus clouds as well as some LQ clouds beneath an aerosol layer. In both cloud situations, clouds are mostly retrieved in an accurate way. In general, however, the detection works best for spatially extended cloud states. The probabilities for the cloud state, $P(q)$, and the corresponding certainty measure show that some clouds can be classified more easily than others, i.e. when the probability for a particular state is close to 1, corresponding to high values of the certainty parameter. This is the case, for example, for the large IC clouds and some LQ clouds and clear-sky pixels in the example figures.

However, the examples also highlight challenging situations for the retrieval. In the DARDAR curtain, SC and MP cloud tops often appear together in a cloud and alternate on small spatial scales. ProPS is often not able to resolve this small-scale variability. Another challenge is posed by optically thin ice clouds. When ProPS fails to detect these TI clouds, it often classifies these pixels either as the cloud state below (if the overlying TI cloud is optically very thin, so that the radiation from the cloud below is largely transmitted through the overlying ice cloud) or as MP (if the overlying TI cloud is somewhat thicker and the radiation signals from a cloud below containing liquid particles mix with the overlying TI cloud signal). This effect often happens at the edges of large ice clouds, which are typically optically very thin and/or do not fill an entire SEVIRI pixel. An example can be seen in Fig. 6a at the edges of the large ice cloud on the right. To overcome this shortcoming, a combination of ProPS with a cloud product that identifies multilayered clouds would make sense in the future (as is, for instance, planned for the EarthCARE multi-spectral imager; Hünerbein et al., 2023). Another challenge, again related to optically thin clouds, is the misclassification of MP, SC or LQ clouds as TI when they are optically thin, e.g. during formation or dissipation. These optically thin clouds are typically characterized by high values of $\mathrm{BTD}_{10.8-12}$. Since the vast majority of pixels with high $\mathrm{BTD}_{10.8-12}$ values correspond to TI clouds, ProPS, being a statistical method, tends to label pixels with high $\mathrm{BTD}_{10.8-12}$ values as TI clouds.

Sometimes, the ProPS q^* is spatially slightly shifted against the DARDAR results, especially in the high-latitude example in Fig. 6a, where q^* is slightly shifted to the left relative to q_{dardar} in some cases. This is most likely due to the different viewing geometries of the two instruments. Further, as SEVIRI looks at the clouds from a given angle, a high cloud can cover a neighbouring lower cloud from SEVIRI's perspective. In addition, the cloud cover in the rest of the SEVIRI 2D pixel can be different from that in the overflight swath of the polar-orbiting satellite, and there can be a time difference of up to 7.5 min between the satellites. These effects could explain some of the differences between the ProPS and DARDAR classifications, especially for high-certainty pixels, where we expect the classification to be correct. However, these effects are difficult to account for in a quantitative evaluation (see Sect. 8.2) and lead to lower probabilities of detection.
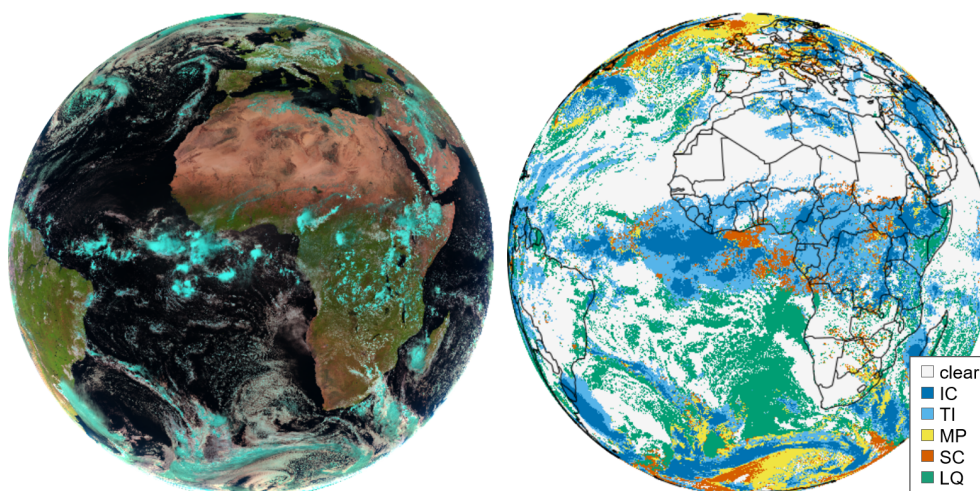
Figure 5. False-colour RGB composite (left) and example application of ProPS (right) for a SEVIRI scene obtained on 25 April 2022 at 12:00 UTC.

The example figures also demonstrate that the cloud situation is often complex, with multi-layered clouds at different altitudes, cloud-phase changes on small scales and other atmospheric factors such as aerosols. The certainty parameter can be an indicator of the complexity of the scene: complicated cloud scenes, such as multi-layered clouds or rapidly changing phases on small scales, tend to have lower certainty values compared to simpler scenarios. For example, the certainty drops from almost 1 to lower values in Fig. 6a to the left and right of the thick ice cloud, where it becomes thinner with underlying liquid layers.

To get an impression of how ProPS compares to other cloud and phase retrieval algorithms, we additionally conducted a comparison of ProPS with the most recent version of the CM SAF CLoud property dAtAset using SEVIRI – Edition 3 (CLAAS-3) for 12 example scenes. CLAAS-3 distinguishes between clear sky, warm liquid, supercooled liquid and ice clouds. We find a good general agreement between the two methods, with differences mainly constrained to cloud edges and the transition regions between different phases. In general, ProPS classifies more pixels as cloudy than CLAAS-3, especially small, warm cumulus clouds, and categorizes more pixels as thin ice than CLAAS-3. A detailed discussion can be found in the Appendix (see Figs. B1 and B2).

8.2   POD and FAR

In the following, we only consider pixels with a homogeneous cloud state over at least three consecutive pixels along the DARDAR curtain. It is difficult for SEVIRI to resolve the cloud state on smaller scales, as mentioned in the section above. Furthermore, isolated cloud state pixels may be artefacts of the DARDAR product, which we try to exclude.

Figure 7 shows the overall performance of ProPS evaluated pixel by pixel against the DARDAR cloud state for the 6 months of validation data. We distinguish between cloud and phase detection. Figure 7a and c show the numbers of clear and cloudy pixels according to DARDAR, and the number of pixels identified as clear and cloudy by ProPS are colour coded. The upper row shows this validation for the daytime version of ProPS, while the lower row shows it for the nighttime version. The probability of detection (POD) of clouds (clear sky) is defined as the percentage of pixels classified as cloudy (clear) by both ProPS and DARDAR relative to the pixels classified as cloudy (clear) by DARDAR. With this definition, the POD for clear sky is 86 %, and for clouds it is 93 %. Optically thin TI clouds and small, warm LQ clouds are the clouds which are most difficult to detect: of all the undetected clouds (i.e. the red part of the "DARDAR cloudy" bar in Fig. 7a), 54 % are TI clouds and 37 % are LQ clouds. Difficulties in detecting TI clouds are expected since passive sensors are less sensitive to optically thin clouds than lidar instruments. LQ clouds are particularly difficult to detect when they occur over bright surfaces or are embedded in (thick) aerosol layers. Small LQ clouds that do not fully cover SEVIRI pixels and therefore go undetected also play a role. For the same reasons, TI and LQ are again the two most problematic cloud phases when looking at false alarms: of all the false alarms (i.e. the red part of the "DARDAR clear" bar in Fig. 7a), 40 % are classified as TI and 43 % are classified as LQ clouds by ProPS. Looking at these results the other way around, this also implies that one can be very sure that there really is a cloud at pixels classified as SC, MP or IC by ProPS during the day and that pixels classified as clear by ProPS are almost never SC, MP or IC clouds.

As expected, the nighttime version of ProPS performs slightly worse than the daytime version, with a POD of 76 % for clear sky and 95 % for clouds. The nighttime version
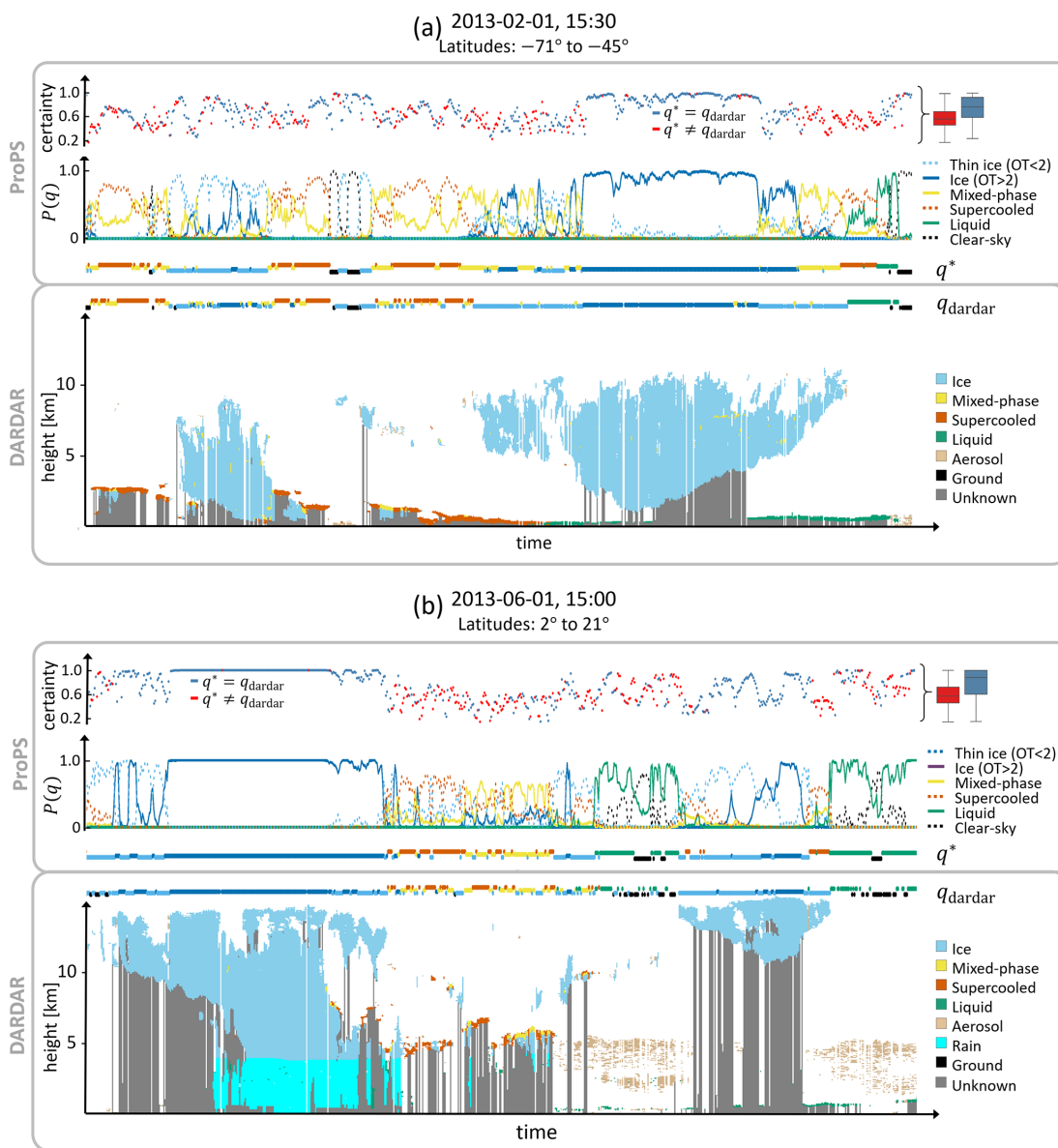
Figure 6. Example of the application of ProPS to DARDAR tracks in **(a)** high latitudes and **(b)** low latitudes. The bottom part of each panel shows the DARDAR curtain coarsened to SEVIRI resolution; the corresponding results of the ProPS algorithm (the probabilities $P(q)$) are shown in the panels above. The cloud state retrieved from DARDAR, q_{dardar}, and the most likely cloud state from ProPS, q^*, along the track are shown in between (using the same colour code as for $P(q)$). Above the $P(q)$ panels, the corresponding certainties of the ProPS results are shown, with the colour code indicating whether q^* agrees with q_{dardar}. The box plots on the right show the quartiles of the certainty measure for disagreement ($q^* \neq q_{\text{dardar}}$; red) and agreement ($q^* = q_{\text{dardar}}$; blue).

tends to classify too many pixels as cloudy (the red part of the "DARDAR clear" bar in Fig. 7c). This is particularly the case for LQ clouds, which have similar temperatures to the surface and are therefore difficult to detect using thermal channels alone.

Figure 7b and d show the phase detection performance of ProPS for the pixels that are correctly classified as cloudy by the daytime and nighttime versions of ProPS, respectively. The POD is defined analogously to that for cloud detection.

For the daytime version, the POD for IC, TI, MP, SC and LQ is 91 %, 78 %, 52 %, 58 % and 86 %, respectively. For the calculation of these POD values, for IC (TI) clouds, the other ice classification, TI (IC), was also counted as correctly classified since it is the same thermodynamic phase. The POD values show that the majority of pixels are correctly classified by ProPS. The phase classification works especially well for IC and LQ clouds. The TI clouds which are not correctly classified by ProPS are mainly optically very thin TI clouds with
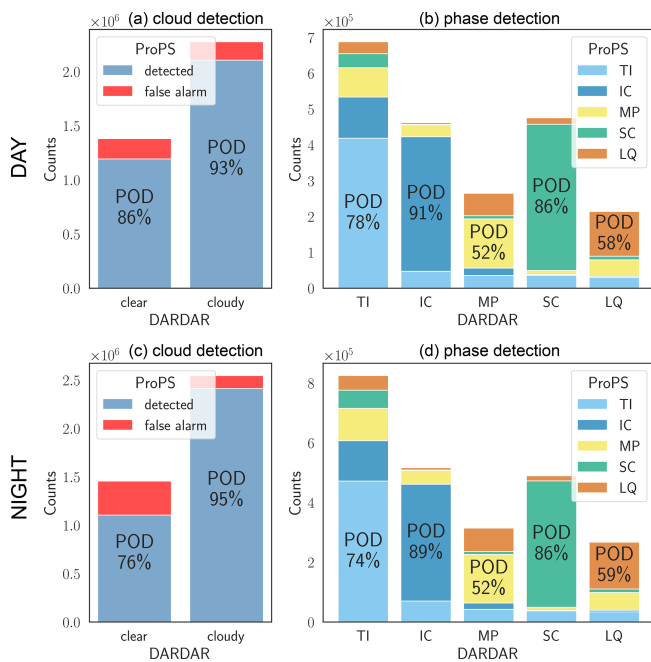
Figure 7. Cloud and phase detection for the day version **(a, b)** and the night version **(c, d)** of the ProPS method. For IC and TI, we count both ice classifications as correct in the POD values.

other clouds below. As explained in Sect. 8.1, these pixels are often classified as either MP or as the cloud phase of the cloud below. Figure 7b shows that it is difficult to distinguish between MP and SC, with many MP cloud tops being classified as SC and vice versa. This difficulty is expected since SC and MP cloud tops occur in very similar circumstances (at similar latitudes, cloud-top temperatures and cloud types) and alternate on relatively small scales (see Fig. 6). In addition, an MP cloud top may consist mainly of liquid droplets and therefore has very similar radiative properties to an SC cloud top. Unfortunately, there is no parameter that quantifies the liquid fraction of MP pixels in DARDAR, so we have no way of checking the performance of ProPS MP detection as a function of liquid fraction. Nevertheless, results show the ability of ProPS to also identify the most challenging phases, MP and SC (more than half of the DARDAR MP and SC pixels are correctly classified by ProPS; see the numbers discussed above).

Interestingly, the nighttime phase classification performs remarkably well, almost on par with the daytime version. To understand why this is the case, we studied examples in the SEVIRI disc and compared the phase classification performed using only thermal channels against that performed using only solar channels for the retrieval. We find that there are easier-to-classify (unambiguous) cloud-phase cases for which the classification obtained using only thermal or only solar channels is correct; hence, in these situations, using a combination of thermal and solar channels does not lead to different results. For the more complex cases, the classifica-

tion is challenging when using both thermal and solar channels, and the combination of solar and thermal information does not lead to a significant increase in correctly detected phases. However, the certainty of the retrieval increases considerably when all channels are used. Since solar channels contain valuable information on the phase, as outlined in Sect. 4, the increase in certainty when using all channels shows that the solar channels do indeed enhance the accuracy of phase determination while boosting the confidence of the obtained results. It has also been shown in previous studies that the use of solar channels increases accuracy in phase detection (Baum et al., 2000). Note that the two algorithm versions only show similar performances if we consider the cases where a cloud has been correctly (according to DARDAR) detected. For cloud detection, the thermal and solar channels have complementary advantages: solar channels are very helpful for detecting low clouds, which have similar temperatures to the surface, while thermal channels have advantages for detecting optically very thin clouds. Therefore, the combination of the selected thermal and solar channels is the best option for reliable cloud and phase detection, but the similarity of the performance of ProPS during daytime and nighttime allows for a smooth transition from day to night.

Recall that the output of ProPS contains not only the most likely cloud state, q^*, but also the probabilities for all cloud states. In cases where q^* does not match DARDAR, the second most likely cloud state often does. This is especially true for MP and SC clouds: when q^* does not match the DARDAR classification of MP (SC), 68 % (65 %) of these pixels have MP (SC) as their second most likely cloud phase. Hence, if both the most likely and the second most likely cloud states are considered to be correct, the POD increases to 84 % for both MP and SC. This means that we can gain information from the second most likely cloud-state result.

8.3 Relation to the certainty parameter

One of the advantages of the Bayesian approach is the certainty parameter for the retrieval (see Sect. 3.3). For the example curtains in Fig. 6, the mean certainty values are shown on the right for pixels where ProPS and DARDAR agree or disagree. Where ProPS and DARDAR agree, the average certainty is higher, indicating that the certainty measure is meaningful. However, as the examples in Fig. 6 show, this is only true on average – there are still cases with a low level of certainty that are correctly identified and vice versa.

Figure 8 gives an overview of the relation to the certainty parameter for the 6 months of validation data for the daytime version of ProPS. It shows the POD and false alarm rate (FAR) for cloud detection and phase determination (given that a cloud was detected) for each phase separately and their average (weighted by the counts of each phase) per certainty bin of width 0.1. The two lower panels show the number of occurrences of the certainty values. The average POD for cloud detection is high ($> 90 \%$) for almost all cer-
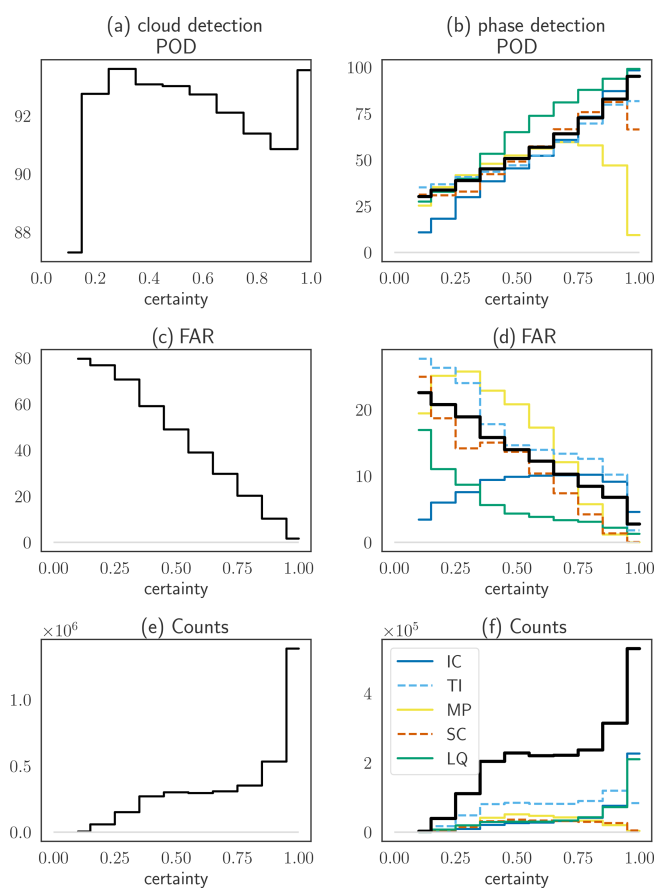
Figure 8. POD of **(a)** cloud and **(b)** phase detection (given that a cloud was detected) for each phase separately (in colour) and their weighted average (in black) as a function of the certainty parameter. FAR for **(c)** cloud and **(d)** phase detection. **(e)** Number of occurrences of certainty values. **(f)** Number of occurrences of certainty values given that a cloud was detected (in black) and the contributions from each phase (as classified by DARDAR; in colour).

Figure 9. POD **(a, b)** and counts of occurrences **(c, d)** of cloudy **(a, c)** and clear-sky **(b, d)** pixels in the SEVIRI disc for the daytime version of ProPS. The POD and counts were computed in latitude–longitude bins of $2.5° \times 2.5°$ for the 6 months of validation data.

tainty values; the FAR decreases monotonically with increasing certainty. This means that ProPS tends to overestimate cloud amount at low certainty values, as also mentioned in Sect. 8.2, but it has an increased detection accuracy at higher certainty values. For phase determination, the average POD increases monotonically with the certainty parameter, while the average FAR decreases. Hence, the certainty parameter is a useful tool for deciding whether to trust a result.

From the number of occurrences of certainty values (lower panels in Fig. 8) and the examples in Fig. 6, we can see that the most unambiguous cases are clear sky, IC and LQ clouds (if their spatial extent is large enough to fill whole SEVIRI pixels). MP, SC and TI clouds have lower certainty values on average than the other cloud states.

8.4 Performance on the SEVIRI disc

To better characterize the performance of ProPS, we evaluate its POD on the SEVIRI disc for the 6 months of validation data. This evaluation is shown in Figs. 9 and 10 for cloud detection and phase detection (given a detected cloud), respectively. Here, we show the results for the daytime version; the results for the nighttime version can be found in the Appendix (see Figs. C1 and C2). The top panels show the POD of each cloud state, and the lower panels show the corresponding distribution of the number of occurrences of each cloud state according to DARDAR.

Figure 9 shows that cloud detection is most challenging over deserts, such as those in northern and southern Africa. Clear-sky detection is most challenging at the ITCZ and some regions in high latitudes. Looking at the distribution of occurrences, it can be seen that the regions where cloud detection and clear-sky detection are most challenging correspond to the regions with the fewest occurrences of each.

The same is mostly true for the detection of TI, MP, SC and LQ phases (see Fig. 10). For instance, MP and SC have their highest detection rates in high latitudes, where they occur most often. The detection of IC clouds, on the other hand, is uniformly high over the whole SEVIRI disc.

For the nighttime version of ProPS, the POD of clouds is similar to that for the daytime version, while the POD of clear sky is slightly lower almost everywhere in the SEVIRI disc (see Fig. C1). This suggests that ProPS tends to overestimate cloudiness during the night. The spatial distribution of the
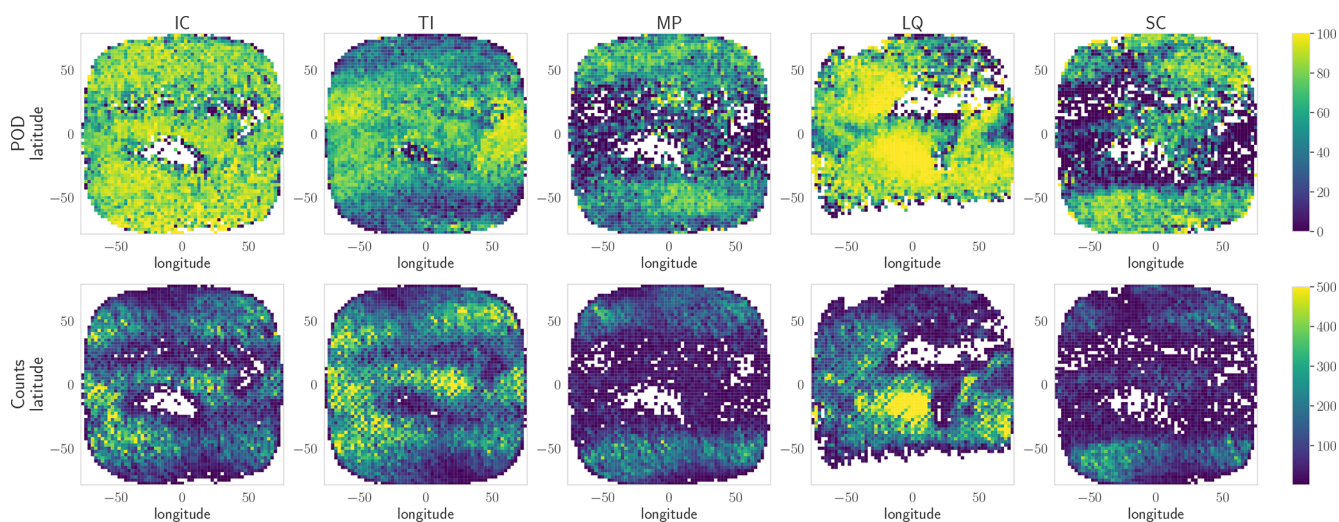
Figure 10. POD (upper row) and counts of occurrences (lower row) of the different phases in the SEVIRI disc for the daytime version of ProPS. The POD and counts were computed in latitude–longitude bins of $2.5° \times 2.5°$ for the 6 months of validation data.

POD for the different phases is very similar to that for the daytime version (see Fig. C2).

9 Conclusions

This study presents ProPS, a new method for cloud detection and phase determination using SEVIRI aboard the geostationary satellite Meteosat Second Generation. ProPS distinguishes between clear sky, optically thin ice (TI) cloud, optically thick ice (IC) cloud, mixed-phase (MP) cloud, supercooled liquid (SC) cloud and warm liquid (LQ) cloud. The lidar–radar cloud product DARDAR is used as a reference, and a Bayesian approach is applied to combine the cloud and phase information from different SEVIRI channels and prior knowledge. For the probabilities used in the Bayesian approach, we carefully select SEVIRI channels and their dependencies, which are used as conditions in the probabilities in order to optimize the information content of the SEVIRI channels. We implement both daytime and nighttime versions of the algorithm with combinations of SEVIRI channels at wavelengths of 0.6, 1.6, 8.7, 10.8 and 12 μm, along with a texture parameter derived from the 10.8 μm channel. The result of this Bayesian approach is a probability for each cloud state (clear sky and the various cloud phases) per SEVIRI pixel. This allows us to select the most likely cloud state as the final result. ProPS effectively transfers the advanced cloud and phase detection capabilities of DARDAR to the SEVIRI geostationary imager.

We validate the method using 6 months of independent collocated DARDAR data. Our findings show that the daytime algorithm successfully detects 93 % of clouds and 86 % of clear-sky pixels. It also shows good performance in accurately classifying cloud phases compared to DARDAR data, with probability of detection (POD) values of 91 %, 78 %,

52 %, 58 % and 86 % for IC, TI, MP, SC and LQ, respectively. Distinguishing between MP and SC poses the greatest challenge in phase classification, as there is a tendency for MP cloud tops to be classified as SC and vice versa. This is expected, as SC and MP cloud tops occur in very similar circumstances (e.g. at similar latitudes and cloud-top temperatures) and can have similar radiative properties if the MP cloud top consists predominantly of liquid droplets. However, it should be emphasized that ProPS is capable of distinguishing between them in more than 50 % of the cases. The primary challenge for the nighttime version lies in detecting low LQ clouds, particularly when their temperatures are similar to the surface temperature; the nighttime version of ProPS tends to overestimate the occurrence of these LQ clouds. However, the nighttime version of ProPS performs nearly as well as the daytime version in terms of cloud-phase detection. This indicates that ProPS is suitable for studying the complete daily cycle of cloud phases. Nevertheless, the algorithm is expected to perform best for each location during the times of the day corresponding to the overflight periods where the sza and umu values as well as their combinations (during the daytime) are covered by the DARDAR data set. Similarly, the prior information used in the retrieval process is only representative of the specific overflight times.

An advantage of the ProPS method is its ability to assign a certainty to the results: in the validation, we observe that the POD of phase detection consistently increases with certainty, providing a straightforward measure of the reliability of the results.

Thus, ProPS represents a significant advancement in discriminating cloud-top phases compared to traditional retrieval methods. This distinction is crucial for studying ice in the atmosphere, understanding mixed-phase cloud properties and investigating the cloud radiative forcing associated

with phase transitions. The new method enables the study of microphysical and macrophysical cloud properties of clouds with different phases, in particular MP and SC clouds, which have been rarely investigated from geostationary satellites so far. The geostationary perspective allows the analysis of the temporal evolution of clouds with different phases as well as phase transitions. SEVIRI, which has been in operation for 2 decades (2004–2024), provides an extensive data set that can be used effectively in conjunction with this method to make valuable statistical comparisons with climate models. Furthermore, ProPS has the advantage of providing probabilities for each cloud state. This could be a valuable additional parameter for comparison with climate models. In terms of further development of the ProPS method, the algorithm can be extended to other satellites with only a few modifications – by using for instance the spectral-band adjustment factors proposed by Piontek et al. (2023) – since similar channels to those used for ProPS are available in most currently operational polar- and geostationary-satellite passive imagers. The Flexible Combined Imager (FCI) aboard the satellite following on from MSG (Meteosat Third Generation – MTG, launched on 13 December 2022; Durand et al., 2015) has additional channels in the near infrared which contain information on the cloud phase (e.g. the 2.2 μm or 3.8 μm channel) available. However, in order to incorporate and use channels that are not available to SEVIRI and contain phase information, one first needs to collect a data set of collocated active observations to compute the necessary probabilities. In the future, this could be done with the EarthCARE satellite (Wehr et al., 2023) (launched in May 2024). Furthermore, working with a Bayesian approach offers an additional advantage: the method can be easily adapted to incorporate input from numerical weather prediction (NWP) models as prior probabilities (as suggested by Mackie et al., 2010). This modification would allow the use of NWP-model-derived probabilities for cloud presence and cloud phases as part of the method's framework. This integration promises to improve the accuracy and reliability of the ProPS method in future applications.

Appendix A: Examples of probabilities

To provide readers with a visual understanding of the Bayesian probabilities computed using the kernel density estimation (KDE) method, we present additional examples in Fig. A1. The figure showcases the probabilities for specific channels (or channel combinations), namely $BTD_{10.8-8.7}$, $BTD_{10.8-12}$, $R_{1.6}$ and $RR_{1.6/0.6}$, given the cloud state q (in different colours). The values for the additional conditions are displayed in the figure for each channel (or channel combination).
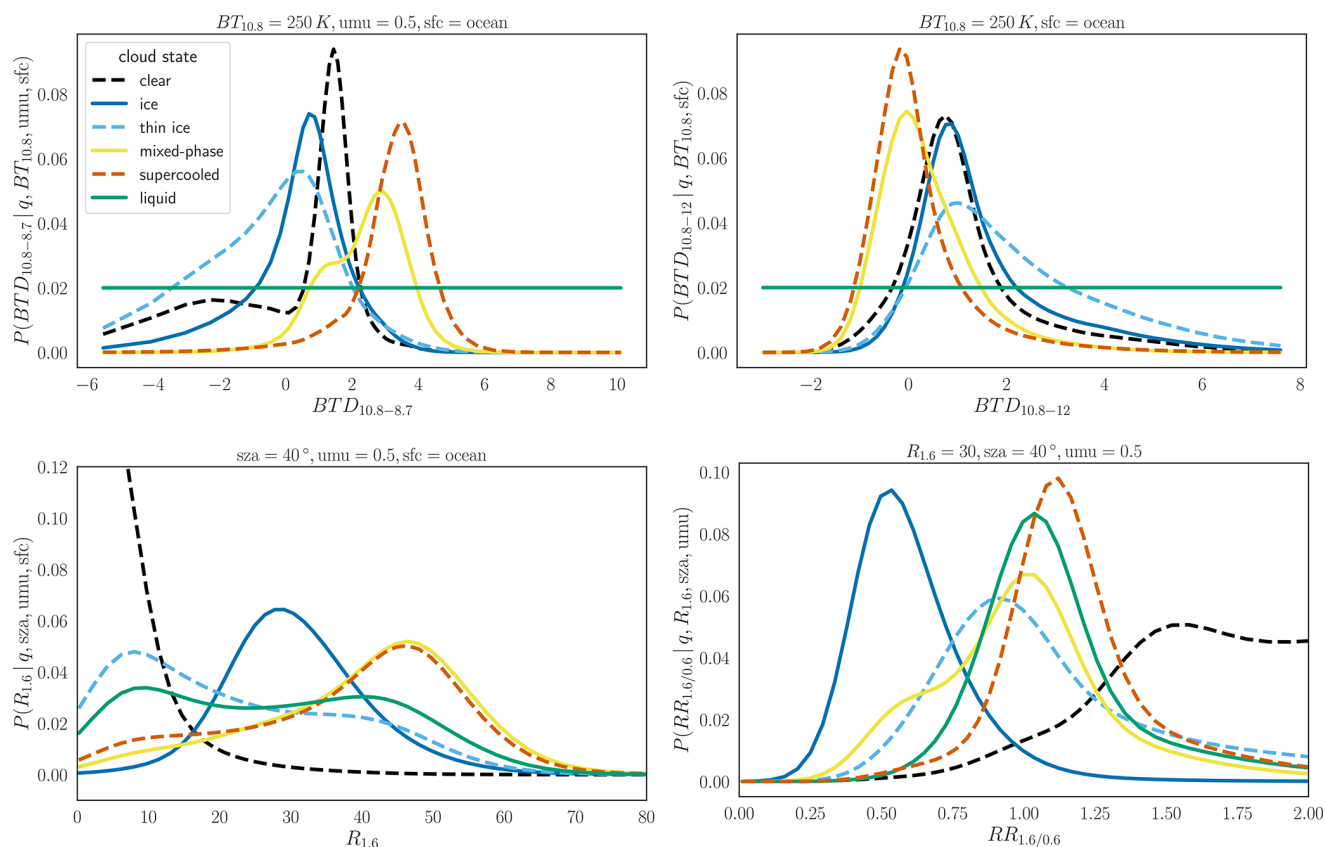
Figure A1. Examples of probabilities for different channels (or channel combinations) computed using KDE.

Appendix B: Comparison of ProPS and CLAAS-3

In order to better characterize ProPS, we conduct a comparison to the CM SAF CLoud property dAtAset using SEVIRI – Edition 3 (CLAAS-3) product, which was released in 2022 (Meirink et al., 2022). This new edition of the CLAAS product offers an extended phase classification system that distinguishes between clear sky and liquid, supercooled, and various ice cloud types; we condensed the various ice cloud types into one ice cloud category for simplification.

The CLAAS-3 cloud detection method, called CMA-prob, shows some similarities to ProPS, especially because it uses a Bayesian approach based on the CALIPSO/CALIOP (but not the CloudSat/CPR) cloud mask as the ground truth and a selection of visible and infrared SEVIRI channels as inputs (Karlsson et al., 2017). While a similar probabilistic methodology is used for ProPS and CMA-prob, their tactics differ slightly: CMA-prob does not use conditions (except for surface types) for the probabilities, instead subtracting pre-calculated image feature thresholds from each channel (or channel combination). These thresholds are dynamic, depending, for instance, on satellite geometry and atmospheric conditions. In contrast to ProPS, CMA-prob assumes that the different SEVIRI channels (or channel combinations) are independent. Another deviation from ProPS is that CMA-prob excludes thin ice clouds with optical thicknesses smaller than 0.2 to prevent overfitting. For the pixels classified as cloudy by the initial procedure CMA-prob, CLAAS-3 employs a (separated) cloud-top phase determination. This relies on a series of threshold tests utilizing SEVIRI channels at wavelengths of 3.8, 6.3, 8.7, 10.8, 12.0 and 13.4 μm as well as clear- and cloudy-sky simulated IR radiances and brightness temperatures. Additionally, consistency with the cloud optical thickness and particle effective radius retrieval from solar and NIR channel combinations is demanded (Meirink et al., 2022).

To compare ProPS and CLAAS-3, we use 12 SEVIRI scenes sampled in different seasons and at different times of day. Figure B1 shows one such scene. The circumstances in which ProPS and CLAAS-3 differ in the figure are similar for the other scenes used in the comparison. Figure B2 shows statistics that compare the classifications of CLAAS-3 and ProPS across all 12 scenes. Overall, the figures show that there is good general agreement between the two methods. In Fig. B1, the positions and phases of the clouds generally agree well when looking at the "big picture". However, there are differences in the details. For cloud detection, discrepancies between ProPS and CLAAS-3 could stem on the one hand from differences in the training data sets (ProPS employs DARDAR, while CLAAS-3 utilizes data from CALIPSO). On the other hand, there are some differences in the selection of SEVIRI channels and the conditions/thresholds employed as well as in the implementation of the Bayesian approach. These nuances likely contribute to the observed differences in cloud and phase detection.

We find that ProPS classifies more pixels as cloudy than CLAAS-3: for the 12 scenes, ProPS classified 62 % of all pixels as cloudy, while CLAAS-3 classified 57 % as cloudy. The differences between ProPS and CLAAS-3 are often found at the cloud edges, especially for small-scale warm cumulus and thin cirrus clouds, both of which are, in general, difficult cloud types to detect (e.g. the pink areas in the tropics and the cumulus deck west of Africa in Fig. B1). The agreement is better during the day than during the night, as expected. In particular, low, warm clouds are difficult to distinguish from the surface using IR channels alone, leading to the larger discrepancies between ProPS and CLAAS-3 during the night compared to the day. During the day, ProPS and CLAAS-3 agree on the classification of 81 % of all pixels; during the night, they agree on 78 % of all pixels. For thin ice clouds, the difference between the two methods might come (partly) from the exclusion of clouds with an optical thickness smaller than 0.2 in CLAAS-3. In general, ProPS tends to overestimate rather than underestimate the amount of cloud (as discussed in Sect. 6), i.e. it is a clear-sky-conservative algorithm, whereas CLAAS-3 seems to be a cloud-conservative algorithm. Exceptions are obtained for high satellite zenith angles ($> 70°$) and bright surfaces (deserts, ice and snow), where CLAAS-3 has higher cloudiness values compared to ProPS.

Next, we take a look at the phase categorization of both methods. ProPS has an additional phase category, namely MP, which has no direct correspondence in CLAAS-3. We find that clouds classified as MP by ProPS are mostly categorized as supercooled by CLAAS-3; almost no ProPS MP clouds are classified as ice by CLAAS-3. The CLAAS-3 supercooled clouds are also the largest contribution to the ProPS SC category. The main differences in phase detection (just as for cloud detection) are found at cloud edges or at the transition regions between different phases (for instance, at the transition between supercooled and warm liquid clouds over the Southern Ocean in Fig. B1). The phase category of ProPS which differs the most from CLAAS-3 is thin ice clouds (see the TI bar in Fig. B2): ProPS categorizes more pixels as thin ice than CLAAS-3 does. In most cases, ProPS and CLAAS-3 agree on the existence and positions of thin ice clouds; however, they often have a larger extent in ProPS (see the yellow regions in Fig. B1 at ice cloud edges). These differences might be due to the mentioned exclusion of clouds with an optical thickness smaller than 0.2 in CLAAS-3. The high sensitivity of ProPS to thin ice might, however, also lead to false alarms. CLAAS-3 categorizes parts of the SC and MP categories of ProPS as warm liquid (the green parts of the MP and SC bars in Fig. B2), suggesting a tendency towards categorizing clouds as warmer types in the CLAAS-3 classification scheme compared to ProPS.
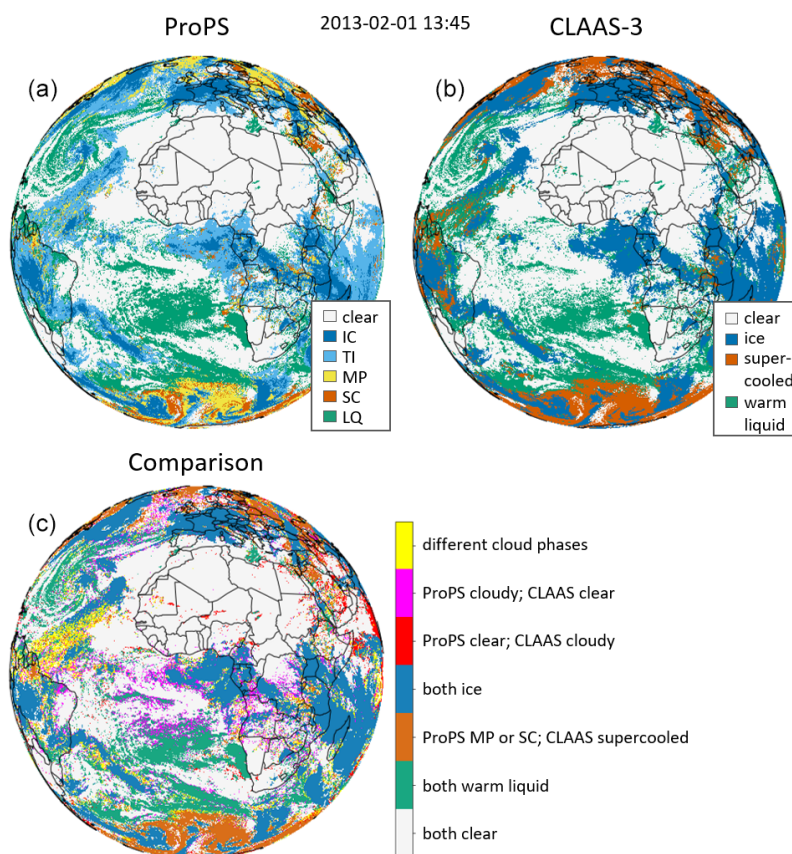
Figure B1. Comparison of ProPS with the CM SAF CLoud property dAtAset using SEVIRI – Edition 3 (CLAAS-3) for one example SEVIRI scene. Panels **(a)** and **(b)** show the results from both methods. Panel **(c)** shows the comparison of the ProPS and CLAAS-3 results.
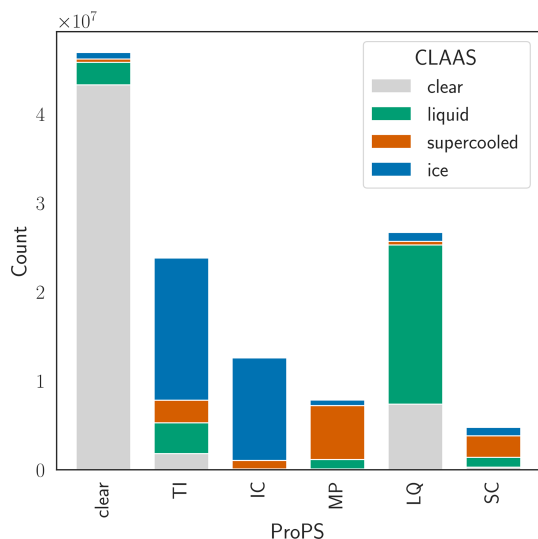
Figure B2. Statistics from the comparison of ProPS with CLAAS-3 over 12 SEVIRI scenes sampled in different seasons and at different times of day.

Appendix C: Performance of the nighttime version of ProPS on the SEVIRI disc

In Figs. C1 and C2, we show the POD for cloud detection and phase detection (given a detected cloud), respectively, on the SEVIRI disc for the 6 months of validation data when using the nighttime version of ProPS. The upper panels show the POD of each cloud state, and the lower panels show the corresponding distribution of the number of occurrences of each cloud state according to DARDAR. The figures show that the POD of clear sky is worse in the nighttime version almost everywhere in the SEVIRI disc, except for the desert regions on the African continent. The POD of clouds, on the other hand, is similar to that for the daytime version, suggesting that ProPS has a tendency to overestimate cloudiness during the night. The distribution of the POD across the different phases is very similar to that for the daytime version.
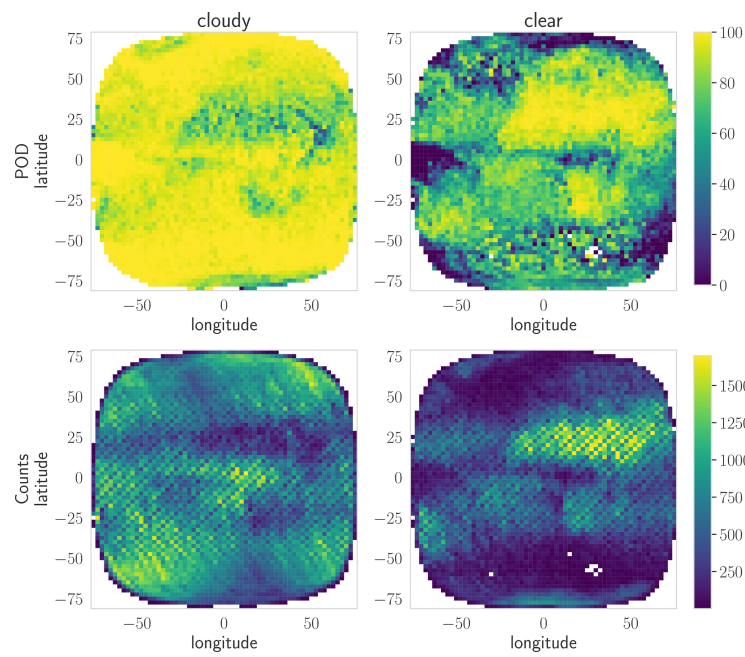
Figure C1. As Fig. 9 but for the nighttime version of ProPS.
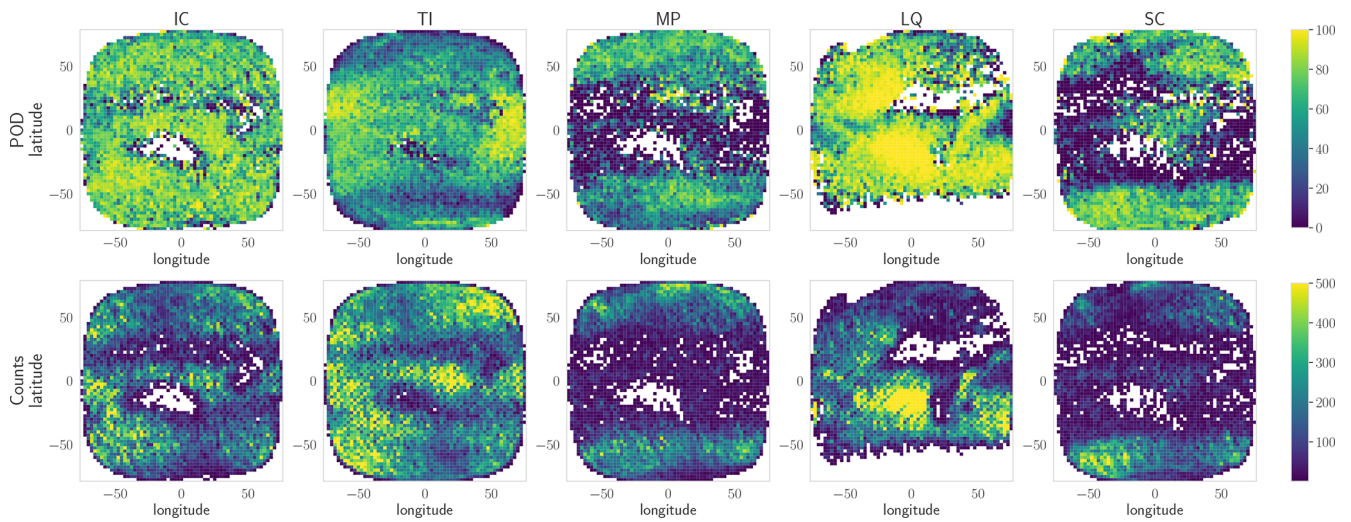
Figure C2. As Fig. 10 but for the nighttime version of ProPS .

Author contributions. All authors contributed to the project through discussions. JM and LB conceived the concept of this study. JM developed the presented methods and carried out the analysis with help from LB and valuable feedback from BM. JM and DP implemented the algorithm for the retrieval. CV supervised the project and provided scientific feedback. JM took the lead in writing the manuscript. All authors provided feedback on the manuscript.

References

Ackerman, S. A., Smith, W. L., Revercomb, H. E., and Spinhirne, J. D.: The 27–28 October 1986 FIRE IFO Cirrus Case Study: Spectral Properties of Cirrus Clouds in the 8–12 µm Window, Mon. Weather Rev., 118, 2377–2388, https://doi.org/10.1175/1520-0493(1990)118<2377:TOFICC>2.0.CO;2, 1990.

Atkinson, J. D., Murray, B. J., Woodhouse, M. T., Whale, T. F., Baustian, K. J., Carslaw, K. S., Dobbie, S., O'Sullivan, D., and Malkin, T. L.: The importance of feldspar for ice nucleation by mineral dust in mixed-phase clouds, Nature, 498, 355–358, https://doi.org/10.1038/nature12278, 2013.

Baum, B. A., Soulen, P. F., Strabala, K. I., King, M. D., Ackerman, S. A., Menzel, W. P., and Yang, P.: Remote sensing of cloud properties using MODIS airborne simulator imagery during SUCCESS: 2. Cloud thermodynamic phase, J. Geophys. Res.-Atmos., 105, 11781–11792, https://doi.org/10.1029/1999jd901090, 2000.

Baum, B. A., Menzel, W. P., Frey, R. A., Tobin, D. C., Holz, R. E., Ackerman, S. A., Heidinger, A. K., and Yang, P.: MODIS Cloud-Top Property Refinements for Collection 6, J. Appl. Meteorol. Clim., 51, 1145–1163, https://doi.org/10.1175/JAMC-D-11-0203.1, 2012.

Benas, N., Finkensieper, S., Stengel, M., van Zadelhoff, G.-J., Hanschmann, T., Hollmann, R., and Meirink, J. F.: The MSG-SEVIRI-based cloud property data record CLAAS-2, Earth Syst. Sci. Data, 9, 415–434, https://doi.org/10.5194/essd-9-415-2017, 2017.

Benedetti, A.: CloudSat AN-ECMWF ancillary data interface control document, technical document, CloudSat Data Processing Cent., FortCollins, Colo., 2005.

Bessho, K., Date, K., Hayashi, M., Ikeda, A., Imai, T., Inoue, H., Kumagai, Y., Miyakawa, T., Murata, H., Ohno, T., Okuyama, A., Oyama, R., Sasaki, Y., Shimazu, Y., Shimoji, K., Sumida, Y., Suzuki, M., Taniguchi, H., Tsuchiyama, H., Uesawa, D., Yokota, H., and Yoshida, R.: An Introduction to Himawari-8/9 – Japan's New-Generation Geostationary Meteorological Satellites, J. Meteorol. Soc. Jpn. II, 94, 151–183, https://doi.org/10.2151/jmsj.2016-009, 2016.

Bock, L., Lauer, A., Schlund, M., Barreiro, M., Bellouin, N., Jones, C., Meehl, G. A., Predoi, V., Roberts, M. J., and Eyring, V.: Quantifying Progress Across Different CMIP Phases With the ESMValTool, J. Geophys. Res.-Atmos., 125, e2019JD032321, https://doi.org/10.1029/2019JD032321, 2020.

Ceccaldi, M., Delanoë, J., Hogan, R. J., Pounder, N. L., Protat, A., and Pelon, J.: From CloudSat-CALIPSO to EarthCare: Evolution of the DARDAR cloud classification and its comparison to airborne radar-lidar observations, J. Geophys. Res.-Atmos., 118, 7962–7981, https://doi.org/10.1002/jgrd.50579, 2013.

Cesana, G., Kay, J. E., Chepfer, H., English, J. M., and Boer, G.: Ubiquitous low-level liquid-containing Arctic clouds: New observations and climate model constraints from CALIPSO-GOCCP, Geophys. Res. Lett., 39, L20804, https://doi.org/10.1029/2012GL053385, 2012.

Cesana, G., Waliser, D. E., Jiang, X., and Li, J.-L. F.: Multi-model evaluation of cloud phase transition using satellite and reanalysis data, J. Geophys. Res.-Atmos., 120, 7871–7892, https://doi.org/10.1002/2014JD022932, 2015.

Cesana, G. V., Khadir, T., Chepfer, H., and Chiriaco, M.: Southern Ocean Solar Reflection Biases in CMIP6 Models Linked to Cloud Phase and Vertical Structure Representations, Geophys. Res. Lett., 49, e2022GL099777, https://doi.org/10.1029/2022GL099777, 2022.

Choi, Y.-S., Ho, C.-H., Park, C.-E., Storelvmo, T., and Tan, I.: Influence of cloud phase composition on climate feedbacks, J. Geophys. Res.-Atmos., 119, 3687–3700, https://doi.org/10.1002/2013JD020582, 2014.

Chylek, P., Robinson, S., Dubey, M. K., King, M. D., Fu, Q., and Clodius, W. B.: Comparison of near-infrared and thermal infrared cloud phase detections, J. Geophys. Res., 111, D20203, https://doi.org/10.1029/2006JD007140, 2006.

Coopman, Q., Hoose, C., and Stengel, M.: Analysis of the Thermodynamic Phase Transition of Tracked Convective Clouds Based on Geostationary Satellite Observations, J. Geophys. Res.-Atmos., 125, e2019JD032146, https://doi.org/10.1029/2019JD032146, 2020.

Coopman, Q., Hoose, C., and Stengel, M.: Analyzing the Thermodynamic Phase Partitioning of Mixed Phase Clouds Over the Southern Ocean Using Passive Satellite Observations, Geophys. Res. Lett., 48, e2021GL093225, https://doi.org/10.1029/2021GL093225 , 2021.

Cover, T. M. and Thomas, J. A.: Elements of Information Theory, John Wiley & Sons, https://doi.org/10.1002/047174882X, 2005.

Delanoë, J. and Hogan, R. J.: A variational scheme for retrieving ice cloud properties from combined radar, lidar, and infrared radiometer, J. Geophys. Res., 113, D07204, https://doi.org/10.1029/2007JD009000, 2008.

Delanoë, J. and Hogan, R. J.: Combined CloudSat-CALIPSO-MODIS retrievals of the properties of ice clouds, J. Geophys. Res., 115, D00H29, https://doi.org/10.1029/2009JD012346, 2010.

Doutriaux-Boucher, M. and Quaas, J.: Evaluation of cloud thermodynamic phase parametrizations in the LMDZ GCM by using POLDER satellite data, Geophys. Res. Lett., 31, L06126, https://doi.org/10.1029/2003GL019095, 2004.

Durand, Y., Hallibert, P., Wilson, M., Lekouara, M., Grabarnik, S., Aminou, D., Blythe, P., Napierala, B., Canaud, J.-L., Pigouche, O., Ouaknine, J., and Verez, B.: The flexible combined imager onboard MTG: from design to calibration, SPIE Remote Sensing, https://doi.org/10.1117/12.2196644, 2015.

EUMETSAT: High Rate SEVIRI Level 1.5 Image Data – MSG – 0 degree, EUMETSAT [data set], https://user.eumetsat.int/catalogue/EO:EUM:DAT:MSG:HRSEVIRI, last access: 28 June 2024.

Ewald, F., Groß, S., Wirth, M., Delanoë, J., Fox, S., and Mayer, B.: Why we need radar, lidar, and solar radiance observations to constrain ice cloud microphysics, Atmos. Meas. Tech., 14, 5029–5047, https://doi.org/10.5194/amt-14-5029-2021, 2021.

Friedl, M. A., Sulla-Menashe, D., Tan, B., Schneider, A., Ramankutty, N., Sibley, A., and Huang, X.: MODIS Collection 5 global land cover: Algorithm refinements and characterization of new datasets, Remote Sens. Environ., 114, 168–182, https://doi.org/10.1016/j.rse.2009.08.016, 2010.

Gregory, D. and Morris, D.: The sensitivity of climate simulations to the specification of mixed phase clouds, Clim. Dynam., 12, 641–651, https://doi.org/10.1007/BF00216271, 1996.

Hahn, V., Meerkötter, R., Voigt, C., Gisinger, S., Sauer, D., Catoire, V., Dreiling, V., Coe, H., Flamant, C., Kaufmann, S., Kleine, J., Knippertz, P., Moser, M., Rosenberg, P., Schlager, H., Schwarzenboeck, A., and Taylor, J.: Pollution slightly enhances atmospheric cooling by low-level clouds in tropical West Africa, Atmos. Chem. Phys., 23, 8515–8530, https://doi.org/10.5194/acp-23-8515-2023, 2023.

Heidinger, A. K., Evan, A. T., Foster, M. J., and Walther, A.: A Naive Bayesian Cloud-Detection Scheme Derived from CALIPSO and Applied within PATMOS-x, J. Appl. Meteorol. Clim., 51, 1129–1144, https://doi.org/10.1175/JAMC-D-11-02.1, 2012.

Hersbach, H., Bell, B., Berrisford, P., Biavati, G., Horányi, A., Muñoz Sabater, J., Nicolas, J., Peubey, C., Radu, R., Rozum, I., Schepers, D., Simmons, A., Soci, C., Dee, D., anf Thépaut, J.-N.: ERA5 hourly data on single levels from 1940 to present, Copernicus Climate Change Service (C3S) Climate Data Store (CDS) [data set], https://doi.org/10.24381/cds.adbb2d47, 2018,

Hogan, R. J., Francis, P. N., Flentje, H., Illingworth, A. J., Quante, M., and Pelon, J.: Characteristics of mixed-phase clouds. I: Lidar, radar and aircraft observations from CLARE'98, Q. J. Roy. Meteor. Soc., 129, 2089–2116, https://doi.org/10.1256/rj.01.208, 2003.

Hünerbein, A., Bley, S., Horn, S., Deneke, H., and Walther, A.: Cloud mask algorithm from the EarthCARE Multi-Spectral Imager: the M-CM products, Atmos. Meas. Tech., 16, 2821–2836, https://doi.org/10.5194/amt-16-2821-2023, 2023.

Intergovernmental Panel on Climate Change (IPCC): Climate Change 2021 – The Physical Science Basis: Working Group I Contribution to the Sixth Assessment Report of the Intergovernmental Panel on Climate Change, edited by: Masson-Delmotte, V., Zhai, P., Pirani, A., Connors, S. L., Péan, C., Berger, S., Caud, N., Chen, Y., Goldfarb, L., Gomis, M. I., Huang, M., Leitzell, K., Lonnoy, E., Matthews, J. B. R., Maycock, T. K., Waterfield, T., Yelekçi, O., Yu, R., and Zhou, B., Cambridge University Press, https://doi.org/10.1017/9781009157896, 2023.

Karlsson, K.-G., Anttila, K., Trentmann, J., Stengel, M., Meirink, J. F., Devasthale, A., Hanschmann, T., Kothe, S., Jääskeläinen, E., Sedlar, J., Benas, N., van Zadelhoff, G.-J., Schlundt, C., Stein, D., Finkensieper, S., Håkansson, N., Hollmann, R., Fuchs, P., and Werscheck, M.: CLARA-A2: CM SAF cLoud, Albedo and surface RAdiation dataset from AVHRR data – Edition 2, Satellite Application Facility on Climate Monitoring (CM SAF) [data set], https://doi.org/10.5676/EUM_SAF_CM/CLARA_AVHRR/V002, 2017.

Key, J. R. and Intrieri, J. M.: Cloud Particle Phase Determination with the AVHRR, J. Appl. Meteorol., 39, 1797–1804, https://doi.org/10.1175/1520-0450-39.10.1797, 2000.

Kirschler, S., Voigt, C., Anderson, B. E., Chen, G., Crosbie, E. C., Ferrare, R. A., Hahn, V., Hair, J. W., Kaufmann, S., Moore, R. H., Painemal, D., Robinson, C. E., Sanchez, K. J., Scarino, A. J., Shingler, T. J., Shook, M. A., Thornhill, K. L., Winstead, E. L., Ziemba, L. D., and Sorooshian, A.: Overview and statistical analysis of boundary layer clouds and precipitation over the western North Atlantic Ocean, Atmos. Chem. Phys., 23, 10731–10750, https://doi.org/10.5194/acp-23-10731-2023, 2023.

Knap, W. H., Stammes, P., and Koelemeijer, R. B. A.: Cloud Thermodynamic Phase Determination from Near-Infrared Spectra of Reflected Sunlight, J. At-

mos. Sci., 59, 83–96, https://doi.org/10.1175/1520-0469(2002)059<0083:CTPDFN>2.0.CO;2, 2002.

Komurcu, M., Storelvmo, T., Tan, I., Lohmann, U., Yun, Y., Penner, J. E., Wang, Y., Liu, X., and Takemura, T.: Intercomparison of the cloud water phase among global climate models, J. Geophys. Res.-Atmos., 119, 3372–3400, https://doi.org/10.1002/2013JD021119, 2014.

Korolev, A., McFarquhar, G., Field, P. R., Franklin, C., Lawson, P., Wang, Z., Williams, E., Abel, S. J., Axisa, D., Borrmann, S., Crosier, J., Fugal, J., Krämer, M., Lohmann, U., Schlenczek, O., Schnaiter, M., and Wendisch, M.: Mixed-Phase Clouds: Progress and Challenges, Meteor. Mon., 58, 51–550, https://doi.org/10.1175/AMSMONOGRAPHS-D-17-0001.1, 2017.

Kox, S., Bugliaro, L., and Ostler, A.: Retrieval of cirrus cloud optical thickness and top altitude from geostationary remote sensing, Atmos. Meas. Tech., 7, 3233–3246, https://doi.org/10.5194/amt-7-3233-2014, 2014.

Krebs, W., Mannstein, H., Bugliaro, L., and Mayer, B.: Technical note: A new day- and night-time Meteosat Second Generation Cirrus Detection Algorithm MeCiDA, Atmos. Chem. Phys., 7, 6145–6159, https://doi.org/10.5194/acp-7-6145-2007, 2007.

Li, W., Zhang, F., Lin, H., Chen, X., Li, J., and Han, W.: Cloud Detection and Classification Algorithms for Himawari-8 Imager Measurements Based on Deep Learning, IEEE T. Geosci. Remote, 60, 1–17, https://doi.org/10.1109/TGRS.2022.3153129, 2022.

Listowski, C., Delanoë, J., Kirchgaessner, A., Lachlan-Cope, T., and King, J.: Antarctic clouds, supercooled liquid water and mixed phase, investigated with DARDAR: geographical and seasonal variations, Atmos. Chem. Phys., 19, 6771–6808, https://doi.org/10.5194/acp-19-6771-2019, 2019.

Loveland, T. R. and Belward, A. S.: The IGBP-DIS global 1km land cover data set, DISCover: First results, Int. J. Remote Sens., 18, 3289–3295, https://doi.org/10.1080/014311697217099, 1997.

Mackie, S., Embury, O., Old, C., Merchant, C. J., and Francis, P.: Generalized Bayesian cloud detection for satellite imagery. Part 1: Technique and validation for night-time imagery over land and sea, Int. J. Remote Sens., 31, 2573–2594, https://doi.org/10.1080/01431160903051703, 2010.

Marchant, B., Platnick, S., Meyer, K., Arnold, G. T., and Riedi, J.: MODIS Collection 6 shortwave-derived cloud phase classification algorithm and comparisons with CALIOP, Atmos. Meas. Tech., 9, 1587–1599, https://doi.org/10.5194/amt-9-1587-2016, 2016.

Masiello, G., Serio, C., Venafra, S., DeFeis, I., and Borbas, E. E.: Diurnal variation in Sahara desert sand emissivity during the dry season from IASI observations, J. Geophys. Res.-Atmos., 119, 1626–1638, https://doi.org/10.1002/jgrd.50863, 2014.

Matus, A. V. and L'Ecuyer, T. S.: The role of cloud phase in Earths radiation budget, J. Geophys. Res.-Atmos., 122, 2559–2578, https://doi.org/10.1002/2016JD025951, 2017.

Mayer, J., Ewald, F., Bugliaro, L., and Voigt, C.: Cloud Top Thermodynamic Phase from Synergistic Lidar-Radar Cloud Products from Polar Orbiting Satellites: Implications for Observations from Geostationary Satellites, Remote Sens., 15, 1742, https://doi.org/10.3390/rs15071742, 2023.

Meirink, J. F., Karlsson, K.-G., Solodovnik, I., Hüser, I., Benas, N., Johansson, E., Håkansson, N., Stengel, M., Selbach,

N., Marc, S., and Hollmann, R.: CLAAS-3: CM SAF CLoud property dAtAset using SEVIRI – Edition 3, Satellite Application Facility on Climate Monitoring (CM SAF) [data set], https://doi.org/10.5676/EUM_SAF_CM/CLAAS/V003, 2022.

Menzel, W. P., Baum, B. A., Strabala, K. I., and Frey, R. A.: Cloud top properties and cloud phase: MODIS Algorithm Theoretical Basis Document, ATBD-MOD-04, Theoretical Basis Document, 2002.

Merchant, C. J., Harris, A. R., Maturi, E., and Maccallum, S.: Probabilistic physically based cloud screening of satellite infrared imagery for operational sea surface temperature retrieval, Q. J. Roy. Meteor. Soc., 131, 2735–2755, https://doi.org/10.1256/qj.05.15, 2005.

Mioche, G., Jourdan, O., Ceccaldi, M., and Delanoë, J.: Variability of mixed-phase clouds in the Arctic with a focus on the Svalbard region: a study based on spaceborne active remote sensing, Atmos. Chem. Phys., 15, 2445–2461, https://doi.org/10.5194/acp-15-2445-2015, 2015.

Moser, M., Voigt, C., Jurkat-Witschas, T., Hahn, V., Mioche, G., Jourdan, O., Dupuy, R., Gourbeyre, C., Schwarzenboeck, A., Lucke, J., Boose, Y., Mech, M., Borrmann, S., Ehrlich, A., Herber, A., Lüpkes, C., and Wendisch, M.: Microphysical and thermodynamic phase analyses of Arctic low-level clouds measured above the sea ice and the open ocean in spring and summer, Atmos. Chem. Phys., 23, 7257–7280, https://doi.org/10.5194/acp-23-7257-2023, 2023.

Nakajima, T. and King, M. D.: Determination of the Optical Thickness and Effective Particle Radius of Clouds from Reflected Solar Radiation Measurements. Part I: Theory, J. Atmos. Sci., 47, 1878–1893, https://doi.org/10.1175/1520-0469(1990)047<1878:DOTOTA>2.0.CO;2, 1990.

Okamoto, H., Sato, K., and Hagihara, Y.: Global analysis of ice microphysics from CloudSat and CALIPSO: Incorporation of specular reflection in lidar signals, J. Geophys. Res., 115, D22209, https://doi.org/10.1029/2009JD013383, 2010.

Pavolonis, M.: GOES-R Advanced Baseline Imager (ABI) Algorithm Theoretical Basis Document For Cloud Type and Cloud Phase, University of Wisconsin-Madison, 2010.

Pavolonis, M. J., Heidinger, A. K., and Uttal, T.: Daytime Global Cloud Typing from AVHRR and VIIRS: Algorithm Description, Validation, and Comparisons, J. Appl. Meteorol., 44, 804–826, https://doi.org/10.1175/JAM2236.1, 2005.

Pavolonis, M. J., Sieglaff, J., and Cintineo, J.: Spectrally Enhanced Cloud Objects – A generalized framework for automated detection of volcanic ash and dust clouds using passive satellite measurements: 2. Cloud object analysis and global application, J. Geophys. Res.-Atmos., 120, 7842–7870, https://doi.org/10.1002/2014JD022969, 2015.

Piontek, D., Bugliaro, L., Müller, R., Muser, L., and Jerg, M.: Multi-Channel Spectral Band Adjustment Factors for Thermal Infrared Measurements of Geostationary Passive Imagers, Remote Sens., 15, 1247, https://doi.org/10.3390/rs15051247, 2023.

Platnick, S., King, M., Ackerman, S., Menzel, W., Baum, B., Riedi, J., and Frey, R.: The MODIS cloud products: algorithms and examples from terra, IEEE T. Geosci. Remote, 41, 459–473, https://doi.org/10.1109/TGRS.2002.808301, 2003.

Platnick, S., Meyer, K. G., King, M. D., Wind, G., Amarasinghe, N., Marchant, B., Arnold, G. T., Zhang, Z., Hubanks, P. A., Holz, R. E., Yang, P., Ridgway, W. L., and Riedi, J.: The MODIS Cloud

Optical and Microphysical Products: Collection 6 Updates and Examples From Terra and Aqua, IEEE T. Geosci. Remote, 55, 502–525, https://doi.org/10.1109/TGRS.2016.2610522, 2017.

Ricaud, P., Del Guasta, M., Lupi, A., Roehrig, R., Bazile, E., Durand, P., Attié, J.-L., Nicosia, A., and Grigioni, P.: Supercooled liquid water clouds observed over Dome C, Antarctica: temperature sensitivity and cloud radiative forcing, Atmos. Chem. Phys., 24, 613–630, https://doi.org/10.5194/acp-24-613-2024, 2024.

Schmetz, J., Pili, P., Tjemkes, S., Just, D., Kerkmann, J., Rota, S., and Ratier, A.: An Introduction to Meteosat Second Generation (MSG), B. Am. Meteorol. Soc., 83, 992–992, https://doi.org/10.1175/1520-0477(2002)083<0977:AITMSG>2.3.CO;2, 2002.

Shannon, C. E. and Weaver, W.: A mathematical model of communication, University of Illinois Press, Urbana, IL, 11, 11–20, 1949.

Silverman, B. W.: Density estimation for statistics and data analysis, vol. 26, CRC press, https://doi.org/10.1201/9781315140919, 1986.

Stephens, G. L., Vane, D. G., Boain, R. J., Mace, G. G., Sassen, K., Wang, Z., Illingworth, A. J., O'connor, E. J., Rossow, W. B., Durden, S. L., Miller, S. D., Austin, R. T., Benedetti, A., and Mitrescu, C.: THE CLOUDSAT MISSION AND THE A-TRAIN: A New Dimension of Space-Based Observations of Clouds and Precipitation, B. Am. Meteorol. Soc., 83, 1771–1790, https://doi.org/10.1175/BAMS-83-12-1771, 2002.

Strandgren, J., Fricker, J., and Bugliaro, L.: Characterisation of the artificial neural network CiPS for cirrus cloud remote sensing with MSG/SEVIRI, Atmos. Meas. Tech., 10, 4317–4339, https://doi.org/10.5194/amt-10-4317-2017, 2017.

Tan, I., Storelvmo, T., and Zelinka, M. D.: Observational constraints on mixed-phase clouds imply higher climate sensitivity, Science, 352, 224–227, https://doi.org/10.1126/science.aad5300, 2016.

Wang, Z.: Level 2 Combined Radar and Lidar Cloud Scenario Classification Product Process Description and Interface Control Document, JPL Rep 22, 2012.

Wang, Z., Letu, H., Shang, H., Zhao, C., Li, J., and Ma, R.: A Supercooled Water Cloud Detection Algorithm Using Himawari-8 Satellite Measurements, J. Geophys. Res.-Atmos., 124, 2724–2738, https://doi.org/10.1029/2018JD029784, 2019.

Węglarczyk, S.: Kernel density estimation and its application, ITM Web Conf., 23, 00037, https://doi.org/10.1051/itmconf/20182300037, 2018.

Wehr, T., Kubota, T., Tzeremes, G., Wallace, K., Nakatsuka, H., Ohno, Y., Koopman, R., Rusli, S., Kikuchi, M., Eisinger, M., Tanaka, T., Taga, M., Deghaye, P., Tomita, E., and Bernaerts, D.: The EarthCARE mission – science and system overview, Atmos. Meas. Tech., 16, 3581–3608, https://doi.org/10.5194/amt-16-3581-2023, 2023.

Winker, D. M., Pelon, J. R., and McCormick, M. P.: The CALIPSO mission: spaceborne lidar for observation of aerosols and clouds, in: Lidar Remote Sensing for Industry and Environment Monitoring III, edited by: Singh, U. N., Itabe, T., and Liu, Z., SPIE, ISSN 0277-786X, https://doi.org/10.1117/12.466539, 2003.

Zhang, D., Wang, Z., and Liu, D.: A global view of midlevel liquid-layer topped stratiform cloud distribution and phase partition from CALIPSO and CloudSat measurements, J. Geophys. Res., 115, D00H13, https://doi.org/10.1029/2009JD012143, 2010.

Zhou, G., Wang, J., Yin, Y., Hu, X., Letu, H., Sohn, B.-J., Yung, Y. L., and Liu, C.: Detecting Supercooled Water Clouds Using Passive Radiometer Measurements, Geophys. Res. Lett., 49, e2021GL096111, https://doi.org/10.1029/2021GL096111, 2022.

List of abbreviations

τ	optical thickness
ABI	Advanced Baseline Imager
ACI	aerosol-cloud interactions
AHI	Advanced Himawari Imager
AI	artificial intelligence
ATBD	Algorithm Theoretical Basis Document
BT	brightness temperature
BTD	brightness temperature difference
CALIOP	Cloud-Aerosol Lidar with Orthogonal Polarization
Cb-TRAM	Cumulonimbus Tracking and Monitoring
CCN	cloud condensation nuclei
CiPS	Cirrus Properties for SEVIRI
CLAAS-3	CLoud property dAtAset using SEVIRI - Edition 3
CMIP6	Coupled Model Intercomparison Project Phase 6
CPR	Cloud Profiling Radar
CTH	cloud top height
CTP	cloud top phase
CTT	cloud top temperature
DARDAR	liDAR/raDAR
DNN	deep neural network
EarthCARE	Earth Clouds, Aerosols and Radiation Explorer
ECMWF	European Centre for Medium-Range Weather Forecasts
EUMETSAT	European Organisation for the Exploitation of Meteorological Satellites
FCI	Flexible Combined Imager

HRV	high resolution visible
IC	ice
INP	ice nucleating particles
IPCC	Intergovernmental Panel on Climate Change
IR	infrared
LQ	warm liquid
MODIS	Moderate Resolution Imaging Spectroradiometer
MP	mixed-phase
MSG	Meteosat Second Generation
MTG	Meteosat Third Generation
NN	neural network
ProPS	PRObabilistic cloud top Phase retrieval for SEVIRI
R$_{\text{eff}}$	effective radius
RT	radiative transfer
SC	supercooled liquid
SENS4ICE	Sensors for Certifiable Hybrid Architectures for Safer Aviation in Icing Environment
SEVIRI	Spinning Enhanced Visible and Infrared Imager
SO	Southern Ocean
specMACS	spectrometer of the Munich Aerosol Cloud Scanner
TI	optically thin ice
TOA	top of atmosphere
UV	ultraviolet
WBF	Wegener-Bergeron-Findeisen

Bibliography

S. A. Ackerman, W. L. Smith, H. E. Revercomb, and J. D. Spinhirne. The 27-28 october 1986 FIRE IFO cirrus case study: Spectral properties of cirrus clouds in the 8-12 μm window. *Monthly Weather Review*, 118(11):2377–2388, nov 1990. doi: 10.1175/1520-0 493(1990)118<2377:TOFICC>2.0.CO;2.

J. D. Atkinson, B. J. Murray, M. T. Woodhouse, T. F. Whale, K. J. Baustian, K. S. Carslaw, S. Dobbie, D. O'Sullivan, and T. L. Malkin. The importance of feldspar for ice nucleation by mineral dust in mixed-phase clouds. *Nature*, 498(7454):355–358, jun 2013. doi: 10.1038/nature12278.

C. Aubry, J. Delanoë, S. Groß, F. Ewald, F. Tridon, O. Jourdan, and G. Mioche. Lidar–radar synergistic method to retrieve ice, supercooled water and mixed-phase cloud properties. *Atmospheric Measurement Techniques*, 17(12):3863–3881, July 2024. ISSN 1867-8548. doi: 10.5194/amt-17-3863-2024.

B. A. Baum, P. F. Soulen, K. I. Strabala, M. D. King, S. A. Ackerman, W. P. Menzel, and P. Yang. Remote sensing of cloud properties using MODIS airborne simulator imagery during SUCCESS: 2. cloud thermodynamic phase. *Journal of Geophysical Research: Atmospheres*, 105(D9):11781–11792, may 2000. doi: 10.1029/1999jd901090.

B. A. Baum, W. P. Menzel, R. A. Frey, D. C. Tobin, R. E. Holz, S. A. Ackerman, A. K. Heidinger, and P. Yang. MODIS cloud-top property refinements for collection 6. *Journal of Applied Meteorology and Climatology*, 51(6):1145–1163, jun 2012. doi: 10.1175/JA MC-D-11-0203.1.

D. Baumgardner, R. Newton, M. Krämer, J. Meyer, A. Beyer, M. Wendisch, and P. Vochezer. The cloud particle spectrometer with polarization detection (cpspd): A next generation open-path cloud probe for distinguishing liquid cloud droplets from ice crystals. *Atmospheric Research*, 142:2–14, June 2014. ISSN 0169-8095. doi: 10.1016/j.atmosres.2013.12.010.

N. Benas, S. Finkensieper, M. Stengel, G.-J. van Zadelhoff, T. Hanschmann, R. Hollmann, and J. F. Meirink. The MSG-SEVIRI-based cloud property data record CLAAS-2. *Earth System Science Data*, 9(2):415–434, jul 2017. doi: 10.5194/essd-9-415-2017.

N. Benas, I. Solodovnik, M. Stengel, I. Hüser, K.-G. Karlsson, N. Håkansson, E. Johansson, S. Eliasson, M. Schröder, R. Hollmann, and J. F. Meirink. Claas-3: the third edition of the cm saf cloud data record based on seviri observations. *Earth System Science Data*, 15(11):5153–5170, Nov. 2023. ISSN 1866-3516. doi: 10.5194/essd-15-5153-2023.

T. Bergeron. On the physics of clouds and precipitation. *Proc. 5th Assembly UGGI, Lisbon, Portugal, 1935*, pages 156–180, 1935.

K. Bessho, K. Date, M. Hayashi, A. Ikeda, T. Imai, H. Inoue, Y. Kumagai, T. Miyakawa, H. Murata, T. Ohno, A. Okuyama, R. Oyama, Y. Sasaki, Y. Shimazu, K. Shimoji, Y. Sumida, M. Suzuki, H. Taniguchi, H. Tsuchiyama, D. Uesawa, H. Yokota, and R. Yoshida. An introduction to himawari-8/9 - japan's new-generation geostationary meteorological satellites. *Journal of the Meteorological Society of Japan. Ser. II*, 94(2): 151–183, 2016. doi: 10.2151/jmsj.2016-009.

L. Bock, A. Lauer, M. Schlund, M. Barreiro, N. Bellouin, C. Jones, G. A. Meehl, V. Predoi, M. J. Roberts, and V. Eyring. Quantifying progress across different CMIP phases with the ESMValTool. *Journal of Geophysical Research: Atmospheres*, 125(21): e2019JD032321, oct 2020. doi: 10.1029/2019JD032321.

A. Bodas-Salcedo, K. D. Williams, M. A. Ringer, I. Beau, J. N. S. Cole, J.-L. Dufresne, T. Koshiro, B. Stevens, Z. Wang, and T. Yokohata. Origins of the solar radiation biases over the southern ocean in cfmip2 models*. *Journal of Climate*, 27(1):41–56, Jan. 2014. ISSN 1520-0442. doi: 10.1175/JCLI-D-13-00169.1.

O. Bruno, C. Hoose, T. Storelvmo, Q. Coopman, and M. Stengel. Exploring the cloud top phase partitioning in different cloud types using active and passive satellite sensors. *Geophysical Research Letters*, 48(2), jan 2021. doi: 10.1029/2020GL089863.

L. Bugliaro, T. Zinner, C. Keil, B. Mayer, R. Hollmann, M. Reuter, and W. Thomas. Validation of cloud property retrievals with simulated satellite radiances: a case study for SEVIRI. *Atmospheric Chemistry and Physics*, 11(12):5603–5624, jun 2011. doi: 10.5194/acp-11-5603-2011.

M. Ceccaldi, J. Delanoë, R. J. Hogan, N. L. Pounder, A. Protat, and J. Pelon. From CloudSat-CALIPSO to EarthCare: Evolution of the DARDAR cloud classification and its comparison to airborne radar-lidar observations. *Journal of Geophysical Research: Atmospheres*, 118(14):7962–7981, jul 2013. doi: 10.1002/jgrd.50579.

P. Ceppi, F. Brient, M. D. Zelinka, and D. L. Hartmann. Cloud feedback mechanisms and their representation in global climate models. *WIREs Climate Change*, 8(4), may 2017. doi: 10.1002/wcc.465.

G. Cesana and H. Chepfer. Evaluation of the cloud thermodynamic phase in a climate model using CALIPSO-GOCCP. *Journal of Geophysical Research: Atmospheres*, 118 (14):7922–7937, jul 2013. doi: 10.1002/jgrd.50376.

G. Cesana and T. Storelvmo. Improving climate projections by understanding how cloud phase affects radiation. *Journal of Geophysical Research: Atmospheres*, 122(8):4594–4599, apr 2017. doi: 10.1002/2017JD026927.

G. Cesana, J. E. Kay, H. Chepfer, J. M. English, and G. Boer. Ubiquitous low-level liquid-containing arctic clouds: New observations and climate model constraints from CALIPSO-GOCCP. *Geophysical Research Letters*, 39(20), oct 2012. doi: 10.1029/2012 GL053385.

G. Cesana, D. E. Waliser, X. Jiang, and J.-L. F. Li. Multimodel evaluation of cloud phase transition using satellite and reanalysis data. *Journal of Geophysical Research: Atmospheres*, 120(15):7871–7892, aug 2015. doi: 10.1002/2014JD022932.

G. V. Cesana, T. Khadir, H. Chepfer, and M. Chiriaco. Southern ocean solar reflection biases in CMIP6 models linked to cloud phase and vertical structure representations. *Geophysical Research Letters*, 49(22):e2022GL099777, nov 2022. doi: 10.1029/2022GL 099777.

A. Cheng, K.-M. Xu, Y. Hu, and S. Kato. Impact of a cloud thermodynamic phase parameterization based on calipso observations on climate simulation. *Journal of Geophysical Research: Atmospheres*, 117(D9), 2012. doi: https://doi.org/10.1029/2011JD017263.

Q. Coopman, C. Hoose, and M. Stengel. Analysis of the thermodynamic phase transition of tracked convective clouds based on geostationary satellite observations. *Journal of Geophysical Research: Atmospheres*, 125(11):e2019JD032146, jun 2020a. doi: 10.1029/ 2019JD032146.

Q. Coopman, J. Riedi, S. Zeng, and T. J. Garrett. Space-based analysis of the cloud thermodynamic phase transition for varying microphysical and meteorological regimes. *Geophysical Research Letters*, 47(6), mar 2020b. doi: 10.1029/2020GL087122.

Q. Coopman, C. Hoose, and M. Stengel. Analyzing the thermodynamic phase partitioning of mixed phase clouds over the southern ocean using passive satellite observations. *Geophysical Research Letters*, 48(7), apr 2021. ISSN 1944-8007. doi: 10.1029/2021GL093225.

J. Delanoë and R. J. Hogan. A variational scheme for retrieving ice cloud properties from combined radar, lidar, and infrared radiometer. *Journal of Geophysical Research*, 113 (D7):D07204, apr 2008. doi: 10.1029/2007JD009000.

J. Delanoë and R. J. Hogan. Combined CloudSat-CALIPSO-MODIS retrievals of the properties of ice clouds. *Journal of Geophysical Research*, 115(D4):0148–0227, jul 2010. doi: 10.1029/2009JD012346.

J. Delanoë, A. Protat, O. Jourdan, J. Pelon, M. Papazzoni, R. Dupuy, J.-F. Gayet, and C. Jouan. Comparison of airborne in situ, airborne radar–lidar, and spaceborne radar–lidar retrievals of polar ice cloud properties sampled during the POLARCAT

campaign. *Journal of Atmospheric and Oceanic Technology*, 30(1):57–73, jan 2013. doi: 10.1175/JTECH-D-11-00200.1.

D. Donovan and A. Van Lammeren. Combined lidar and radar cloud particle effective size retrievals made during clara. *Physics and Chemistry of the Earth, Part B: Hydrology, Oceans and Atmosphere*, 25(2):115–120, Jan. 2000. ISSN 1464-1909. doi: 10.1016/S146 4-1909(99)00136-7.

M. Doutriaux-Boucher and J. Quaas. Evaluation of cloud thermodynamic phase parametrizations in the LMDZ GCM by using POLDER satellite data. *Geophysical Research Letters*, 31(6):L06126, mar 2004. doi: 10.1029/2003GL019095.

P. Dubuisson, V. Giraud, J. Pelon, B. Cadet, and P. Yang. Sensitivity of thermal infrared radiation at the top of the atmosphere and the surface to ice cloud microphysics. *Journal of Applied Meteorology and Climatology*, 47(10):2545–2560, oct 2008. doi: 10.1175/2008 JAMC1805.1.

Y. Durand, P. Hallibert, M. Wilson, M. Lekouara, S. Grabarnik, D. Aminou, P. Blythe, B. Napierala, J.-L. Canaud, O. Pigouche, J. Ouaknine, and B. Verez. The flexible combined imager onboard MTG: from design to calibration. In R. Meynart, S. P. Neeck, and H. Shimoda, editors, *Sensors, Systems, and Next-Generation Satellites XIX*, volume 9639, page 963903. International Society for Optics and Photonics, SPIE Remote Sensing, 2015. doi: 10.1117/12.2196644. URL https://doi.org/10.1117/12.2196644.

C. Emde, R. Buras-Schnell, A. Kylling, B. Mayer, J. Gasteiger, U. Hamann, J. Kylling, B. Richter, C. Pause, T. Dowling, and L. Bugliaro. The libRadtran software package for radiative transfer calculations (version 2.0.1). *Geoscientific Model Development*, 9 (5):1647–1672, may 2016. doi: 10.5194/gmd-9-1647-2016.

F. Ewald, T. Kölling, A. Baumgartner, T. Zinner, and B. Mayer. Design and characterization of specMACS, a multipurpose hyperspectral cloud and sky imager. *Atmospheric Measurement Techniques*, 9(5):2015–2042, may 2016. doi: 10.5194/amt-9-2015-2016.

F. Ewald, S. Groß, M. Wirth, J. Delanoë, S. Fox, and B. Mayer. Why we need radar, lidar, and solar radiance observations to constrain ice cloud microphysics. *Atmospheric Measurement Techniques*, 14(7):5029–5047, jul 2021. doi: 10.5194/amt-14-5029-2021.

W. Findeisen. Kolloid-meteorologische vorgänge bei niederschlagsbildung. *(No Title)*, 55: 121, 1938.

S. Finkensieper, J. F. Meirink, G.-J. van Zadelhoff, T. Hanschmann, N. Benas, M. Stengel, P. Fuchs, R. Hollmann, and M. Werscheck. Claas-2: Cm saf cloud property dataset using seviri - edition 2. 2016. doi: 10.5676/EUM_SAF_CM/CLAAS/V002.

R. M. Forbes and M. Ahlgrimm. On the representation of high-latitude boundary layer mixed-phase cloud in the ecmwf global model. *Monthly Weather Review*, 142(9):3425–3445, Sept. 2014. ISSN 1520-0493. doi: 10.1175/MWR-D-13-00325.1.

P. Forster, T. Storelvmo, K. Armour, W. Collins, J.-L. Dufresne, D. Frame, D. Lunt, T. Mauritsen, M. Palmer, M. Watanabe, M. Wild, and H. Zhang. The earth's energy budget, climate feedbacks, and climate sensitivity. *Climate Change 2021: The Physical Science Basis. Contribution of Working Group I to the Sixth Assessment Report of the Intergovernmental Panel on Climate Change*, 2021. doi: 10.1017/9781009157896.009.

A. Garnier, J. Pelon, P. Dubuisson, M. Faivre, O. Chomette, N. Pascal, and D. P. Kratz. Retrieval of cloud properties using CALIPSO imaging infrared radiometer. part i: Effective emissivity and optical depth. *Journal of Applied Meteorology and Climatology*, 51 (7):1407–1425, jul 2012. doi: 10.1175/JAMC-D-11-0220.1.

A. Gettelman and S. C. Sherwood. Processes responsible for cloud feedback. *Current Climate Change Reports*, 2(4):179–189, Oct. 2016. ISSN 2198-6061. doi: 10.1007/s406 41-016-0052-8.

D. Gregory and D. Morris. The sensitivity of climate simulations to the specification of mixed phase clouds. *Climate Dynamics*, 12(9):641–651, jul 1996. doi: 10.1007/BF0021 6271.

V. Hahn, R. Meerkötter, C. Voigt, S. Gisinger, D. Sauer, V. Catoire, V. Dreiling, H. Coe, C. Flamant, S. Kaufmann, J. Kleine, P. Knippertz, M. Moser, P. Rosenberg, H. Schlager, A. Schwarzenboeck, and J. Taylor. Pollution slightly enhances atmospheric cooling by low-level clouds in tropical west africa. *Atmospheric Chemistry and Physics*, 23(15): 8515–8530, aug 2023. doi: 10.5194/acp-23-8515-2023.

J. Hansen, M. Sato, P. Kharecha, and K. von Schuckmann. Earth's energy imbalance and implications. *Atmospheric Chemistry and Physics*, 11(24):13421–13449, Dec. 2011. ISSN 1680-7324. doi: 10.5194/acp-11-13421-2011.

J. E. Hansen and L. D. Travis. Light scattering in planetary atmospheres. *Space Science Reviews*, 16(4):527–610, Oct. 1974. ISSN 1572-9672. doi: 10.1007/BF00168069.

B. E. Harrop and D. L. Hartmann. The role of cloud radiative heating within the atmosphere on the high cloud amount and top-of-atmosphere cloud radiative effect. *Journal of Advances in Modeling Earth Systems*, 8(3):1391–1410, Aug. 2016. ISSN 1942-2466. doi: 10.1002/2016MS000670.

A. Heidinger, Y. Li, B. Baum, R. Holz, S. Platnick, and P. Yang. Retrieval of cirrus cloud optical depth under day and night conditions from modis collection 6 cloud property data. *Remote Sensing*, 7(6):7257–7271, June 2015. ISSN 2072-4292. doi: 10.3390/rs70 607257.

A. K. Heidinger, M. J. Pavolonis, R. E. Holz, B. A. Baum, and S. Berthier. Using CALIPSO to explore the sensitivity to cirrus height in the infrared observations from NPOESS/VIIRS and GOES-r/ABI. *Journal of Geophysical Research*, 115, apr 2010. doi: 10.1029/2009JD012152.

R. J. Hogan, P. N. Francis, H. Flentje, A. J. Illingworth, M. Quante, and J. Pelon. Characteristics of mixed-phase clouds. i: Lidar, radar and aircraft observations from CLARE'98. *Quarterly Journal of the Royal Meteorological Society*, 129(592):2089–2116, jul 2003. doi: 10.1256/rj.01.208.

C. Hoose and O. Möhler. Heterogeneous ice nucleation on atmospheric aerosols: a review of results from laboratory experiments. *Atmospheric Chemistry and Physics*, 12(20): 9817–9854, Oct. 2012. ISSN 1680-7324. doi: 10.5194/acp-12-9817-2012.

Y. Hu, D. Winker, M. Vaughan, B. Lin, A. Omar, C. Trepte, D. Flittner, P. Yang, S. L. Nasiri, B. Baum, R. Holz, W. Sun, Z. Liu, Z. Wang, S. Young, K. Stamnes, J. Huang, and R. Kuehn. CALIPSO/CALIOP cloud phase discrimination algorithm. *Journal of Atmospheric and Oceanic Technology*, 26(11):2293–2309, nov 2009. doi: 10.1175/2009 JTECHA1280.1.

Y. Huang, S. T. Siems, M. J. Manton, A. Protat, and J. Delanoë. A study on the low-altitude clouds over the southern ocean using the DARDAR-MASK. *Journal of Geophysical Research: Atmospheres*, 117(D18):n/a–n/a, sep 2012. doi: 10.1029/2012JD017800.

Y. Huang, A. Protat, S. T. Siems, and M. J. Manton. A-train observations of maritime midlatitude storm-track cloud systems: Comparing the southern ocean against the north atlantic. *Journal of Climate*, 28(5):1920–1939, feb 2015. doi: 10.1175/JCLI-D-14-00169 .1.

A. Hünerbein, S. Bley, S. Horn, H. Deneke, and A. Walther. Cloud mask algorithm from the EarthCARE multi-spectral imager: the m-CM products. *Atmospheric Measurement Techniques*, nov 2022. doi: 10.5194/egusphere-2022-1240.

T. Inoue. On the temperature and effective emissivity determination of semi-transparent cirrus clouds by bi-spectral measurements in the 10μm window region. *Journal of the Meteorological Society of Japan. Ser. II*, 63(1):88–99, 1985. doi: 10.2151/jmsj1965.63. 1_88.

Intergovernmental Panel on Climate Change (IPCC). *Climate Change 2021 – The Physical Science Basis: Working Group I Contribution to the Sixth Assessment Report of the Intergovernmental Panel on Climate Change.* Cambridge University Press, 2021. doi: 10.1017/9781009157896.

International Air Transport Association (IATA). 2021 safety report. Technical report, 2022.

J. H. Jiang, H. Su, C. Zhai, V. S. Perun, A. Del Genio, L. S. Nazarenko, L. J. Donner, L. Horowitz, C. Seman, J. Cole, A. Gettelman, M. A. Ringer, L. Rotstayn, S. Jeffrey, T. Wu, F. Brient, J. Dufresne, H. Kawai, T. Koshiro, M. Watanabe, T. S. LÉcuyer, E. M. Volodin, T. Iversen, H. Drange, M. D. S. Mesquita, W. G. Read, J. W. Waters, B. Tian, J. Teixeira, and G. L. Stephens. Evaluation of cloud and water vapor simulations in

cmip5 climate models using nasa "a-train" satellite observations. *Journal of Geophysical Research: Atmospheres*, 117(D14), July 2012. ISSN 0148-0227. doi: 10.1029/2011JD01 7237.

E. Jäkel, M. Wendisch, F. Ewald, and T. Kölling. Analysis of the vertical distribution of the thermodynamic phase in tropical deep-convective clouds. 2016. doi: 10.1364/HISE .2016.HTu2F.1.

Z. A. Kanji, L. A. Ladino, H. Wex, Y. Boose, M. Burkert-Kohn, D. J. Cziczo, and M. Krämer. Overview of ice nucleating particles. *Meteorological Monographs*, 58:11–133, Jan. 2017. ISSN 0065-9401. doi: 10.1175/AMSMONOGRAPHS-D-16-0006.1.

J. R. Key and J. M. Intrieri. Cloud particle phase determination with the AVHRR. *Journal of Applied Meteorology*, 39(10):1797–1804, oct 2000. doi: 10.1175/1520-0450-39.10.1797.

A. Khain, M. Pinsky, and A. Korolev. Combined effect of the wegener–bergeron–findeisen mechanism and large eddies on microphysics of mixed-phase stratiform clouds. *Journal of the Atmospheric Sciences*, 79(2):383–407, feb 2022. doi: 10.1175/JAS-D-20-0269.1.

M. King, Y. Kaufman, W. Menzel, and D. Tanre. Remote sensing of cloud, aerosol, and water vapor properties from the moderate resolution imaging spectrometer (modis). *IEEE Transactions on Geoscience and Remote Sensing*, 30(1):2–27, 1992. ISSN 0196-2892. doi: 10.1109/36.124212.

G. Kirchhoff. Über das verhältnis zwischen dem emissionsvermögen und dem absorptionsvermögen der körper für wärme und licht. *Von Kirchhoff bis Planck: Theorie der Wärmestrahlung in Historisch-kritischer Darstellung*, pages 131–151, 1978.

S. Kirschler, C. Voigt, B. E. Anderson, G. Chen, E. C. Crosbie, R. A. Ferrare, V. Hahn, J. W. Hair, S. Kaufmann, R. H. Moore, D. Painemal, C. E. Robinson, K. J. Sanchez, A. J. Scarino, T. J. Shingler, M. A. Shook, K. L. Thornhill, E. L. Winstead, L. D. Ziemba, and A. Sorooshian. Overview and statistical analysis of boundary layer clouds and precipitation over the western north-atlantic ocean. *Atmospheric Chemistry and Physics*, may 2023. doi: 10.5194/egusphere-2023-898.

W. H. Knap, P. Stammes, and R. B. A. Koelemeijer. Cloud Thermodynamic Phase Determination from Near-Infrared Spectra of Reflected Sunlight. *Journal of the Atmospheric Sciences*, 59(1):83–96, jan 2002. doi: 10.1175/1520-0469(2002)059<0083: CTPDFN>2.0.CO;2.

M. Komurcu, T. Storelvmo, I. Tan, U. Lohmann, Y. Yun, J. E. Penner, Y. Wang, X. Liu, and T. Takemura. Intercomparison of the cloud water phase among global climate models. *Journal of Geophysical Research: Atmospheres*, 119(6):3372–3400, 2014. doi: https://doi.org/10.1002/2013JD021119. URL https://agupubs.onlinelibrary.wile y.com/doi/abs/10.1002/2013JD021119.

T. Koop, B. Luo, A. Tsias, and T. Peter. Water activity as the determinant for homogeneous ice nucleation in aqueous solutions. *Nature*, 406(6796):611–614, Aug. 2000. ISSN 1476-4687. doi: 10.1038/35020537.

A. Korolev and P. R. Field. The effect of dynamics on mixed-phase clouds: Theoretical considerations. *Journal of the Atmospheric Sciences*, 65(1):66–86, Jan. 2008. ISSN 0022-4928. doi: 10.1175/2007JAS2355.1.

A. Korolev, G. McFarquhar, P. R. Field, C. Franklin, P. Lawson, Z. Wang, E. Williams, S. J. Abel, D. Axisa, S. Borrmann, J. Crosier, J. Fugal, M. Krämer, U. Lohmann, O. Schlenczek, M. Schnaiter, and M. Wendisch. Mixed-phase clouds: Progress and challenges. *Meteorological Monographs*, 58:51–550, jan 2017. doi: 10.1175/AMSMON OGRAPHS-D-17-0001.1.

A. V. Korolev, G. A. Isaac, S. G. Cober, J. W. Strapp, and J. Hallett. Microphysical characterization of mixed-phase clouds. *Quarterly Journal of the Royal Meteorological Society*, 129(587):39–65, Jan. 2003. ISSN 1477-870X. doi: 10.1256/qj.01.204.

S. Kox, L. Bugliaro, and A. Ostler. Retrieval of cirrus cloud optical thickness and top altitude from geostationary remote sensing. *Atmospheric Measurement Techniques*, 7 (10):3233–3246, oct 2014. doi: 10.5194/amt-7-3233-2014.

W. Krebs, H. Mannstein, L. Bugliaro, and B. Mayer. Technical note: A new day- and night-time meteosat second generation cirrus detection algorithm MeCiDA. *Atmospheric Chemistry and Physics*, 7(24):6145–6159, dec 2007. doi: 10.5194/acp-7-6145-2007.

B. Kärcher and U. Lohmann. A parameterization of cirrus cloud formation: Heterogeneous freezing. *Journal of Geophysical Research: Atmospheres*, 108(D14), July 2003. ISSN 0148-0227. doi: 10.1029/2002JD003220.

J. Li, Q. Lv, M. Zhang, T. Wang, K. Kawamoto, S. Chen, and B. Zhang. Effects of atmospheric dynamics and aerosols on the fraction of supercooled water clouds. *Atmospheric Chemistry and Physics*, 17(3):1847–1863, feb 2017. doi: 10.5194/acp-17-1847-2017.

W. Li, F. Zhang, H. Lin, X. Chen, J. Li, and W. Han. Cloud detection and classification algorithms for himawari-8 imager measurements based on deep learning. *IEEE Transactions on Geoscience and Remote Sensing*, 60:1–17, 2022. doi: 10.1109/TGRS.2022.31 53129.

K. N. Liou. *An Introduction to Atmospheric Radiation*. Academic Press, San Diego, CA, USA and London, United Kingdom, 2nd edition edition, 2002. ISBN ISBN 9780124514515.

C. Listowski, J. Delanoë, A. Kirchgaessner, T. Lachlan-Cope, and J. King. Antarctic clouds, supercooled liquid water and mixed phase, investigated with DARDAR: geographical and seasonal variations. *Atmospheric Chemistry and Physics*, 19(10):6771–6808, may 2019. doi: 10.5194/acp-19-6771-2019.

E. P. Luke, P. Kollias, and M. D. Shupe. Detection of supercooled liquid in mixed-phase clouds using radar doppler spectra. *Journal of Geophysical Research*, 115(D19), oct 2010. doi: 10.1029/2009JD012884.

K. Mao, Z. Yuan, Z. Zuo, T. Xu, X. Shen, and C. Gao. Changes in global cloud cover based on remote sensing data from 2003 to 2012. *Chinese Geographical Science*, 29(2): 306–315, Mar. 2019. ISSN 1993-064X. doi: 10.1007/s11769-019-1030-6.

B. Marchant, S. Platnick, K. Meyer, G. T. Arnold, and J. Riedi. MODIS collection 6 shortwave-derived cloud phase classification algorithm and comparisons with CALIOP. *Atmospheric Measurement Techniques*, 9(4):1587–1599, apr 2016. doi: 10.5194/amt-9-1 587-2016.

A. V. Matus and T. S. L'Ecuyer. The role of cloud phase in earths radiation budget. *Journal of Geophysical Research: Atmospheres*, 122(5):2559–2578, mar 2017. doi: 10.1 002/2016JD025951.

B. Mayer and A. Kylling. Technical note: The libRadtran software package for radiative transfer calculations - description and examples of use. *Atmospheric Chemistry and Physics*, 5(7):1855–1877, jul 2005. doi: 10.5194/acp-5-1855-2005.

J. Mayer, L. Bugliaro, B. Mayer, D. Piontek, and C. Voigt. Bayesian cloud top phase determination for meteosat second generation. *EGUsphere*, 2024:1–32, 2024. doi: 10.5 194/egusphere-2023-2345. URL https://egusphere.copernicus.org/preprints/2 024/egusphere-2023-2345/.

D. T. McCoy, I. Tan, D. L. Hartmann, M. D. Zelinka, and T. Storelvmo. On the relationships among cloud cover, mixed-phase partitioning, and planetary albedo in gcms. *Journal of Advances in Modeling Earth Systems*, 8(2):650–668, May 2016. ISSN 1942-2466. doi: 10.1002/2015MS000589.

C. McErlich, A. McDonald, A. Schuddeboom, and I. Silber. Comparing satellite- and ground-based observations of cloud occurrence over high southern latitudes. *Journal of Geophysical Research: Atmospheres*, 126(6), Mar. 2021. ISSN 2169-8996. doi: 10.1029/ 2020JD033607.

G. M. McFarquhar, S. Ghan, J. Verlinde, A. Korolev, J. W. Strapp, B. Schmid, J. M. Tomlinson, M. Wolde, S. D. Brooks, D. Cziczo, M. K. Dubey, J. Fan, C. Flynn, I. Gultepe, J. Hubbe, M. K. Gilles, A. Laskin, P. Lawson, W. R. Leaitch, P. Liu, X. Liu, D. Lubin, C. Mazzoleni, A.-M. Macdonald, R. C. Moffet, H. Morrison, M. Ovchinnikov, M. D. Shupe, D. D. Turner, S. Xie, A. Zelenyuk, K. Bae, M. Freer, and A. Glen. Indirect and semi-direct aerosol campaign: The impact of arctic aerosols on clouds. *Bulletin of the American Meteorological Society*, 92(2):183–201, Feb. 2011. ISSN 1520-0477. doi: 10.1175/2010bams2935.1.

D. Menekay. Comparative analysis of optical in-situ probes and themsg satellite for improved detection of aircraft icingconditions. Master's thesis, Technical University Munich, 2023.

S. D. Miller, Y.-J. Noh, and A. K. Heidinger. Liquid-top mixed-phase cloud detection from shortwave-infrared satellite radiometer observations: A physical basis: Liquid-top mixed-phase cloud detection. *Journal of Geophysical Research: Atmospheres*, 119(13): 8245–8267, July 2014. ISSN 2169-897X. doi: 10.1002/2013JD021262.

G. Mioche, O. Jourdan, M. Ceccaldi, and J. Delanoë. Variability of mixed-phase clouds in the arctic with a focus on the svalbard region: a study based on spaceborne active remote sensing. *Atmospheric Chemistry and Physics*, 15(5):2445–2461, mar 2015. doi: 10.5194/acp-15-2445-2015.

H. Morrison, P. Zuidema, A. S. Ackerman, A. Avramov, G. de Boer, J. Fan, A. M. Fridlind, T. Hashino, J. Y. Harrington, Y. Luo, M. Ovchinnikov, and B. Shipway. Intercomparison of cloud model simulations of arctic mixed-phase boundary layer clouds observed during SHEBA/FIRE-ACE. *Journal of Advances in Modeling Earth Systems*, 3(2):n/a–n/a, feb 2011. doi: 10.1029/2011MS000066.

M. Moser, C. Voigt, T. Jurkat-Witschas, V. Hahn, G. Mioche, O. Jourdan, R. Dupuy, C. Gourbeyre, A. Schwarzenboeck, J. Lucke, Y. Boose, M. Mech, S. Borrmann, A. Ehrlich, A. Herber, C. Lüpkes, and M. Wendisch. Microphysical and thermodynamic phase analyses of arctic low-level clouds measured above the sea ice and the open ocean in spring and summer. *Atmospheric Chemistry and Physics*, 23(13):7257–7280, jul 2023. doi: 10.5194/acp-23-7257-2023.

J. Mülmenstädt, O. Sourdeval, J. Delanoë, and J. Quaas. Frequency of occurrence of rain from liquid-, mixed-, and ice-phase clouds derived from a-train satellite retrievals. *Geophysical Research Letters*, 42(15):6502–6509, Aug. 2015. ISSN 1944-8007. doi: 10.1 002/2015GL064604.

S. L. Nasiri and B. H. Kahn. Limitations of bispectral infrared cloud phase determination and potential for improvement. *Journal of Applied Meteorology and Climatology*, 47(11): 2895–2910, nov 2008. doi: 10.1175/2008JAMC1879.1.

Y.-J. Noh and S. D. Miller. Detection of mixed-phase clouds from shortwave and thermal infrared satellite observations. pages 43–67, 2018. doi: 10.1016/B978-0-12-810549-8.0 0003-9.

F. Parol, J. C. Buriez, G. Brogniez, and Y. Fouquart. Information content of AVHRR channels 4 and 5 with respect to the effective radius of cirrus cloud particles. *Journal of Applied Meteorology*, 30(7):973–984, jul 1991. doi: 10.1175/1520-0450-30.7.973.

M. Pavolonis and C. Calvert. Enterprise Algorithm Theoretical Basis Document For Cloud Type and Cloud Phase. Technical report, NOAA NESDIS CENTER for SATELLITE APPLICATIONS and RESEARCH, 2020.

M. J. Pavolonis. Advances in extracting cloud composition information from spaceborne infrared radiances—a robust alternative to brightness temperatures. part i: Theory. *Journal of Applied Meteorology and Climatology*, 49(9):1992–2012, sep 2010. doi: 10.1175/2010JAMC2433.1.

C. A. Peterson, X. Huang, X. Chen, and P. Yang. Synergistic use of far- and mid-infrared spectral radiances for satellite-based detection of polar ice clouds over ocean. *Journal of Geophysical Research: Atmospheres*, 127(9), May 2022. ISSN 2169-8996. doi: 10.1029/2021JD035733.

D. Piontek. *A novel machine learning-based satellite retrieval of volcanic ash for Meteosat covering the petrological variability.* PhD thesis, Ludwig-Maximilians-University Munich, 2022.

D. Piontek, L. Bugliaro, R. Müller, L. Muser, and M. Jerg. Multi-channel spectral band adjustment factors for thermal infrared measurements of geostationary passive imagers. *Remote Sensing*, 15(5):1247, feb 2023. doi: 10.3390/rs15051247.

S. Platnick, K. G. Meyer, M. D. King, G. Wind, N. Amarasinghe, B. Marchant, G. T. Arnold, Z. Zhang, P. A. Hubanks, R. E. Holz, P. Yang, W. L. Ridgway, and J. Riedi. The MODIS cloud optical and microphysical products: Collection 6 updates and examples from terra and aqua. *IEEE Transactions on Geoscience and Remote Sensing*, 55(1): 502–525, jan 2017. doi: 10.1109/TGRS.2016.2610522.

H. Pruppacher and J. Klett. Microphysics of clouds and precipitation. *Atmospheric and Oceanographic Sciences Library*, 2010. ISSN 1383-8601. doi: 10.1007/978-0-306-48100-0.

R. M. Rauber and A. Tokay. An explanation for the existence of supercooled water at the top of cold clouds. *Journal of the Atmospheric Sciences*, 48(8):1005–1023, apr 1991. doi: 10.1175/1520-0469(1991)048<1005:AEFTEO>2.0.CO;2.

P. Ricaud, M. D. Guasta, A. Lupi, R. Roehrig, E. Bazile, P. Durand, J.-L. Attié, A. Nicosia, and P. Grigioni. Supercooled liquid water clouds observed over dome c, antarctica: temperature sensitivity and surface radiation impact. *Atmospheric Chemistry and Physics*, 24(1):613–630, jun 2024. doi: 10.5194/acp-2022-433.

J. Schmetz, P. Pili, S. Tjemkes, D. Just, J. Kerkmann, S. Rota, and A. Ratier. An introduction to meteosat second generation (MSG). *Bulletin of the American Meteorological Society*, 83(7):992–992, jul 2002. doi: 10.1175/1520-0477(2002)083<0977: AITMSG>2.3.CO;2.

T. J. Schmit, P. Griffith, M. M. Gunshor, J. M. Daniels, S. J. Goodman, and W. J. Lebair. A closer look at the abi on the goes-r series. *Bulletin of the American Meteorological Society*, 98(4):681–698, Apr. 2017. ISSN 1520-0477. doi: 10.1175/BAMS-D-15-00230.1.

M. D. Shupe, S. Y. Matrosov, and T. Uttal. Arctic mixed-phase cloud properties derived from surface-based sensors at sheba. *Journal of the Atmospheric Sciences*, 63(2):697–711, Feb. 2006. ISSN 0022-4928. doi: 10.1175/JAS3659.1.

M. D. Shupe, J. S. Daniel, G. de Boer, E. W. Eloranta, P. Kollias, C. N. Long, E. P. Luke, D. D. Turner, and J. Verlinde. A focus on mixed-phase clouds: The status of ground-based observational methods. *Bulletin of the American Meteorological Society*, 89(10):1549–1562, Oct. 2008. ISSN 1520-0477. doi: 10.1175/2008bams2378.1.

G. L. Stephens, D. G. Vane, R. J. Boain, G. G. Mace, K. Sassen, Z. Wang, A. J. Illingworth, E. J. O'connor, W. B. Rossow, S. L. Durden, S. D. Miller, R. T. Austin, A. Benedetti, and C. Mitrescu. The cloudsat mission and the a-train: A new dimension of space-based observations of clouds and precipitation. *Bulletin of the American Meteorological Society*, 83(12):1771–1790, Dec. 2002. ISSN 1520-0477. doi: 10.1175/BAMS-83-12-1771.

K. I. Strabala, S. A. Ackerman, and W. P. Menzel. Cloud properties inferred from 8-12-μm data. 33(2):212–229, feb 1994. doi: 10.1175/1520-0450(1994)033<0212:CPIFD>2.0.CO;2.

J. Strandgren. The life cycle of anvil cirrus clouds from a combination of passive and active satellite remote sensing. 2018. doi: 10.5282/edoc.22789.

J. Strandgren, L. Bugliaro, F. Sehnke, and L. Schröder. Cirrus cloud retrieval with MSG/SEVIRI using artificial neural networks. *Atmospheric Measurement Techniques*, 10(9):3547–3573, sep 2017. doi: 10.5194/amt-10-3547-2017.

C. J. Stubenrauch, W. B. Rossow, S. Kinne, S. Ackerman, G. Cesana, H. Chepfer, L. D. Girolamo, B. Getzewich, A. Guignard, A. Heidinger, B. C. Maddux, W. P. Menzel, P. Minnis, C. Pearl, S. Platnick, C. Poulsen, J. Riedi, S. Sun-Mack, A. Walther, D. Winker, S. Zeng, and G. Zhao. Assessment of global cloud datasets from satellites: Project and database initiated by the GEWEX radiation panel. *Bulletin of the American Meteorological Society*, 94(7):1031–1049, jul 2013. doi: 10.1175/BAMS-D-12-00117.1.

C. J. Stubenrauch, A. G. Feofilov, S. E. Protopapadaki, and R. Armante. Cloud climatologies from the infrared sounders AIRS and IASI: strengths and applications. *Atmospheric Chemistry and Physics*, 17(22):13625–13644, nov 2017. doi: 10.5194/acp-17-13625-2017.

R. B. Stull. *Practical meteorology: an algebra-based survey of atmospheric science*. University of British Columbia, 2015. ISBN 978-0-88865-283-6. URL `https://www.eoas.ubc.ca/books/Practical_Meteorology/`.

S. C. Sullivan and C. Hoose. Clouds and their climatic impacts: Radiation, circulation, and precipitation. *Geophysical Monograph Series*, Dec. 2023. ISSN 2328-8779. doi: 10.1002/9781119700357.

I. Tan and T. Storelvmo. Sensitivity study on the influence of cloud microphysical parameters on mixed-phase cloud thermodynamic phase partitioning in cam5. *Journal of the Atmospheric Sciences*, 73(2):709–728, Feb. 2016. ISSN 1520-0469. doi: 10.1175/jas-d-15-0152.1.

I. Tan, T. Storelvmo, and Y.-S. Choi. Spaceborne lidar observations of the ice-nucleating potential of dust, polluted dust, and smoke aerosols in mixed-phase clouds. *Journal of Geophysical Research: Atmospheres*, 119(11):6653–6665, jun 2014. doi: 10.1002/2013JD 021333.

I. Tan, T. Storelvmo, and M. D. Zelinka. Observational constraints on mixed-phase clouds imply higher climate sensitivity. *Science*, 352(6282):224–227, apr 2016. doi: 10.1126/science.aad5300.

W.-K. Tao, S. Lang, X. Zeng, X. Li, T. Matsui, K. Mohr, D. Posselt, J. Chern, C. Peters-Lidard, P. M. Norris, I.-S. Kang, I. Choi, A. Hou, K.-M. Lau, and Y.-M. Yang. The goddard cumulus ensemble model (gce): Improvements and applications for studying precipitation processes. *Atmospheric Research*, 143:392–424, June 2014. ISSN 0169-8095. doi: 10.1016/j.atmosres.2014.03.005.

M. Vázquez-Navarro, H. Mannstein, and S. Kox. Contrail life cycle and properties from 1 year of MSG/SEVIRI rapid-scan images. *Atmospheric Chemistry and Physics*, 15(15): 8739–8749, aug 2015. doi: 10.5194/acp-15-8739-2015.

D. Villanueva, F. Senf, and I. Tegen. Hemispheric and seasonal contrast in cloud thermodynamic phase from a-train spaceborne instruments. *Journal of Geophysical Research: Atmospheres*, mar 2021. doi: 10.1029/2020JD034322.

J. M. Wallace and P. V. Hobbs. *Atmospheric Science - An Introductory Survey*. Elsevier, 2006. ISBN 9780127329512. doi: 10.1016/C2009-0-00034-8.

Z. Wang. Level 2 combined radar and lidar cloud scenario classification product process description and interface control document. *JPL Rep 22*, 2012.

Z. Wang, H. Letu, H. Shang, C. Zhao, J. Li, and R. Ma. A supercooled water cloud detection algorithm using himawari-8 satellite measurements. *Journal of Geophysical Research: Atmospheres*, 124(5):2724–2738, mar 2019. doi: 10.1029/2018JD029784.

A. Weber, T. Kölling, V. Pörtge, A. Baumgartner, C. Rammeloo, T. Zinner, and B. Mayer. Polarization upgrade of specmacs: calibration and characterization of the 2d rgb polarization-resolving cameras. *Atmospheric Measurement Techniques*, 17(5):1419–1439, Mar. 2024. ISSN 1867-8548. doi: 10.5194/amt-17-1419-2024.

T. Wehr, T. Kubota, G. Tzeremes, K. Wallace, H. Nakatsuka, Y. Ohno, R. Koopman, S. Rusli, M. Kikuchi, M. Eisinger, T. Tanaka, M. Taga, P. Deghaye, E. Tomita, and D. Bernaerts. The earthcare mission – science and system overview. *Atmospheric Measurement Techniques*, 16(15):3581–3608, Aug. 2023. ISSN 1867-8548. doi: 10.5194/amt-16-3581-2023.

D. M. Winker, J. R. Pelon, and M. P. McCormick. The calipso mission: spaceborne lidar for observation of aerosols and clouds. In U. N. Singh, T. Itabe, and Z. Liu, editors, *Lidar Remote Sensing for Industry and Environment Monitoring III*. SPIE, Mar. 2003. doi: 10.1117/12.466539.

T. J. Zaremba, R. M. Rauber, G. M. McFarquhar, M. Hayman, J. A. Finlon, and D. M. Stechman. Phase characterization of cold sector southern ocean cloud tops: Results from SOCRATES. *Journal of Geophysical Research: Atmospheres*, 125(24), dec 2020. doi: 10.1029/2020JD033673.

M. D. Zelinka, T. A. Myers, D. T. McCoy, S. Po-Chedley, P. M. Caldwell, P. Ceppi, S. A. Klein, and K. E. Taylor. Causes of higher climate sensitivity in CMIP6 models. *Geophysical Research Letters*, 47(1), jan 2020. doi: 10.1029/2019GL085782.

D. Zhang, Z. Wang, and D. Liu. A global view of midlevel liquid-layer topped stratiform cloud distribution and phase partition from CALIPSO and CloudSat measurements. *Journal of Geophysical Research*, 115:D00H13, feb 2010. doi: 10.1029/2009JD012143.

D. Zhang, D. Liu, T. Luo, Z. Wang, and Y. Yin. Aerosol impacts on cloud thermodynamic phase change over east asia observed with calipso and cloudsat measurements. *Journal of Geophysical Research: Atmospheres*, 120(4):1490–1501, 2015. doi: https://doi.org/10.1002/2014JD022630. URL https://agupubs.onlinelibrary.wiley.com/doi/abs/10.1002/2014JD022630.

D. Zhang, Z. Wang, P. Kollias, A. M. Vogelmann, K. Yang, and T. Luo. Ice particle production in mid-level stratiform mixed-phase clouds observed with collocated a-train measurements. *Atmospheric Chemistry and Physics*, 18(6):4317–4327, mar 2018. doi: 10.5194/acp-18-4317-2018.

G. Zhou, J. Wang, Y. Yin, X. Hu, H. Letu, B.-J. Sohn, Y. L. Yung, and C. Liu. Detecting supercooled water clouds using passive radiometer measurements. *Geophysical Research Letters*, 49(4):e2021GL096111, feb 2022. doi: 10.1029/2021GL096111.

T. Zinner, H. Mannstein, and A. Tafferner. Cb-tram: Tracking and monitoring severe convection from onset over rapid development to mature phase using multi-channel meteosat-8 seviri data. *Meteorology and Atmospheric Physics*, 101(3–4):191–210, May 2008. ISSN 1436-5065. doi: 10.1007/s00703-008-0290-y.

Acknowledgements

This work would not have been possible without the support of many people. First of all, I would like to thank Christiane Voigt for giving me the opportunity to do my PhD at the Institute of Atmospheric Physics of the German Aerospace Center and for supporting my research and my participation in various workshops and conferences. I am very grateful for your scientific guidance, your encouragement and for the fact that you trusted me and gave me the freedom to work on the topics that interested me. I am also very grateful that you supported my interest in participating in flight campaigns. Next, I would like to thank Bernhard Mayer for his supervision of my work, his advice, and for guiding my research with his immense knowledge of cloud physics, remote sensing, and radiative transfer. In particular, I would like to express my deepest gratitude to Luca Bugliaro, who introduced me to the field of cloud remote sensing, helped me throughout my PhD with invaluable feedback, reviewed all my papers, posters and presentations, and always had an open door for questions and discussions. Thank you for sharing your time and knowledge with me, it was always a pleasure to work with you.

This work was funded by the CRC/TR 301 TPChange project. I am very grateful for the financial support and all the opportunities, conferences and workshops for early career researchers that TPChange has provided. I would like to thank Peter Hoor and all the other TPChange coordinators for managing this project and creating such a nice community and environment for discussions. I would also like to thank Vera Bense for organising and coordinating the great early career researchers events. I am grateful to all the members of TPChange for the pleasant working environment.

During my time at the Institute of Atmospheric Physics I had the opportunity to participate in three airborne field campaigns, where I learned a lot about in-situ cloud measurements, flight planning, weather briefings and the excitement of measurement flights. Thanks to the teams from Cirrus-HL in Oberpfaffenhofen, HALO-(AC)^3 in Svalbard and SENS4ICE in Toulouse. I feel very fortunate to have had these opportunities. Thanks to everyone who made these campaigns possible and thanks to Elena de la Torre Castro, Manuel Moser, Johannes Lucke and Deniz Menekay for making these campaign trips so much fun.

I also had the opportunity to spend a month as a visiting scientist at the European Space Agency (ESA) in Frascati. I am very grateful to Diego Fernàndez Prieto for making this visit possible and to Edward Malina for introducing me to everything I needed to know at ESA.